DGK Veröffentlichungen der DGK

Ausschuss Geodäsie der Bayerischen Akademie der Wissenschaften

Reihe C | Dissertationen | Heft Nr. 938

Magdalena Stefanova Vassileva

Satellite Radar Interferometry for Geohazards: From Ground Deformation to Processes Understanding

München 2024

Bayerische Akademie der Wissenschaften

ISSN 0065-5325 ISBN 978-3-7696-5350-2

Diese Arbeit ist gleichzeitig veröffentlicht in:
Wissenschaftliche Arbeiten der Fachrichtung Geodäsie und Geoinformatik der Leibniz Universität Hannover
ISSN 0174-1454, Nr. 398, Hannover 2024

DGK Veröffentlichungen der DGK

Ausschuss Geodäsie der Bayerischen Akademie der Wissenschaften

Reihe C Dissertationen Heft Nr. 938

Satellite Radar Interferometry for Geohazards: From Ground Deformation to Processes Understanding

Von der Fakultät für Bauingenieurwesen und Geodäsie
der Gottfried Wilhelm Leibniz Universität Hannover
zur Erlangung des Grades
Doktor-Ingenieurin (Dr.-Ing.)
genehmigte Dissertation

von

Magdalena Stefanova Vassileva, M. Sc.

München 2024

Bayerische Akademie der Wissenschaften

ISSN 0065-5325 ISBN 978-3-7696-5350-2

Diese Arbeit ist gleichzeitig veröffentlicht in:
Wissenschaftliche Arbeiten der Fachrichtung Geodäsie und Geoinformatik der Leibniz Universität Hannover
ISSN 0174-1454, Nr. 398, Hannover 2024

Adresse der DGK:



Ausschuss Geodäsie der Bayerischen Akademie der Wissenschaften (DGK)

Alfons-Goppel-Straße 11 ● D – 80 539 München

Telefon +49 - 331 - 6264 1685 ● E-Mail post@dgk.badw.de

http://www.dgk.badw.de

Prüfungskommission:

Vorsitzender: Prof. Dr.-Ing. habil. Christian Heipke

Referentin: Prof. Dr. Mahdi Motagh

Korreferenten: Prof. Dr.-Ing. habil. Monika Sester
Prof. Dr. Paolo Tarolli (University of Padova)

Tag der mündlichen Prüfung: 04.03.2024

© 2024 Bayerische Akademie der Wissenschaften, München

Alle Rechte vorbehalten. Ohne Genehmigung der Herausgeber ist es auch nicht gestattet,
die Veröffentlichung oder Teile daraus auf photomechanischem Wege (Photokopie, Mikrokopie) zu vervielfältigen

ISSN 0065-5325 ISBN 978-3-7696-5350-2

Abstract

Every year geohazards, including earthquakes, landslides, volcano eruptions and landslides, claim thousands of lives and result in acute economic, material and environmental losses. Identifying where adverse geological events are occurring or might occur in the future, assessing their magnitude, monitoring their spatiotemporal evolution, and investigating the key physical-mechanical aspects and main driving climatic and environmental factors are the first steps toward the potential prevention and mitigation of geohazards. To gather the needed geohazard knowledge, a multi-sensor and multi-parameter data collection is needed. In the past few decades, Satellite Earth Observation (EO) missions have revolutionized data collection on the Earth's surface by providing cost-effective, large-scale, high-quality and systematic imagery. Nowadays, Satellite Radar Interferometry is increasingly used by different stakeholders to measure ground deformations. The continuous and systematic acquisition of SAR missions opened the opportunity to apply SAR Interferometry for near-real-time geohazard applications. However, many research gaps remain on how to interpret the ground deformation observations and how to derive a comprehensive understanding of the geological process and driving forces that lead to geohazards. These research questions were addressed in this PhD based on three analytical pillars: ground deformation analysis; numerical source modeling; and driving external factors analysis. Five different geohazard events were successfully studied and important insights were derived for all the case studied. The investigation of land subsidence in the municipality of Maceió (Brazil) correlated the ground deformation to deep-seated salt mining cavities instabilities. The analysis of the April 2019 landslide failure in Hoseynabad-e Kalpush village (north–central Iran) shows how a previously relict landslide reactivated following water impoundment. The co-seismic analysis of the Mw 6.6 29th of March 2017 offshore earthquake on the eastern coast of the Kamchatka peninsula (Russia) demonstrates that the area north of the Pacific slab subduction zone has higher seismic and tsunamigenic hazards than previously thought. The study of the 2020 geothermal unrest close to the 2021 Fagradalsfjall eruption site (Iceland) gives insight into the interaction between volcanic processes and geothermal systems for proper geohazard assessment and prediction. The pre-failure analysis of the December 2018 flank collapse at Anak Krakatau volcano (Indonesia) shows that the instability was ongoing for years and accelerations correlated with magma intrusion were detected. The outcomes of this PhD research demonstrate the valuable contribution of InSAR observations to the understanding of geological processes related to geohazard.

Zusammenfassung

Jedes Jahr fordern Georisiken wie Erdbeben, Erdrutsche, Vulkanausbrüche und Erdrutsche Tausende von Menschenleben und führen zu akuten wirtschaftlichen, materiellen und ökologischen Verlusten. Die Identifizierung von Orten, an denen geologische Ereignisse auftreten oder in Zukunft auftreten könnten, die Bewertung ihres Ausmaßes, die Überwachung ihrer räumlichen und zeitlichen Entwicklung und die Untersuchung der wichtigsten physikalisch-mechanischen Aspekte und der wichtigsten treibenden Klima- und Umweltfaktoren sind die ersten Schritte auf dem Weg zu einer möglichen Prävention und Eindämmung von Georisiken. Um das benötigte Wissen über Georisiken zu sammeln, ist eine Multi-Sensor- und Multi-Parameter-Datenerfassung erforderlich. In den letzten Jahrzehnten haben Satellitenmissionen zur Erdbeobachtung (EO) die Datenerfassung auf der Erdoberfläche revolutioniert, indem sie kostengünstige, großflächige, hochwertige und systematische Bilder liefern. Heutzutage wird die Satellitenradarinterferometrie zunehmend von verschiedenen Interessengruppen zur Messung von Bodenverformungen eingesetzt. Die kontinuierliche und systematische Erfassung von SAR-Missionen eröffnete die Möglichkeit, die SAR-Interferometrie für echtzeitnahe Geohazard-Anwendungen einzusetzen. Allerdings gibt es noch viele Forschungslücken bei der Interpretation der Bodenverformungsbeobachtungen und der Ableitung eines umfassenden Verständnisses der geologischen Prozesse und treibenden Kräfte, die zu Georisiken führen. Diese Forschungsfragen wurden in dieser Doktorarbeit auf der Grundlage von drei analytischen Säulen behandelt: Analyse der Bodenverformung, numerische Quellenmodellierung und Analyse der treibenden externen Faktoren. Fünf verschiedene Georisikoereignisse wurden erfolgreich untersucht, und für alle untersuchten Fälle wurden wichtige Erkenntnisse gewonnen. Die Untersuchung von Bodensenkungen in der Gemeinde Maceió (Brasilien) brachte die Bodenverformung mit tiefliegenden Salzabbauhohlräumen in Verbindung. Die Analyse des Erdrutsches vom April 2019 im Dorf Hoseynabad-e Kalpush (Nord-Zentral-Iran) zeigt, wie ein zuvor reliktischer Erdrutsch nach einer Wasseraufstauung reaktiviert wurde. Die koseismische Analyse des Offshore-Erdbebens der Stärke 6,6 vom 29. März 2017 an der Ostküste der Halbinsel Kamtschatka (Russland) zeigt, dass das Gebiet nördlich der Subduktionszone der pazifischen Platte eine höhere seismische und tsunamigene Gefährdung aufweist als bisher angenommen. Die Untersuchung der geothermischen Unruhen im Jahr 2020 in der Nähe der Eruptionsstelle des Fagradalsfjall (Island) im Jahr 2021 gibt Aufschluss über die Wechselwirkung zwischen vulkanischen Prozessen und geothermischen Systemen und ermöglicht eine angemessene Bewertung und Vorhersage von Georisiken. Die Analyse des Flankeneinsturzes vom Dezember 2018 am Vulkan Anak Krakatau (Indonesien) zeigt, dass die Instabilität seit Jahren anhielt und Beschleunigungen, die mit Magmaintrusion korrelierten, festgestellt wurden. Die Ergebnisse dieser Doktorarbeit zeigen den wertvollen Beitrag von InSAR-Beobachtungen zum Verständnis geologischer Prozesse im Zusammenhang mit Georisiken.

To those who don't stay "neutral" or silent in front of social and climate injustices, in times when freedom of speech is free only if it conforms to the mainstream and dominant institutional narrative.

Acknowledgements

This research was a long journey of personal and scientific growth during which I met many amazing people who supported me and contributed to it in different ways. I want to acknowledge the constant human and scientific support of Prof. Mahdi Motagh, who believed in me from the beginning and was an important guide in all aspects of my research. He involved me in so many different projects from which I contributed and learned a lot; he provided me with opportunities to travel get to know different people and food, and see different geohazards; and he always found a way to guarantee economic security for me during my PhD. I want to acknowledge Sigrid Roessner for the motivational discussions and constructive feedback. I want to acknowledge Uli, who taught me that geological maps hide so much information about the earth's processes (might his soul rest in peace). I want to acknowledge Prof. Thomas Walter, who introduced me to the magic world of volcanoes, involved me in many interesting projects and made me part of a group of enthusiastic volcanologists. A special thanks to Alina and Edgar with whom I laughed a lot and learned to be less afraid of walking on active volcanoes. I want to acknowledge Djamil, for the great colleague and friend he has become. I want to acknowledge the indispensable support of Sylvia Magnussen and Christin Skala, without whom I would have never been able to navigate through hardware, software and GFZ bureaucracy. I want to acknowledge all the people with whom I shared field trips, sleeping in tents or fancy hotels, spending hours driving or walking on steep hills, and eating a variety of good dishes or just some canned food. I want to thank all my colleagues with whom I share dog walks, coffees, talks, frustrations and dreams. A special thanks to Freddie and Freddy, who were my main anchors at the beginning of this journey. A special thanks to my InSAR group Julia, Mahmud, Andreas, Wandi, Zhuge, Ritu, Zelong, Haonan, Shagun and many more. To my favourite Latin American colleagues Thyago, Eduardo and Johnny for the professional and human exchanges. I want to thank all the great scientists I had the privilege to collaborate with. I want to acknowledge the editors and reviewers of my papers. Thanks to the committee of my PhD defence: Prof. Monika Sester, Prof. Paolo Tarolli and Prof. Christian Heipke. A special acknowledgement to all the people outside work who supported and tolerated me during these years. To my messed up and loving family, to my mum, to my old friends from my, seems like, other lives. A last spatial acknowledgement goes to Hayfa, my dog and partner in life, who has been with me in these PhD years.

Contents

List of Abbreviations **xvii**

1 Introduction **1**
1.1 Background/motivation . . . 1
1.2 Research question . . . 3
1.2.1 Land subsidence in the municipality of Maceió (Brazil) . . . 4
1.2.2 Landslide failure in Hoseynabad-e Kalpush village (north–central Iran) 4
1.2.3 Offshore earthquake in the eastern coast of Kamchatka peninsula (Russia) . . . 5
1.2.4 Cyclical geothermal unrest at Fagradalsfjall volcano(Iceland) . . . 5
1.2.5 Flank collapse at Anak Krakatau volcano (Indonesia) . . . 5
1.3 Structure of the manuscript . . . 6

2 Methodological Background **7**
2.1 Ground Deformation Analysis . . . 7
2.1.1 InSAR . . . 7
2.1.2 Digital Image Correlation . . . 11
2.2 Numerical Source Modeling . . . 12
2.3 Driving external factors analysis . . . 13

3 Application to Geohazards **15**
3.1 Land Subsidence . . . 15
3.2 Landslide . . . 18
3.3 Tectonic related processes . . . 24
3.3.1 Earthquake . . . 25
3.3.2 Volcanic activities . . . 29

4 Land subsidence in the municipality of Macei **33**
4.1 Abstract . . . 34
4.2 Introduction . . . 34
4.3 Data and methods . . . 36
4.3.1 Multi-temporal DInSAR . . . 36
4.3.2 Inverse numerical modelling . . . 37
4.3.3 2D distinct element modelling . . . 37
4.3.4 Geohazard maps . . . 38
4.4 Results . . . 39
4.4.1 Spatio-temporal evolution of subsidence . . . 39
4.4.2 Modelling the subsidence cause and processes . . . 41
4.5 Discussion . . . 45
4.6 Acknowledgment . . . 48

5 Landslide failure in Hoseynabad-e Kalpush village **51**
5.1 Abstract . . . 52
5.2 Introduction . . . 52
5.3 Description of the study area . . . 54
5.4 Data and methodology . . . 55
5.4.1 Co-failure ground displacement using digital image correlation . . . 58
5.4.2 Kinematics assessment using MT-InSAR . . . 59
5.4.3 External factors . . . 60
5.4.3.1 Precipitation . . . 60
5.4.4 Reservoir water elevation . . . 60
5.4.5 Post-processing . . . 61
5.4.5.1 PCA and ICA . . . 61
5.4.6 Data clustering and time-series segmentation . . . 61
5.4.7 Wavelet analysis . . . 62
5.5 Results . . . 62
5.5.1 External influencing factors . . . 62
5.5.1.1 Precipitation . . . 62
5.5.1.2 Reservoir water elevation . . . 63
5.5.2 Correlation between precipitation and reservoir impoundment . . . 64
5.5.3 Analysis of pre-failure kinematics . . . 65
5.5.3.1 MT-InSAR ground displacement . . . 65
5.5.3.2 Effects of precipitation and the reservoir water level on pre-failure motion . . . 70
5.5.4 Analysis of co-failure kinematics . . . 71
5.5.4.1 DIC ground displacement . . . 71
5.5.4.2 Effects of precipitation and the water reservoir level on the main failure . . . 73
5.5.5 Analysis of post-failure kinematics . . . 73
5.5.5.1 MT-InSAR ground displacement . . . 73
5.5.5.2 Effects of precipitation and reservoir water level changes on post-failure motion . . . 76
5.6 Discussion . . . 77
5.6.1 Pre-failure destabilization following anthropogenic activities . . . 77
5.6.2 From slow-moving retrogressive mechanism to deep-seated translational failure . . . 79
5.6.3 Post-failure stabilization following reservoir discharge . . . 79
5.6.4 Landslide activities on surrounding slopes . . . 80
5.7 Conclusions . . . 81
5.8 Acknowledgment . . . 82

6 Offshore earthquake in the eastern coast of Kamchatka peninsula **83**
6.1 Abstract . . . 84
6.2 Introduction . . . 84
6.2.1 Tectonic background . . . 86
6.2.2 Earthquake-related faulting north of the subduction zone . . . 86
6.3 Data and methods . . . 88
6.3.1 Seismic data . . . 88

6.3.2 DInSAR analysis . . . 90
6.3.3 Geodetic modeling and results . . . 91
6.4 Discussion . . . 95
6.5 Conclusions . . . 98
6.6 Acknowledgment . . . 98

7 Cyclical geothermal unrest at Fagradalsfjall volcano 99
7.1 Abstract . . . 101
7.2 Intruduction . . . 101
7.3 InSAR Data and Method . . . 103
7.4 Results . . . 103
7.4.1 Transient deformation at the Svartsengi HT field . . . 103
7.4.2 Free-air gravity change . . . 105
7.4.3 Seismicity . . . 105
7.4.4 Elastic and poroelastic models . . . 106
7.5 Acknowledgment . . . 109

8 Flank collapse at Anak Krakatau volcano 111
8.1 Abstract . . . 112
8.2 Introduction . . . 112
8.3 InSAR data and method . . . 113
8.4 Result . . . 113
8.4.1 Deformations on the southwest flank of Anak Krakatau . . . 113
8.4.2 Interaction of flank motions and magma intrusions simulated in analogue experiments . . . 115
8.5 Discussion . . . 117
8.6 Acknowledgment . . . 119

9 Summary and Future Perspectives 121
9.1 Summary . . . 121
9.1.1 Land subsidence in the municipality of Maceió (Brazil) . . . 122
9.1.2 Landslide failure in Hoseynabad-e Kalpush village (north–central Iran) 123
9.1.3 Offshore earthquake in the eastern coast of Kamchatka peninsula (Russia) . . . 123
9.1.4 Cyclical geothermal unrest at Fagradalsfjall volcano (Iceland) . . . 123
9.1.5 Flank collapse at Anak Krakatau volcano (Indonesia) . . . 124
9.2 Outlook and ongoing challenges . . . 124

Bibliography 127

List of Figures 151

List of Tables 163

List of Abbreviations

Abbreviation	Description
2D	Two-dimensional.
3D	Three-dimensional.
ALOS	Advanced Land Observing Satellite.
ASI	Agenzia Spaziale Italiana.
CHIRPS	Climate Hazards Group InfraRed Precipitation with Station.
CNR	National Research Council.
COMET	Centre for Observation and Modelling of Earthquakes, Volcanoes and Tectonics.
CSA	Canadian Space Agency.
CWT	Continuous Wavelet Transform.
DEM	Digital Elevation Model.
DLR	German Space Agency.
EnMAP	Environmental Mapping and Analysis Program.
Envisat	Environmental Satellite.
EPOS	European Plate Observing System.
ERS	European Remote Sensing Satellite.
ESA	European Space Agency.
ETAD	Extended Timing Annotation Dataset.
FastICA	Fixed-point Algorithms for Independent Component Analysis.
GFZ	German Research Centre for Geosciences.
GNSS	Global Navigation Satellite System.
GPS	Global Positioning System.
ICA	Independent Component Analysis.
INGV	National Institute of Geophysics and Volcanology.
InSAR	Differential Interferometric Synthetic Aperture Radar.
InSAR	Interferometric Synthetic Aperture Radar.
IREA	Istituto per il Rilevamento Elettromagnetico dell'Ambiente.

Abbreviation	**Description**
ISRO	Indian Space Research Organisation.
JAXA	Japan Aerospace Exploration Agency.
JERS	Japanese Earth Resources Satellite.
JPL	Jet Propulsion Laboratory.
LiCSAR	Looking Into Continents from Space with Synthetic Aperture Radar.
LOS	Line-of-sight.
m.a.s.l.	Metres Above Sea Level.
MTI	Multi temporal InSAR.
NASA	National Aeronautics and Space Administration.
NISAR	NASA-ISRO Synthetic Aperture Radar.
PCA	Principal Component Analysis.
RMSE	Root-mean-square Error.
S1	Sentinel-1.
SAR	Synthetic Aperture Radar.
SBAS	Small Baseline Subset.
SNR	Signal-to-noise Ratio.
SRTM	Shuttle Radar Topography Mission.
SVD	Singular Value Decompositio.
TSX	TerraSAR-X.
UNCTAD	United Nations Conference on Trade and Development.
UNDRR	United Nations Office for Disaster Risk Reduction.
WGS84	World Geodetic System 1984.
XWT	Cross Wavelet Transform.

1 Introduction

1.1 Background/motivation

Geological processes refer to natural forces, such as tectonic subduction and rifting, surface erosion, gravitational slope deformation, chemical weathering and sedimentation, that shape the Earth's crust. They can manifest at the surface as episodic or time-dependent ground deformations of different magnitude, extent and patterns. Their interaction with the built environment can affect the integrity of buildings and infrastructures and therefore jeopardize human life and social and economic development. As a result of the potential risk, adverse geological events, such as earthquakes, volcanic eruptions, land subsidence, sinkholes, debris flows, rockfalls, and other landslides, are referred to as geological hazards or geohazards (Komac and Zorn 2013; Hyndman and Hyndman 2016).

The growth in global population and consequent expansion of densely populated urban areas increases the exposure to geohazards. Over the last 25 years, the world population has increased by 2.1 billion, reaching eight billion at the end of 2022, 57% of which are living in urban areas (UNCTAD 2022). The highest growth is registered in Asia and Oceania (+1.2 billion) and Africa (+0.7 billion) where urbanization drastically increased from 43.3% to 50%. It is estimated that in 2019, 46% of the worldwide population was living under conditions of poverty (with an income of less than $6.90 per day) (World Bank, 2022). People living under conditions of food insecurity, lack of safety, gender, race and mental and physical ability discrimination, social and economic inequalities and limited access to health care are less likely to be able to stay safe during a geohazard event, not to mention prepare for and recover from their effects (Ogie and Pradhan 2019; Contreras et al. 2020). Consequently, they are more vulnerable to geohazards, which at the same time aggravate further those social and security issues.

Every year geohazards cause thousands of human casualties and injuries, damage to buildings and infrastructures, loss of productivity, disruption of supply chains, loss of livelihoods, mental health issues, and disruption of education and health care. Studies show that as of 2015, 2.7 billion people live in earthquake hazard areas, against 1.4 billion in 1975; 14 million people live near one of the 220 most dangerous volcanoes. The most devastating event of 2023 happened on February 6., when 7.8 and 7.5 magnitude earthquakes and successive aftershocks struck southern Turkey and northern Syria. As of March, international media reported that the direct fatalities from the earthquakes were over 50 thousand, and millions of people were displaced from their destroyed or under risk of collapsing homes. Earthquakes and tsunamis are among the most devastating geohazards, with estimates of more than half of a million fatalities and 2 billion injuries in the past two decades linked to them (UNDRR 2022). However, while large disaster events are reported in international disaster management databases, tens of thousands of small-scale disaster events occurring at a higher frequency than their large counterparts each year are often not accounted for. An analysis of records in 104 countries found that between 2005 and 2017, small and medium, localized and frequent disasters caused 68% of all economic

losses (UNDRR 2022). A recent study has shown that significantly larger proportions of the globe are exposed to rainfall-triggered landslide hazards than considered before, affecting especially linear infrastructure, such as roads and power transmission. Between 1995 and 2014, 3876 landslides caused a total of 163,658 deaths and 11,689 injuries in 128 countries (Haque et al. 2019). The increase in the frequency of extreme precipitation events as a direct consequence of climate change will also increase the frequency of such meteorologically induced landslides (Gariano et al. 2017). Anthropogenic activities, including the overexploitation of natural resources, are influencing the occurrence, frequency and intensity of geohazards and the consequent human, environmental and economic loss (Gill and Malamud 2017). According to the latest research, by 2040, 19% of the world's population will be affected by land subsidence (Herrera-García et al. 2021). Cascade effects can also follow main geohazard events, introducing secondary hazards whose impact might be even more severe: landslides following earthquake events or flash floods; a tsunami following a landslide failure inside a water body (Sharma et al. 2018; Patrick et al. 2020).

To prevent or mitigate the human and economic impact of disasters, a comprehensive understanding of the geological processes that are behind the geohazard is essential. This includes identifying where a geohazard is occurring or might occur in the future, assessing its magnitude and monitoring its evolution, understanding the process mechanism involved, identifying potential precursors that might lead to major events, and investigating the main driving climatic and environmental factors. In this regard, it is necessary to apply a multidisciplinary approach based on multi-sensor and multi-parameter data. However, for in-depth geological process understanding relying on data provided by in-situ measurements is not always possible due to low or no data availability in many areas around the world. Indeed, installing and maintaining in situ instruments can be costly; they have limited spatial coverage; usually, it is not known when and where a geohazard might occur and, therefore, impossible to plan accordingly where to install them; additionally the areas of interest can be difficult to access.

The outstanding development of Satellite Earth Observation (EO) missions in the past few decades has revolutionized data collection on the Earth's surface (Gomes et al. 2020). Spaceborne radar, hyperspectral, multispectral and optical imaging systems are nowadays providing a quasi-global coverage with consistent acquisition plans of multisensor and multi-parameter geospatial data. Since the launch of the first EO satellites in the 70s, advances have been made in improving the spatial, temporal, spectral and radiometric resolutions (Tomás and Li 2017). The new generation satellites reach very high resolution (lower than one m for Terrasar-X, Cosmo Skymed and Pleiades) to medium resolution (10-15 m for Landsat-8 and Sentinel-2). Constellation missions of two satellites (such as Sentinel-1) to more than hundreds of satellites (such as PlanetScope) provide data acquisitions even daily. Recently launched hyperspectral satellite ENMAP provides 246 contiguous bands. All these missions increase the capability to capture the dynamic nature of geological processes in time and over large areas. In particular, Synthetic Aperture Radar Interferometry (SAR) has evolved into one of the main geodetic techniques for monitoring surface deformations due to its high accuracy in measuring ground displacement, wide-area coverage and cost-effectiveness (Bernardi et al. 2021).

The capability to detect and monitor ground deformations in time and space increased rapidly with the advances of new SAR missions and performative Interferometric SAR (InSAR) technologies, including new algorithms and powerful cloud computing sources (Euillades et al. 2021). Past and currently operational SAR missions, such as ERS (ESA),

Envisat (ESA), TerraSAR-X (DLR), Radarsat (CSA), JERS (JAXA), ALOS (JAXA), and COSMO-SkyMed (ASI) have provided data over many parts of the world for decades, although with inconsistent acquisition plans or limited repeat cycle. The launch of new generation SAR missions such as the European Space Agency's Sentinel-1 constellation and the upcoming NASA and Indian Space Agency NISAR mission, which aim for continuous and systematic acquisition of data with up to weekly revisited time, opened the opportunity to apply InSAR as a near-real-time geohazard monitoring technology. Moreover, their free-of-charge data availability policy makes InSAR applications economically affordable compared to traditional observation methods.

Nowadays, InSAR is already a standard space geodetic technique applied to observe time ground deformation from local to continental scale. The continuously expanding SAR data archives increase InSAR's capability to perform back analysis of disastrous events. However, many research gaps remain on how to interpret the ground deformation observations and how to derive a comprehensive understanding of the geological process and driving forces that lead to geohazards.

1.2 Research question

The main scientific aim of the present PhD research is to investigate several geohazard events based on ground deformation measurements using InSAR techniques. This includes constraining the onset of the ground deformation in time and space, tracking its time evolution and identifying transients in the rate that may indicate the forthcoming of more significant catastrophic events. For completeness of the analysis and a deeper insight into the process mechanism and its driving factors, InSAR observations are combined with additional remote sensing and in-situ measurements publicly available over the area. Inverse numerical models are applied to constrain the location and simplified geometry of subsurface sources for a better understanding of the underground processes related to the observed surface deformation pattern. Finding and understanding the correlation between transient ground displacement signals and seasonal ground displacement signals with environmental variables can contribute to the ability to identify external factors that trigger or enhance a geological process. Comprehending what kind of information can be derived from InSAR for each specific geohazard is an essential part of this work for achieving a more complete understanding of geological processes. The present research contributes to designing an individual workflow for each geohazard in order to answer as best as possible the following research questions.

- How does the specific geological process occur on the surface? What is the magnitude of ground deformation? Does it evolve in space and time, and if so, how? Are there any transients in displacement detectable as evidence for potentially forthcoming, more severe events?

- What is the type of underground process which is the source of the observed ground deformation? Where is the main source located? What is its overall and approximate geometry? How does it evolve in space and time?

- What are the main environmental, climatic and anthropogenic factors controlling the evolution of the geological process? How do they correlate with the ground deformation observation and the deeper processes?

Five different geohazard events located in different geographical regions were analyzed: land subsidence in the municipality of Maceió (Brazil); landslide failure in Hoseynabad-e Kalpush village (north–central Iran); offshore earthquake in the eastern coast of Kamchatka peninsula (Russia); geothermal unrest close to Fagradalsfjall eruption site (Iceland); and tsunamigenic flank collapse at Anak Krakatau volcano (Indonesia). The analyzed events involved different types of geological processes: tectonic plate dynamics, deep-seated cavity instabilities, gravitational mass movements, and gas and magmatic intrusions. A brief description of the case studies, motivation and more specific research questions are presented in the following subsections.

1.2.1 Land subsidence in the municipality of Maceió (Brazil)

Sinkhole formations and infrastructure fractures have intensified in some densely populated neighbourhoods of Maceió following a period of heavy precipitation in February 2018. In this same area of the city, underground salt mining has been performed since the 1970s. This anthropogenic activity was considered one of the potential causes, and investigated as such. Despite the mining activity spread under densely populated areas, systematic monitoring of the stability of the area was never implemented; therefore, long-term in-situ measurements related to ground motion, the salt cavities' conditions and groundwater levels were not available. In the aftermath, the Geological Survey of Brazil conducted a one-year multi-disciplinary survey using newly installed instruments, ad hoc data collection and 2 years of InSAR observations, investigating four potential hypotheses for the ongoing instability: geotechnical characteristics of the soils, groundwater exploitation, regionally active tectonic structure and salt mining activities. The investigation concluded that salt mining was most likely the main cause of the subsidence. After these outcomes, all extraction activities were stopped and the authorities started to evacuate the area, with more than 40,000 people displaced and 14,000 houses placed under demolition orders. However, in spite of the investigation, many other aspects of the ongoing geological instability were not questioned and remain unknown. The aim of this work is to address these research gaps over the Maceió land subsidence. This includes detecting when and where the subsidence process started; how it evolved in time and space; constraining the source location and verifying the causes; investigating the spatio-temporal evolution of the sub-ground process; and correlating the ground deformation with further potential environmental driving factors.

1.2.2 Landslide failure in Hoseynabad-e Kalpush village (north–central Iran)

Between mid-March and the beginning of April 2019, 28 out of the 31 provinces of Iran were affected by intense rainfall, leading to widespread flash flooding and thousands of landslides, especially in the northern regions of the country. At this time, a catastrophic landslide occurred in Hoseynabad-e Kalpush village in Semnan Province on a slope downstream from a recently built dam reservoir. The failure damaged more than 300 houses in Hoseynabad-e Kalpush village, of which 163 had to be evacuated due to the severity of the destruction. In the aftermath of the catastrophic failure, several aspects of the Hoseynabad-e Kalpush landslide mechanism remained unknown. The area surrounding the dam reservoir had not been monitored by in-situ instruments when the infrastructure was placed and put into operation. This research aims to investigate whether the landslide

was active before the dam construction; when and under which conditions it was reactivated; how the destabilization evolved over time and space in the prefailure period; what the magnitude and the extent of the landslide failure was and how it evolved; which were the main external driving factors for the landslide to occur; whether the landslide was still active in the aftermath of the failure.

1.2.3 Offshore earthquake in the eastern coast of Kamchatka peninsula (Russia)

On the 29th of March 2017, a Mw 6.6 earthquake occurred off the northeastern Kamchatka coast. Although this region is proximate to a very complex tectonic setting, it was considered of low-level earthquake and tsunami hazard. This is also the reason why only a few seismic stations were deployed in the northern part of the peninsula where the Yuzhno-Ozernovskoe earthquake occurred. Several hypocenter seismic and focal mechanism solutions were given by national and global seismological centres. Although the focal mechanisms were quite similar for all the given solutions, the suggested epicentre locations varied in the range of 40 km, making it difficult to identify the actual active fault and its connection to the regional geodynamic setting. The aim of this research is to gather better insight into the ongoing geodynamic processes of this region. In this regard, the main goal is to constrain in a more robust way the earthquake epicentre and identify the active fault location, geometry and rupture parameters. This information then allows us to connect the identified active fault to the regional tectonic processes.

1.2.4 Cyclical geothermal unrest at Fagradalsfjall volcano(Iceland)

In March 2021, the Fagradalsfjall volcanic system on Iceland's Reykjanes Peninsula started to erupt after an 870-year quiet period and sustained eruption for 6 months. The effusive eruption did not produce any damage to infrastructure or other disruptions for the local population. During the year leading up to the eruption, three uplift episodes followed by a lower magnitude subsidence occurred at the Svartsengi geothermal field 8 km west of the eruption site. Earthquake swarms were produced simultaneously with the inflation episodes, while seismicity decreased during the deflation episodes. Since the cyclic event occurred next to the re-injection site of the Svartsengi geothermal power plant, initially it was unclear whether the source of deformation was anthropogenically induced or connected to the regional volcanic processes. The aim of this research is to identify in time and space the cyclic inflation and deflation episodes and investigate their sub-ground sources. This study is an investigation of the potential interactions of tectonic spreading, magmatic reservoirs and supercritical magmatic fluids with hydrothermal reservoirs.

1.2.5 Flank collapse at Anak Krakatau volcano (Indonesia)

After 6 months of moderate eruptions, a massive flank collapse occurred at Anak Krakatau volcano on 22 December 2018. A total of 2 km^3 of material from the volcanic island collapsed into the ocean, triggering tsunami waves that reached a height of 85 m at a neighbouring island 4 km away. The tsunami hit the populated coasts of Northwest Java and Southern Sumatra causing several hundreds of human fatalities. An early tsunami warning system was installed and active in the area during the flank collapse. However, since it was designed for earthquake-induced tsunamis, no warning was produced. This

event highlights the need for alternative means for early tsunami warning methods in case of catastrophic failures in ocean islands. The aim of this research is to investigate potential flank instability precursors prior to flank failures that can be used for such purposes. This research also aims to provide an understanding of how magmatic intrusions interact with destabilizing flanks.

1.3 Structure of the manuscript

This PhD work is organized as a cumulative research contribution, based on individual research studies published in international peer-reviewed scientific journals.

Chapter 2 describes briefly the main analytical pillars used in this PhD research, which includes ground deformation analysis, numerical source modeling and driving external factors analysis.

Chapter 3 introduces the fundamental physical-mechanical aspects of the geological process analyzed in this PhD research, which includes land subsidence, landslide, earthquake and volcanic-related activities. The main focus is on the induced ground deformations, sources and driving forces. The second part of each subsection includes the state-of-the-art InSAR technology applied to the specific geological process.

The results of the five case studies are published in well-recognized scientific journals as three first-author and two co-author contributions. They are included as separate chapters in this manuscript.

Chapter 4 includes the first-author publication "A decade-long silent ground subsidence hazard culminating in a metropolitan disaster in Maceió, Brazil".

Chapter 5 includes the first-author publication "Reactivation of an old landslide in north–central Iran following reservoir impoundment: results from multisensor satellite time-series analysis".

Chapter 6 includes the first-author publication "The 29 March 2017 Yuzhno-Ozernovskiy Kamchatka Earthquake: Fault Activity in An Extension of the East Kamchatka Fault Zone as Constrained by InSAR Observations".

Chapter 7 includes the co-author publication "Cyclical geothermal unrest as a precursor to Iceland's 2021 Fagradalsfjall eruption".

Chapter 8 includes the co-author publication "Interactions of magmatic intrusions with the multiyear flank instability at Anak Krakatau volcano, Indonesia: Insights from InSAR and analogue modelling".

2 Methodological Background

Adverse geological processes related to geohazard manifest at the surface as episodic or time-dependent ground deformations of different intensity, extent, pattern and temporal evolution. Measuring and analyzing their temporal and spatial evolution is essential for geohazard mapping and assessment. This is achieved by exploiting EO data and in particular SAR and InSAR techniques. Numerical models are used to constrain the geophysical source parameters and connect what is observed on the surface to the underground geophysical mechanisms. Climatic and anthropogenic factors, including precipitation, surface water levels, land cover change and topographic reshaping, can foster or even trigger adverse geological conditions. Therefore, the understanding of how they control the geological processes is crucial for geohazard assessment and mitigation. The research is based on three main analytical pillars: ground deformation analysis; numerical source modelling; and driving external factors analysis (see Fig. 2.1).

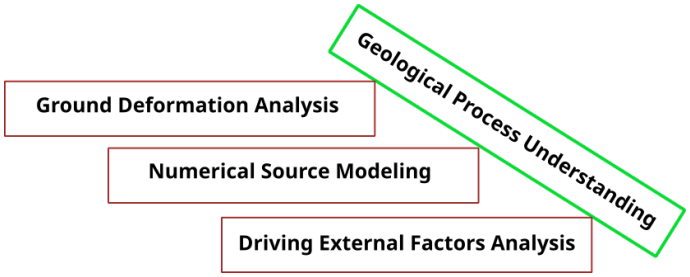


Figure 2.1: Scheme of the methodology pillars

2.1 Ground Deformation Analysis

2.1.1 InSAR

SAR Interferometry (InSAR) is a microwave remote sensing technique that exploits the difference in phase shift (interferogram) between two consecutive and geometrically compatible Single Look Complex SAR acquisitions (primary and secondary) to reveal surface topography or surface motion (Hanssen 2001). By deducting the topographic contribution, the component related to the ground deformation is recovered. This extension is called Differential InSAR (DInSAR). However, the DInSAR still contains ramps related to atmospheric delay, DEM-related artifacts, orbit errors and noise. InSAR is capable of measuring the ground motion only when the displacement gradient between two neighbouring pixels is smaller than π (equivalent to half the sensor wavelength), otherwise, an interferometric ambiguity is introduced. This is a measure of the sensor's sensitivity to the ground motion and it depends on the sensor wavelength: 1.5 cm for the X-band, 2.7 cm for the C-band and 11.5 cm for the L-band.

The phase difference in a single pixel is expressed as follows:

$$\Delta\phi_{int} = \phi_{displ} + \phi_{topo} + \phi_{atm} + \phi_{orb} + \phi_{noise} + 2k\pi \tag{2.1}$$

where: φ_{displ} is the displacement phase component; φ_{topo} is the topographic phase component; φ_{atm} is the atmospheric phase component; φ_{orb} is the phase component due to the orbital errors; φ_{noise} is the noise; k is an integer value called phase ambiguity.

Phase unwrapping is used to reconstruct the absolute change of phase from the 2π interferometric cycles, i.e. absolute displacement. This is done concerning a stable reference point or a point of known deformation rate, for instance from GNSS measurements.

A single-pair InSAR is characterized by a signal-to-noise ratio that allows the detection of ground deformations with centimetre-level accuracy. This is because standard InSAR is limited by temporal and geometrical decorrelation, as well as phase distortions induced by atmospheric artifacts and topographic residuals. More advanced multi-temporal InSAR connects a stack of SAR images of the same geographical region collected over some time and enables estimating the time series of surface deformation. These techniques enable the mitigation of atmospheric and DEM-related artifacts, improving the quality of the ground displacement measurements and reaching up to mm-level accuracy.

DInSAR is sensitive to deformations along the LOS direction. Therefore, the sensitivity to the real ground deformation field depends on the SAR acquisition geometry and the 3D displacement vector. SAR missions follow a sun-synchronous, near-polar orbit so that the orbital angle is approximately along the north-south direction. The sensors are normally right-looking, and therefore the sensor will face the same ground target with a different geometry during its ascending and descending orbit passes. The angle at which the sensor is pointed towards the Earth is called off-nadir or look angle and varies between 20 and 50° for the different image moods (Spotlight, Stripmap, TOPSAR). It also varies from the near to the far range within the same image. For instance, Sentinel-1 off-nadir images range between 29° (for near-range) and 46° (for far-range). The incidence angle is defined as the angle between the radar beam center and the normal to the local geodetic ground surface. Usually, the Earth's curvature is neglected, and under this condition, the incidence angle corresponds to the look angle of the sensor. DInSAR has full sensitivity to motion parallel to the incidence angle. However, in general, it is more sensitive to vertical displacement than horizontal. On the horizontal plane, it is more sensitive to east-west oriented motion and the sensitivity decreases in the north-south direction, thus becoming negligible for orientation parallel to the orbit pass (see Fig. 2.2).

Coherence is a key parameter that measures the amount of correlation between two SAR images and indicates the level of phase noise. It is estimated as the complex correlation between two SLC SAR images and combines both phase and amplitude components. The coherence varies between 0 and 1 (0 refers to no correlation and 1 to perfect correlation). Since InSAR relies on comparing the phase of each pixel in two or more images, the phases should be coherent enough in their radar reflection to be comparable (Hanssen 2001). The loss of coherence, i.e. decorrelation, depends on several factors. Geometric decorrelation occurs when the ground target in the two images is viewed from a slightly different angle, resulting in different scattering contributions within the same pixel area. Geometric decorrelation is more pronounced for volumetrically scattered objects such as canopy and extremely rough surfaces, and the degree of decorrelation increases as the baseline increases. Temporal decorrelation is caused by changes in the surface backscatter characteristics over time and depends on the underlying surface type. The longer the time between two SAR acquisitions, the larger the probability that the surface has changed

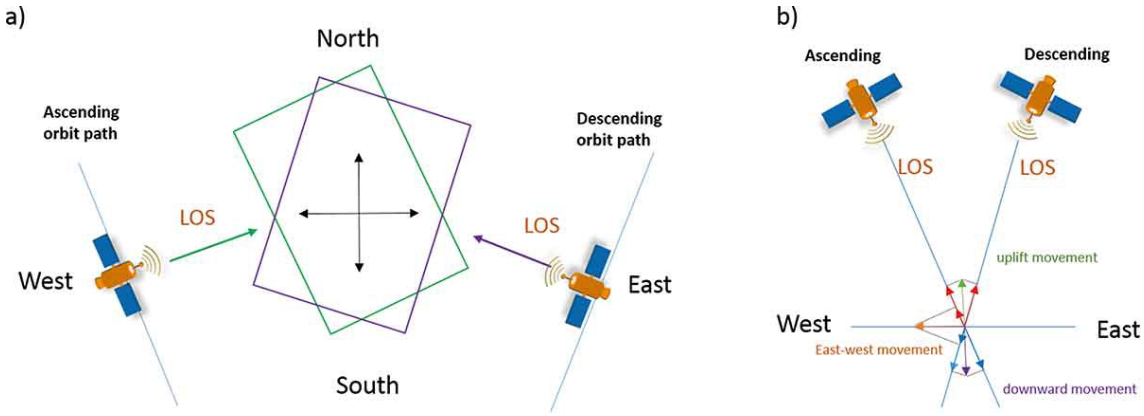


Figure 2.2: InSAR deformation sensitivity from ascending and descending orbital path: (a) with respect to the azimuth direction; (b) concerning the LOS direction; positive movement in red and negative movement in blue, vertical component (in green uplift movement and in violet downward movement) and east-west component (in orange from west to east movement) (from Vassileva et al. 2017)

and is even completely decorrelated. A typical example is cropland and forest canopy, whose vegetation status can change drastically throughout two acquisitions, even in a short period. The loss of coherence is proportional to the density of vegetation and inversely proportional to the SAR wavelength: shorter wavelengths are more affected by coherence losses than longer wavelengths. Severe ground deformations also lead to a loss of coherence due to the phase ambiguity and potential complete or partial change of land cover (i.e. a landslide collapse over a vegetated area will destroy the canopy, resulting in a change in surface type).

Errors in DInSAR measurements can be of different types, character and origin. It can be distinguished between phase errors, methodology errors and data gaps and they can be originated in the radar system, in the processor or the processing steps (Bürgmann et al. 2000). Some errors are random and depend on the scattering mechanism and the sensor parameters, while others are systematic and spatially correlated, such as atmospheric artifacts. The final DInSAR/MTI error quantification is very difficult, almost impossible to perform because the different error contributions propagate both in time and space through all the processing steps and their effect also changes in time and space. To reduce random phase noise and enhance the signal-to-noise ratio, spatial or frequency domain adaptive filtering algorithms can be applied (Goldstein and Werner 1998), together with image multi-looking, the latter reducing the pixel resolution. Phase delay due to the differences in atmospheric conditions (water vapor, pressure, and temperature in the troposphere) between two SAR acquisitions is one of the main concerns in InSAR processing. To reduce the atmospheric artifacts, numerical modeling using external data sources, i.e. GNSS and weather sensors can be used, although these methods might also remove large-scale and minor ground deformations. Orbit uncertainty effects produce additional ramps over the entire scene which can be removed by polynomial fitting (Du et al. 2021). Several methods have been developed to estimate ionospheric effects which affect mainly low-frequency SAR acquisitions, and consequently remove them from the InSAR contribution (Zhang et al. 2022a). Other errors related to radar distortions in topographic regions, temporal and

geometric decorrelations, and phase ambiguity, can be mitigated by masking the areas highly affected.

The strategies to reduce the above-mentioned errors, are based on the specific geological process, the ground deformation magnitude and extent and consequent area of interest characteristics, including land cover and topography. The ground displacement accuracy can be assessed using external GNSS and geodetic levelling measurements, although those are rarely available and provide point measurements (Casu et al. 2006).

In this research, the Small Baseline Subset (SBAS) technique proposed by Bernandino in 2002 was used. It is particularly suitable for distributed/natural scatterers (low vegetation, cropland, soil) and for producing long-time series analyses of several years. SBAS is based on a multi-master SAR image combination. To mitigate the effect of spatial and temporal decorrelations and to increase the number of point measurements in space and time, InSAR pairs characterized by short temporal separation and small perpendicular baseline are built (Berardino et al. 2002; Lanari et al. 2007).

The displacement obtained from the interferogram formed by images i and j can be written as:

$$d_{ij} = d_i + d_{i+1} + d_{i+2} + ... + d_{j-1} \tag{2.2}$$

The incremental displacement can be substituted by the velocity v:

$$d_{ij} = \Delta t_i v_i + \Delta t_{i+1} v_{i+1} + \Delta t_{i+2} v_{i+2} ... + \Delta t_{j-1} v_{j-1} \tag{2.3}$$

with t denoting the acquisition date and $\Delta t_i = t_{i+1} - t_i$ the time interval.

The resulting system of equations can be written as:

$$\mathbf{Av} = \mathbf{d} \tag{2.4}$$

where:

$$\mathbf{A}_{ij} = [0... \underbrace{0}_{\text{i-1}} \; \Delta t_i \; \Delta t_{j-1} \; 0... \underbrace{0}_{\text{n}}] \tag{2.5}$$

$$\mathbf{v} = [v_1 \; v_2 ... v_n]^T \tag{2.6}$$

with n indicating the total number of acquisitions and 0 indicating the pairs not covered by interferograms, the system can be extended to all the available displacement subsets by chronologically ordering the acquisitions.

The usage of multiple subsets helps to increase the temporal sampling rate, however, as a consequence, the system is rank-deficient and has infinite solutions. An approximate solution for this problem can be found, e.g., by applying the Singular value decomposition (SVD) with a minimum-norm criterion (Berardino et al., 2002; Lanari et al., 2004). In particular, the algorithm used exploits a two-step inversion. The first inversion, after assuming a displacement model such as a polynomial model, estimates the best-fit parameters and retrieves the modelled displacement rate and residual topography concerning the reference DEM. Before the second inversion, the previously estimated topographic residuals are removed. The second inversion is then performed, obtaining the displacement solution corresponding to each acquisition date. To remove the atmospheric phase artifacts characterized by a high spatial and low temporal correlation, a spatial low pass and a temporal high pass filter are applied to the displacement time series. However, before applying the filter, the displacement model component is removed to preserve it during the

filtering. The outcome is the average modelled displacement and displacement time series corrected from atmospheric effects and DEM-related errors.

The SBAS approach can provide ground displacement information with precisions of 1-2 mm/year for temporal and spatial coherent areas, and therefore comparable with GPS measurements. However, the measured precision decreases with decreasing temporal and spatial coherence, i.e. over cropland or naturally vegetated areas or snow. The precision depends also on the number of valid interferograms: a higher number leads to a higher precision.

2.1.2 Digital Image Correlation

Digital Image Correlation (DIC), also known as pixel offset tracking, is an image processing technique that measures surface displacement by determining the pixel offset between two acquisitions collected over the same area at different times (see Fig. 2.3). The set of two or more images is first geometrically aligned with sub-pixel accuracy using automatically selected control points (Guizar-Sicairos et al. 2008). Subsequently, the internal misalignment between pairs of images, i.e. primary and secondary images, is estimated by using a moving window and finding the reference subset within the search image (Pan and Li 2011).

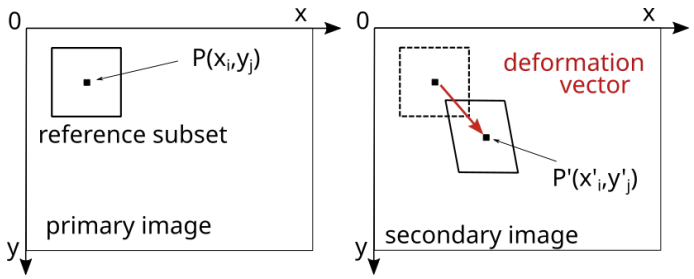


Figure 2.3: Scheme of DIC basic principle

This is done by calculating the maximum correlation between the reference subset and all possible values within the search image. The most common correlation techniques are the normalized cross-correlation (NCC) which operates in the spatial domain, and the fast Fourier transformation (FFT) which operates in the frequency domain. In this research, the FFT approach was adopted as developed by (Bickel et al. 2018). The cross-correlation CC is expressed as:

$$CC(i,j) = IFFT(\frac{F_0(u,V)G_0^*(u,v)}{|F_0(u,V)G_0^*(u,v)|}) \tag{2.7}$$

where IFFT is the inverse of the discrete Fourier transform, F(u,v) is the FFT of the matching window from the primary image, and G*(u,v) is the complex conjugate of the FFT of the matching window from the secondary image. Once the misalignment is determined, the relative displacement in the given time is calculated. DIC is sensitive to displacements along the two spatial directions orthogonal to the LOS direction, while it has no sensitivity to the LOS direction. Therefore, compared to InSAR, it has the advantage of providing information on the horizontal deformations in both east-west and north-south directions.

2.2 Numerical Source Modeling

The relationship between surface deformation vector **d** and source parameters **G** is expressed by the equation:

$$\mathbf{d} = \mathbf{G}(\mathbf{m}) + e \tag{2.8}$$

where: **G** is the Green's function which describes the crust medium and e is the error function. The geophysical parameters can be retrieved by solving the inverse problem:

$$m = (\mathbf{G}^T\mathbf{G})^{-1}\mathbf{G}^T\mathbf{d} \tag{2.9}$$

The optimal model parameters are retrieved using an optimization method that minimizes the difference between the deformation observations and those predicted by the model.

Subsurface geological sources, including faults, cavities, cracks, magma chambers and dykes can be modelled as a confined part of the crust with a certain shape such as point pressure, rectangular dislocation and penny-shaped crack. In many cases, there is no information about the geological stratigraphy and geotechnical parameters of the area. Therefore, the local crust is usually approximated as homogeneous, isotropic and elastic half-spaces. Ground displacement observation with a radially symmetrical pattern can be described using the point-pressure Mogi source model (Mogi 1958). The source model parameters are the horizontal location, the depth and the volume change of the deformation source (see Fig. 2.4).

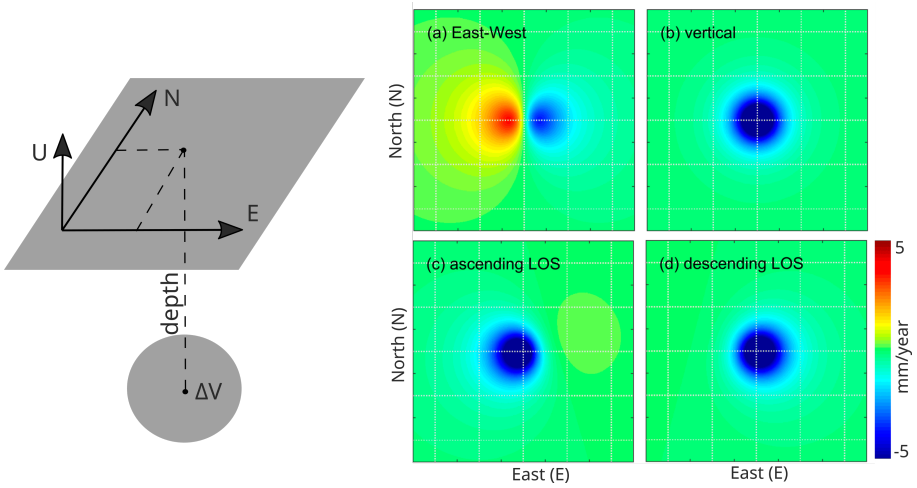


Figure 2.4: Mogi source scheme and simulated velocities in (a) vertical and (b) horizontal components and (c) ascending and (d) descending LOS directions (adapted from Fuhrmann and Garthwaite 2019)

More complex pattern ground deformations invert using the Okada model (Okada 1985) which relates the surface displacement to a 2-D rectangular dislocation source model (see Fig. 2.5). The dislocation plane geometry and orientation can be described by several parameters. The extension is defined by the width and length of the rectangular plane. The location expressed as east, north and depth coordinates can refer to its centre or one of the rectangle corners. The strike angle is the azimuth concerning the North of the plane projection onto the Earth's surface. The dip angle is the steepest descent perpendicular to

the strike and describes the inclination of the plane from the horizontal. It varies between 0° (horizontal) and 90° (vertical). The slip vector given by the slip magnitude and rake angle, describes the magnitude and the direction of the dislocation motion along the plane.

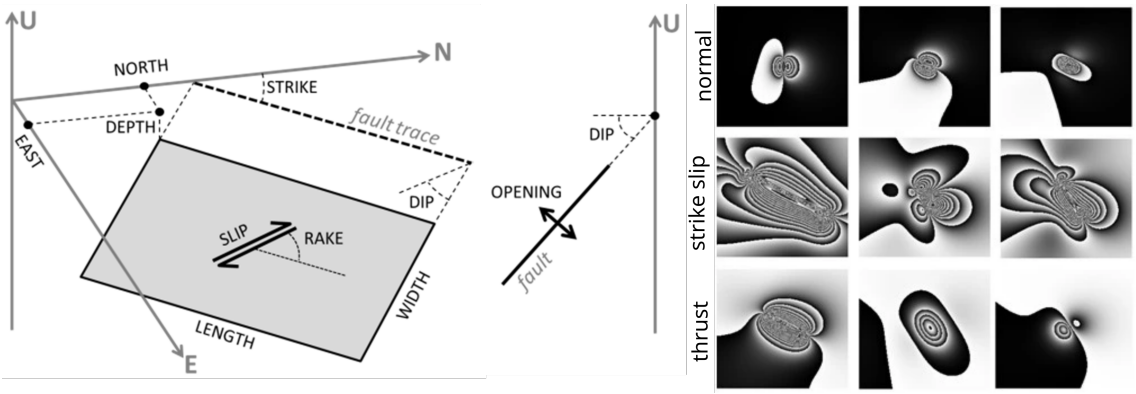


Figure 2.5: Rectangle source model scheme and simulated interferograms using the Okada forward mode for a normal fault (upper row), strike-slip fault (middle row) and thrust fault (lower row) (adapted Picchiani et al. 2012 and Atzori et al. 2014)

2.3 Driving external factors analysis

Additional multi-sensor satellite remote sensing data can be used to derive geographical information and quantify parameters relative to climatic and anthropogenic factors that might be involved in triggering or enhancing the geological process dynamics. Single or time-series optical images can be used to derive land cover and land cover change maps. This information can contribute to assessing the condition of deforestation (Torres et al. 2021) and urbanization growth (Mendiratta and Gedam 2018) in specific areas of interest. Optical and SAR acquisitions can be used to estimate water bodies' surface extension, which combined with DEM and bathymetry models, enables the extraction of the water level changes in time (Simon et al. 2015; Pipitone et al. 2018). Water level trends of water bodies can be also obtained using altimetry remote sensing acquisitions (El-Shirbeny and Abutaleb 2018). Topographic changes can be estimated by comparing different time DEM, globally available, such as the Shuttle Radar Topography Mission (SRTM) with data acquired in 2000 (Rabus et al. 2003) and the TanDEM-X DEM with data acquired between 2010 and 2015 (Rizzoli et al. 2017), or DEM ad-hoc generated using tri-stereo optical images (Aati and Avouac 2020) and bi-static InSAR (Hu et al. 2021). Soil moisture and vegetation indices can be retrieved from optical, thermal and microwave sensors (Binte Mostafiz et al. 2021; Li et al. 2021). Precipitation and snowfall are measured from space using infrared and microwave sensors (Hou et al. 2014). Other precipitation datasets, such as The Climate Hazards group Infrared Precipitation with Stations (CHIRPS) dataset, are globally available and built by incorporating data from several satellite products and combining them with available rainfall stations (Funk et al. 2015).

To investigate the potential influence of external factors or events on the geological process kinematics, it is important to select representative ground displacement time series and to identify main deformation patterns. Several strategies can be adopted based on the case study. One strategy for time-series extraction is to select a single point or a small window (Fobert et al. 2021; Jones et al. 2022). Other approaches propose first identifying

in supervised or unsupervised ways clusters of displacements and plotting their average displacement values over time (Emil et al. 2021; Festa et al. 2023). Main time-series patterns can be identified using statistical methods (Bovenga et al. 2021; Mirmazloumi et al. 2022) or principal component analysis (Cohen-Waeber et al. 2018). Once changes in trends have been identified, they can be correlated to potential external factor influences. Potential seasonal variations in the time series can be more easily detected in the time-frequency domain by applying Continuous Wavelet Transform (CWT) (Torrence and Compo 1998; Tomás et al. 2016).

3 Application to Geohazards

3.1 Land Subsidence

Land subsidence is the process that involves the loss of land elevation mainly as a result of solid or fluid underground mobilization. It can range from gradual and broad regional lowering usually affecting soft sediments to more local and sudden collapses forming sinkholes. Many large metropolitan cities are nowadays affected by land subsidence with negative socio-economic effects due to devastating consequences to the stability of buildings and infrastructures, interruption to important facilities and even human fatalities (Herrera-García et al. 2021; Bagheri-Gavkosh et al. 2021) (see Fig. 3.1). Land subsidence might also interact with other processes, triggering cascade effects. For instance, in deltaic and coastal areas the danger of inundation increases with the presence of land subsidence (Shirzaei et al. 2021).



Figure 3.1: Fieldwork photos depicting building and infrastructure damages due to land subsidence: **a** and **b** from Maceio' (Brazil) taken in December 2022; **c**, **d** and **e** from Hambach area (Germany) taken by M. Vassileva in June 2023

The driving causes can be a variety of natural and anthropogenic processes, often superposed and acting at different depths, time ranges, and extent scales (Tosi et al. 2009). Overexploitation of groundwater resources that leads to aquifer depletion and irreversible aquifer-system compaction is one of the most commonly encountered human-induced causes worldwide (Tzampoglou et al. 2023). Further, human-induced causes are related to underground mining and oil and gas extraction (Simeoni et al. 2017; Guzy and Malinowska 2020) and compaction of unconsolidated sediments and alluvium soil due to building load

(Ciampalini et al. 2019). Other causes for land subsidence can be associated with karst dissolutions in evaporite rocks (Al-Halbouni et al. 2021), permafrost thawing (de la Barreda-Bautista et al. 2022) and shrinking and oxidation of organic soil due to groundwater level drops in cases of land drainage and reclamation (Verberne et al. 2023). Based on the acting depth, the source of land subsidence can be shallow (50 m up to the ground surface), medium (between 50 and 400m) and deep (deeper than 400 m). For instance, aquifer compaction due to groundwater exploitation occurs mainly at medium depth, oil and petroleum extraction and consequent ground compaction occur at deep depth, while shrinkage and oxidation of organic soil as well as alluvium compaction due to building load occur at shallow depth (Bagheri-Gavkosh et al. 2021).

There are two main mechanisms governing the underlying process that lead to land subsidence (see Fig. 3.2). The first is related to fluid (water, oil, gas) withdrawal from below the ground and consequent compaction of the solid matrices of that layer (Zhu et al. 2015). The rock compaction extends its effect to the overburden layers up to the ground surface. The compressibility of the rock, i.e. volume decrease related to changes in applied stress, and the boundary conditions both play a major role in the compaction process. If the overburden layer does not expand laterally, the volume of the subsidence bowl is equal to the compaction volume at depth. A subsidence bowl tends to be approximately symmetric, even if the compaction in the underlying volume is not. However, the presence of faults or material anisotropy can change the shape of the bowl.

The second mechanism is related to solid grain remotion from the underground system produces underground cavities and cave systems, which can destabilize and partially or totally collapse under the overburden load (Desir et al. 2018). This mechanism is mainly related to the dissolution of evaporite rocks, i.e. rock-salt (halite), gypsum and limestone. The dissolution can be naturally driven by groundwater percolation, with the condition that the water is unsaturated with calcium sulfate (CaSO4) or sodium chloride (NaCl) and it flows through the system. The dissolution can also be induced by human activities such as salt solution mining, which involves pumping water through wells into the subterranean salt deposits, where the salt is dissolved and the saturated brine is then pumped back to the surface.

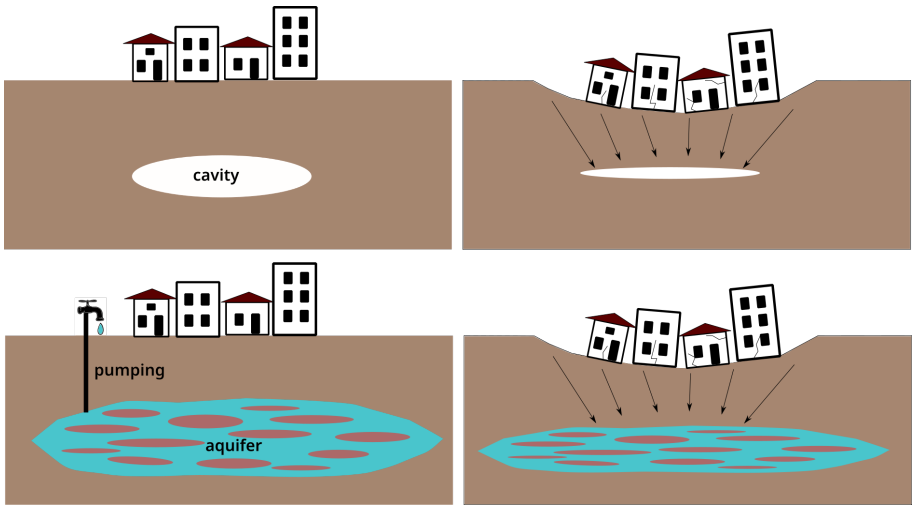


Figure 3.2: Scheme of land subsidence causes

Quite often, especially at the onset of the occurrence, land subsidence goes unnoticed, only to be discovered later on, when severe damage has already taken place. At this stage, undertaking effective remedial measures to mitigate the associated environmental and socioeconomic impact may prove tremendously expensive. Although the predominant motion in land subsidence is vertical, horizontal movements also occur, with maximum values in the transition zone. Large horizontal movements can have devastating effects on pipelines and other extensive surface structures.

InSAR is a suitable technique for land subsidence detection and monitoring, due to the predominance of a vertical ground displacement component (see Fig.3.3). In case, only one SAR acquisition geometry is available, it is a common practice to ignore the horizontal component and project the LOS displacement to the vertical-only component (Fernández-Torres et al. 2022). However, this simplification introduces an error over areas where the horizontal displacement is present and can affect further hazard and risk analysis based on angular distortion. In areas where the horizontal component is moving toward the sensor the simplified method overestimates the vertical components; in areas where the horizontal component is moving away from the sensor, the simplified method underestimates the vertical component. The error can reach more than 40% of the value of the horizontal component (Samieie-Esfahany et al. 2010). It is also true that the horizontal ground displacement component is larger in the transition zone from stable to unstable, and not over the centre where the vertical component reaches its maximum values and therefore this simplification provides quite an accurate estimation of the magnitude of maximum subsidence. By combining ascending and descending LOS ground displacement maps, the 2D displacement vector can be estimated and vertical and horizontal components can be derived (Cigna et al. 2021). The estimated horizontal component is projected along the east-west direction, and displacement oriented north-south is not observable. Some 3D ground displacement models have been also proposed which exploit the symmetric relationship between land subsidence and horizontal movement in the case of mining (Fan et al. 2021).

Land subsidence occurs mainly in urban areas, characterized by persistent scatterers and higher InSAR coherence (Khan et al. 2022). However, it can also occur in natural and vegetated areas, such as peatland, cropland, and urban grassland, or extend over a larger area and therefore result in reduced InSAR coherence. In some cases, by applying SBAS techniques it is possible to derive good coverage of points, at the expense of the final ground displacement accuracy (Figueroa-Miranda et al. 2020). Since land subsidence can produce deformation trends of the order of a few centimetres to a few decimeters per year, these values are far above the SBAS noise levels. Moreover, land subsidence normally has non-linear behaviour, with a slower rate at the beginning which can last for decades, an acceleration stage that can occur in a short period of time (months or years), which in some cases can be followed by abrupt subsidence and even collapse in a few days or hours. By multi-temporal InSAR analysis, it is possible to identify such transients in kinematics and associate them with geomechanical behaviour (Rygus et al. 2023).

Constraining the potential source of deformation is important for the understanding of the ongoing geological processes and driving forces underneath. Indeed, although simple, inverse elastic numerical models can provide overall information related to geometry, volumetric and pressure changes and location of the geological process, contributing to the final interpretation of the geohazard (Furst et al. 2021).

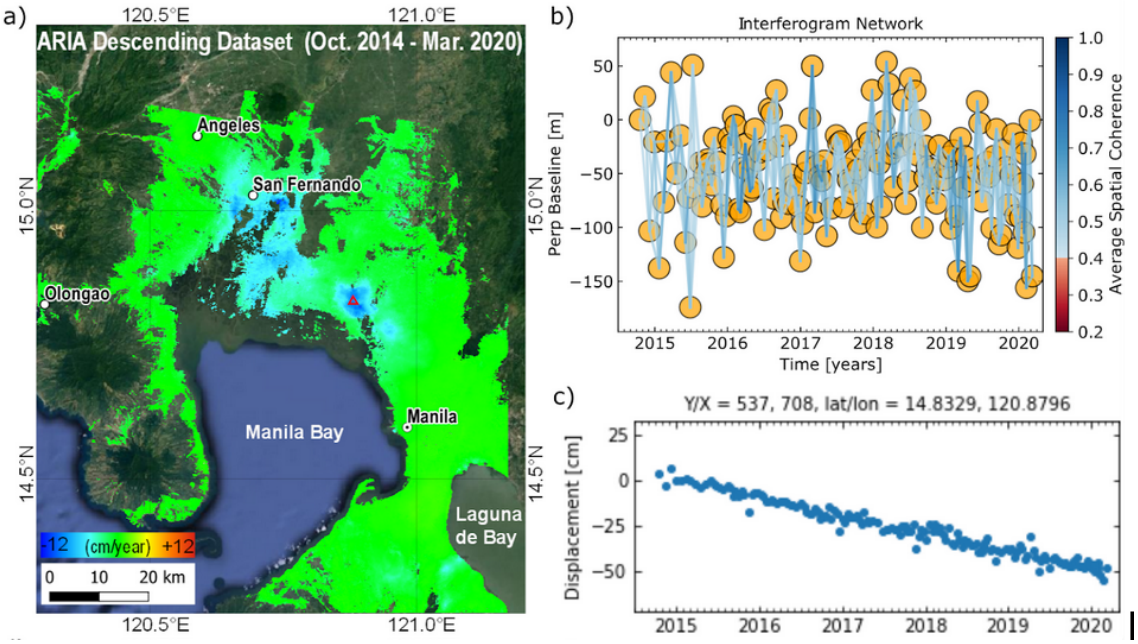


Figure 3.3: Land subsidence over Manila region (Philippines) derived from Sentinel-1 ARIA products for the period between October 2014 and March 2020. **a**, average displacement ascending LOS velocity maps; red triangles represent the displacement time series plotted in **c**; **b**, InSAR connection graphs. Background imagery Google Earth Image Landsat/Copernicus, Map data ©2021. (adapted after Piter et al. 2021)

3.2 Landslide

Landslides are geomorphological processes that involve the downslope movement of soil or rock along a surface of rupture under the effects of gravity. They contribute to the geomorphic evolution of the environment creating new topography. However, landslides are a major hazard to people and infrastructure in hilly and mountainous environments (see Fig. 3.4). They are part of a broader class of mass movement, which includes ice and snow avalanches and lahars, i.e. a mix of volcanic ash and water.

Based on the type of movement, which describes the internal mechanism of mass displacements, landslides are classified into fall, topple, slide, spread and flow. In addition to that, landslides are described by the type of geotechnical material involved (rock, clay, mud, silt, sand, gravel, boulders, debris, peat, and ice) since it influences their mechanical behavior. Landslides can range from extremely and very rapid (moving decimeters or meters per second) such as debris flows (flow of saturated debris in channel slopes steeper than 10–20°), to extremely and very slow (moving a millimetre per year), such as rock/clay/silt rotational slides, which can last for decades.

Landslides occur when the forces acting downslope (shear stress) exceed the shear strength of the soil or rock material which is determined by its intrinsic cohesive and frictional properties. Typically, this happens along a thin zone of intense shear strain, which eventually can develop into a surface of rapture. The condition of slope instability is influenced by the geology, topography, and hydrological conditions. Water infiltration, in the form of rainfall, snow melting or groundwater level rise, as a result of reservoir impoundment, or rising in surface water levels are among the main factors that drive slope



Figure 3.4: Fieldwork photos depicting landslide affected areas: **a**, Dorud (Lorestan, Iran) taken in September 2019;**b**, and **c**, Golestan Province (Iran) taken in September 2019;**d**, Maceio' (Brazil) taken by M. Vassileva in December 2022

instabilities (Duc 2013). Anthropogenic activities, including building loading, road cutting, and open-pit mines increase the shear stress. Landslides can occur as a cascade effect of some other hazardous event, such as earthquakes (Owen et al. 2008) and volcanic activity (Ablay and Hürlimann 2000) or themself trigger subsequent hazards, including tsunamis (Løvholt et al. 2020) and flooding (Ruiz-Villanueva et al. 2017) (see Fig. 3.5).

Not all landslides occur as catastrophic events. In some cases, they follow imperceptible slow downward motion, i.e. creep, at rates that can range from millimetres to several meters per year which can last even for decades. However, slow-moving landslides, under certain internal and environmental conditions, can accelerate rapidly and even fail catastrophically and this is why they are often seen as potential precursors before landslide failures. Most of the slow-moving landslides are deep-seated (thickness > 3 m) and occur in weak or highly damaged, clay-rich soils and rocks. The main external factor for triggering or reactivating slow-moving landslides is water infiltration, mainly rainfall-induced, which can build pore-water pressure and consequently decrease the shear strength.

Slow-moving landslides can develop also on the flanks of volcanic edifices and they can collapse due to both external forces, including weathering and permafrost degradation, and internal forces related to shallow volcano-tectonic processes, including magma intrusions and weakening of the rock by hydrothermal alteration. Flank collapses on volcanic islands are extremely dangerous to coastal areas due to their tsunami-triggering potential.

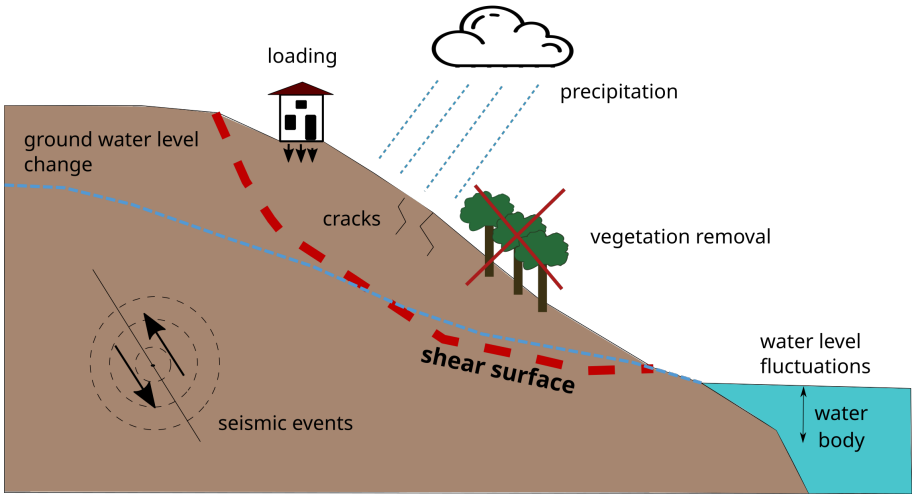


Figure 3.5: Scheme of landslide main external driving factors

Typical morphological features are the depletion zone on the top, from where the failed material descends and an accumulation zone at the bottom, where the material deposits (see Fig. 3.6). The scarp is the steep, nearly vertical, region of removed mass at the upper edge of the landslide where the landslide failure surface ruptures the ground surface. The crown is the non-displaced material adjacent to the highest parts of the main scarp. The surface of rupture, also named shear surface, is the sliding interface of the landslide, above which lays the main landslide body. If the surface ruptures in the direction of movement, the landslide is advancing; if the surface ruptures upward, the landslide is retrogressive; if the surface of the rupture is extending at one or both lateral margins, the landslide is widening. The flanks are the lateral non-displaced material adjacent to the main body where the rapture created shear fracture zones. Minor scarps due to internal shearing can also appear along the flanks. The foot is the material deposited in the accumulation zone, beyond the surface of rupture, while the toe is the lower border of the landslide, that separates the accumulated material and the untouched terrain.

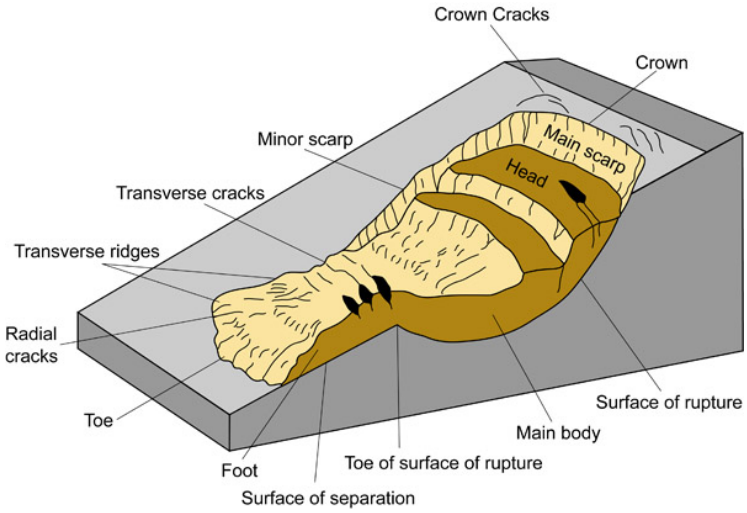


Figure 3.6: Scheme of landslide main features (after Idaho Geological Survey)

InSAR is a suitable technique for detecting landslides, characterized by ground deformation of the order of a few mm/year to 1.6 m/year. It has been widely used to detect new and unknown slow-moving landslides to update landslide inventory maps (Hussain et al. 2023), reconstruct recent catastrophic landslides history (Yi et al. 2022) and systematically monitor the kinematic evolution of targeted landslide-prone areas (Zhang et al. 2022b). Therefore, it can be applied for a regional-scale landslide analysis and an in-depth investigation of a single landslide (see Fig. 3.7).

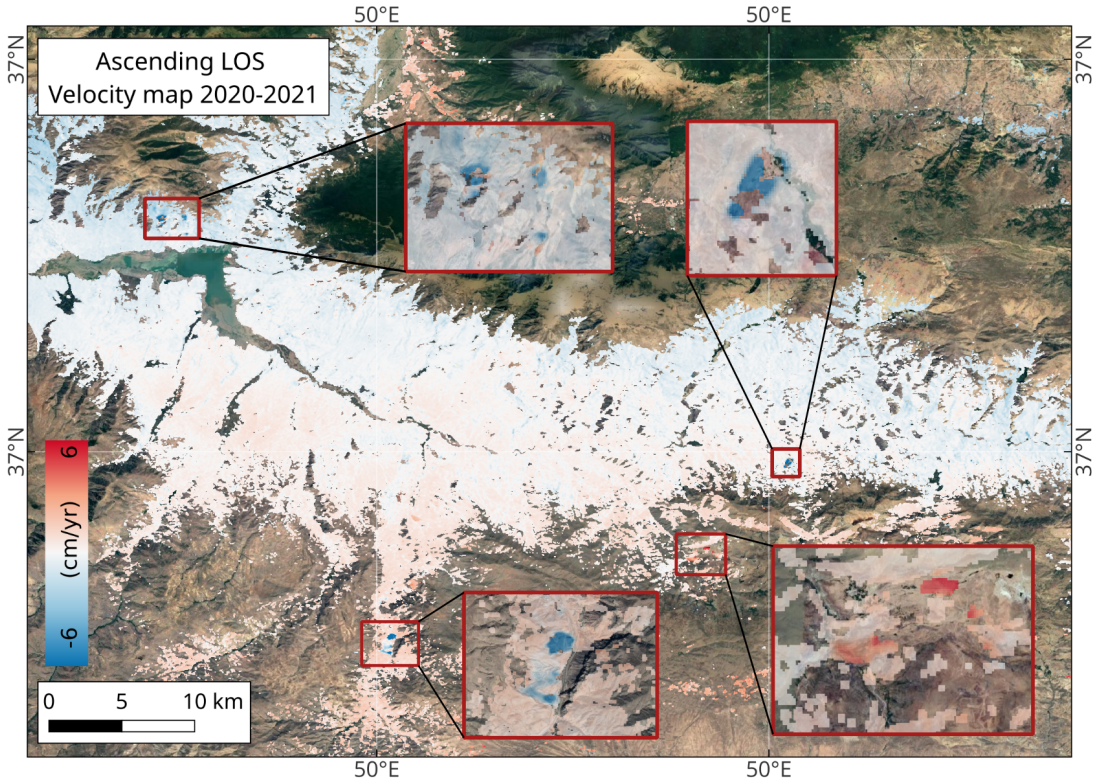


Figure 3.7: Regional scale average ascending LOS velocity for 2020-2021 using Sentinel-1 data over north-west Iran; zoomed rectangles show some landslide-affected slopes. Data processed by M. Vassileva.

However, the successful application of InSAR for downslope ground deformations requires a favourable acquisition geometry relative to the landslide morphology and orientation, i.e. slope and aspect angles (van Natijne et al. 2022). The slope angle is defined as the steepest downward direction (0°-90°), and the aspect angle is defined as the clockwise angle from the north (0°-360°). These topography parameters can be estimated from available global or more precise local digital elevation models. Geometric distortion related to the effect of topography on the radar signal (radar shadow and layover,) can limit the InSAR application when the landslide is located within the geometric distortion. The slope facing the satellite will have lower spatial resolution caused by the foreshortening radar distortions than the slope facing away from the satellite. For this reason, the downslope ground deformations detected by both orbits are more pronounced in terms of motion away from the sensor (see Fig. 3.8). The full landslide deformation vector can be obtained when the landslide motion is exactly parallel to the LOS direction: slope equal to the incidence angle

of acquisition and aspect perpendicular to the orbit flight direction (approximately east-west direction). For slopes lower than the incidence angle, InSAR sensitivity decreases; for topographies steeper than the SAR incidence angle, the slope will be affected by shadow radar distortions and therefore will have no data. When the landslide deformation vector is perpendicular to the LOS, the InSAR system is insensitive to the real motion (Aslan et al. 2020). The InSAR sensitivity to the motion decrees also with respect to the aspect angle: higher sensitivity for east-west oriented motion; and nearly insensitive to north-south direction motion (see Fig. 3.9).

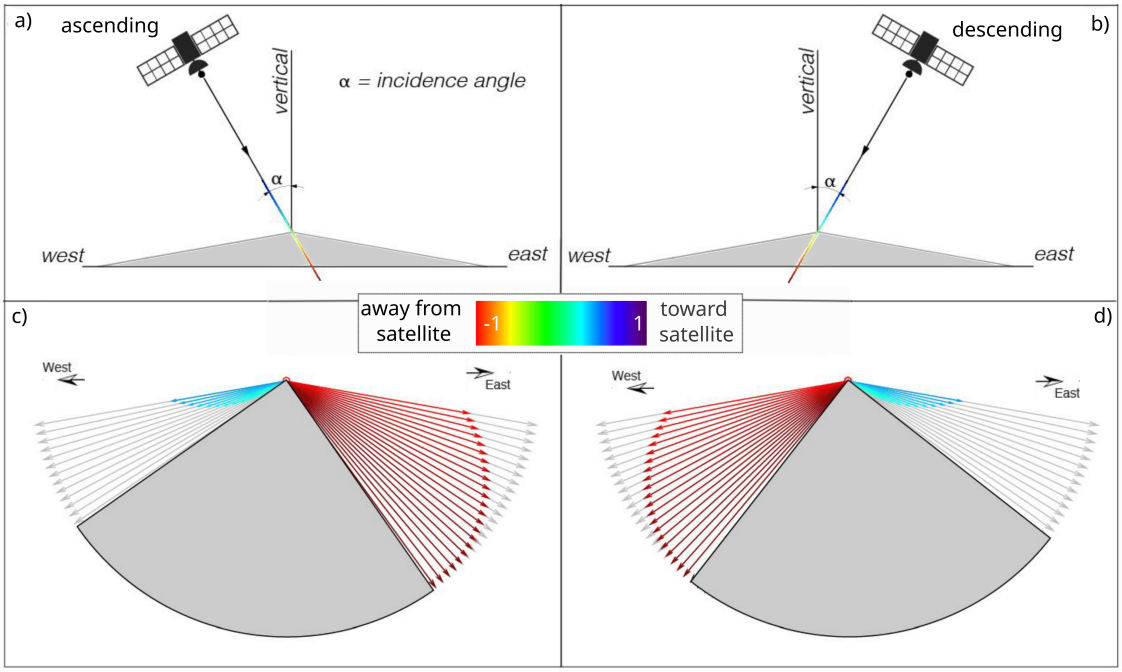


Figure 3.8: InSAR LOS sensitivity to slope motion for different slope angles. **a**, ascending and **b**, descending acquisition geometries; jet-coloured arrows define the amount of ground deformation of the unit vector detectable from ascending **c** and descending **d** viewing geometries for different downslope motions; negative values (hot colours) indicate slope moving away from the sensor, and positive values (cold colours) indicate slope moving toward the sensor; grey arrows define the deformation of the unit vector; the grey area defines the slope angles with no sensitivity in LOS (adapted after Aslan et al. 2020).

There are several strategies regarding deriving more easily interpretable deformation maps. One is to project separately ascending and descending LOS to the maximum slope. However, due to the landslide orientation and slope, the particular acquisition geometry will have lower or higher sensitivity and therefore the final slope projection can present some differences which need to be faced (Kang et al. 2017). Another strategy is to combine the two acquisition geometries and derive vertical and horizontal components (Choe et al. 2021). Indeed when the slopes are quite gentle and the landslide is approximately east-west oriented, this strategy provides interesting results, since it allows to separate the main landslide motion contained in the horizontal component and possible vertical pattern which depends more on local differences in slope and possible seasonal elastic behaviors of the shallower layers.

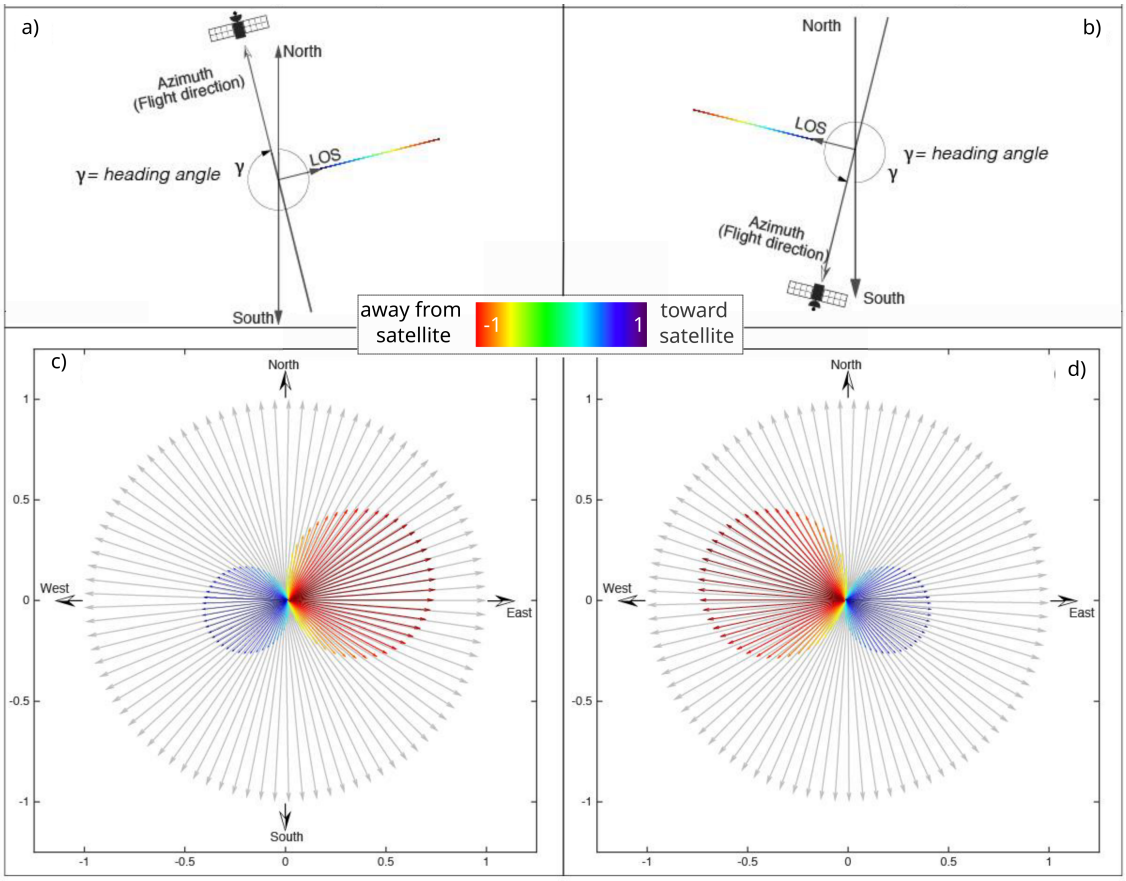


Figure 3.9: InSAR LOS sensitivity to slope motion for different aspect angles. **a**, ascending and **b**, descending acquisition geometries; jet-coloured arrows define the amount of ground deformation of the unit vector detectable from ascending **c** and descending **d** viewing geometries for different aspect motion directions; negative values (hot colours) indicate slope moving away from the sensor, and positive values (cold colours) indicate slope moving toward the sensor; grey arrows define the deformation of the unit vector (adapted after Aslan et al. 2020).

A key factor for the correct interpretation of the landslide dynamic and correlation with external potential driving factors is the extraction of representative ground displacement time series. There are several available post-processing strategies. The simple is to choose and extract the time information over selected points or small windows of pixels, based on topographic changes or other factors (geological unit changes, land cover, ground displacement velocities) (Yao et al. 2022). Another strategy is to use PCA and ICA to derive the principle displacement patterns and then extract from those the independent components which would give information regarding main trends, changes in trend and seasonality (Cohen-Waeber et al. 2018). A further strategy is to apply spatial clustering based on one or more factors such as topography, slope, ground displacement velocities etc. and estimate average displacement trends for each of them (Rygus et al. 2023). Rainfall-driven landslides for instance show seasonal variations that can be identified with MTI (Xu et al. 2019). The potential precursor deformation translated into an accelerating trend before the main landslide collapse can occur weeks to hours before the landslide failure (Shi et

al. 2022). The time scale of these precursors can be beyond the satellite SAR missions' revisiting time or can be easily masked by noise or some seasonal effects. This makes InSAR application for landslide failure prediction more challenging or even not applicable (Moretto et al. 2021). Ground-based techniques are preferred for failure prediction purposes which include extensometers, distometers, survey stations and prisms, and slope stability radar. Nonetheless, it remains a challenge to effectively detect precursory tertiary creep due to the inadequate field of view of the instrument, the unsuitable choice of the site where this was installed or insufficient area coverage. In this case, backward MTI analysis and large spatial coverage of the displacement maps can identify unstable slopes and guide experts in the choice of in-situ instruments.

Over areas covered by vegetation, both in natural and rural environments, InSAR coherence loss due to a decrease in the intensity and stability of the microwave signal, affects the applicability of this technique. In these settings, exploitation of long wavelengths, such as the L-band, characterized by a greater ability to penetrate through vegetation canopy, can lead to the retrieval of higher spatial density of displacement observations (Darvishi et al. 2018). For landslides moving too rapidly for InSAR capabilities, SAR and optical-based pixel offset techniques can be used to measure these displacements (Lacroix et al. 2022).

3.3 Tectonic related processes

The tectonic plate interactions are responsible for most of the earthquakes and volcanic activity (see Fig. 3.10). Governed by the convective forces generated inside the asthenosphere, the oceanic and continental tectonic plates are moved relative to each other: ascent movement drifts plates apart from each other forming divergent margins; the descend motion moves the plates towards each other forming convergent boundaries (Coltice et al. 2019). The most active divergent plate boundaries occur between oceanic plates where the magma rises to the surface and generates a new oceanic crust, such as the Mid-Atlantic Ridge. More recent divergent plate boundaries are continental rift zones where extension and thinning of continental crust occur, forming rift valleys, such as the Rio Grande Rift and the East African Rift. In case of continental crust collision, the crust is uplifted and results in mountain belts such as the Alps, Andes and Himalayas. When the collision involves oceanic crust plates, one plate descends into the mantle beneath the other plate forming a subduction zone. Above the subduction zone long chains of active volcanoes with intense seismic activity develop like the Aleutian Arc and the Andean Volcanic Belt. Two plates can slide horizontally past one another, forming transform margins such as the San Andreas Fault.

Most earthquakes occur along zones of high seismicity, which coincide with the plate tectonic boundaries (Varga et al. 2012). Mid-ocean ridges and transform margins are characterized by shallow earthquakes (usually less than 30 km deep), while in subduction zones earthquake hypocentre can reach up to 700 km depth. However, although rare, earthquakes can occur also in intraplate along zones of rock weakness, i.e. Fault Zones, indicating that the plates are not rigid and deform in their interiors (Talwani 2017).

There are about 1,350 potentially active volcanoes worldwide, not counting the volcanic belts along the mid-oceanic ridges. 75% of the volcanoes are concentrated along the coasts of the Pacific Ocean, in what is known as the Ring of Fire. About 500 of those 1,350 volcanoes have erupted in historical time. Most volcanoes occur on the plate tectonic

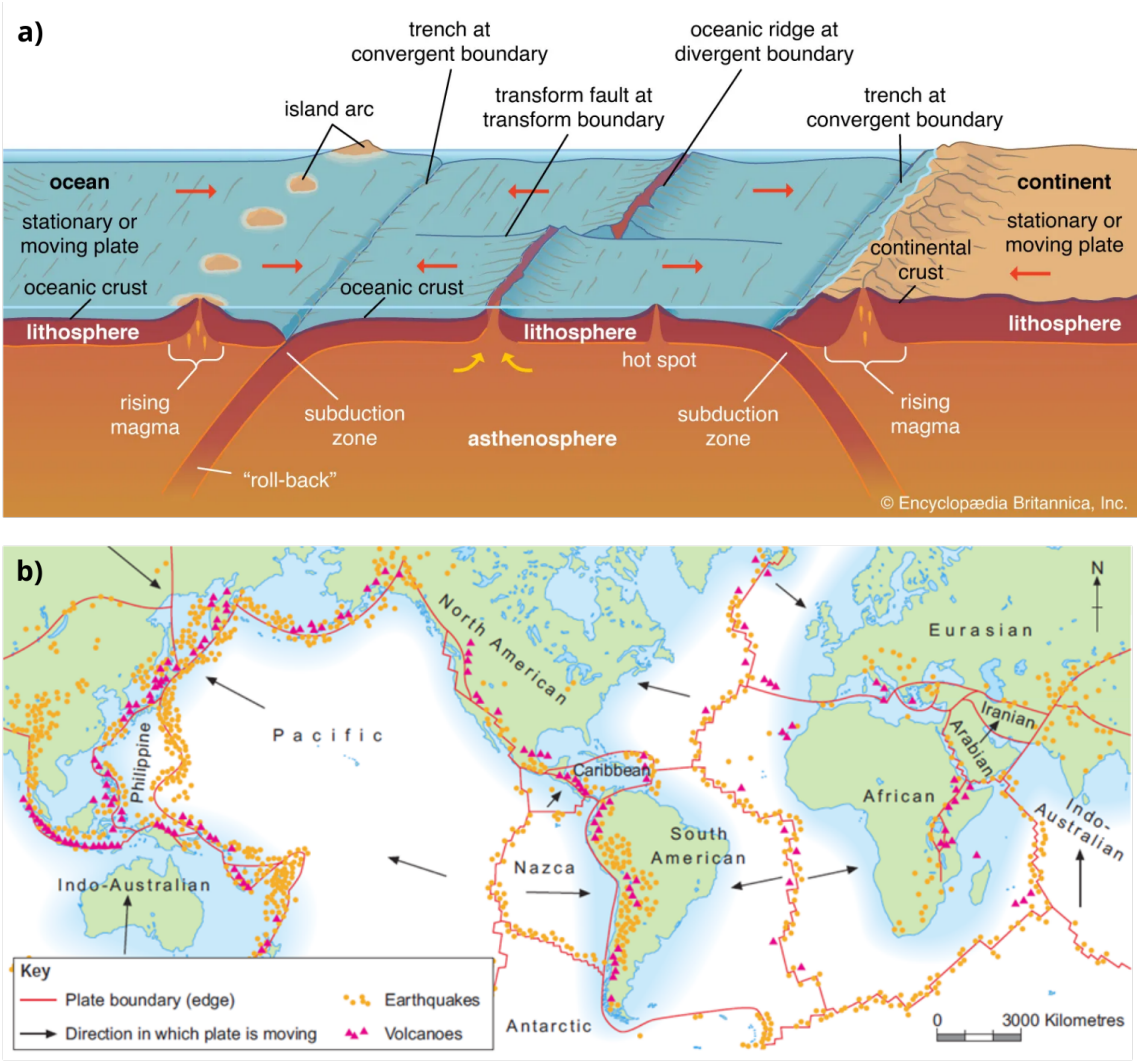


Figure 3.10: **a**, Scheme of the plate tectonic main activities (after ©2023 Encyclopædia Britannica, Inc.). **b**; global distribution of major earthquakes and active volcanoes (after thegeographeronline.net under the licence CC BY-NC-SA 4.0 Deed).

boundaries. However, there are so-called "hotspots'" where volcanoes are formed far from those margins such as the Hawaii island.

3.3.1 Earthquake

Earthquakes are violent and abrupt shakings of the ground caused by the sudden release of slowly accumulating strain energy along a rock fracture (fault), under the action of the tectonic plate motion (Kanamori and Brodsky 2004) (see Fig. 3.11). During the intra-seismic stage, the two rock blocks on either side of the fault are locked by friction. With time, stress is built up on the locked fault due to the plate motion. When the stress of the moving blocks exceeds the friction forces, the fault starts to rupture and the accumulated energy is released in the form of a seismic wave. The seismic wave starts to propagate through the earth's crust and along the surface producing ground shaking (co-

seismic stage). Depending on its size and location, an earthquake can trigger liquefaction, landslides and in some coastal areas, tsunamis (Marano et al. 2010). In the post-seismic stage, aftershocks can follow the main shock several hours, months, or even years later due to the relaxation of other parts of the fault caused by stress redistribution. Observations of the seismic cycle, the cyclic accumulation and release of strain, and stress redistribution over the entire region after an earthquake play a key role in estimating the likelihood in time and space of future earthquakes (Scholz 2019). Moreover, the change in stress after the fault rupture can influence the behavior of neighbouring faults and volcanoes (Seropian et al. 2021).



Figure 3.11: Private visit photos depicting earthquake-affected areas: **a**, surface rupture of the fault along Monte Vettor (central Italy) caused by the 24th of August 2016 earthquake; **b** and **c** building damages caused by the same earthquake in a nearby village. Photos taken by M. Vassileva in August 2023.

Based on the different stress conditions governed by the plate tectonic motions, the sense of slip and therefore the type of fault that forms will be different (see Fig. 3.12). In the case of dip-slip faults which move vertically, the rock block above and below the flat plane is referred to as hanging wall and footwall respectively. In normal faults, the hanging wall moves downward relative to the footwall in response to tensional stress. It results in rock extension and surface subsidence. Tensional stress happens at divergent plate boundaries where two plates are moving away from each other. This is typical along areas of continental

rifting, such as the Great Rift Valley of East Africa where a medium-magnitude earthquake between 5.0 and 6.0 are produced. In reverse faults, the hanging wall slips up over the footwall under the action of compressional forces which happens normally at convergent plate boundaries. The result is rock compaction and uplift of the ground. When the dip angle is 45^{o} or less, the fault is called a thrust fault, while faults with over 45^{o} dips are called megathrust faults. Along these faults, some of the largest seismic events have been generated as the 9.5 Mw Valdivia earthquake that occurred in 1960 along the Peru-Chile trench. In strike-slip faulting the two rock bodies are sliding sideways with respect to each other under the action of shear stress that occurred at transform boundaries. Based on the sense of motion the fault can be right or left lateral. A typical example is the East Anatolian Fault, where in February 2023 a 7.8 earthquake occurred.

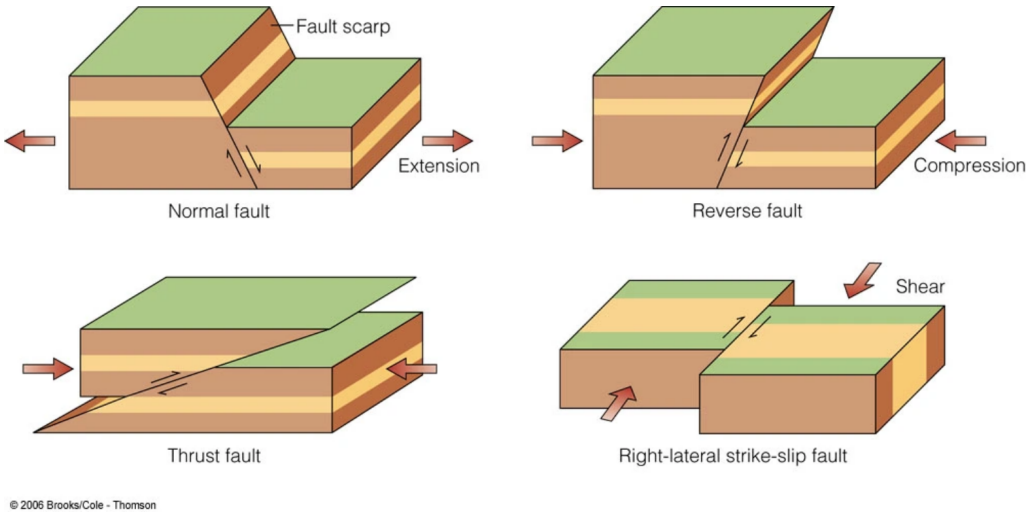


Figure 3.12: Types of faults (after ©2006 Brooks/Cole - Thomson).

The point where the fault begins to rupture is called hypocentre. The point on the surface directly above the hypocentre and the first to experience earthquake waves is called the epicentre. The earthquake magnitude depends on the size of the area of rupture. Faults are relatively planar fractures in the crust and therefore can be modeled as rectangle dislocations. The magnitude of the fault relative displacement during the rupture is defined by the slip parameter and the fault slip mechanism is given by the rake. In particular, the slip expresses the movement of the hanging wall relative to the footwall. The rake angle is measured anticlockwise and indicates 0 for left-lateral strike-slip, 180 for right-lateral strike-slip, -90° for normal fault and 90° for reverse fault.

InSAR is now routinely used following an earthquake to retrieve the ground displacement and invert for a source model that can provide useful knowledge of the geophysical properties of the fault rupture. Shallow earthquakes of a moderate and higher magnitude (<6) result in episodic deformations on the ground of the order of a few decimeters to a few meters which can affect large areas extending across different cities and even different countries. The coseismic displacement is typically measured from a single-pair InSAR using a pre- and a post-earthquake SAR acquisition. For better constraint of the real deformation field and consequently more correct inference of the fault source, it is always preferable to combine ascending and descending geometry ground displacement maps. The Okada elastic dislocation model provides a good representation of the surface and internal

deformation generated by shear and tensile faults in a homogeneous half-space (Huang et al. 2019). Indeed, earthquakes can occur at faults with different orientations, dipping angles and ruptures characterized by different rupture areas, and slip and rake angles, and therefore result in a variety of ground deformation patterns. For instance, normal faulting produces predominant uplift on the hanging wall and subsidence deformation on the footwall (Wang et al. 2014). Fault ruptures with predominant horizontal south-north components of displacement such as the case of strike-slip fault oriented south-north, cannot be constrained using InSAR and in such cases, alternative techniques such as optical and SAR pixel offset need to be implemented (He et al. 2023). When ground deformation is too high for InSAR capability, especially in proximity to the ruptured fault, additional geodetic techniques need to be used (Elliott et al. 2020) (see Fig. 3.13).

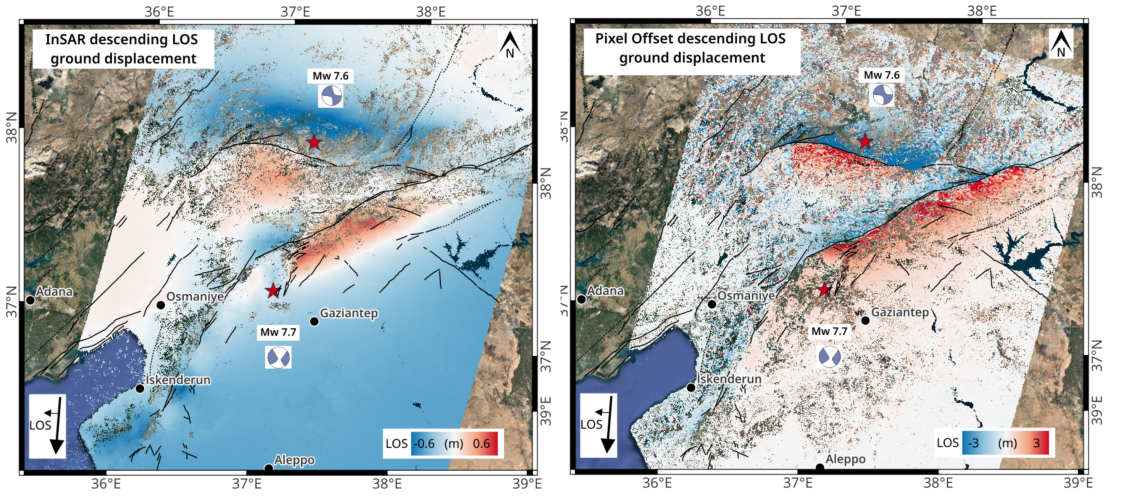


Figure 3.13: InSAR and pixel offset descending LOS ground displacement maps of the February 6 2023 Turkey/Syrian earthquake; same Sentinel-1 image pairs, orbit 21, acquired on January 29 and February 10 2023. InSAR processed by M. Vassileva. Pixel offset processed by Mahmud Haghshenas Haghighi. Active fault from Emre et Al. 2013. Epicentres of main shocks and moment tensors from Geofon. Background Google Satellite Map (Imagery @2023 TerraMetrics).

The stress changes on nearby faults (Verdecchia et al. 2018) and volcanoes (Bonali et al. 2015) produced by the earthquake can be inferred from the obtained source model and contribute to identifying potential faults' rapture and volcano activity triggered by the earthquake. By subtracting the main fault source contribution from the interferometric signal, the residual signal can be associated with landslides or liquefaction triggered by the earthquake and therefore contribute to identifying potential cascade geohazards. Potential aftershocks following the main event can contribute to building the cumulative ground displacement signal detected by InSAR and can be difficult or impossible to separate the different contributions. In this case, using higher temporal frequency resolution seismic data, to constrain the different sources in space can also help to distinguish their different contribution to the ground deformation. The post-seismic ground displacement that might follow moderate or large magnitude earthquakes in the months or even years after the event, can be monitored in time using MTI, contributing to evaluate whether cascade geohazards can be triggered following the main event. Inter-seismic deformations associated with the build-up of elastic strain before major fault ruptures can also be detected using MTI. For

the aim of seismic hazard assessment, it is important systematically to monitor active fault systems. This application offers a medium-range forecast tool although the small rates of a few mm to a few cm per year of intra-seismic deformation, and the large surface distribution of tens to hundred km make it harder to distinguish the intra-seismic ground displacement signal from atmospheric errors. Transient post-seismic and progressive inter-seismic displacements enable researchers to improve earthquake cycle models.

3.3.2 Volcanic activities

A volcano is the opening in the earth's surface in the form of a vent or feature, from which the magma erupts as lava, tephra, i.e. solid fragments and glasses, i.e. water vapour (H2O), carbon dioxide (CO2), and sulfur dioxide (SO2). Magma is pushed upward in the earth's crust by the ascent convection currents, and because it is less dense than the surrounding rock, can further rise through cracks across the solid crust up to the surface. These magma-filled fractures are referred to as dykes when they are sub-vertical and as sills when they are horizontal. When the magma cannot rise further it starts to accumulate at different depths creating over time magma chambers or along sills, i.e. planar sheet (see Fig. 3.14). Inflation of the ground, emissions of steam and gas from small vents in the ground as well as seismic swarms caused by the rising magma can precede the eruption (Schmincke 2004).

Based on magma viscosity, temperature, chemical composition and gas content, volcanoes can produce effusive or explosive eruptions (see Fig. 3.14). Basaltic magma characterized by low viscosity, i.e. poor in silica and rich in iron and magnesium, mainly produces effusive eruptions, where fluid lava is outpoured from the vent/feature generating lava flows. Andesite magmas characterized by higher viscosity, i.e. rich in silica, tend to trap the gas bubbles resulting in a build-up of pressure and explosive eruption. Fragmented and quickly solidified lava, tephra, and gasses are violently ejected into the air. Volcanic ash can be carried by the wind many km away from the vent. Lapilli and bombs that fall back around the vent, can rapidly move downslope along the volcano flanks producing pyroclastic flows.

The volcano edifice can be characterized by different size, shape and steepness (see Fig. 3.14). It is composed of different layers of volcanic material deposited during successive eruptions. Strato volcanoes are steep-sided cones formed from layers of highly viscous lava and pyroclastic material ejected during explosive eruptions. The thick lava cannot travel far down the slope and therefore it accumulates and cools, forming steep and high cones. It can reach slopes of about 30–35° and heights of more than 2400 m. They are usually found at convergent plate boundaries, such as Klyuchevskoy Volcano (Kamchatka), Mount Etna (Sicily) and Hekla (Iceland). Shield volcanoes are large volcanoes formed almost entirely of effusive lava flows which produce gentle slopes less than 10° steep. They are usually found at divergent boundaries and sometimes at volcanic hotspots, such as Mount Kilauea and Mauna Loa (Hawaii) and Piton de la Fournaise (Reunion). Cinder cone volcanoes are conical-like steep and small in size hills of less than 400 m with a bowl-shaped crater at the summit. They form during explosive eruptions when fragments solidify and fall as tephra and scoria around the vent forming the cone. They are the most common type of volcano in the world and many monogenetic volcanoes, meaning that they erupt only once in a life, are cinder cones. Some examples of cinder cone volcanoes are Cerro Negro (Nicaragua) and Hverfjall (Iceland). A Lava Dome forms from the slow extrusion of highly viscous lava that cannot flow away and instead accumulates around the vent. The lava dome can grow

in an endogenous or exogenous way. In the first case, as new lava is extruded into the dome interior it accumulates beneath the previous already solidified strata. The effect is a lateral spreading and vertical inflation of the overburdened layers. In the second case, the lava erupts directly at the surface via an internal discontinuity forming new surface lobes (exogenous growth). Some lava dome eruptions start with highly explosive events due to the gas released from the magma that reaches the surface. In other cases, when the dome grows too steep, it can destabilize and partially or completely collapse producing pyroclastic flows. Lava domes are often found on the sides of craters of stratovolcanoes, such as at Shiveluch (Kamchatka) and Mount St. Helens (USA). Submarine eruptions in hot spots and mid-oceanic ridges may produce seamounts, which can rise above sea level and form volcanic islands or arcs such as Kurile Islands.

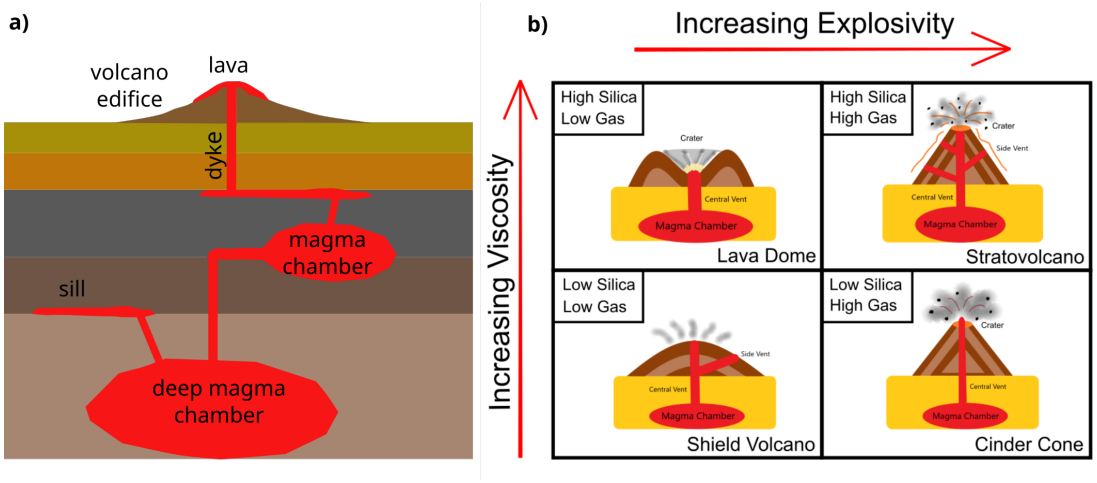


Figure 3.14: **a**, volcanic scheme with main features; **a**, types of volcanic edifice related to magma viscosity and type of eruption (source National Park Service / Astrid Garcia)

The edifice of active volcanoes is affected by magma chamber inflation and deflation cycles, new lava and tephra deposition on the flanks after eruption and eruption-related seismicity. Therefore the flanks, especially for steep volcanoes, might be insatiable and even collapse under the action of both external and internal forces. Flank instabilities and potential collapses into the ocean are extremely dangerous to coastal areas due to their tsunami-triggering potential.

Subsurface hydrothermal systems in volcanic regions arise from the interaction between the magmatic sources and hydrological features and manifest at the surface as hot springs, fumaroles, diffuse soil degassing and mud pools. In such hydrothermal systems, large quantities of steam and hot water are generated with the potential to be used to produce geothermal power. These processes also alter the surrounding rock material decreasing its strength conditions. Indeed, when such alterations occur on slopes, it can create a potential for a landslide.

Examples of geological processes which are connected to volcanic activities are shown in Fig. 3.15.

At active volcanoes, magmatic processes related to magma and gas migration, inflation and deflation cycles of magma chambers and hydrothermal circulation can produce ground deformations of the order of a few mm to a few decimeters (Biggs and Pritchard 2017). Such deformations can last from a few hours to years and can be precursors of upcoming

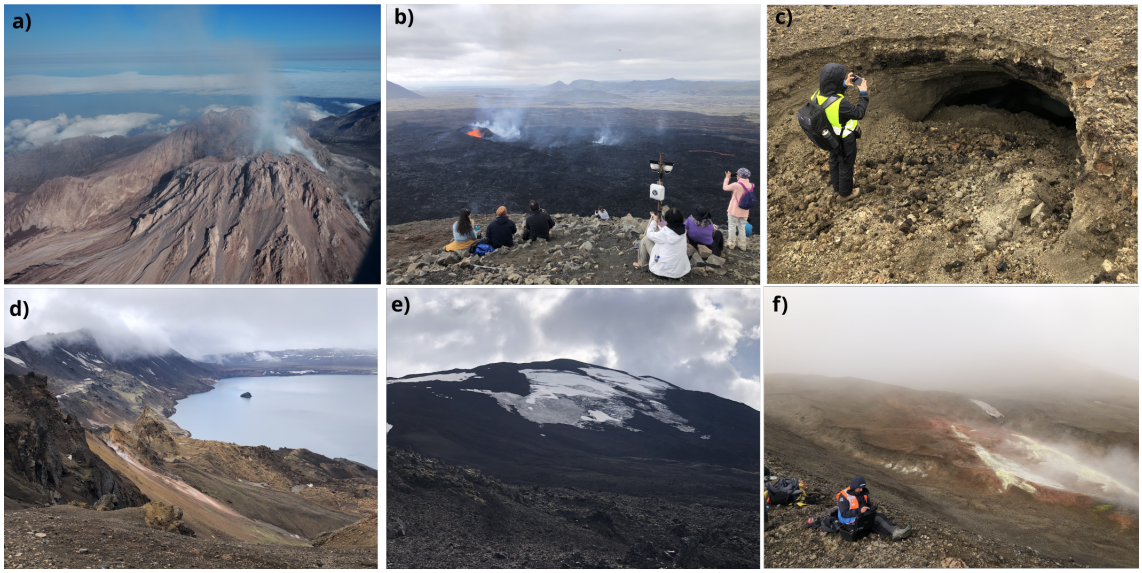


Figure 3.15: Fieldwork photos. **a**, active dome growth on Shiveluch (Russia); **b**, Fagradalsfjall 2023 effusive eruption (Iceland); **c**, sinkhole formations over lava and tephra deposits in Askja (Iceland); **d**, landslide on Askja crater (Iceland); **e**, rock glacier instabilities at Hekla summit (Iceland); **f**, hydrothermal alterations at the eastern slope of Askja crater. Photos taken by M. Vassileva in July/August 2023

volcanic eruptions and infer the location, volume change, and shape of the magma body causing the crustal deformation via analytical elastic modeling or more complex viscoelastic and finite element models.

DInSAR and MTI are nowadays operatively used over active volcanoes for near-real-time detection of volcanic unrest (Poland and Zebker 2022) (see Fig. 3.16). The ground above the magma source is uplifting when new magma comes from deeper sources or when withdrawn due to lateral migration or upward intrusion to the surface as dyke or silk. When the magma chamber is partially or totally emptied in case of lateral migration or direct eruption, the ground above subsides. Volcanic flanks can be monitored using MTI, and potential instabilities can be detected (Schaefer et al. 2019). The MTI application on volcanic flanks is similar to the case of landslides. However, together with the flank downslope displacement signal, additional volcanic signals can be overlapped, and the triggers of the landslide can be also magmatic-related (Carnemolla et al. 2023). Volcanoes can have steep topography and therefore the lateral pushing or contraction can also have an important contribution (Ebmeier et al. 2013). Therefore for a better constraint of the magmatic source in terms of depth and volume, it is preferable to jointly invert ascending and descending LOS ground displacement datasets (Xu et al. 2023).

InSAR has very limited application in the case of very steep volcanoes, glacier volcanoes, volcanoes covered by ice sheets, snow or dense vegetation. InSAR application is limited also in the case of fast deformations of the orders of some meters per day or week (Dualeh et al. 2023). Indeed, dome growth can be very rapid (Zorn et al. 2019). Volcano morphology can drastically change during eruption episodes and therefore updated post-eruption DEM needs to be acquired anew to improve the InSAR results. When the volcano shows activity only a few days to hours before an eruption, the SAR acquisition revisits time might not be enough. The integration with in-situ instruments such as seismometers and GNSS stations,

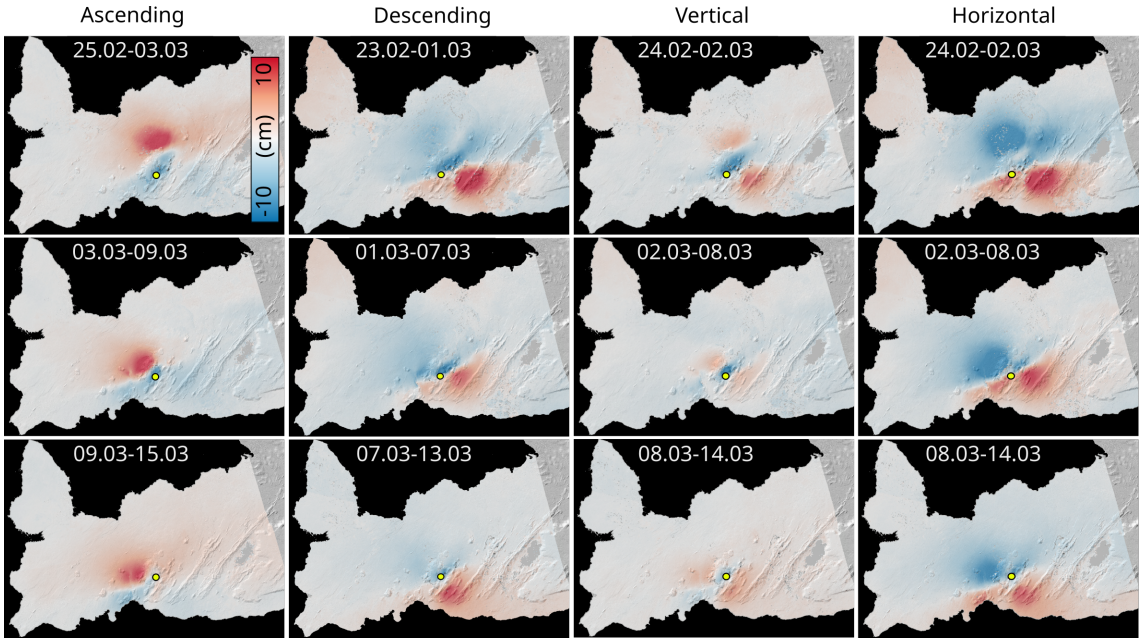


Figure 3.16: InSAR ground displacement observations for the 3 weeks before the 19th March Fagradalsfjall 2021 eruption; Sentinel-1 data in ascending and descending geometry were used; vertical and horizontal ground displacement components were derived by combining the two LOS geometries; positive values in Ascending and Descending maps for motion away from the sensor, positive values for uplift motion and positive values for eastward motion. Data processed by M. Vassileva.

contributes to a better time coverage of the measurements (Corsa et al. 2022). InSAR observations can also be used to select suitable sites for new GNSS station installations to ensure a more complete in-space data coverage.

4 Land subsidence in the municipality of Macei

This chapter was published as:

Magdalena Vassileva, Djamil Al-Halbouni, Mahdi Motagh, Thomas R. Walter, Torsten Dahm and Hans-Ulrich Wetzel.**A decade-long silent ground subsidence hazard culminating in a metropolitan disaster in Maceió, Brazil.** *Scientific Reports* 11, 7704 (2021), doi.org/10.1038/s41598-021-87033-0

Some minor changes were applied with respect to the original publication: the Data and methods chapter was moved up after the Introduction; some minor typos were corrected.

Author contribution statement:

As first author, I contributed most to the work including conceptualization of the work, methodology development, SAR data collection, MTI data processing, geophysical source inversion modelling, geohazards analysis, validation, interpretation, writing the original draft, reviewing and editing successive manuscript versions and visualization. Djamil Al-Halbouni performed DEM processing and data visualization. All co-authors contributed to the discussion, reviewing and editing of the manuscript.

Method summary:

In this work, MTI analysis was performed to characterize the spatiotemporal evolution of land subsidence over a 16-year time span. A multisensor and multi-geometry dataset of Envisat (ascending and descending orbit paths), Alos-1 (ascending orbit path), Alos-2 (ascending and descending orbit paths) and Sentinel-1 (descending orbit path) SAR acquisitions was used. A vertical-only approach was used to homogenise the different datasets. Precipitation data were extracted from CHIRPS and a local rain station. Representative time series over the major deforming areas were extracted and their main displacement rates were analysed for correlations with precipitation time series. Ascending and descending InSAR data for several years were jointly inverted to derive the best-fit point and dislocation elastic source models. The distinct element method (DEM) was used to simulate the mechanical failure of deep-seated cavities along a 2D transect considering the specific regional geologic setting. The simulated ground deformations were compared after the InSAR observations. Main conclusions about the deep-seated geological processes and the influence of external factors were finally derived based on the results.

Supplementary Material:

Supplementary material was not included in the chapter and can be found on the following link under the voice Supplementary Information.

4.1 Abstract

Ground subsidence caused by natural or anthropogenic processes affects major urban areas worldwide. Sinkhole formation and infrastructure fractures have intensified in the federal capital of Maceió (Alagoas, Brazil) since early 2018, forcing authorities to relocate affected residents and place buildings under demolition. In this study, we present a 16-year history (2004-2020) of surface displacement, which shows precursory deformations in 2004-2005, reaching a maximum cumulative subsidence of approx. 200 cm near the Mundaú Lagoon coast in November 2020. By integrating the displacement observations with numerical source modelling, we suggest that extensive subsidence can be primarily associated with the removal of localized, deep-seated material at the location and depth where salt is mined. We discuss the accelerating subsidence rates, the influence of severe precipitation events on the aforementioned geological instability, and related hazards. This study suggests that feedback destabilization mechanisms may arise in evaporite systems due to anthropogenic activities, fostering enhanced and complex superficial ground deformation.

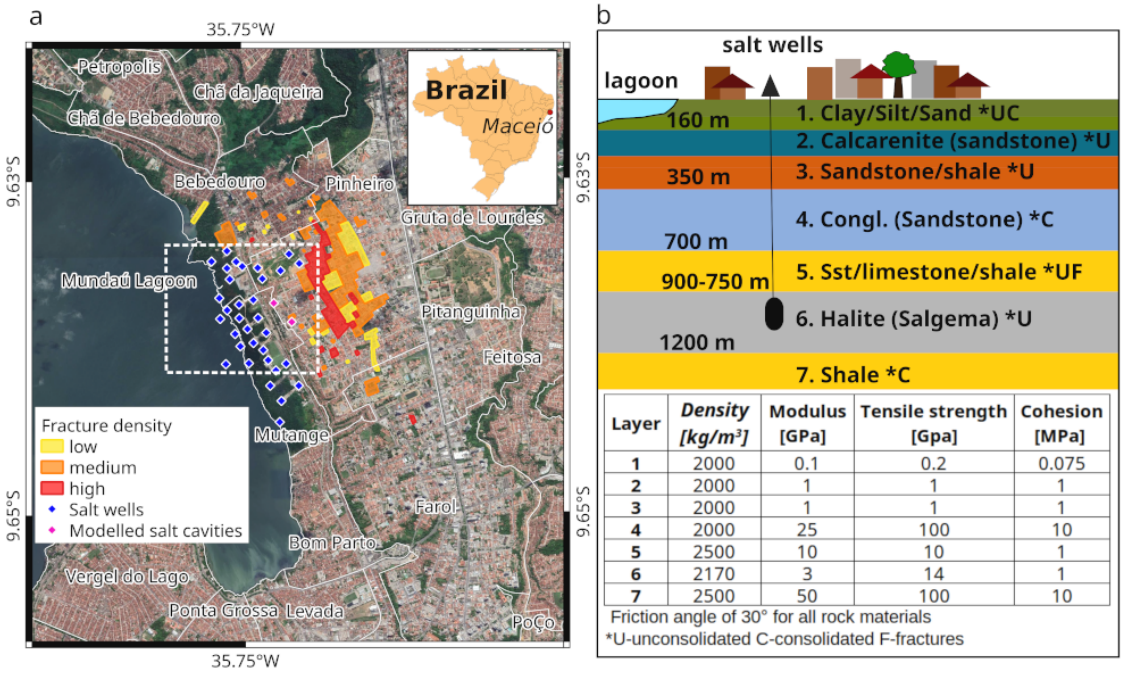
4.2 Introduction

Land subsidence affects many highly populated urban areas of the world, either as a consequence of extensive groundwater depletion, such as in Tehran (Motagh et al. 2008; Haghshenas Haghighi and Motagh 2019), Las Vegas (Bell et al. 2008), Beijing (Chen et al. 2016), and Tucson (Kim et al. 2015), as a combined effect of loading and compaction of unconsolidated lacustrine sediments, such as in Mexico City (Cabral-Cano et al. 2008; Solano-Rojas et al. 2020), or via construction dewatering8 and underground mining (Parmar et al. 2019; Riesgo Fernández et al. 2020; Zhu et al. 2020).

However, naturally or anthropogenically induced evaporite dissolution with consequent ground subsidence also occurs in several parts of the world, such as the salt dissolution cases of the Permian and Triassic evaporitic terrain in the UK (Cooper 2002), numerous Triassic and Tertiary evaporite areas in Spain (Lucha et al. 2008), Quaternary sediment subrosion in the Dead Sea (Yechieli et al. 2016; Al-Halbouni et al. 2017, 2021) and many areas underlying the Permian basin in the United States (Martinez et al. 1998; Johnson 2008). Evaporite dissolution and consequent ground subsidence pose a severe geohazard for overlying urban areas, such as Zaragoza in Spain (Sevil et al. 2017), Tuzla in Bosnia and Herzegovina (Mancini et al. 2009), and Wieliczka in Poland (Perski et al. 2009).

In particular, salt (halite, or NaCl) is the most soluble evaporite rock that is widespread in continental regions. Freshwater percolation through halite layers rapidly dissolves these evaporites, leading to the formation of subsurface voids that, as they widen, can reach unstable conditions and provoke the roofs of these voids to collapse. A series of successive roof failures can cause the cavity to migrate upward, reaching the overburden layers. If the cavity's roof, i.e., the rocks above it is not rigid enough, the cavity may collapse, with surface effects that can range from slow subsidence to sudden collapse and formation of sinkholes (Martinez et al. 1998).

Solution mining refers to the extraction of salt by injecting water through wells drilled into subterranean deposits, dissolving the salts and pumping the resulting brine back to the surface, leaving brine-filled cavities behind (Johnson 2005; Cooper 2020). Since 1970, a total of 35 industrial brine extraction wells have been installed along the Mundaú Lagoon coast in the urban area of Maceió, and more precisely, in the neighbourhoods of Mutange,



Layer	*Density [kg/m³]*	Modulus [GPa]	Tensile strength [Gpa]	Cohesion [MPa]
1	2000	0.1	0.2	0.075
2	2000	1	1	1
3	2000	1	1	1
4	2000	25	100	10
5	2500	10	10	1
6	2170	3	14	1
7	2500	50	100	10

Friction angle of 30° for all rock materials
*U-unconsolidated C-consolidated F-fractures

Figure 4.1: (a) Overview of the study area. Yellow, orange, and red polygons represent respectively areas with low, medium and high concentrations of fractures in buildings and infrastructures (assessment conducted by CPRM in 201825). Blue and magenta diamonds show the locations of all installed salt wells since 1970. Specifically, magenta diamonds highlight the two cavities used in the DEM. The White dashed polygon is the area in Fig. 4.3a. Inset shows the geographical location of Maceió. (b) Simplified geological stratigraphic model and table of the rock material properties used in this study. Background for (a) Google Earth CNES/Airbus imagery. (a) was plotted in QGIS (v 3.16, https://www.qgis.org/en/site/).

Bebedouro, and Pinheiro (Fig. 4.1a). Maceió, the capital city of the Brazilian state of Alagoas, lies in the Sergipe-Alagoas salt basin, which formed along the Brazilian coast during South Atlantic rifting and was initiated in the Late Jurassic to Early Cretaceous. A variety of mostly consolidated sediments associated with different geneses and geological periods fill the basin.

At the beginning of 2018, fractures on both buildings and roads started to develop in the neighbourhood of Pinheiro following a rainfall event on the 15th of February and a magnitude 2.4 earthquake (Brazilian local magnitude scale) on the 3rd of March (Fig. 4.1a). Due to the high geohazard impact on the local population, the case received much national media attention. A total of 6,356 buildings were classified as risk zones and placed under demolition by the Brazilian authorities, with consequences for 25,000 residents, who were or still have to be relocated to other parts of the city, and considerable changes occurred for the urban setting of the affected districts (S&P Global 2020).

Several causes, including water depletion and pre-existing geological structure reactivation, have been investigated by the Brazilian Geological Service (Serviço Geologico do Brazil - CPRM), which performed a systematic survey and analysis between 06.2018 and 04.2019 (CPRM-SERVIÇO GEOLÓGICO DO BRAZIL 2019). Recently installed seismic stations registered very shallow seismicity (hypocentre < 1 km) under the lagoon and the neighbourhood of Pinheiro on the 1st of February 2019. A gravimetry survey showed neg-

ative anomalies (bodies with a lower density than the surrounding rocks) over the salt extraction area. An audio-magnetotelluric (AMT) investigation also detected low conductivity at approximately 900 m depth, which corresponds to the underground extraction layer. Sonar measurements of the salt cavities have detected upward migration and enlargement and occasional total or partial collapses in most of them. The 3rd of March 2018 seismic event with a hypocentre of approximately 1 km was later attributed to possible cavity collapse. Geodetic measurements using Sentinel-1 SAR data during 04.2016 and 12.2018 detected cumulative subsidence reaching 40 cm with a maximum close to the lagoon shoreline. Geological and geotechnical observations also identified several very shallow discontinuities visible in outcrops that have fostered erosion effects due to surface water infiltration, further increasing the geological instability.

In this study, for the first time, we present a 16-year history of the spatio-temporal evolution of subsidence in the city of Maceió. For this purpose, we analysed a large archive of synthetic aperture radar (SAR) data from past and current operational satellite missions between 2004 and 2020, highlighting the importance and effectiveness of the Interferometric SAR (InSAR) technique for monitoring geological instabilities. To test the underlying cause of the subsidence pattern, we used 3D geophysical source inversion and 2D geomechanical simulation. Different 3D elastic source models were tested to explain the overall deformation pattern. The distinct element method (DEM) allowed us to explicitly analyse subsidence due to mechanical failure of deep-seated cavities along a 2D transect in the regional geologic setting. We investigate the possible influence of meteorological factors and discuss whether the subsidence has been constant or accelerated in recent times. We further exploit interferometric measurements to highlight the dynamic evolution of the subsidence hazard by generating dynamic geohazard maps that are valuable for further infrastructure risk assessment.

4.3 Data and methods

4.3.1 Multi-temporal DInSAR

We measured surface displacement for the last 16 years using the multi-temporal DInSAR technique and exploited the full archive of multi-sensor SAR data from past and currently operational satellite missions. We adopted the Small BAseline Subset (SBAS) algorithm (Berardino et al. 2002) implemented in the commercial software ENVI/SARscape. SBAS is based on a combination of interferograms characterized by small normal and temporal baselines, allowing us to maximize spatial and temporal coherence. The main characteristics of the six independent SAR datasets processed in this study are illustrated in supplementary Fig. S1 and Table S1. The Envisat ASAR C-band and the Alos-1 Palsar L-band SAR missions cover the period of 10.2003-01.2011. A four-year gap in acquisitions is present between 01.2011 and 02.2015. The currently operational Sentinel-1 C-band and Alos-2 Palsar L-band missions cover the period from 02.2015 to 07.2020. The SBAS connection graphs are plotted in supplementary Fig. S2. Some selected wrapped phase displacement maps are shown in supplementary Fig. S3.

Since both ascending and descending acquisitions covering the same period and with the same time resolution were available only for the periods of 03.2005-03.2006 and 03.2015-09.2019, we ignored the horizontal component and converted the line-of-sight (LOS), i.e., direction from the satellite to the ground, displacement into vertical-only components. For

the data overlap periods, we chose the dataset characterized by higher spatial coherence and temporal density, while for the data gap period, we performed a polynomial regression considering the average velocities of one year before and one after the time gap.

We estimated the residuals between the decomposed vertical component and the simplified vertical-only component for the period of 10.2016-09.2019. The approximate error is equal to two-thirds of the horizontal velocity, and in the case of the westward horizontal component, the vertical displacement is overestimated in the ascending geometry and underestimated in the descending geometry when assuming a vertical-only component. Nevertheless, the final error in the area of maximum subsidence due to the vertical-only simplification for the Sentinel-1 dataset, which has a descending geometry, is on the order of 1-2 cm/year.

The SBAS overall velocity error was estimated for each dataset by calculating the velocity mean and standard deviation over regions assumed to be stable (supplementary Table S1). The estimated overall error is on the order of 1-2 mm/year in the LOS direction, which means for the cumulative displacement for the whole data period, the error is on the order of a few cm. However, while this overall trend does not significantly affect the final interpretation and results, localized errors characterized by higher values may be present in the dataset, with consequent misinterpretations, i.e., a subsidence hazard in the region outside the main deforming areas.

4.3.2 Inverse numerical modelling

We performed geophysical elastic source inversion using the modelling module of ENVI/SARscape and by jointly inverting one ascending and one descending measurement for five separate periods: 03.2015-03.2016 (Alos-2 PALSAR ascending and descending); 03.2016-03.2017 (Alos-2 PALSAR ascending and descending); 10.2016-10.2017 (Alos-2 PALSAR ascending and Sentinel-1 descending); 10.2017-09.2018 (Alos-2 PALSAR ascending and Sentinel-1 descending); and 09.2018-09.2019 (Alos-2 PALSAR ascending and Sentinel-1 descending). We constrained the source parameters by minimizing the misfit between predicted and observed surface displacements (Marquardt 1963). First, we subsampled the displacement datasets using a regular grid with two different sampling densities of 50 m and 150 m over the area of subsidence and the surroundings and generated a set of approximately 650 point measurements. Initially, we set up a point pressure source (Mogi 1958) by leaving all source parameters unconstrained: volume change, depth, and coordinates of the source centre. Afterwards, we inverted the measurements for a rectangular model dislocation (Okada 1985) by assuming a pure vertical opening (dip=0°, rake = 0° and slip=0) and by fixing the horizontal location of the centre of the rectangle with the coordinates retrieved from the point pressure source modelling. We retrieved the best-fitting depth, strike, and opening values assuming a rectangular crack of 600×150 m. By varying the length and width parameters, the opening value changed; however, the volume change estimated as length*width*opening remained quite constant.

4.3.3 2D distinct element modelling

We performed 2D distinct element modelling (DEM) with PFC2D V5 software from Itasca. The DEM simulates the material as an assemblage of discrete and rigid particles of different radii and geomechanical parameters (Cundall and Strack 1979). The particles are bonded together using the so-called soft-contact approach, which allows them to rotate and overlap

at contact points, simulating mechanical interaction. For a proper representation of the matrix between grains, the parallel-bond scheme was used, which allows the simulation of shear and tensile crack formation and block rotations (Potyondy and Cundall 2004). Based on the available stratigraphic information, we set up the configuration of the material layers and properties (supplementary Fig. S4). Detailed parameters of the simulated geologic materials and parameters as well as geometries are given in supplementary Tables S2 and S3.

We installed the two cavities by deleting the particles at a specific depth and according to the size detected by the sonar measurements. The two cavities had centre point depths of 1010 m and 1070 m and sizes of approximately 14100 m3 and 31400 m3 for M30 and M31, respectively. Instantaneous particle deletion was followed by the setting of temporarily high bond strengths to avoid dynamic effects. To simulate the geomechanical behaviour of the subsurface, two independent scenarios, pressurized conditions (S1) and depressurized conditions (S2), were used. For S1, a pressure of 2.758 MPa, equivalent to the reported salt-mining pressure in this area, was initially injected into the cavity walls, which were simulated as explicit radial forces onto the inner rim particles. The modelling was redone with different initial conditions, including a lower pressure of 1.5 MPa and reproducing possible mining depressurized/inactive conditions.

Different aspects should be considered in terms of uncertainty. First, it is important to highlight that the geomechanical model that was performed is a 2D model along a transect. The disk-shaped particles contain a third particle dimension of size one, which is added for correct calculations. Therefore, it might overestimate the instability due to missing bonds in the third dimension, and it is not possible to compare the volume changes directly with those retrieved in the 3D geophysical source inversion. Second, the model resolution (model size vs. particle radii) and bulk rock parameter calibration contain another uncertainty in particle-based simulations (Potyondy and Cundall 2004). However, extensive experience with similar simulation setups has recently been achieved, and particle scale parameters have been adjusted by applying findings from available simulated compression and tension tests (Al-Halbouni et al. 2018, 2019) on material samples used in this study (consolidated rock, unconsolidated rock, and halite). Third, DEM models have an intrinsic uncertainty due to random particle packing, a feature also observable in natural geologic depositional environments. Therefore, a repetition of four models per scenario was performed with different random particle assemblies. The resulting error margin in the subsidence calculation for the total collapse of both cavities (scenario S2) is plotted in supplementary Fig. S4b. The error is low at the margins of the 2D transect and higher with values up to approximately 50 cm in the part most affected by deformation. Due to the discontinuous nature of the model, each random assembly produces also different structures in the subsurface and at the surface. An even larger number of model generations would decrease the error. We restricted the detailed stress and crack analysis to a representative model for each scenario and have shown that the subsidence determined by InSAR is within the range of the simulated subsidence, even close to the mean of all assemblies.

4.3.4 Geohazard maps

Geological instability hazard maps were produced based on the angular distortion (Skempton and Macdonald 1956; Fernández-Torres et al. 2020; Cigna and Tapete 2020), which was calculated as the ratio of the subsidence horizontal gradient between two adjacent pixels to the horizontal distance between them, equivalent to 15 m of pixel size. The sub-

sidence horizontal gradient was calculated from the Sentinel-1 LOS displacement maps for the cumulative periods of 10.2016-10.2017, 10.2016-10.2018, 10.2016-10.2019, and 10.2016-07.2020. We classified angular distortion into five hazard levels (supplementary Table S4) based on the limiting criteria available in the geotechnical literature and standards (Skempton and Macdonald 1956; Burland and Wroth 1975; Eurocode 7).

4.4 Results

4.4.1 Spatio-temporal evolution of subsidence

Multi-temporal and multi-sensor InSAR processing (see the data and methods section) has resulted in a high-resolution ground subsidence map of Maceió (Fig. 4.2). This map shows the spatio-temporal evolution of the subsiding area, which affects large parts of the neighbourhoods of Bebedauro, Mutange, and Pinheiro (Figs. 1 and 2).

Early in the time series, since at least the second half of 2004, concentrically shaped subsidence patches gradually started to develop close to the Mundaú Lagoon coast with an initial maximum average velocity of approximately 4 cm/year (Figs. 2 and 6a). In the following years, the displacement gradually intensified to approximately 10 cm/year in 2007-2008 and reached approximately 12 cm/year in 2010-2011. In the second period of SAR data coverage that extends from 03.2015 to 11.2020, an initial subsidence velocity of approximately 12 cm/year was observed (2015-2016), which is similar to the period of 2010-2011. We assume that during the data gap from 02.2011 until 03.2015, the subsidence rate did not change. A slight increase in velocity to 17 cm/year was observed in 2016-2017, which then drastically increased during the second half of 2017, reaching a maximum of 27 cm/year (Fig. 4.6a and b). As the rate of subsidence has increased, the area affected by subsidence has also enlarged considerably. The maximum velocity has decreased to 20 cm/year since the beginning of 2020. A maximum cumulative ground subsidence of approximately 50 cm (over the 5-year period covering half of the first dataset), 46 cm (over the four-year data gap using data interpolation), and 105 cm (over the 5 year-period covering half of the second dataset) was estimated for the three periods, with a total maximum subsidence for the whole period from 07.2004 until 11.2020 of more than 2 m (Fig. 4.2c and d).

For the periods where both ascending and descending SAR acquisitions were available, we also derived the east-west horizontal component of displacement (Fig. 4.2l-p) (Motagh et al. 2017). The horizontal displacement maps show a westward motion in accordance with the slope of the subsidence, which increases with increasing subsidence, although the displacement is still a few cm/year. The area of maximum horizontal displacement does not coincide with the area of maximum subsidence since the horizontal component is related to the vertical displacement gradient rather than its absolute value. Therefore, our projection of the line-of-sight InSAR displacement in the vertical direction is a valid approximation in areas where the subsidence reaches its maximum values.

From the area covered by InSAR observations, we estimate a minimum cumulative surface volume loss of 7.9E+05 m3. However, the volume loss is much larger because a considerable part of the displacement is hidden underwater.

The vertical displacement time series also highlights other regions of ongoing subsidence. South of the lagoon, $\tilde{3}$ km south of the main subsidence region, we find localized subsidence that has been occurring since 2007, which affects parts of the coastal districts of Bom Parto

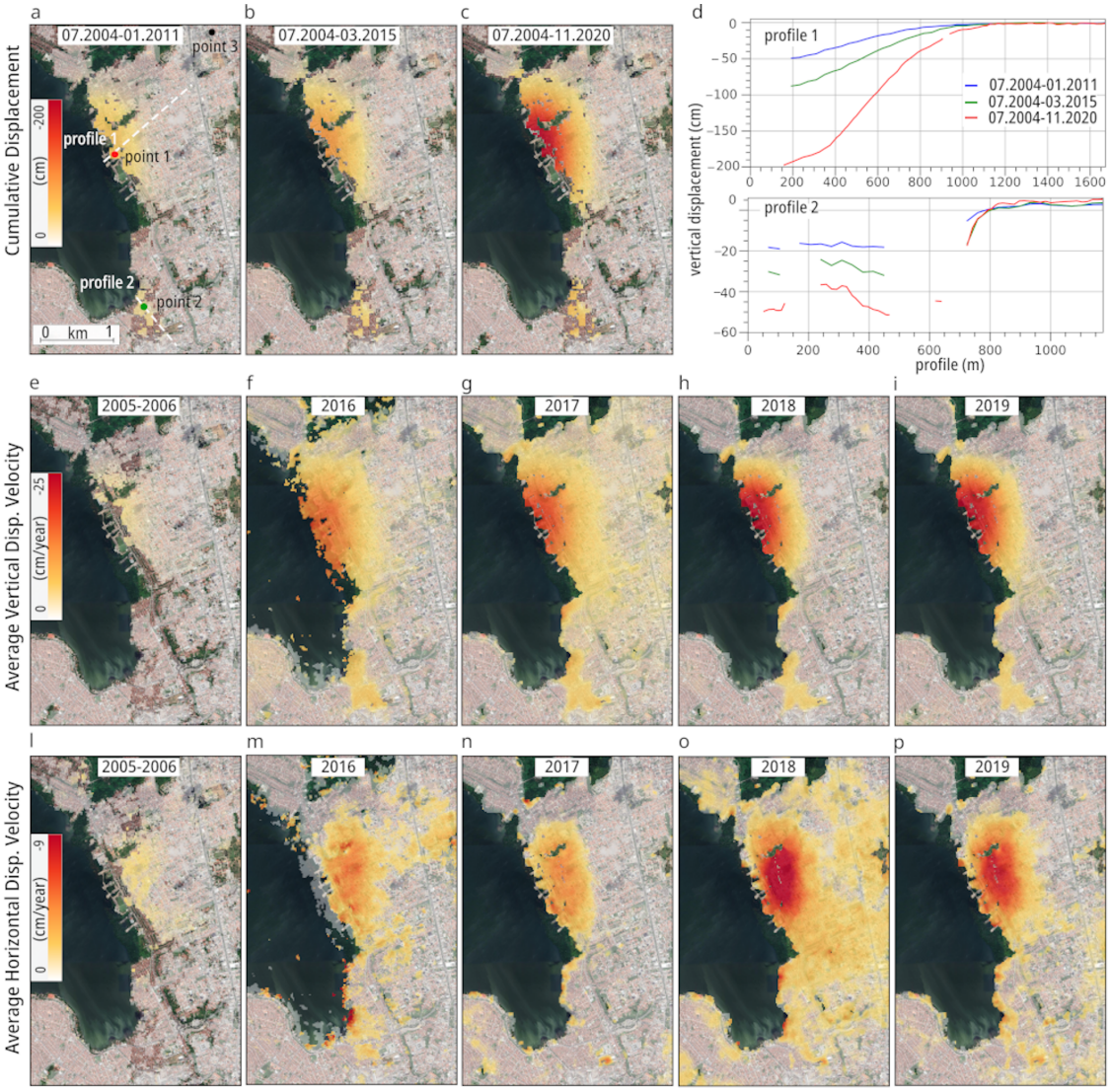


Figure 4.2: InSAR time series results. (a-c) Cumulative vertical subsidence maps obtained by projecting the LOS component into vertical only and combining in time and space all available displacement datasets. Red, green, and black dots show the locations of the time series plotted in Fig. 4.6 respectively point 1 (in the main subsiding area), point 2 (in the minor subsiding area) and point 3 (in the hypothetically stable area). White lines show profiles 1 and 2 plotted in (d) where the blue line refers to the period 07.2004-01.2011, green for 07.2004-03.2015, and red for 07.2004-11.2020. Ascending and descending displacements have been combined for the periods where both geometries were available to retrieve (e-i) vertical and (l-p) horizontal average displacement velocities. The horizontal negative values refer to westward motion. Background Google Earth CNES/Airbusimagery. The figures (except d) were plotted in QGIS (v. 3.16, https://www.qgis.org/en/site/).

and Levada. Subsidence in this location has been characterized by an almost constant average vertical velocity of 4 cm/year until the beginning of 2020, after which the trend has quite suddenly decreased to 1 cm/year and sometimes to 0 cm/year (Fig. 4.6a and b). While this trend differs from the accelerating trend in the main subsidence region, the vertical displacement map suggests that the two subsidence regions are spatially connected through a displacement pattern that can be traced along large parts of the coast and that is characterized by an NNW-SSE orientation, which is possibly indicative of a much larger source region (Fig. 4.2e-i).

4.4.2 Modelling the subsidence cause and processes

Ground subsidence observations in urban areas can be better understood by simulating source processes, which we approached using two modelling strategies. First, we realized a source inversion that considered simplified sources in elastic host rocks only. Second, we develop more complex numerical models to explore the propagation of subsurface cavities, changing stress conditions, fracture formation, and subsidence.

The geodetic data inversion was derived for two displacement source models: point model (Mogi 1958) and rectangular crack model (Okada 1985) in isotropic elastic half-space. For the point model, the observed ground subsidence is assumed to be related to a sub-ground pressure change caused by a spherical depressurised point source. This is then converted to volume. For the rectangular crack model, the observed subsidence is assumed to be related to a volume change due to a near-horizontal fracture that is closing. Both source models can be associated with the withdrawal of fluids and/or removal of sub-ground solid materials (Heimlich et al. 2015; Sreejith et al. 2020). In the case of salt mining, the volume loss might be attributed to the extraction of salt31. The search for the best modelling parameters was performed in a non-linear inversion scheme (see data and methods) by repeating hundreds of simulations until the misfit between the data and model was minimized. The resulting point pressure model provides a good approximation of the centre of the displacement source, while the rectangular crack model allows the retrieval of information regarding the possible spatial distribution and orientation of the displacement source.

The retrieved source parameters for the point pressure and rectangular crack source for the five different one-year intervals are shown in Table 1 (Fig. 4.3a and b). The best-fitting source models (Fig. 4.3c) are located at a depth of 600-1000 m, which is coincident with the halite layer (750-950 m). In the point pressure model, the centre of displacement, and therefore the east-north source location, remains constant through time and coincides with the centre of the salt mining area, while the rectangular crack model shows a SE-NW source orientation, which is in alignment with the spatial distribution of the wells. A general upward movement is visible from the two models: from 774 m to 653 m for the point pressure source model and from 953 m to 807 m for the rectangle source model. A comparison of the two models shows that the point pressure source model results in higher volume changes, although a shallower source depth compared to the rectangular crack model. A volume loss on the order of E+05 m3, which is comparable to the size of a single salt cavity, occurs every year. Therefore, the hypothesis of salt dissolution as the main cause of subsidence is plausible. A rapid increase in volume loss from 3.6E+05 to 5.3E+05 for the point pressure source and from 2.7E+05 to 4.2E+05 for the rectangular crack source appears between the second (03.2016-03.2017) and third (10.2016-10.2017) datasets and is accompanied by a downward movement of the source. These two datasets

	Point source model				Rectangular source model 600 × 150 m			
Time interval	East (m)	North (m)	Vol. loss (m^3)	Depth (m)	Opening (m)	Vol. loss (m^3)	Strike (°)	Depth (m)
03.2015–03.2016	198,124	8,933,762	3.9E + 05	774	− 3.4	3.0E + 05	175	953
03.2016–03.2017	198,198	8,933,687	3.6E + 05	730	− 3.0	2.7E + 05	171	873
10.2016–10.2017	198,108	8,933,746	5.3E + 05	777	− 4.6	4.2E + 05	155	962
10.2017–09.2018	198,127	8,933,793	5.8E + 05	697	− 5.2	4.6E + 05	165	857
09.2018–09.2019	198,179	8,933,841	5.4E + 05	653	− 4.9	4.4E + 05	164	807

Table 4.1: Elastic modelling parameters for point source model and 600 × 150 m rectangular crack source model for five-time intervals.

have a 5-month overlapping period, and therefore, the drastic volume change increases most likely occurred during the second half of 2017, which is coincident with the rapid displacement acceleration observed in the InSAR time series (see the discussion section).

More complex numerical models explore how such cavity sources may eventually develop into anelastic processes and subsidence (Al-Halbouni et al. 2019). Geomechanical models of the subsidence process have been developed to compare the InSAR subsidence along a 2D transect crossing the surface projection of salt cavities M30 and M31 (Figs. 1a and 3a), which are located inside the residential area of Pinheiro. Two independent injection pressure scenarios (S1 and S2) were used to test the different geomechanical stages of the cavity evolution, surrounding crack propagation, stress development, and induced surface displacement that occur under different initial conditions. The first scenario (S1) considers a higher cavity pressure compared to the surrounding soil and simulates mining conditions. The working pressure usually stabilizes the salt cavities during dissolution mining. The second scenario (S2) considers a hypothetical lower cavity pressure, caused by depressurization and aims to simulate inactive mining conditions (CPRM-SERVIÇO GEOLÓGICO DO BRAZIL 2019).

From the first simulation scenario (S1) under working pressure conditions of P = 2.758 MPa, the following four model stages occur: 1) initial fracturing of the cavity margin due to the injected pressure; 2) fracturing of the roof layer, the formation of concentric cracks in the salt-rock layer around the cavities, and fracture propagation in the overburden shale layer; 3) weakening of the roof layer and collapse of the shallower cavity (M30); and 4) upward fracture propagation, cavity migration, and stoping. Only one cavity collapsed entirely under these pressure conditions. The crack evolution and simulated surface displacement compared to the subsidence InSAR observations are depicted in Fig. 4.4. The maximum subsidence reached the final stage is 1.7 m, which occurs approximately 80 m NW of the central point of the profile and coincides with the maximum cumulative subsidence detected in that location in 10.2019. This final surface subsidence profile is rather smooth with little inhomogeneity due to discrete rock mass movement.

From the second, independent simulation scenario (S2) under inactive, depressurized initial conditions of P = 1.5 MPa, the following four model stages occur: 1) an initially stable pressurized cavity; 2) weakening of the individual compressive stress arches around the cavities and stress concentration in the large spanning compressive stress arch; 3) weakening of the roof layer, total collapse of the shallower cavity (M30) and partial collapse of the deeper cavity (M31), and fracture propagation into the overlying limestone/sandstone and shale (layer no. 5); 4) disruption of the large compressive stress arch, total collapse of the second cavity (M31) and upward fracture propagation with surface deformation. Crack evolution follows a similar pattern as the pattern in scenario S1 with working pressure

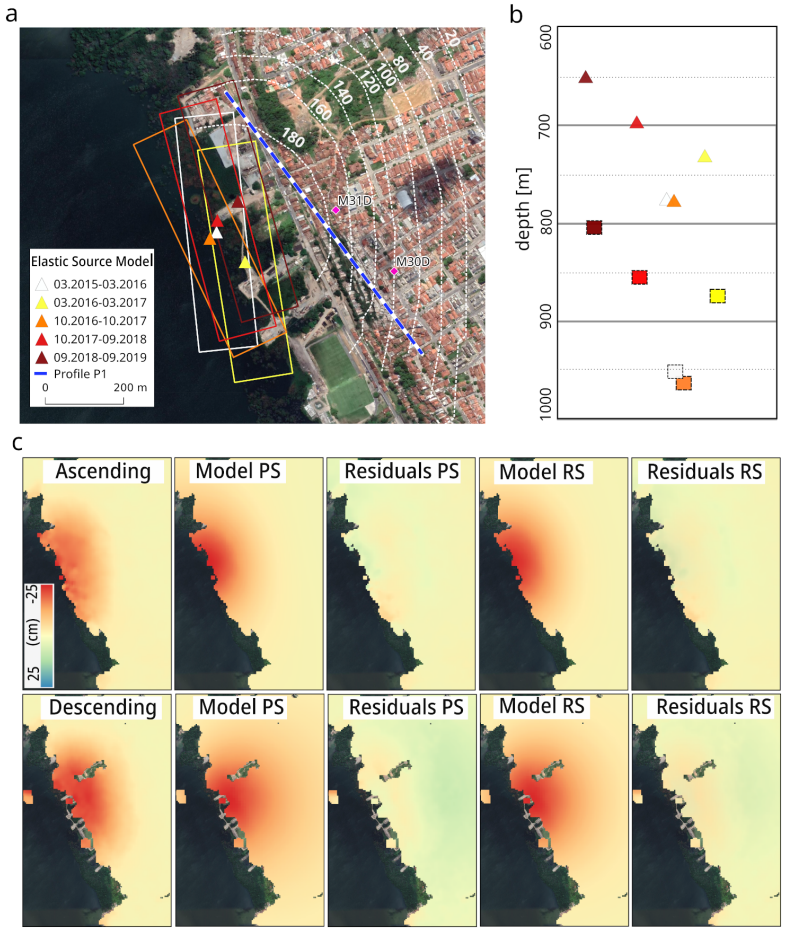


Figure 4.3: Inverse numerical model results. (a) Horizontal location of the best-fitting source models between 2016 and 2019: triangle symbology for point source model and dashed rectangle symbology for rectangular crack source model with different colours expressing the different dates as in legend. Dashed white isolines represent the cumulative displacement for the period 07.2004-11.2020. Magenta diamonds show the detailed location of the two cavities (M31D and M30D) modelled in DEM. The blue-white line shows the profile P1 used for the DEM subsidence simulation (see Figs. 4b and 5b). (b) Vertical profile reveals the depth of the best-fitting source models: triangles for point pressure source and rectangles for rectangle crack source (same colour convention indicating the date). X-axes is an indicative NW-SE along with the coast profile, not in scale. (c) InSAR ascending (Alos-2 data) and descending (Sentinel-1 data) observations for the period 2018-2019, best-fit model and relative residuals calculated by subtracting the model to the observations. PS indicates point source model; RS indicates rectangle crack source model. Background Google Earth CNES/Airbus imagery. The figures (except b) were plotted in QGIS (v. 3.16, https://www.qgis.org/en/site/).

conditions, although stages 3 and 4 are reached faster. Fig. 4.5 shows the compressive stress conditions and the simulated surface displacement compared to the subsidence InSAR observations. After stage 3, a total maximum vertical displacement of almost 2 m was achieved at approximately 125 m NW of the central point of the profile, above the centre of cavity M31. Further, one metre of subsidence is related to the final stage 4, which indicates ongoing subsidence due to progressive collapses and compaction. This resulting

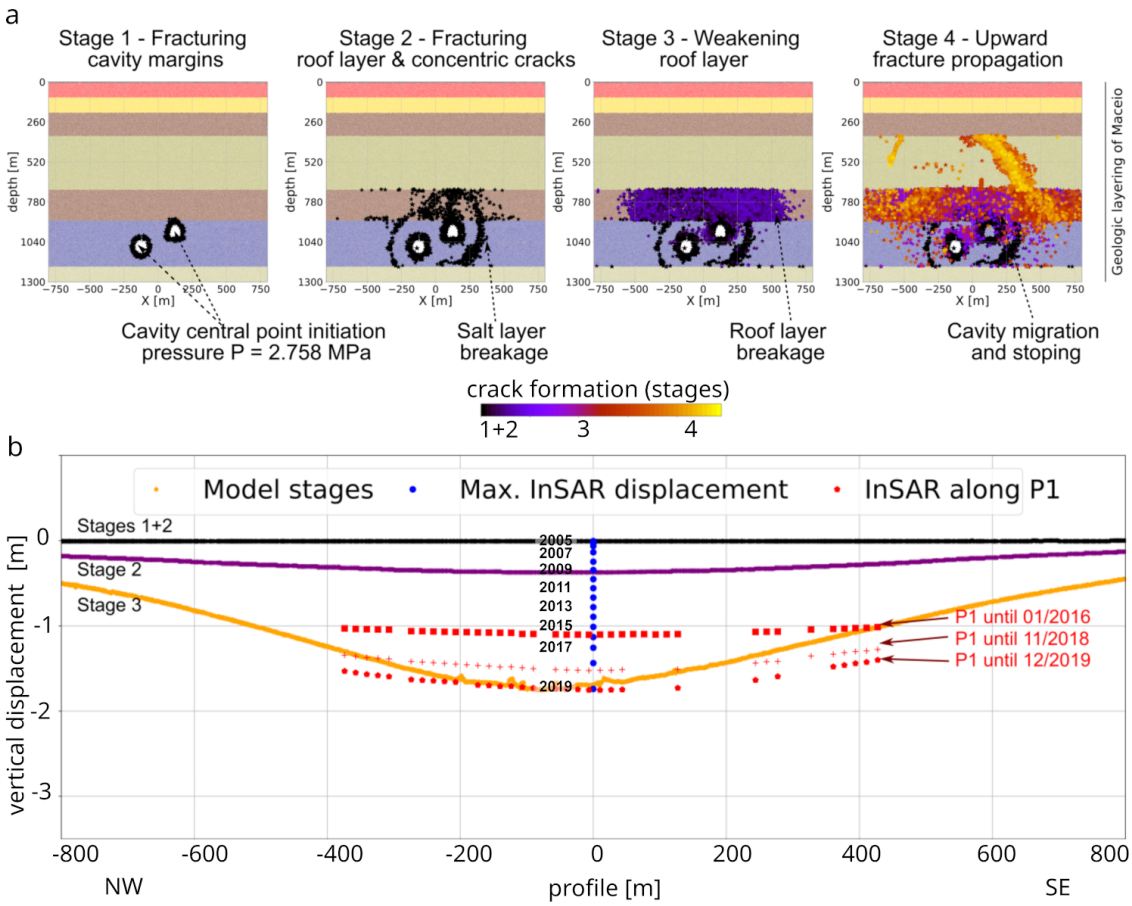


Figure 4.4: Simulated DEM subsidence models for pressurized cavity scenario (S1, P = 2.758 MPa). (a) Crack and fracture evolution representation of the four stages of cavity collapse is shown in a black-purple-yellow colour scale; the stratified background represents the geological layering model (see data and methods). (b) Induced surface deformations for the four stages (black-purple-yellow colour scale) compared to InSAR surface subsidence results along profile P1 (Fig. 4.3a). The figures were plotted using Matplotlib python library using data from simulations and InSAR time series data along profile P1.

final surface subsidence profile shows many inhomogeneities due to the development of fracturing and compression ridges at the surface.

Both simulated pressure cases show that the cavities already experience mechanical instability during working pressure conditions, with consequent roof collapses, upward cavity migration, and fracture propagation into rigid upper layers. The geomechanical condition is aggravated if the cavities are depressurized, leading to further collapses and ground displacement with more inhomogeneities at the surface.

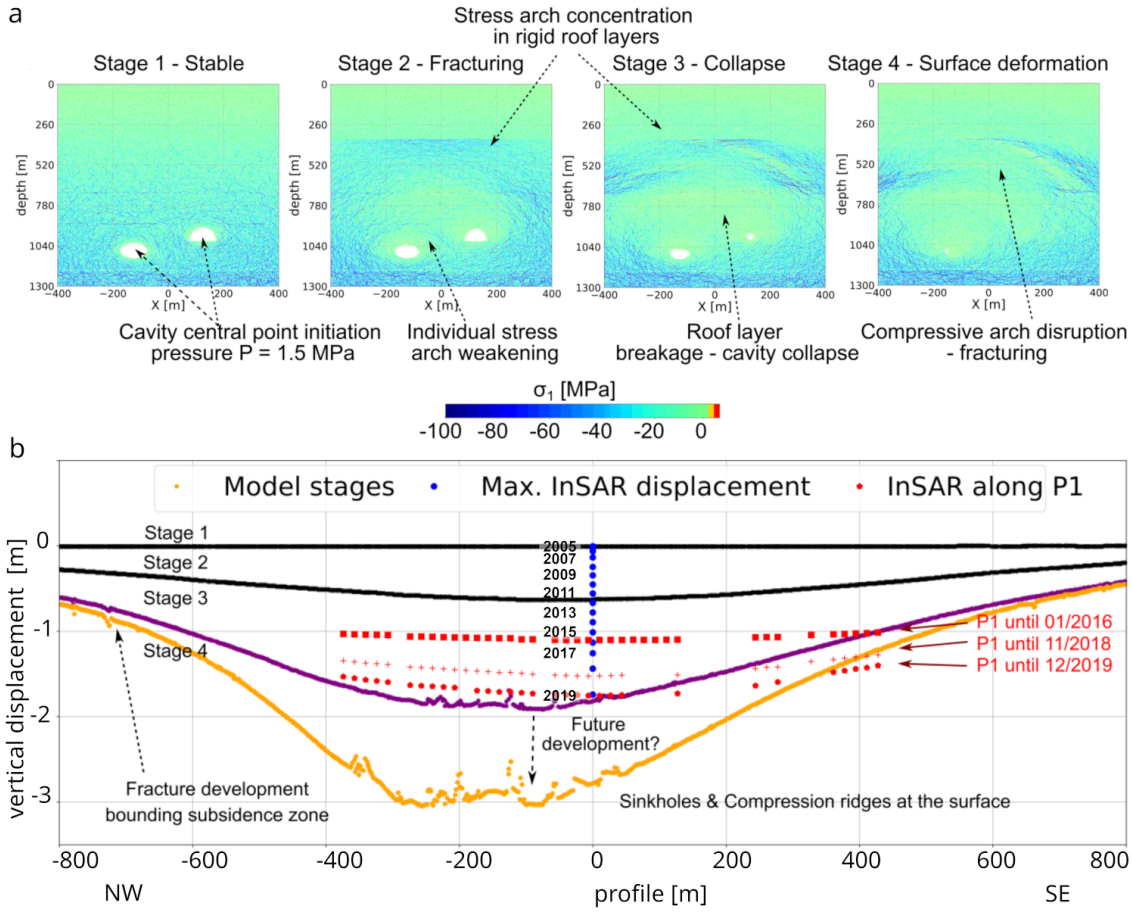


Figure 4.5: Simulated DEM subsidence models for depressurized cavity scenario (S2, P = 1.5 MPa). (a) Maximum compressive stress representation of the four stages of cavity collapse; blue colour shows higher values of compressive stress. (b) Induced surface deformations for the four stages (black-purple-yellow colour scale) compared to InSAR surface subsidence results along profile P1 (Fig. 4.3a). The figures were plotted using Matplotlib python library using data from simulations and InSAR time series data along profile P1.

4.5 Discussion

In this study, we investigated the ongoing geological instabilities in Maceió by integrating multi-temporal InSAR analysis with source modelling using elastic inversion and the distinct element method. The main outcomes from our results are that the subsidence in Maceió 1) started to gradually evolve almost two decades ago with slow acceleration at the beginning and faster acceleration in the last 4 years; 2) reached a maximum cumulative value close to the lagoon coast of approximately 2 m at the end of 2020; 3) is attributable to a depth source between 700 to 1000 m that coincides with the salt cavity locations; 4) both active/pressurized and inactive/depressurized salt mining conditions led to mechanical instability of the cavities with local upward migration and likely partial to total cavity collapses, and 5) developed from the deforming cavities cracks propagated upward towards the shallower layers.

Almost two decades of displacement observations highlight the gradual spatio-temporal evolution of the main subsidence process. The displacement observations also show the presence of a second minor unstable area on the south coast of the lagoon that is characterized by block-caving subsidence.

By integrating the displacement observations with numerical source modelling, we suggest that extensive subsidence can be primarily associated with the removal of localized, deep-seated material at the location and depth where salt is mined. This makes other explanations that associate geological instability with distributed surface water percolation or only with the destabilization of pre-existing geological structures highly unlikely. The DEM also shows that deep cavities in the "salgema" salt layer can, even under higher working pressure conditions, mechanically create cracks in the upper layers that eventually lead to large-scale subsidence and small-scale surface features. In conclusion, the deep mining horizon with resulting high surrounding environmental pressure and local rock mechanical conditions are the main reasons for the instability of cavities in this salt layer.

Rock fracturing, including in upper layers, as observed in Maceió, is an explicit indicator of geomechanical degradation. Cracking of the surface layers and weakening of the bulk material eventually enables strong water percolation from rather superficial aquifers into deeper underground areas, with a potential increase in material dissolution and erosion. This process can lead to a feedback mechanism responsible for superficial ground deformation and even to enhanced local subsidence. The connection between accelerated subsidence and extreme rainfall is further discussed. The ongoing process of mechanical destabilization is indicated by the fact that even though all mining activities have stopped since mid-2019, the displacement observations show a decreasing trend only from the beginning of 2020. Additionally, the known existing geological structures can foster water percolation and be reactivated if they spatially intersect the upward-moving cavities, provoking further surface displacement. This may be the genesis of the minor area of subsidence south of the lagoon, which subsides as a unique block, has an approximately constant rate and follows an NNW-SSE orientation, similar to the dominant regional fault system.

In the 16-year long term, the InSAR data suggest a significant increase in subsidence rates. We examine the short-term and long-term fluctuations observed and compare them to extrinsic influences (Fig. 4.6). Specifically, our InSAR data suggest an acceleration in the subsidence rates in 2017 (Fig. 4.6a and b). This concurs with hydrometeorological extremes affecting the region. Precipitation data from the Maceió meteorological station integrated with the Climate Hazards Group InfraRed Precipitation with Station (CHIRPS) precipitation data suggest that the period of May-July 2017 was characterized by almost double the average rate of rainfall. Concurring with this rainfall event, the InSAR data show an acceleration of 10 cm/year during the second half of 2017 (Fig. 4.6b). More short-term fluctuations associated with annual rain are depicted, implying that rainfall control might only be relevant for rainfall cumulative extremes (such as in 2017) but not for season-dependent fluctuations (Fig. 4.6c). These observations may allow the development of a threshold for the triggered ability in the future but necessitates further studies on longer time series. Due to the low temporal resolution of the other SAR acquisitions in the period from 2004 to 2011, it is not possible to reliably identify any correlation between ground subsidence trends and precipitation.

Knowing the dimensions and changes of subterranean cavities is of major importance for engineering mining and hazard assessment. We herein compared the overall volume

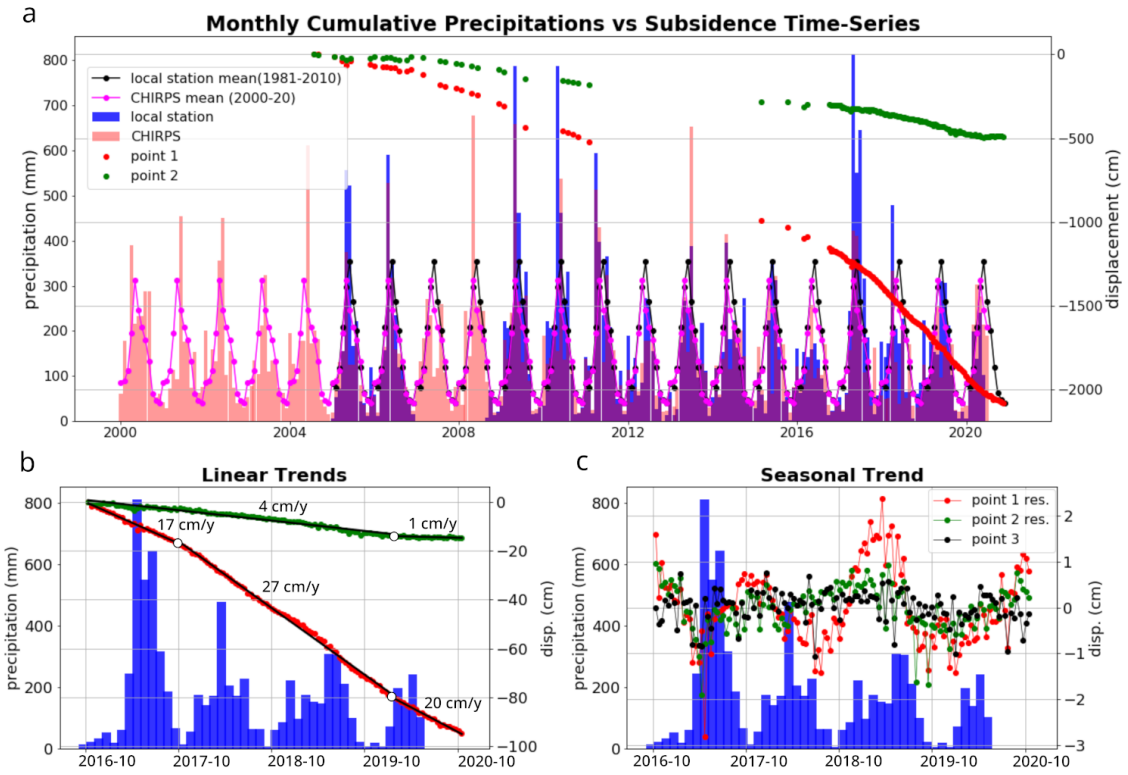


Figure 4.6: Long and short term vertical displacement time-series and local rainfall data. The location of the plotted points is shown in Fig. 4.2a. (a) 16-year long time-series: red (point 1) in the area of maximum displacement and green (point 2) in the minor subsiding region. Displacement values are on the right axis. Rainfall values are on the left axis: black dots and lines for local station mean values; purple dots and lines for CHIRPS mean values; blue histogram for local station monthly cumulative precipitations; pink histogram for CHIRPS monthly cumulative precipitations. (b) 4-year short time series for points 1 and 2 and histogram of local station monthly cumulative precipitations. Black-lines are the linear displacement interpolation representing the velocity trends; white dots show changes in a linear trend. (c) Seasonal trends: red and green dots of the residual estimated by subtracting a 3-grad polynomial trend from the displacement time-series for point 1 (point 1 res.) and point 2 (point 2 res.) respectively and black dots showing the displacement time-series of point 3 in a potentially stable area. The figures were plotted using Matplotlib python library using InSAR time series and precipitation data.

loss derived by the analytical model with the salt cavity sizes, to obtain an overall idea of the possible cavity collapses. To calculate the whole volume loss, we used the forward modelling method to simulate the complete subsidence ellipsoid for the period of 2004-2020; we obtained a minimum overall volume loss of 26.6E+05 m3, which is 3 times more than the volume loss estimated only from the InSAR observations. Considering an average salt cavity size of approximately 3E+05 m3, the above volume loss is equivalent to the total collapse of almost 9 salt cavities. This estimation has to be considered conservative (a "minimum"), as natural effects such as material dilation of the sediment cover and anthropogenic refilling of cavities have not been taken into account. Indeed, from elastic modelling, we obtain an approximate subsurface volume loss of 22.5E+05 m3 for the point

pressure source and of 17.7E+05 m3 for the rectangular crack only for the 03.2015-09.2020 period.

In subsiding areas, the damage to buildings and infrastructures is related to the strain changes that occur due to differential settlement (Skempton and Macdonald 1956). A good indicator of such a strain factor is the angular distortion, which is calculated as the ratio of the subsidence horizontal gradient, i.e., the differential settlement and the distance between the two considered points. Therefore, for infrastructure risk assessment and emergency management, angular distortion provides more appropriate information than displacement information alone. Moreover, since subsidence is a dynamic process, hazard evolution is dynamic.

Based on the aforementioned assumption, we properly classified angular distortion into hazard levels (see data and methods), and we derived cumulative geohazard maps for the last 4 years (Fig. 4.7a-d). The relationship between high angular distortion and damage occurs in the zone where the ground gradually transitions from stable to unstable conditions. Indeed, the surface cracks detected during a ground survey conducted by the CPRM in 2018 occur in the region of higher angular distortion and form concentric patterns around the maximum subsidence area. The second area of subsidence south of the lagoon has higher hazard levels around the perimeter, which highlights block-wise subsidence. We estimated the cumulative subsidence hazard by simulating an additional year of subsidence at the same rate as that in 2019-2020 (Fig. 4.7e). Potentially high levels of future hazards may develop in the middle region of the concentrically shaped subsidence and then gradually develop towards both the east, i.e., the transition region, and west, i.e., the area of maximum subsidence. The dynamic character of the subsidence hazard is well depicted by the angular distortion velocity map (Fig. 4.7f), where a higher velocity indicates the areas where the hazard evolves more rapidly.

In addition, some inland areas are also classified as having a high hazard level, though they are far from the main unstable region and include some edge effects along the lagoon coast. These areas must be separately investigated because they could either be related to local processes or be the product of InSAR processing errors, as discussed in the data and methods section.

4.6 Acknowledgment

We are grateful to Marcos Carnaúba for providing great help in retrieving local information. We thank the Brazilian Geological Service (Serviço Geologico do Brazil—CPRM) for making the technical reports of their surveys and analysis publicly available. We thank the Japanese space agencies for ALOS-1 and 2 satellite SAR data. ALOS-2 data is copyright of the Japanese Aerospace Agency and was provided under proposal 1162. We thank the European space agencies for freely providing ENVISAT and Sentinel-1 satellite SAR data.

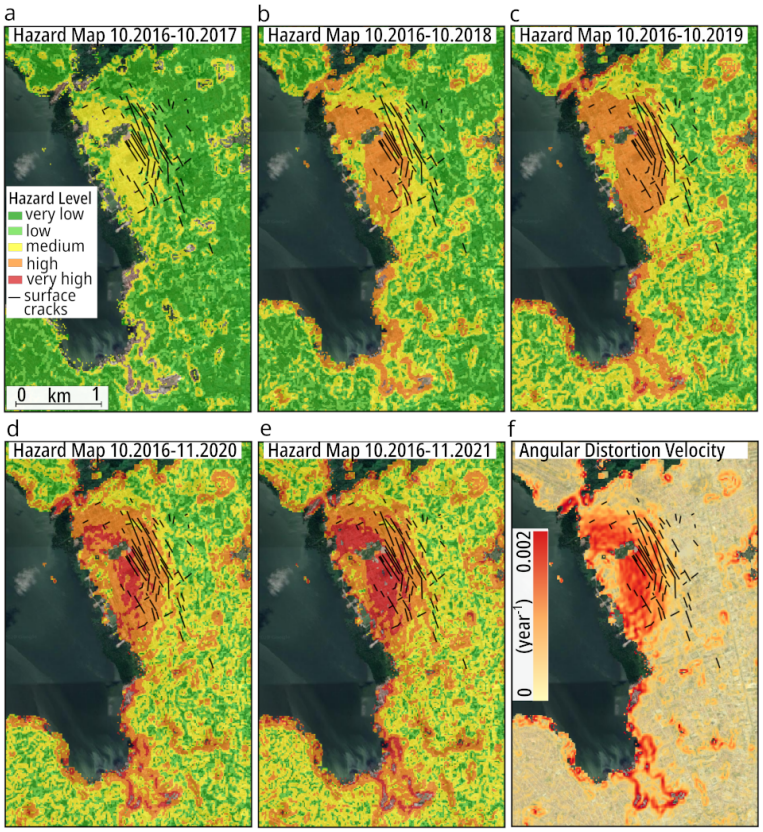


Figure 4.7: Subsidence hazard based on angular distortion values (horizontal strain). (a-d) Cumulative hazard maps are classified into five levels based on an appropriate threshold (see data and method). (e) Hazard simulation of accumulated subsidence predicted by adding one further year (11.2020 - 11.2021) assuming constant displacement rate same as 2019-2020 (f) Angular distortion velocity, estimated over the period 2016-2020, highlights in red the areas with faster hazard evolution. Background Google Earth CNES/Airbus imagery. The figures were plotted in QGIS (v. 3.16, https://www.qgis.org/en/site/).

5 Landslide failure in Hoseynabad-e Kalpush village

This chapter was published as:

Magdalena Vassileva, Mahdi Motagh, Sigrid Roessner and Zhuge Xia. **Reactivation of an old landslide in north–central Iran following reservoir impoundment: results from multisensor satellite time-series analysis.** *Engineering Geology* (2023), doi.org/10.1016/j.enggeo.2023.107337

Some minor changes were applied with respect to the original publication: some minor typos were corrected.

Author contribution statement:

As first author, I contributed most to the work including conceptualization of the work, methodology development, SAR data collection, MTI data processing, external factor estimation, geohazards analysis, validation, interpretation, writing the original draft, reviewing and editing successive manuscript versions and visualization. Zhuge Xia performed PCA/ICA processing. All co-authors contributed to the discussion, reviewing and editing of the manuscript.

Method summary:

In this work, MTI and DIC analysis were performed to characterize the spatiotemporal evolution of the landslide during the pre-, co- and post-failure stages. A multisensor and multi-geometry dataset of Envisat (ascending and descending orbit paths) and Sentinel-1 (ascending and descending orbit paths) SAR acquisitions was used. Horizontal and vertical displacement components were derived by combining ascending and descending geometries. PCA and ICA analysis over the landslide areas was conducted for the pre- and post-failure ground displacement time series. A spatial clustering method and piecewise segmentation approach were developed to extract representative pre- and post-failure ground displacement time series. Reservoir water levels were extracted using Landsat-8 and PlanetScope data. Precipitation data were extracted from CHIRPS. A correlation analysis was conducted between main displacement rates and external factors. The potential seasonal displacement signal was analysed using Cross Wavelet Transform. Main conclusions about the landslide kinematics and main driving factors were finally derived based on the results.

Supplementary Material:

Supplementary material was not included in the chapter and can be found on the following link under the voice Appendix A. Supplementary data.

5.1 Abstract

Water impoundment combined with more frequent precipitation extremes due to climate change increases landslide hazards on the slopes surrounding dam reservoirs. In situ monitoring systems in these potential landslide-prone areas are often unavailable, making landslide failures challenging to forecast. This paper describes a multisensor and multivariate remote sensing approach using data from Envisat, Sentinel-1, Landsat and PlanetScope satellites to reconstruct the spatiotemporal evolution of the mechanism and causes of the March 2019 landslide failure backside of the dam reservoir in Hoseynabad-e Kalpush village, north–central Iran. Statistical analysis and time series clustering are performed to derive the main landslide kinematic features from multitemporal interferometric synthetic aperture radar (MT-InSAR) analysis. We also exploit GIS and wavelet analysis to correlate potential external driving factors with landslide kinematics. Envisat and Sentinel-1 MT-InSAR analyses revealed that a previously stable old landslide was reactivated following reservoir impoundment in early 2013. As the reservoir water level rose during the following years up to 34 m in 2019, the landslide displacement rate gradually increased from 3.5 cm/yr to 8.4 cm/yr, and the destabilization gradually propagated upslope. At this stage, seasonal precipitation effects were detected only in the vertical component, indicating swelling and shrinkage movements of the shallower soil layer. The reactivated landslide accelerated and catastrophically failed following the exceptional precipitation in early 2019, producing a horizontal shift of $\leq$ 40 m, detected with optical image digital correlation. In the aftermath, the landslide continued to move with a decreasing trend until final stabilization in October 2021. Our study demonstrates how combined observations derived from multisensor satellite remote sensing data can be used to assess landslide precursors and kinematics, as well as the influence of climatic and anthropogenic factors on the instability of slopes surrounding water reservoirs. This is especially relevant in data-scarce areas.

5.2 Introduction

Landslide hazards represent one of the major threats to human life, settlements and infrastructures (Petley 2012). They are mainly driven by complex interactions between relief, geological structures and hydrogeological processes that change the pore-water pressure between soil particles, altering the stress conditions within the subsurface shear zones embedded in the slopes (Iverson 2000). Anthropogenic activities and weather extremes partly due to climate change considerably influence slope hydrogeological conditions, increasing landslide hazards (Picarelli et al. 2021). In particular, in recent decades, dam reservoirs and other water management infrastructures have been widely reported as intensifying landslide activities within water reservoir lakes (Panizzo et al. 2005; Kaczmarek et al. 2015; Yin et al. 2016; Jones et al. 2021) during impoundment (Jiang et al. 2015) or for subsequent water level fluctuations caused by water regulations (Zhang et al. 2020) due to changes in the groundwater conditions on the surrounding slopes. In the case of earth dams, built up by compacting successive layers of earth, instability might be developed on the embankments as well its surroundings on slopes downstream due to groundwater infiltration or uncontrolled seepage, i.e., water infiltration through the soil and development of erosional features with consequent conduit leakage and piping (Lee et al. 2022). However, the combined effect of reservoir water level changes and exceptional meteorological

conditions on influencing slope instabilities downstream of water reservoirs are still poorly studied and understood. In many cases, in situ monitoring systems that provide a sufficient number of spatiotemporal datasets related to landslide kinematics, hydrogeological conditions and triggering factors, e.g., precipitation records and reservoir water levels, are unavailable. In this regard, satellite remote sensing missions have provided great numbers of observations that have contributed significantly to landslide research in the past two decades (Singhroy 2009; Casagli et al. 2016). In particular, long-term operational global satellite missions, such as Landsat, Sentinel-1 and -2 and PlanetScope, allow a decadal retrospective analysis of landslides before their main failure with the goal of better understanding failure mechanisms and their influencing factors. Ground deformation during the life cycle of a landslide can be analyzed using advanced remote sensing techniques. Digital image correlation (DIC) of optical and SAR data provides measurements of large downslope motion on the order of 1 m/day (Mazzanti et al. 2020; Xiong et al. 2020). Multitemporal synthetic aperture radar interferometry (MT-InSAR) techniques allow monitoring of slow-moving landslides that experience deformations from a few centimeters to a few meters per year (Colesanti and Wasowski 2006; Bovenga et al. 2012; Hilley et al. 2004; Motagh et al. 2013; Teshebaeva et al. 2015; Bianchini et al. 2015; Rosi et al. 2018; Liu et al. 2021).

Satellite remote sensing observations can also provide information about anthropogenic, environmental and climatic variables influencing slope instabilities, such as land cover and land use change detection (E. D. Chaves et al. 2020), hydrometeorological data (Khan et al. 2021; Uwihirwe et al. 2022), spatiotemporal distributions of water bodies (Keys and Scott 2018) and soil moisture parameters (Zhuo et al. 2019).

Advanced statistical methods allow the detailed analysis of changes in spatial and temporal patterns in remote sensing data for landslide hazard zonation and better process understanding, e.g., the relationship between ground deformations and potential environmental triggering forces. These include statistical displacement classification based on a best-fitting trend model (Berti et al. 2013; Mirmazloumi et al. 2022), principal component analysis (PCA) for data dimensionality reduction (Chaussard et al. 2014; Cohen-Waeber et al. 2018; Wang et al. 2022; Peng et al. 2022), independent component analysis (ICA) for decomposing a mixed signal (Xia et al. 2023), and wavelet transform (WT) analysis to extract seasonality and analyze the time lag between slope instability and external triggering factors (Tomás et al. 2016).

In this study, various geodetic and statistical remote sensing approaches are combined to study the March 2019 Hoseynabad-e Kalpush landslide failure. Between mid-March and the beginning of April 2019, 28 out of the 31 provinces of Iran were affected by intense rainfall, leading to widespread flash flooding and thousands of landslides, especially in the northern regions of Iran (Motagh et al. 2020). In particular, a catastrophic landslide occurred in Hoseynabad-e Kalpush village in Semnan Province on a slope adjacent to a dam reservoir. ≤ 300 houses were damaged, and 163 houses had to be evacuated completely due to the severity of the destruction and the danger to their residents downstream of the reservoir (Fig. 5.1a).

In the aftermath of the catastrophic failure several aspects of the Hoseynabad-e Kalpush landslide mechanism have remained unknown: (1) Was the landslide previously inactive, and if yes, when and under which conditions was it reactivated? (2) Were there any displacement precursors of the impending failure, and if yes, when did they start? (3) To what extent did the increase in the water level of the nearby reservoir and groundwater change in its surroundings contribute to the failure, and to what extent was rainfall the driving

force? (4) Were there any post-failure displacements, and when did the landslide become inactive? Answering all of the questions above in a profound scientific way is the goal of this study and is an important step toward a better physical understanding of landslide rupture mechanisms and risk assessment occurring in the areas surrounding water reservoirs. The landslide-affected area was not monitored with any in situ instruments, and no in situ data regarding precipitation, water levels, and hydrogeological conditions were available for this study. Therefore, we completely rely on a combination of spaceborne radar and optical remote sensing-based methods to address all the questions above. We derive ground deformations before, during and after the main failure and analyze the time correlation between changes in the displacement patterns with precipitation and reservoir water level. Precipitation time series over the region are estimated from meteorological models based on satellite and ground-based observations. Reservoir water levels are measured by combining the digital elevation model with shoreline vectors extracted from optical satellite data using a GIS-based approach. We discuss the main findings and the potential and limits of using satellite remote sensing methods only for landslide studies. A field survey conducted in the summer of 2019 has provided ground observations and evidence of the landslide process and its consequences.

5.3 Description of the study area

Hoseynabad-e Kalpush is a village of 3,514 inhabitants and a total of 1,013 households (general census of 2016) situated in the Semnan Province in north–central Iran (Fig. 5.1a). This region is geologically located at the border between the two structural zones of Kopeh Dagh–Binalood and East Alborz and includes geological units related to both zones. According to the 1:100,000 Dozin geological map, the oldest rock units in the study area are thin- to medium-layered argillaceous limestones with intercalations of marl and cherty limestone that are part of the Jurassic Chamanbid and Mozduran Formations, respectively. The equivalent layers of the upper red formation overly these limestones, with alternations of marl, conglomerate, sandstone and mudstone of Neogene age. The youngest stratified unit in the studied area is made up of Quaternary clay flat (Fig. 5.1b). The closeness to the intraplate boundary between the Iran and Turan plates makes this region tectonically active, as it is crossed by many thrust and right strike-slip faults. Hills and valleys characterize the morphology of the surrounding area, with altitudes ranging between 1200 and 1400 meters above sea level (m.a.s.l.) and an average slope steepness of 15°. Old landslides shape the landscape in Hoseynabad-e Kalpush; indeed, the 2019 failure occurred inside the boundaries of an old relict landslide (see Fig. 5.1b). The local climate is predominantly semiarid with two well-defined seasons: hot–dry summer and cold–wet winter. $\leq$ 70% of the average rainfall in this region falls between December and April, while June through August often has no precipitation. The predominant land cover of the region is cropland, with some small built-up areas. Landsat-5 and -8 images acquired between 1996 and 2013 show that in these two decades, the region underwent a drastic transformation in land cover, mainly from forest to cropland (see Supplementary S1). A reservoir earth dam for water control and supply was built south of the village in the nearby valley. The dam construction started in 2008 and was completed at the beginning of 2013 when the water impoundment started, as reported from the Regional Water Company of Semnan.

Fieldwork conducted in July and September 2019 in the area provided some ground evidence of the slope processes and their consequences (Fig. 5.2). According to locals, the first

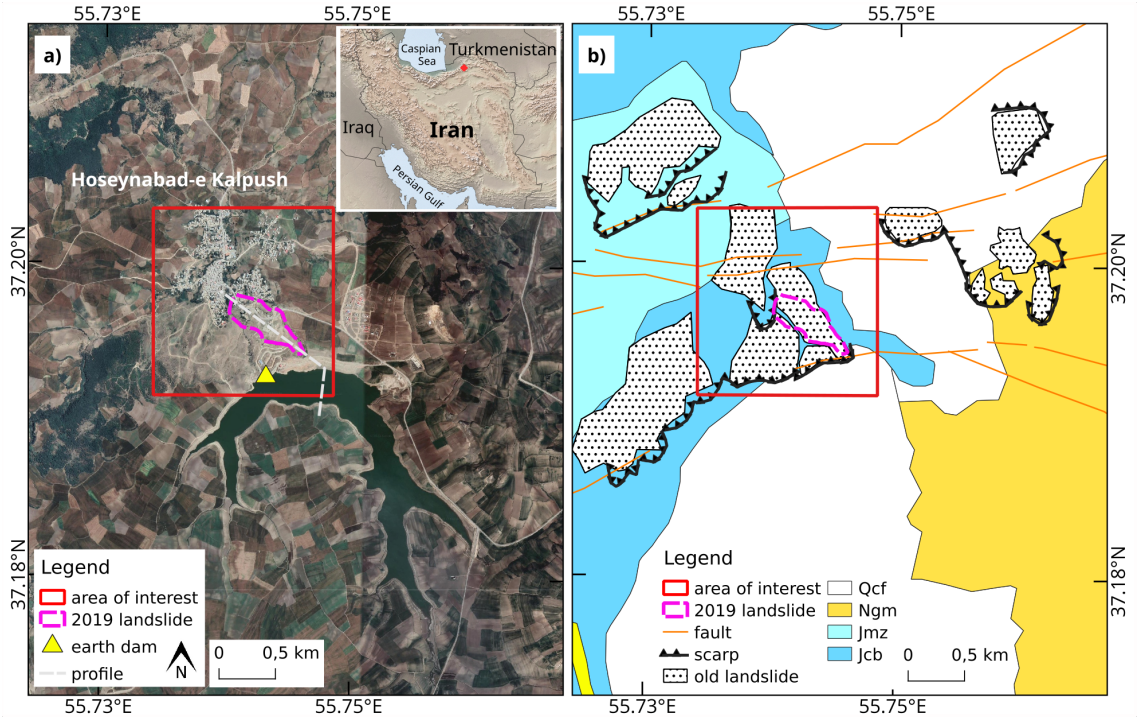


Figure 5.1: Overview of the regional setting and landslide area. (a) Satellite optical image (Google ©Imagery CNES/ Airbus Maxar Technologies) and country scale inset map (Natural Earth I with Shaded Relief and Water © 2012. Natural Earth). (b) Geological map modified after ©Geological Survey of Iran for the Dozin geological map 1:100000 using remote sensing data interpretation; Qcf indicates clay flat, Ngm indicates red to brownish marl, siltstone and sandstone with intercalations of conglomerate (Upper red Formation equivalent), Jmz indicates Pale-gray, thick-bedded to massive cherty limestone (Mozduran Formation); Jcb indicates Pale-gray to cream, thin to medium bedded argillaceous limestone with marl intercalations (Chamanbid Formation).

minor cracks on buildings and terrain appeared in approximately 2016. In mid-February 2019 authorities started gradually demolishing the residential houses in the landslide area due to aggravation of the slope instabilities. The trend intensified further in early March 2019 and turned into the main landslide failure around the 20th of March, which damaged 300 houses and destroyed the road connecting to the dam (see Fig. 5.2a, b and g). Erosional features and sag ponds were observed in several locations on the main landslide body and in proximity to the flanks (Fig. 5.2a, d and e). Gully erosion features were visible on the adjacent old landslide (Fig. 5.1f and g).

5.4 Data and methodology

In this work, we exploited a combination of spaceborne SAR and optical satellite remote sensing data to evaluate the complete life cycle of the Hoseynabad-e Kalpush landslide (see Table 1 and Fig. 5.3). Eleven PlanetScope images (Planet Labs PBC 2017) acquired between November 2018 and May 2019 were used to analyze the co-failure ground displacement between March and May 2019. The data have a 3-m pixel resolution and are radiometrically corrected, orthorectified and projected onto a UTM grid. We used



Figure 5.2: Field photos of the landslide area from July 2019: (a) damaged buildings and sag ponds; (b) damaged road on the upper part of the landslide; (c) post-failure satellite optical images over Hoseynabad-e Kalpush village from June 2019 (Google ©Imagery CNES/ Airbus Maxar Technologies) same extent as red rectangle in Fig. 5.1a; topographic contours (white lines) derived from the 30 m resolution Shuttle Radar Topography Mission (SRTM) digital elevation model; yellow rectangle locate the dam; magenta outline shows the landslide extent; (d) sag ponds in proximity to the northeastern flank; (e) tension cracks and fissures on the landslide northeastern scarp (f) and (g) Southwestern adjacent old landslide showing gully erosion features.

radar images acquired by Envisat Advanced Synthetic Aperture Radar (ASAR) C-band (©European Space Agency) and Sentinel-1A C-band SAR (© 2021 Copernicus) sensors to assess pre- and post-failure ground deformation. For Envisat, there were 21 images in an ascending radar geometry (orbit path 13) from October 2004 to August 2010 and 32 images in a descending radar geometry (orbit path 20) from July 2003 to September 2010 suitable for interferometry. The currently operational Sentinel-1A mission has been available over the area since October 2014 in both ascending (orbit path 57) and descending radar geometries (orbit path 64). Based on the co-failure analysis, the Sentinel-1A acquisitions were subdivided into pre- and post-failure datasets. The pre-failure dataset covers October 2014 to mid-March 2019, with 97 and 92 images in ascending and descending radar geometries, respectively. The post-failure dataset covers mid-May 2019 to the beginning of December 2021, with 56 and 50 images in ascending and descending radar geometries, respectively. Finally, we used 30 m pixel resolution Landsat-8 images (42 images) from April 2013 to June 2016 and the 3 m pixel resolution PlanetScope (65 images) from July 2016 to December 2021 to derive the reservoir's monthly water elevation. We used the 30 m resolution Shuttle Radar Topography Mission (SRTM) (Earth Resources Observation and Science (EROS) Center 2017) as a digital elevation model (DEM) in the different processing steps.

satellite	orbit	pixel resolution	dates	num.of images	information
Landsat-8	-	30 m	11.04.2013-10.09.2016	42	water elevation
PlanetScope	-	3 m	22.08.201- 20.12.2021	65	
			10.11.2018- 26.05.2019	11	co-failure
Envisat	ascending (path 13)	15 m	05.10.2004-10.08.2010	21	pre-failure
	descending (path 20)		09.07.2003-15.09.2010	32	
Sentinel-1	ascending (path 57)	15 m	21.10.2014-17.03.2019	97	pre-failure
			16.05.2019-07.12.2021	56	post-failure
	descending (path 64)		10.10.2014-18.03.2019	92	pre-failure
			17.05.2019-08.12.2021	50	post-failure

Table 5.1: Summary information of the SAR and optical satellite remote sensing datasets.

The overall methodology used in this study is depicted in Fig. 5.4. First, we derived the co-failure ground displacement based on optical data using DIC. We assessed the kinematic failure mechanism and delineated the landslide-affected area (see Fig. 5.4 I). Then, we evaluated the slope kinematics and derived ground displacement time series before and after the main failure using the MT-InSAR technique (see Fig. 5.4 II). We analyzed the temporal pattern of precipitation using a quasi-global rainfall dataset of The Climate Hazards Group InfraRed Precipitation with Station data (CHIRPS). Monthly reservoir water elevations were derived using a GIS-based approach by combining the SRTM DEM which models the topography before the dam construction and optical remote sensing data from Landsat-8 and PlanetScope (see Fig. 5.4 III). Pre- and post-failure ground displacements were further post-processed using several statistical approaches (see Fig. 5.4 IV).

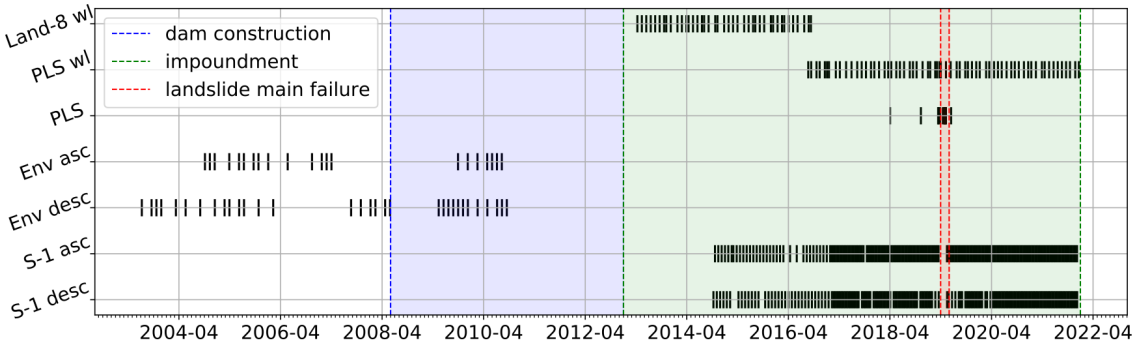


Figure 5.3: Time distribution of the SAR and optical satellite remote sensing acquisitions. The abbreviations indicate Land-8 (Landsat-8), PLS (PlanetScope), Env (Envisat), S-1 (Sentinel-1), asc (ascending) and desc (descending) orbit paths. The data used for the reservoir water elevation extraction are indicated with "wl".

The MT-InSAR outputs provide thousands of ground deformation measurement points and their associated time series. To better analyze the spatio-temporal variations in the displacement field, first, we used principal component analysis (PCA) to reduce the data dimensionality and independent component analysis (ICA) to extract underlying data trends. We further exploited a clustering algorithm to partition the landslide body into regions with similar instability characteristics and applied a piecewise linear regression to separate transient trends from potential seasonal effects in the time series of each cluster. We also investigated the correlation between the ground deformation and external factors, i.e., precipitation and reservoir water elevations using a Wavelet approach. The different processing steps are explained in more detail in the following subsections.

5.4.1 Co-failure ground displacement using digital image correlation

We applied digital image correlation (DIC) using a fast Fourier transform (FFT) approach developed by Bickel et al. (2018) to measure the horizontal magnitude of landslide failure using a multitemporal dataset of optical PlanetScope images (see Fig. 5.4 I). DIC estimates the 2D component of the ground motion in east–west and north–south directions and derives the horizontal ground displacement vector defined by direction and displacement magnitude. Since this technique is not sensitive to vertical displacement, it can slightly underestimate the downslope movement in areas with steeper slopes. To prepare the data for processing, we extracted the red band from each multispectral optical image, subsampled the multitemporal images to the same area, and converted the original 16-bit data to 8-bit data. The algorithm geometrically aligns the images using control points and evaluates the internal sub-pixel misalignment using a moving template window.

We estimated the incremental motion for several secondary images acquired between the beginning of April and the end of May 2019 via the same reference image acquired on the 10th of November 2018. Images acquired between December and March are entirely or partially covered by snow; therefore, they were unsuitable for cross-correlation processing due to the high noise level and were visually inspected for potential landslide-related offsets. Nonzero displacement was detected in the surrounding hypothetical stable areas due to systematic image coregistration errors. We calculated and removed this shift from the whole dataset. The final results were checked for plausibility, and a null value was assigned

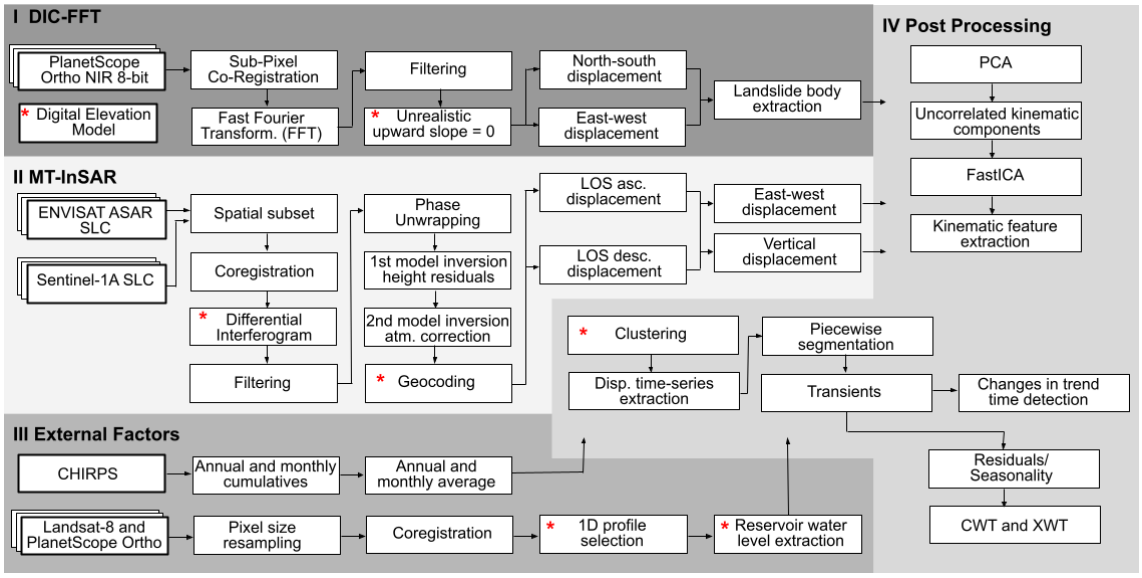


Figure 5.4: Flowchart of the main data and processing workflow. Abbreviation: DIC-FFT (Digital Image Correlation with Fast Fourier Transform), MT-InSAR (Multi-temporal Synthetic Aperture Radar Interferometry), NIR (near-infrared), SLC (single-look-complex), CHIRPS (Climate Hazards Group InfraRed Precipitation with Station data), CWT (Continuous Wavelet Transform), XWT (Cross Wavelet Transform), PCA (Principal Component Analysis), FastICA (Fast Independent Component Analysis). Bold rectangles show the input data. The red star indicates the processing steps where the Digital Elevation Model was used as input.

to those displacement values that indicated unrealistic upward slope directions (see Results and Fig. 5.14). Finally, we extracted the landslide body extent by delineating the area's outline, showing significant horizontal shifts.

5.4.2 Kinematics assessment using MT-InSAR

We applied the small baseline subset (SBAS) technique (Berardino et al. 2002), as implemented in the ENVI SARscape® software, to detect the line-of-sight (LOS) ground displacement before and after the landslide failure. We generated differential interferograms by connecting the prime image with the two images before and after within the timeline. For Sentinel-1A datasets, the considered temporal baseline ranged between 12 and 96 days, while the spatial baseline is not of concern due to the earth-fixed orbital tube of the satellite that guarantees short distances between passages. For Envisat datasets, both temporal baselines (average value of 364 days) and spatial baselines (average value of 389 m) constituted the main limitation in retrieving reliable, coherent pixels for ground deformation analysis and hindering the reliable detection of small creep signals (< 1 cm) in the study area. We performed multilook processing, resulting in a pixel size of 15 m for Sentinel-1A and 25 m for Envisat, and applied a Goldstein filter (Goldstein and Werner 1998) using a kernel window size of 18 pixels. The topographic signal was removed using the 30m resolution SRTM. The snow coverage in the winter period reduces the quality (coherence) of the interferograms from December to March. Therefore, an average coherence threshold of 0.2 was used in the unwrapping step to guarantee the temporal connection between the pairs (Darvishi et al. 2018). This means that some unwrapping errors might have

been introduced during the period of low coherence, which we checked for the extracted time series and eventually corrected.

Vertical and horizontal ground displacements were derived for the Sentinel-1 datasets by combining linearly interpolated in-time LOS ascending and descending observations at the pixel level (Vassileva et al. 2021). We considered a constant incidence angle for all pixels in both image geometries, deriving approximate vertical and horizontal component equations. We did not apply vertical and horizontal decomposition to the Envisat ground displacement datasets due to the low density of measurement points in space and time (see Results and Figs. 8, 10 and 15).

5.4.3 External factors

5.4.3.1 Precipitation

We retrieved precipitation measurements from January 2000 until January 2022 from the Climate Hazards Group InfraRed Precipitation with Station data (CHIRPS) (Funk et al. 2015). CHIRPS incorporates 0.05° resolution satellite imagery with available in situ station data to create gridded rainfall time series. It was produced from 1981 to the present with quasi-global coverage (50°S-50°N) and at monthly, pentad and daily time steps. We used Google Earth Engine (GEE) to access the "CHIRPS Daily: Climate Hazards Group InfraRed Precipitation with Station Data (Version 2.0 Final)" dataset. From the daily estimations, we derived the monthly and annual precipitation values, and estimated the 22-year long-term monthly and annual average precipitation (see Results and Fig. 5.4). We also estimated the cumulative sum over each year from June to May, which we refer to as "cumulative precipitation" in the text. This convention was chosen instead of the standard for the northern hemisphere October to September water year since in the case of northeast Iran it better visualizes the dry versus the rainy seasons.

5.4.4 Reservoir water elevation

We used a GIS-based approach to estimate the time series of reservoir water elevations along a 1D profile. First, we visually delineated the water shoreline using a time series of Landsat-8 and PlanetScope optical data between April 2013 and December 2021. Then, we overlaid the shoreline vector data onto the digital elevation model and extracted the water elevation at each date. We used the 30 m resolution SRTM DEM, which represents the topography of the valley before dam construction. The water surface elevation was expressed in m.a.s.l., while the water level refers to the water height relative to the lower point on the 1D profile. We chose a profile as close as possible to the landslide slope characterized by gentle topography to better discretize the water elevation variation over time (see Results and Figs. 1a, 5a and 6). We also extracted the entire water body for those months corresponding to reservoir water level peaks and estimated the reservoir water volume expressed in millions of cubic meters (mil.m3) as the volume subtracted from the digital elevation model below the water body extent (see Supplementary 2).

5.4.5 Post-processing

5.4.5.1 PCA and ICA

We post-processed the MT-InSAR horizontal and vertical ground deformation observations over the landslide body using a combined PCA and ICA approach with the aim of extracting the main landslide kinematic features and their spatial distribution. We first applied PCA to reduce the dataset dimensionality and complexity. This is done by extracting the uncorrelated signal from the heterogeneous dataset defined by the largest contribution to the data variance. In other words, the dataset is converted using orthogonal linear transformation to a new coordinate system that maximizes the variance (Draper et al. 2003; Delac et al. 2005). The PCA result extracts uncorrelated time series components; however, these are not necessarily independent, and therefore, different kinematic signals can be mixed together. To separate those potential mixed signals, we applied ICA. The method is based on fitting different temporal functions and finding those that maximize the statistical independence of all the different components (Delac et al., 2005; Draper et al., 2003). Statistical independence was assumed by considering that each component has a non-Gaussian probability distribution and that the sum of each non-Gaussian component tends toward a Gaussian distribution (Hyvarinen et al., 2004). In our processing, we applied FastICA, which performs faster due to the fixed point iteration approach (Hyvärinen and Oja, 2000). From the PCA we kept the largest 10 principal components (PCs). Then we performed ICA and calculated the first 6 independent components (ICs), forming 99% of all eigenvalues. Thereafter, we only kept the first 3 independent components because of their higher contribution (98.5% of the eigenvalues are retained) and regarded the rest as noise. The PCs and ICs accounting for most of the data are plotted as a time series of eigenvalues and mixing matrix respectively (Peng et al. 2022). Their spatial variability is shown as a global normalization score map (see Results and Figs. 11 and 16 and Supplementary S3 and S6).

5.4.6 Data clustering and time-series segmentation

To better understand the spatiotemporal changes in the kinematics of different parts of the landslide, we subdivided the landslide body into clusters with similar cumulative horizontal ground displacements and topographic elevations. This was done for both pre-failure and post-failure observations retrieved from MT-InSAR using a hierarchical clustering algorithm with an agglomerative bottom-up approach (Nielsen 2016). The algorithm first assigns each set of observations to a unique cluster. Then, at each iteration, the clusters are merged based on the similarity of their features expressed as Euclidean distance to define an upper-level cluster. We retrieved the time series of the average horizontal ground displacement and standard deviation within each cluster. For more consistency in retrieving the landslide kinematic behavior, we applied the same clusters to the vertical component and retrieved the average vertical ground displacement and its standard deviation. The above approach results in more robust spatiotemporal deformation mapping, as it reduces the randomness in selecting single points or areas for ground deformation time series extraction. Averaging all the observations inside the clusters also reduces the impact of spatial processing errors related to local decorrelations due to atmosphere, topography and land cover changes (especially in case of snow) in the MT-InSAR analysis.

The extracted time series based on the above clusters were analyzed using piecewise linear regression to discretize the time series into segments with constant velocity and detect when

significant changes in trend (velocity) occurred. We used the PWLF Python package by Jekel and Venter (2019) to perform piecewise linear regression. We developed an iterative workflow to define each time series's best-fitting number of segments. Our criterion is based on imposing a threshold for the minimum velocity gradient between adjacent linear segments and their minimum duration, i.e., segment length. The two thresholds are based on the noise level of the time series and its temporal density. We chose a minimum velocity change of 1 cm/yr and a minimum segment duration of 60 days (see Results and Figs. 12 and 17).

Notably, due to the SAR data gap between September 2010 and October 2014, we cannot directly observe the exact onset of the reactivation of the landslide. Therefore, we performed an extrapolation by fitting a best-fitting model based on statistical analysis to the ground displacement time series. We then calculated the intersection of the model with the time axis by deriving the first derivative and constraining it to zero.

5.4.7 Wavelet analysis

Potential seasonal signals in both horizontal and vertical components were extracted by subtracting the main trends from the ground displacement time series observations. We expanded the datasets into a time-frequency domain using the continuous wavelet transform (CWT) (Torrence and Compo 1998), which is done by applying a series of convolutions along the data time series of a set of wavelets, i.e., scaled functions with zero mean and localized in both frequency and time. To correlate the potential seasonal kinematic signal with precipitation variations, we computed the cross-wavelet transform (XWT) (Grinsted et al. 2004), i.e., the complex conjugate product between the CWT of the ground displacement time series and monthly precipitation. We also applied XWT to correlate water level changes with monthly precipitation. High XWT values define areas with common power in the wavelet spectrum in both time series, indicating common temporal patterns. The phase value represented by the direction of the arrows in the spectral plot refers to the time lag between the two time series, where an in-phase relationship (arrows directed right) indicates a positive correlation, while an anti-phase relationship (arrows directed left) indicates a negative correlation (Haghshenas Haghighi and Motagh 2016; Tomás et al. 2016) (see Results and Figs. 7, 13 and 18).

5.5 Results

5.5.1 External influencing factors

5.5.1.1 Precipitation

The CHIRPS results for the time period between 2000 and 2022 show that the average annual precipitation in the region amounts to 471 mm (Fig. 5.5a and b), with 88% occurring between November and May, 50% occurring between January and March and 25% occurring in January (see Fig. 5.5c). The years 2007, 2009, 2010, 2012 and 2013 were characterized by higher-than-average annual precipitation values of 124 %, 111%, 119%, 109% and 115%, respectively. The years from 2014 to 2018 were characterized by lower or closer to average precipitation values of 80%, 82%, 103%, 94% and 86%, respectively. The year 2019 was characterized by exceptionally high rainfall compared to the long-term average, amounting to 136%, with 90% occurring between January and March and an extreme peak

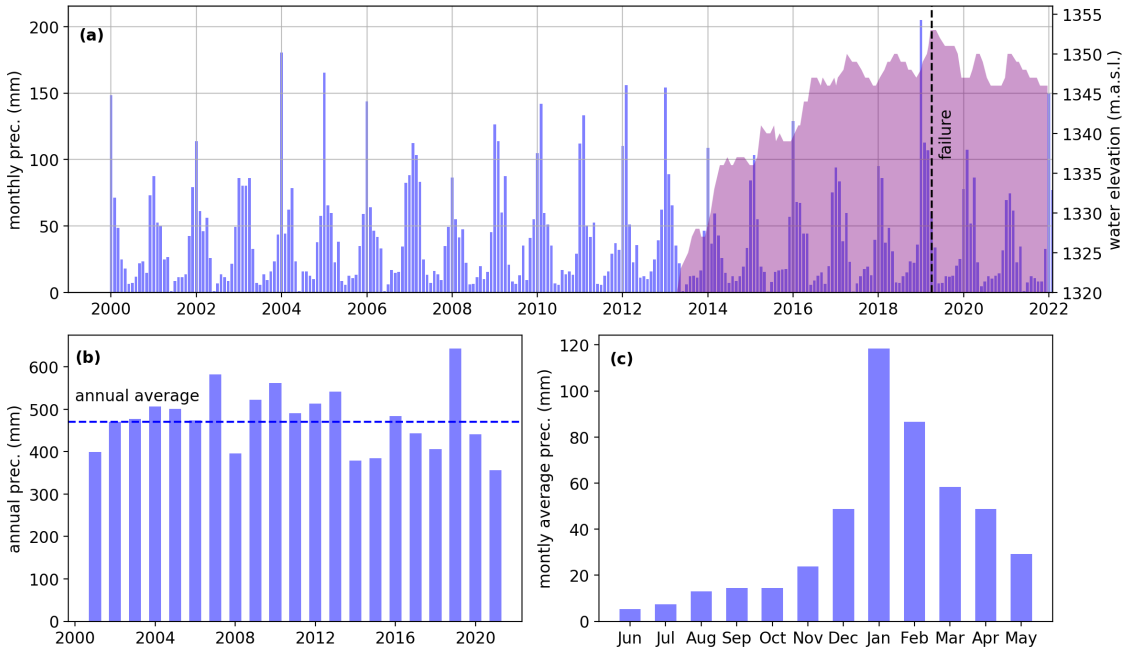


Figure 5.5: Precipitation dataset from CHIRPS and reservoir water elevation derived from optical remote sensing data. (a) Monthly precipitation since 2000 (blue histograms) and reservoir water elevation (purple area); black lines mark the start of the landslide main failure. (b) Annual precipitation; the horizontal blue dotted line shows the estimated 22-year average annual precipitation. (c) 22-year monthly average precipitation.

in January, equivalent to 43%. The following years, 2020 and 2021, were characterized by 93% and 75% of the average values, respectively.

5.5.1.2 Reservoir water elevation

The reservoir water elevation time and space variations are shown in Figs. 5a and 6 respectively. The deepest point along the profile is located at 1319 m.a.s.l., while the deepest point in the whole reservoir is located at 1317 m.a.s.l.. The water impoundment started at the beginning of 2013, and the first optical data acquired in mid-April 2013 showed a water elevation of 1320 m.a.s.l.. The initial impoundment stage lasted until September 2013, when the water elevation rose to 1328 m.a.s.l.. In the following 3 years, the water level increased by several meters after each rainy season, while the level partially decreased by 1 to 3 m during dry seasons. The water level increased by 10 m between January and June 2014, reaching 1337 m.a.s.l.; by 4 m between February and April 2015, reaching 1341 m.a.s.l.; and by 6 m between January and June 2016, reaching 1347 m.a.s.l.. Between June 2016 and February 2019, the water elevation seasonally oscillated between 1346 and 1350 m.a.s.l.. From January to March 2019, when the exceptional rainy period occurred, the reservoir water level increased by 6 m, reaching its maximum elevation ever registered of 1353 m.a.s.l.. After this maximum and the landslide failure, the reservoir water elevation gradually decreased to 1351 m.a.s.l.. between June and July 2019 and then to 1347 m.a.s.l. between November and December 2019. In the following two years, the water elevation seasonally oscillated between 1346 and 1350 m.a.s.l..

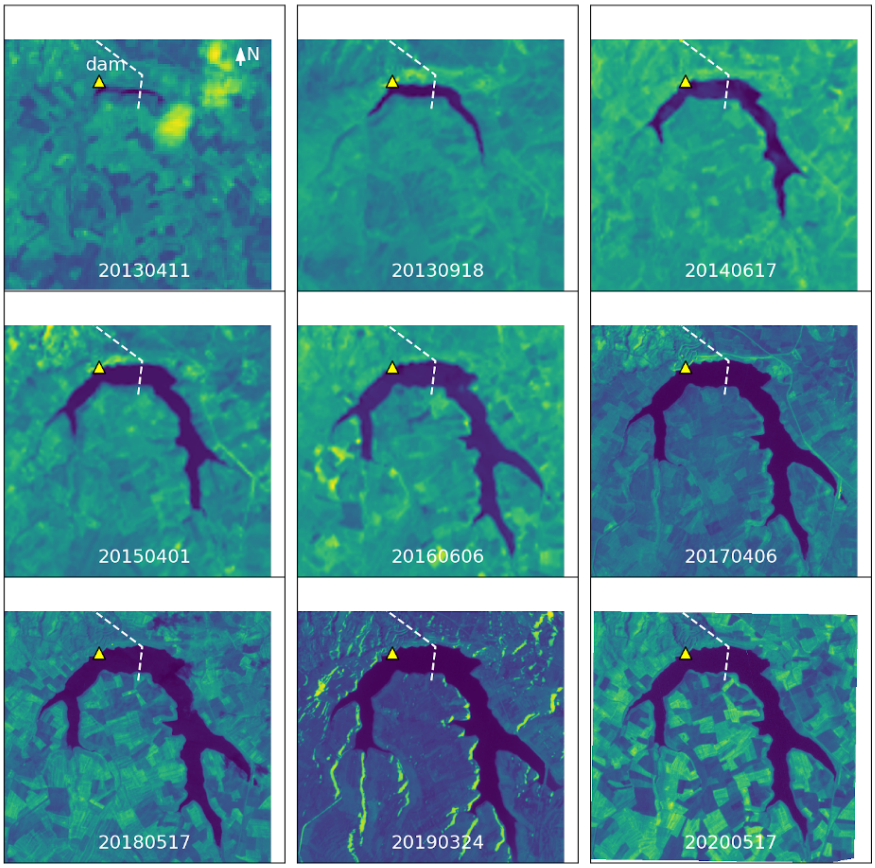


Figure 5.6: Landsat-8 and PlanetScope (Near Infrared band) show the reservoir impoundment. The white line shows the profile used to estimate the water height on the northern shoreline (same profile as in Fig. 5.1a); the yellow triangle depicts the dam structure location; white arrow indicates North.

5.5.2 Correlation between precipitation and reservoir impoundment

The magnitude squared coherence of the cross-wavelet transform between the monthly precipitation and the reservoir water elevation is shown in Fig. 5.7. The high wavelet coherence highlights periods of strong correlation between precipitation and the reservoir water elevation. These periods mainly coincide with the rainy season, during which the water in the reservoir increases. The plot also shows that the initial impoundment stage occurred partially during the 2013 dry season. The arrows in Fig. 5.6 indicate a 3- to 5-month time gap between the precipitation and the water level peaks. This is understandable since the precipitation peak occurred in approximately January, while the water level seasonal peak was reached at approximately the end of the rainy season between April

and June. Initially, the time gap was approximately 5 months. However, it decreased to 3 months after the 2019 exceptional event, when the water level exceeded what seems to be the maximum operational elevation of 1350 m.a.s.l. due to the extreme precipitation season. This shortening in the time gap between the peaks most likely can be explained by the water control policy adopted after the landslide failure, which constrains the maximum reservoir water elevation to 1350 m.a.s.l., and this upper limit is already reached in approximately April.

The wavelet analysis indicates a strong correlation between precipitation and the reservoir water level. However, in the first four years of impoundment, the reservoir water level progressively increased until reaching the operational level in 2016. Therefore, in these years, the magnitude of seasonal water level oscillations (1-2 m) was lower than the main increasing trend of 4 to 10 m/yr. When the operational level was reached, seasonal oscillations were on the order of +-3 m.

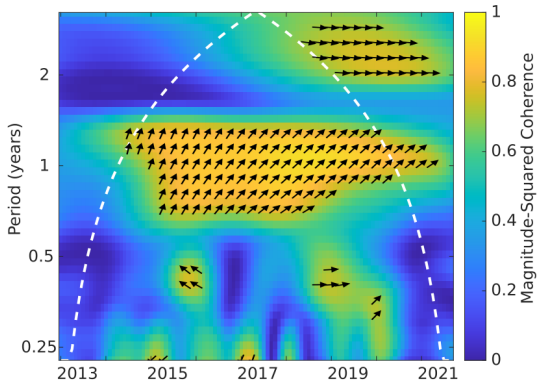


Figure 5.7: Cross Wavelet Transform between monthly precipitation and reservoir water elevation for the period April 2013 to December 2021. Color scale indicates the magnitude squared coherence; arrows indicate the phase difference between the two time series: arrows directed toward right for in-phase relationship; arrows directed toward left for anti-phase relationship. White dashed line shows the cone of influence where the edge effects might disturb the wavelet analysis results.

5.5.3 Analysis of pre-failure kinematics

5.5.3.1 MT-InSAR ground displacement

We used ascending and descending orbit ENVISAT images to derive the cumulative LOS ground displacement from July 2003 to September 2010 before the reservoir impoundment (see Fig. 5.8). The clustering procedure discretized the landslide body into upper and lower parts. Both ascending and descending radar geometries have good coherence on the lower part of the slope; however, only the ascending radar geometry observations partially cover the middle parts of the slope. The observations show relatively stable behavior before dam construction, with some oscillations on the order of 1-2 centimeters, which can be related to seasonal effects or noise due to the low temporal and spatial density of the ENVISAT dataset (see Fig. 5.9a). No SAR data are available between September 2010 and October 2014.

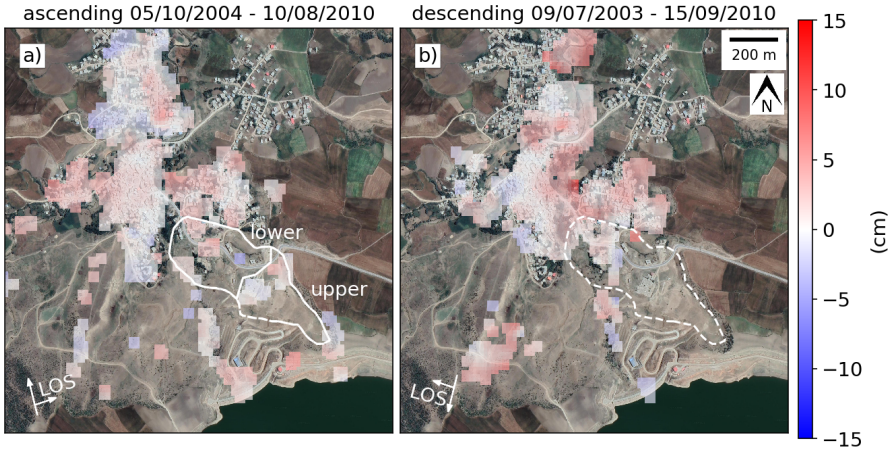


Figure 5.8: Pre-dam cumulative ground displacement from ENVISAT data. a) LOS ascending and b) LOS descending radar geometries; positive values in (a) and (b) refer to displacement toward the sensor. White dashed outlines depict the landslide-affected area. The landslide cluster partition is shown in a). The map extent is the same as in Fig. 5.2c. Background Google ©Imagery CNES/ Airbus Maxar Technologies.

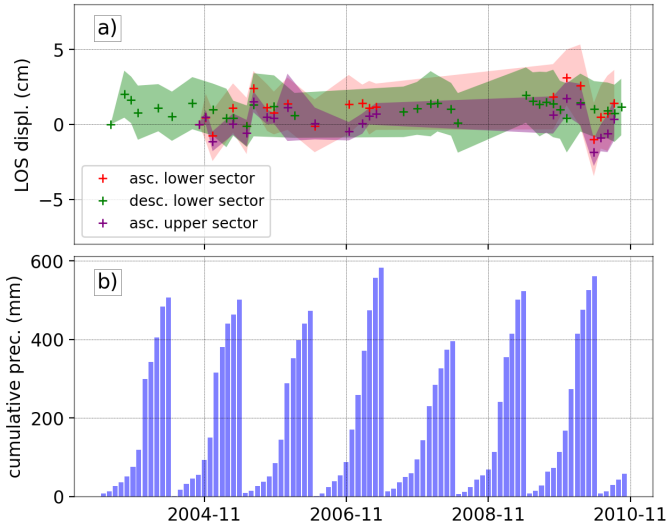


Figure 5.9: Pre-dam construction time series. a) Line of sight (LOS) ground displacements for the upper (only in ascending geometry) and lower (in both ascending and descending geometries) landslide clusters (clusters shown in Fig. 5.8a). Crosses for average values and shaded areas for standard deviation. b) Cumulative precipitation (blue histograms) from June to May successive years (data from CHIRPS).

Sentinel-1 acquisitions have been available over the study area since October 2014. Fig. 5.10 shows the cumulative ground displacement maps up to mid-March 2019 in ascending and descending radar geometries and vertical and east–west motions. The predominant landslide kinematics are horizontal westward motion and reach cumulative values up to 30 cm for the 4 and a half years of observations.

The largest principal components and independent components of the horizontal and vertical ground displacement fields over the landslide body are shown in Fig. 5.11 (Supple-

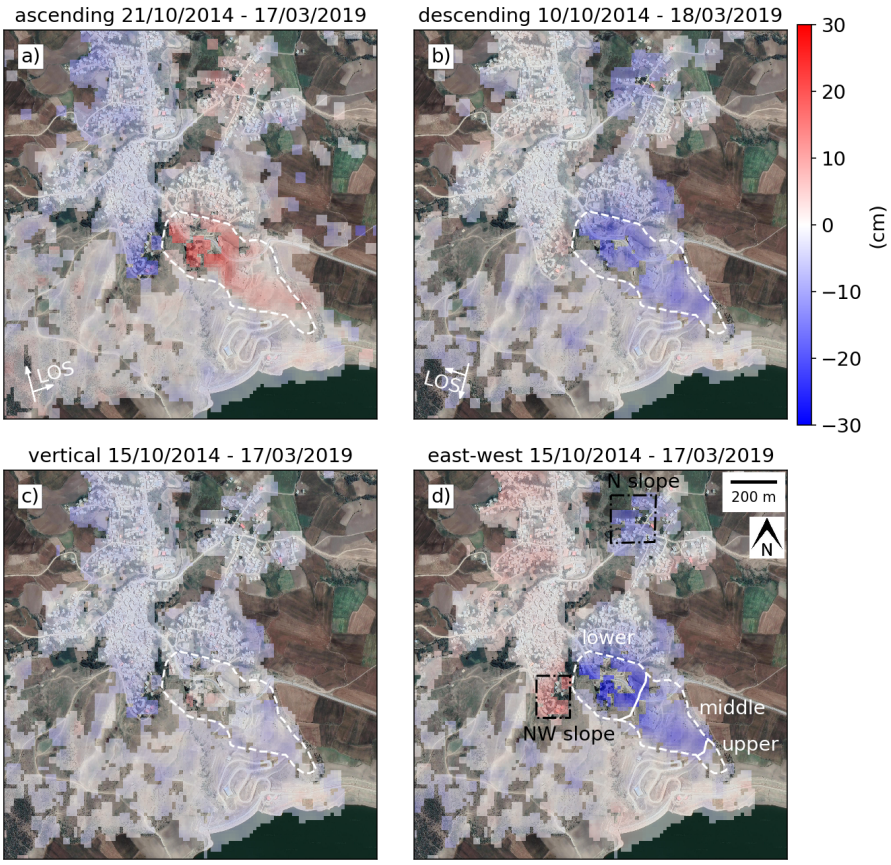


Figure 5.10: Pre-failure cumulative ground displacement from Sentinel-1 data. a) LOS ascending, b) LOS descending radar geometries; positive values in (a) and (b) refer to displacement toward the sensor. (c) Vertical motion; negative values correspond to subsidence. (d) Horizontal motion; negative values refer to westward motion. White dashed outline depicts the landslide-affected area. Black dashed rectangles in d) show additional active landslides. The landslide cluster partition is shown in d). The map extent is the same as in Fig. 5.2c. Background Google ©Imagery CNES/ Airbus Maxar Technologies.

mentary S3). In the horizontal displacement field, 94% of the data variance is explained by a nearly linear westward trend represented in PC1. It is also the component with the highest score over the entire landslide body and therefore can be considered as the predominant pre-failure landslide kinematic. PC2 and PC3 accounting for only 3% and 1.2 % of the data variance, respectively, express some fluctuations in the trend in 2016 and 2017. Although they are broadly distributed over the landslide body their score is approximately zero and therefore their contribution is negligible. The three main ICs show a predominant downslope motion (horizontal east-west) until early 2016, which is mainly visible in IC1 and IC2. After that, all three ICs showed a deceleration in trend and an acceleration again from mid-2017 onward visible only in IC1. Although all three ICs are mainly distributed on the lower and partially on the middle parts of the landslide, IC1 has the most significant score. IC1 also shows some horizontal displacement fluctuations between 2016 and 2018, however, this signal is implausible due to the downslope nature of the landslide mechanism

and it is not seen in the original data (Fig. 5.12a), so it might be an artifact generated in the processing.

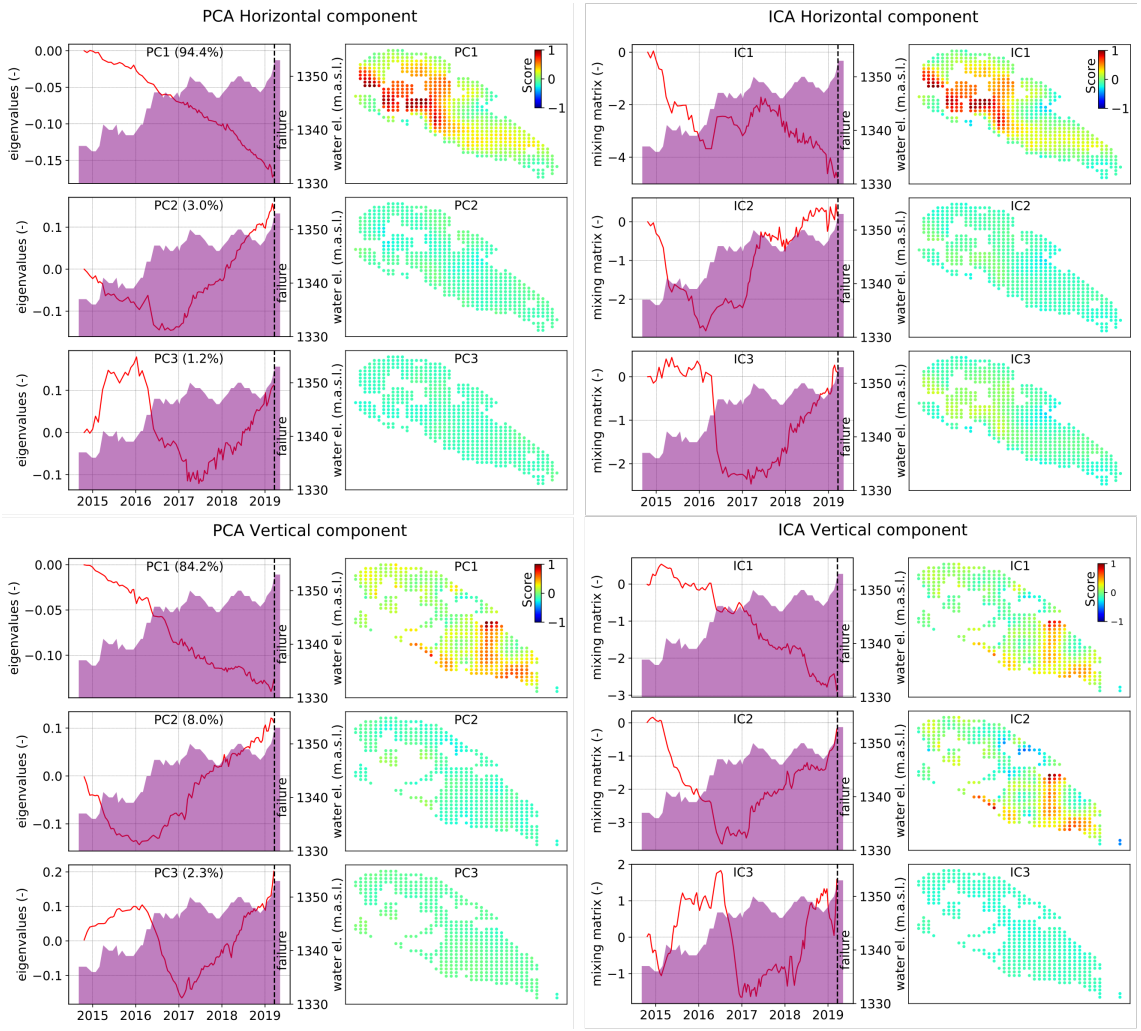


Figure 5.11: Pre-failure PCA and ICA over the landslide area for the horizontal and vertical ground displacement components. The plots show the three largest principal components (left) and independent components (right) together with the reservoir water elevation (purple) and respective score maps for the spatial distribution.

In the vertical displacement field, PC1 shows a predominant downward linear trend that accounts for 84% of the observations. This component is mainly distributed in the upper and partially in the middle parts of the landslide. The second and third PCs account for 8% and 2.3% of the data and have a broader distribution. Their contribution shows a decreasing trend at the beginning of 2016 and at the beginning of 2017 similar to PC2 and PC3 of horizontal ground displacement. IC1 shows a predominant downward trend with some seasonal up-and-down fluctuations, while IC2 shows a deceleration in trend starting from mid-2016. Both IC1 and IC2 are mainly distributed on the upper and partially on the middle parts of the landslide. IC3 shows a 2-year period of fluctuations, however, its score contribution is approximately zero and therefore negligible.

The spatial clustering partitioned the landslide into upper, middle and lower parts, as illustrated in Fig. 5.10d. The extracted ground displacements over the three clusters are shown in Fig. 5.12. All three horizontal ground displacement time series exhibit a predominant nearly linear westward trend similar to PC1 (see Fig. 5.12a and 11). The lower part of the landslide was already moving with an average velocity of -3.5±1.5 cm/yr in 2014-2015. The displacement then accelerated to -5 ±0.3 cm/yr at the beginning of 2016 and to -8.4±1.4 cm/yr at the beginning of 2018. The middle part showed its first signs of instability in late spring 2015, with an initial rate of -2.8±1.5 cm/yr, which accelerated to -4.1±0.6 cm/yr at the beginning of 2017. The upper part was relatively stable until the end of 2016, and afterwards, it started to move with a velocity of -1.6±1.2 cm/yr. The average cumulative east–west ground displacements from October 2014 to March 2019 were 5±3.7, 14.5±4.3 and 24.4±4 cm for the upper, middle and lower parts, respectively. The detrended horizontal ground displacement contains some residual signal which appears to be random noise rather than seasonal variation (see Fig. 5.12c).

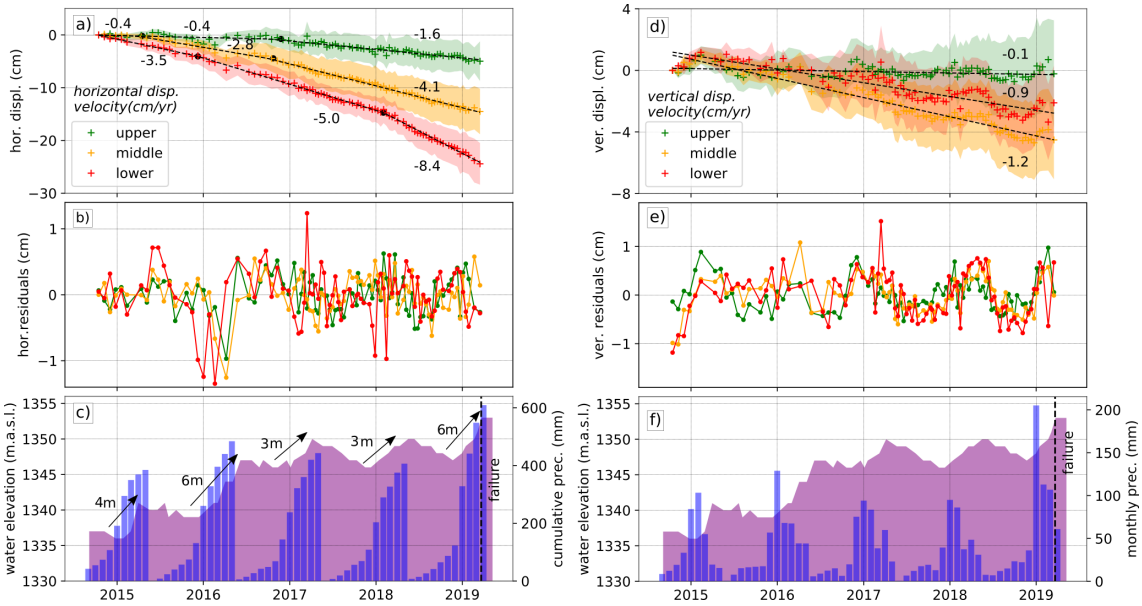


Figure 5.12: Pre-failure time series. Horizontal (a) and vertical (d) ground displacements from the cluster extraction (clusters are shown in Fig. 5.10d): cross symbol for average values; shaded areas for standard deviation; black dashed lines for piecewise segmentation models; black dots for trend changes. Horizontal (b) and vertical (e) residuals after removing the piecewise segmentation model. (c) Cumulative precipitation (blue histograms) from June to May of the successive year (data from CHIRPS). (f) Monthly precipitation (blue histogram) same data source as in c). Dam reservoir water elevation (purple area) plotted both in c and f; vertical black dotted line marks the start of the landslide main failure.

We extrapolated the time series of the lower part of the horizontal ground displacement dataset and found that a quadratic model best fits the observations. The extrapolation dated the start of the destabilization around the beginning of 2013, which corresponds to the start of the reservoir impoundment (see Supplementary S4).

The vertical components extracted for the same landslide clusters (see Fig. 5.10d) showed relatively constant subsidence rates of -0.1±0.5, -1.2±0.5 and -0.9±0.5 cm/yr (cumulative subsidence values of 0.2±3.5, 4.5±2.5 and 2.1±2.4 cm) for the upper, middle and lower

parts, respectively (see Fig. 5.12b) again similar pattern as PC1 (see Fig. 5.11). The vertical ground displacement residuals obtained by subtracting the main trend from the observations follow a clear seasonal behavior, with values oscillating on the order of ±1 cm (see Fig. 5.12e) which could be associated with the fluctuation signal also visible in IC1.

Overall, by applying PCA and IC we can infer about the dominance of a near-linear downslope motion in the pre-failure period as illustrated in Fig. 5.11. It is challenging, however, to precisely partition the behavior of the different parts of the landslide from the obtained PCs and ICs which was instead achieved better by adopting a spatial clustering and time-series piecewise segmentation. This can be due to the predominance of a single kinematic component in both horizontal and vertical displacement and less distinct secondary displacement components. Among the ICs, IC1 of the vertical component seems to contain some seasonality in addition to the main trend, which we observe as residual in the original vertical ground deformation time series.

5.5.3.2 Effects of precipitation and the reservoir water level on pre-failure motion

Before the reservoir impoundment, the lower and middle parts of the landslide were relatively stable during 2007, 2009, and 2010, which were characterized by higher than average precipitation values (see Fig. 5.5a and c). After dam construction, the first InSAR observations showed an already destabilized landslide (see Fig. 5.12a and b). In October 2014, when the Sentinel-1 observations started, the reservoir water elevation was already 1337 m.a.s.l. (water level of 18 m); therefore, a correlation between the onset of water impoundment and landslide reactivation is plausible (see Fig. 5.12a and c). As the water level increased by 4 m in April 2015, the middle part manifested its first sign of instability with a rate of 80% of that of the lower part (from -0.4 mm/yr to -2.8 mm/yr). Eight months later, the lower part accelerated further by 40%, reaching from -3.5 to -5 cm/yr. The water elevation reached 1347 m.a.s.l. (water level of 28 m) by June 2016 and 6 months later, the middle part accelerated by 46% of its previous rate, and at the same time, the upper part started to move at a rate of 40% of that of the middle part. During 2017, no changes in trends were observed over the landslide even though the water elevation rose to 1350 m.a.s.l (water level of 31 m). During the following spring of 2018, when the water elevation was at its seasonal maximum value of 1350 m.a.s.l., the lower part underwent an acceleration of 68% of its previous rate. After that, the motion of the upper, middle and lower parts kept nearly a constant trend until catastrophic failure in March 2019; the lower part was moving at a higher rate, while the middle and lower parts were moving at rates of 50% and 20% of the lower part, respectively. The absence of a clear seasonal pattern in the four-and-a-half-year horizontal ground displacement time series is confirmed by XWT analysis (see Fig. 5.12b and Fig. 5.13) suggesting that the main landslide kinematic motion is not ruled by seasonal forces, i.e., precipitation. Indeed, the reservoir water level, as previously shown, is also positively correlated with precipitation and therefore has a certain seasonality. However, in the first four years of impoundment, the progressive reservoir water level increase occurred at a rate of approximately 5 times higher than its seasonal oscillations and therefore it had a predominant role in driving the landslide kinematics. There is an interesting cluster of correlation in the last 2-3 months (January-March 2019) on the lower part of the landslide with precipitation. Although a likely acceleration of the landslide is expected in that period, it is too speculative to conclude that we can see it in the XWT result given the 12-day time intervals of the observations.

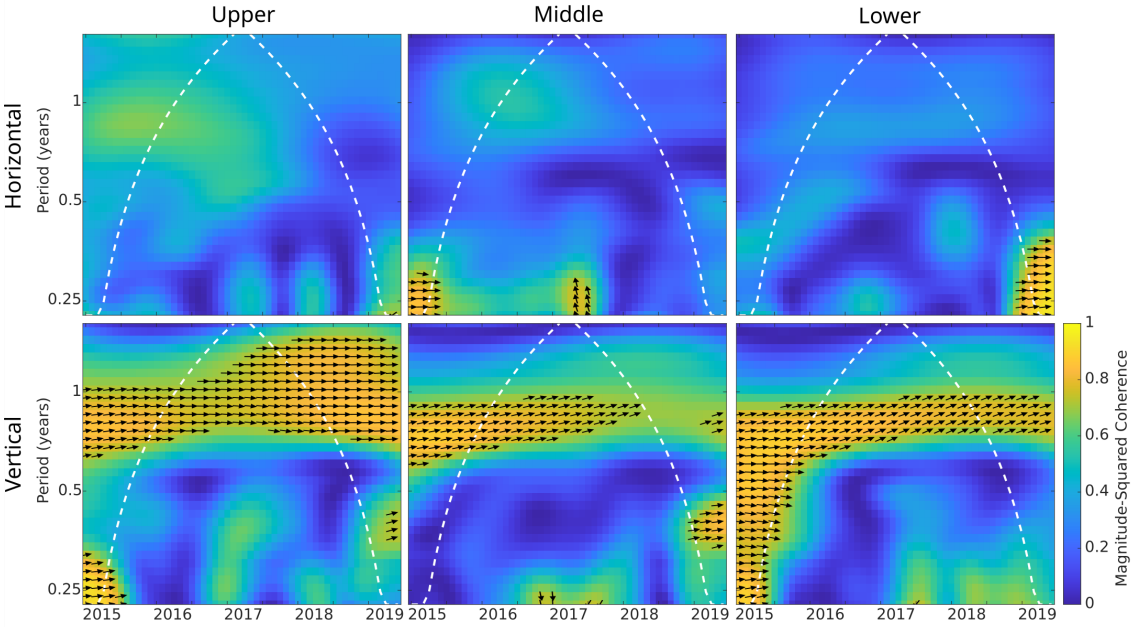


Figure 5.13: Cross Wavelet Transform between monthly precipitation and pre-failure horizontal (upper row) and vertical (lower row) displacement residuals from October 2014 to March 2019. Color scale indicates the magnitude squared coherence; arrows indicate the phase difference between the two time series: arrows directed toward right for in-phase relationship; arrows directed toward left for anti-phase relationship. White dashed line shows the cone of influence where the edge effects might disturb the wavelet analysis results.

The vertical component of displacement also shows a negative trend (see Fig. 5.12d) for the upper, middle and lower parts, although at a much lower rate compared to the horizontal component: 9%, 33% and 16% of the horizontal rate for the upper, middle and lower parts, respectively. This component is mainly related to the downslope motion of the landslide rather than to subsidence. The XWT of the vertical residuals and precipitation showed a clear seasonal pattern in all three parts, which correlated yearly and in-phase with the monthly precipitation values (see Fig. 5.12e and Fig. 5.13). This result most likely indicates swelling and shrinkage movements of the shallower soil layer due to the seasonal change in the soil moisture content.

5.5.4 Analysis of co-failure kinematics

5.5.4.1 DIC ground displacement

Visual analysis of the PlanetScope acquisitions in March 2019 shows a first-appearing horizontal shift of approximately 15 m of the road located on the upper landslide part between March 16 and 27 (see Supplementary S5). This indicates that the main landslide failure started to evolve in approximately the third week of March.

The cumulative horizontal co-failure displacement is shown in Fig. 5.14 for four different periods with reference to November 10, 2018. The results, as expected, show predominantly north-west-oriented motion, coinciding with the downslope direction. The main failure started to develop from the upper part of the landslide and progressed downslope. A

cumulative horizontal shift of approximately 17 m was observed up to April 5 in the upper part, reaching a maximum value of approximately 40 m at the end of the month. Similar high horizontal displacements were observed on the southern flank of the landslide. The main landslide body experienced cumulative horizontal shifts between 8 and 13 m until April 5 and reached 23 m by the end of the month. The lower part underwent a horizontal shift of 8 m up to April 5, reaching 16 m at the end of the month. Some localized areas on the top and the southern flank of the landslide continued moving during May, resulting in an additional horizontal motion of 5 m. This type of kinematic mechanism is typical for deep-seated landslide ruptures with higher horizontal displacement on the upper part where the main scarp is formed and lower horizontal displacement (approximately 20% of the upper displacement) on the bottom part where the deposit mass is accumulated.

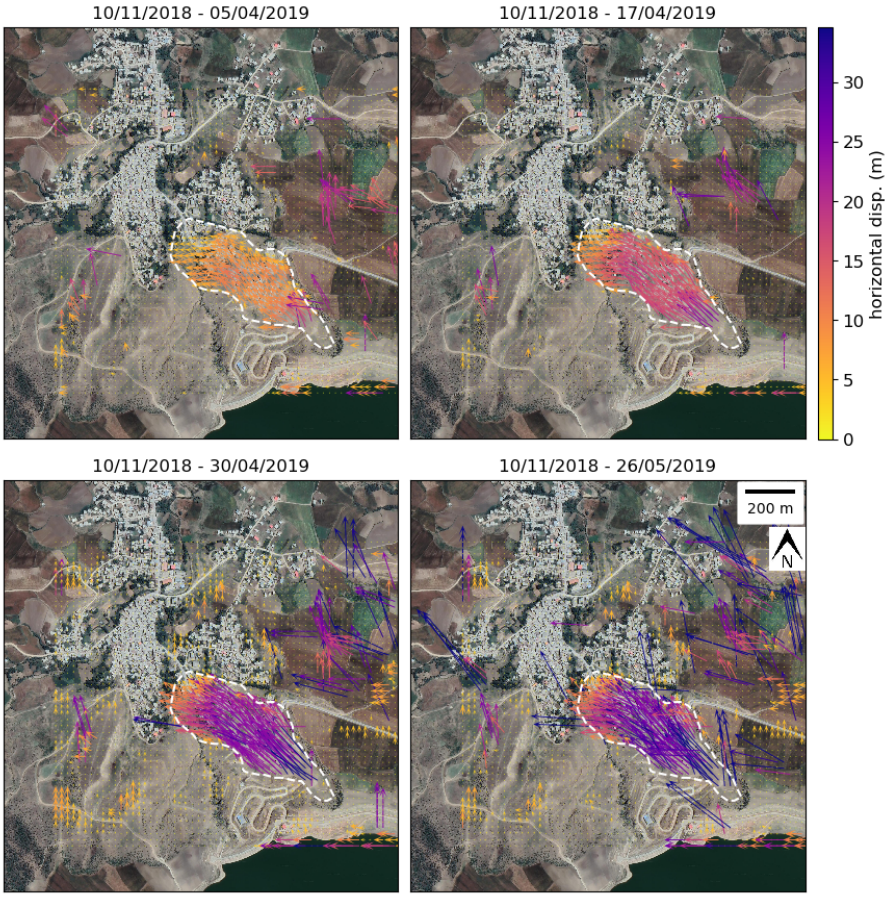


Figure 5.14: Co-failure cumulative horizontal displacement from PlanetScope data. Color scale represents the magnitude value in meters; arrows show the horizontal direction (arrow size proportional with magnitude to emphasize the strongest motion). The landslide-affected area is delimited by a white dashed outline. The map extent is the same as in Fig. 5.2c. Background Google ©Imagery CNES/ Airbus Maxar Technologies.

We digitized the landslide extent using the final cumulative horizontal displacement map from May 26. The estimated area affected by the failure is approximately 1.3x105 m^2. The landslide body coincides with the pre-failure deformation area, and therefore, we can conclude that the rupture occurred on the same shear surface.

5.5.4.2 Effects of precipitation and the water reservoir level on the main failure

In the last three months (from January to March 2019) prior to landslide failure, the precipitation reached 90% of the annual average equivalent, at 425 mm, with an extreme peak in January, which alone comprises 43% of the annual average precipitation equivalent, at 205 mm. In the same three months, the reservoir water level rose by approximately 5 m, reaching its maximum ever registered elevation of 1353 m.a.s.l. (water level of 34 m) in March 2019 (see Fig. 5.5a). The landslide started to fail from the upper part in approximately the third week of March. As we observed in the pre-failure analysis, the lower part was moving at least since the end of 2014, while the upper part started to move at the end of 2016, with a velocity equivalent to 20% of that of the lower part (-1.6 cm/yr compared to -8.1 cm/yr), indicating that the shear strength was degraded over time along the entire surface of rupture. Finally, the combination of precipitation and water level increase most likely has led to the critical value in shear strength and final failure. During April and May, when the landslide failure was further progressing, precipitation was almost absent, while the reservoir water was still at an exceptional level.

5.5.5 Analysis of post-failure kinematics

5.5.5.1 MT-InSAR ground displacement

The Sentinel-1 cumulative post-failure ground displacements from May 2019 to December 2021 in ascending and descending radar geometries and vertical and east–west directions are mapped in Fig. 5.15. The observations show a predominant horizontal east–west component, indicating that the landslide continued to move in the aftermath of the main failure.

The principal and independent components of the horizontal and vertical ground displacement fields over the landslide are shown in Fig. 5.16 (Supplementary S6). In horizontal ground displacement, PC1, accounting for 95% of the data variance and a high positive score over the entire landslide body, shows a decreasing westward trend over time. PC2, accounting for 2% of the data variance, exhibits a minor negative score in the upper–middle landslide part starting from the beginning of 2021 indicating a local acceleration in motion. PC3 accounts for only 0.8% of the data variance and has a negligible score value. The three ICs do not show well-distinct time series and spatial distribution, most likely due to the predominance of a single displacement trend.

In vertical ground displacement, PC1 accounts for 85% of the observations and shows a constant negative trend until the end of 2020 which stabilizes later. This component is distributed all over the entire landslide body. PC2 and PC3 account for 5.6% and 5.7% of the data variance, respectively showing some trend variations at the beginning of 2020 and 2021. However, they have very low score values. IC1 describes the main downward trend and has a positive score over the landslide body. While IC2 does not have a significant spatial distribution, IC3 comprises some annual fluctuations with a negative score over the entire landslide body.

Spatial clustering partitioned the landslide into upper, upper–middle, middle and lower parts, as illustrated in Fig. 5.15d. The extracted horizontal ground displacements over the four clusters are plotted in Fig. 5.17a and b, showing average cumulative values of -6.3±1.5, -11.6±2.2, -7.6±1.4 and -11.8±1.5 cm for the upper, upper–middle, middle and lower layers, respectively. The upper part is characterized by stepwise kinematic behavior,

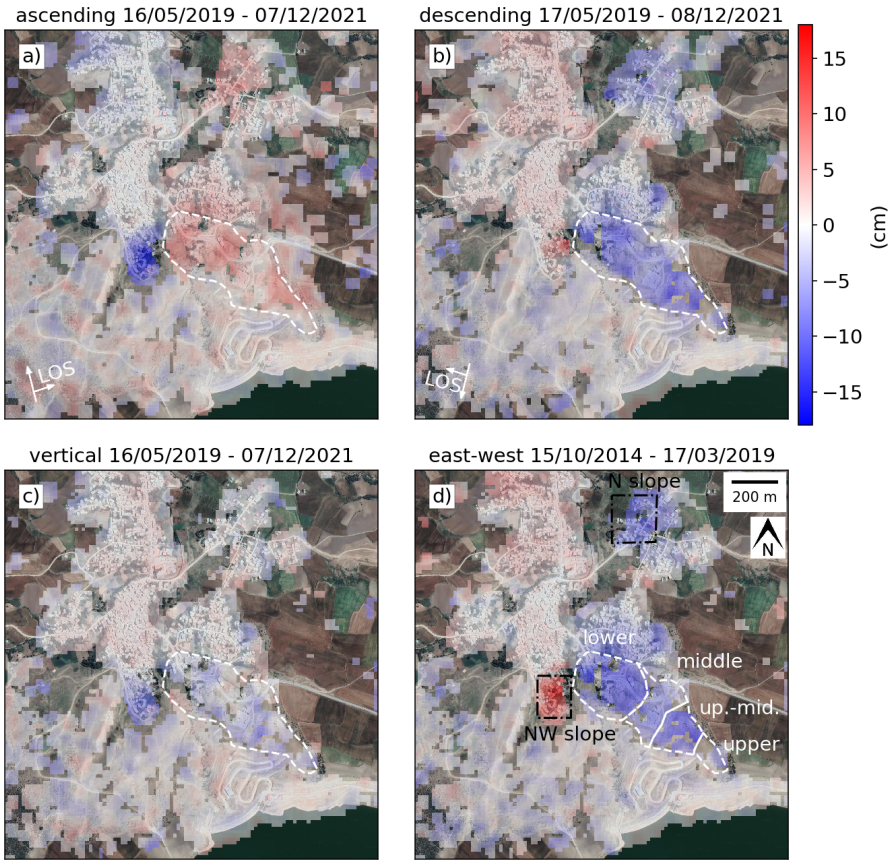


Figure 5.15: Post-failure cumulative ground displacement from Sentinel-1 data. a) LOS ascending, b) LOS descending radar geometries; positive values in (a) and (b) refer to displacement toward the sensor. (c) Vertical motion; negative values correspond to subsidence. (d) Horizontal motion; negative values refer to westward motion. White dashed line outlines depict the landslide-affected area. Black dashed rectangles in d) show additional active landslides. The landslide cluster partition is shown in d). The map extent is the same as in Fig. 5.2c. Background Google ©Imagery CNES/ Airbus Maxar Technologies.

where long-term periods of slow or no motion (-2.1±0.9, -0.2±0.3 and -0.9±0.4 cm/yr) are punctuated with shorter periods of an accelerated trend (-7.7±1 and -24.8±5 cm/yr). Similarly, the upper–middle part shows shorter periods of low or no motion (-0.8±2, -2.2±1 and 0.5±0.6 cm/yr), interspersed with longer periods of higher velocities (-6.9±1 and -5.2±2 cm/yr). On the other hand, the middle and lower parts are characterized by different patterns than the upper half of the landslide (see Fig. 5.17b). We observe an initial linear trend (-4.6±0.5 for the middle part and -8.2±1 cm/yr for the lower part), a short period of stabilization between January and April 2020, and then acceleration again to -11.9±0.2 and -10.8±1.8 cm/yr for the middle and lower parts, respectively. The slope in the trends then decreased to -2±0.3 in the middle part and -3.3±0.3 cm/yr in the lower part around August 2020 before the final stabilization started in October 2021. An updated Sentinel-1 MT-InSAR up to December 2022 of only ascending radar geometry confirmed the final stabilization over the entire landslide (see Supplementary S7). For the vertical ground displacement, we aggregated the clusters into upper (including the upper

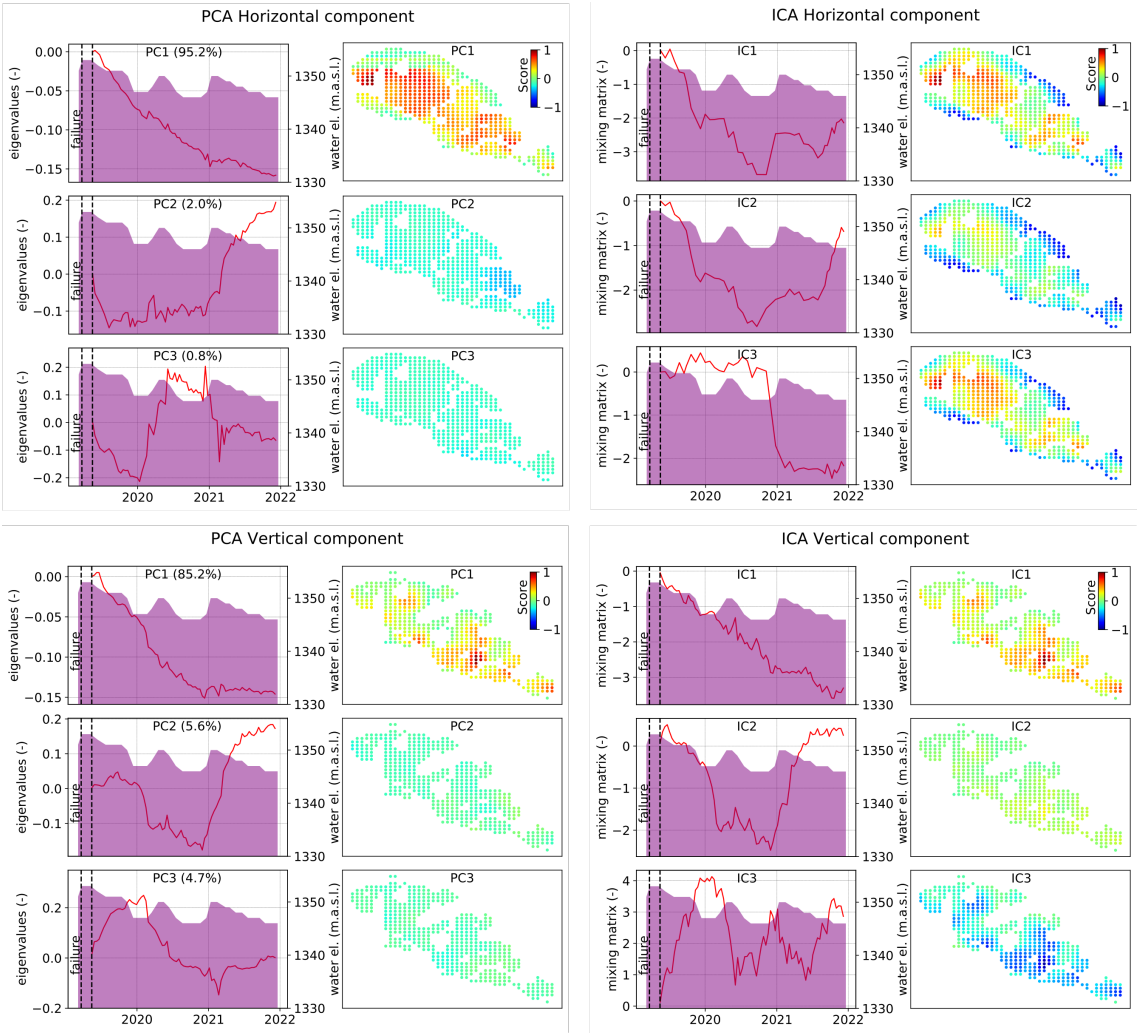


Figure 5.16: Post-failure PCA and ICA over the landslide area for the horizontal and vertical ground displacement components. The plots show the three largest principle components (left) and independent components (right) together with the reservoir water elevation (purple) and respective score maps for the spatial distribution.

and upper–middle parts) and lower (including the middle and lower parts) parts (see Fig. 5.17d). The results show that the upper part initially subsided at a rate of -2.8±1.8 cm/yr, while as of December 2020 onward, it almost stabilized. The lower part, instead, has an overall constant rate of -0.7±0.6 cm/yr. The average cumulative subsidence values from May 2019 to December 2021 were 4.3±2.5 and 2.5±2.3 cm for the upper and lower parts, respectively.

Similar to the pre-failure analysis, PCA and ICA were useful in inferring the predominance of a single kinematic component in both horizontal and vertical motion for the whole landslide body. Supplementing the analysis with spatial clustering and time-series piecewise segmentation helped us to better differentiate between the spatiotemporal behavior of different parts of the landslide.

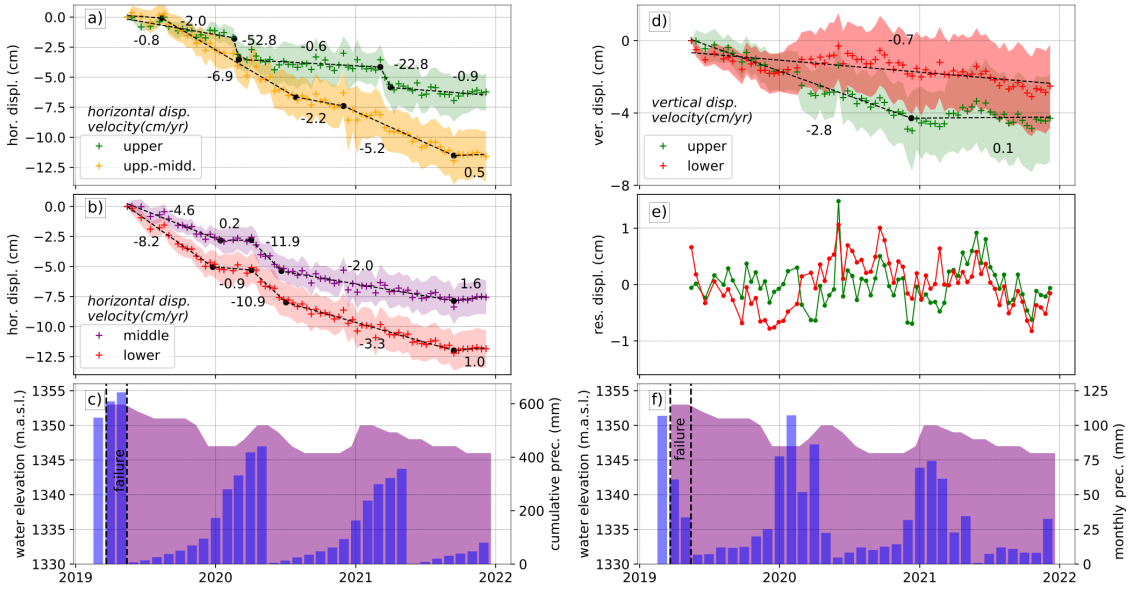


Figure 5.17: Post-failure time series. Horizontal (a) and (b) and vertical (d) ground displacements from the cluster extraction (clusters are shown in Fig. 5.15d): cross symbol for average values; shaded areas for standard deviation; black dashed lines for piecewise segmentation models; black dots for trend changes. (c) Dam reservoir water elevation (purple area) and cumulative precipitation (blue histograms) from June to May of the successive year (data from CHIRPS); arrows show water level decrease. (e) Vertical ground displacement residual vertical; (f) Dam reservoir water elevation (purple area) and monthly precipitation (blue histogram) same data source as in c). Vertical black dotted line in c) and f) marks the start and the end of the landslide main failure.

5.5.5.2 Effects of precipitation and reservoir water level changes on post-failure motion

In the aftermath of the main failure, we see an overall velocity reduction and relative stability of the entire landslide body (see Fig. 5.17a and b). However, the kinematic behavior of the different parts of the landslide correlates differently with respect to precipitation and water level changes. The upper part, which was more stable than the rest of the landslide, moved for a short period of time (2-4 months) during the months of higher precipitation (January- April) in both 2020 and 2021 (see Fig. 5.17a and c). The changes in the trend for the rest of the landslide seem to be more correlated to changes in the reservoir water level. The upper–middle part, which was initially stable between June and August 2019, destabilized in September 2019, when the reservoir water elevation was reduced from 1353 to 1351 m.a.s.l. (see Fig. 5.17a and c). The trend in motion showed deceleration by 34% in July 2020, when the water elevation decreased to its seasonal minimum of 1347 m.a.s.l.. The middle and lower parts presented in an initial short period of stability coinciding with the reservoir water elevation seasonal minimum of 1347 m.a.s.l. between January and March 2020 (see Fig. 5.17b and c). However, these parts destabilized again as the water elevation started to increase to 1350 m.a.s.l. in April 2020. After that, the negative trend of the horizontal ground displacement did not change despite the 2021 seasonal water level increase and finally stabilized starting in October 2021. The CWT between the detrended

horizontal ground displacement and monthly precipitation shows some signal that we considered noise since it is too close to the cone of influence where the edge effects might disturb the wavelet analysis (see Fig. 5.18).

We observed a minor vertical subsidence trend on the lower half of the landslide compared to the upper half, which can be correlated to the gentler slope of 7-10° compared to the slope of 10-14° for the lower and upper halves, respectively. We also checked the vertical displacement residuals for seasonal patterns correlated to precipitation (see Figs. 17d and 18). However, unlike the pre-failure period, vertical displacement in the post-failure stage does not show measurable changes in response to precipitation.

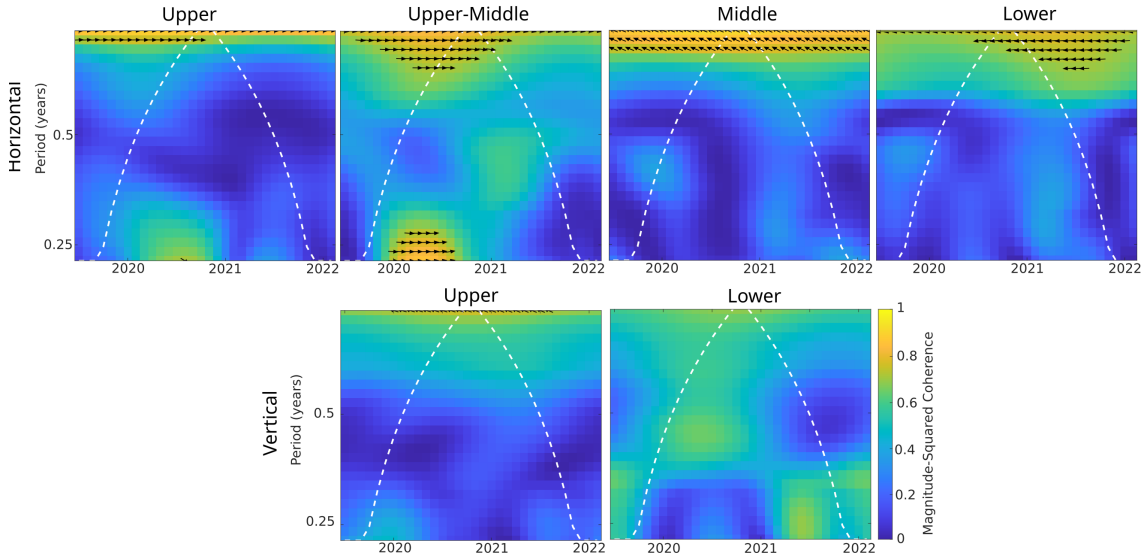


Figure 5.18: Cross Wavelet Transform between monthly precipitation and post-failure horizontal (upper row) and vertical (lower row) displacement residuals from May 2019 to December 2021. Color scale indicates the magnitude squared coherence; arrows indicate the phase difference between the two time series: arrows directed toward right for in-phase relationship; arrows directed toward left for anti-phase relationship. White dashed line shows the cone of influence where the edge effects might disturb the wavelet analysis results.

5.6 Discussion

5.6.1 Pre-failure destabilization following anthropogenic activities

This study demonstrates how combined information from multiple remote sensing satellites can be used to produce long-term geodetic and environmental products that are useful for improving landslide process understanding. The Hoseynabad-e Kalpush landslide case study clearly shows the linkage between anthropogenic and climate factors in influencing landslide dynamics and hazards and how human activities, such as dam construction adjacent to relict landslides can amplify the level of hazard and risk to population and infrastructures (Dai et al. 2002; Tan et al. 2021). Although, the main landslide failure in 2019 caused severe building and road destruction in Hoseynabad-e Kalpush village, according to local residents, the first minor cracks on buildings and terrain appeared in

approximately 2016 (https://www.yjc.ir/fa/news/7015750) approximately three years after the start of the reservoir impoundment. During this period the landslide was creeping at a rate of 3-5 cm/yr. Therefore, Hoseynabad-e Kalpush is another example of the long-term effects of slow-moving landslides on human infrastructure, including damage to buildings, thus putting human life and settlements at risk (Mansour et al. 2011; Nappo et al. 2019; Lacroix et al. 2020). In the period of 2003-2010 before the dam construction, the MT-InSAR analysis did not detect any significant ground deformation on the landslide, even during rainy seasons characterized by above-average annual precipitation. The first Sentinel-1 observations date back to October 2014, approximately one and a half years after the start of the nearby reservoir impoundment, and revealed a horizontal motion of -3.5 cm/yr (see Fig. 5.12a and c). In the following months/years, the displacement trend increased, and the destabilization progressed upward in a retrogressive mechanism.

The series of statistical analyses, including PCA/ICA, clustering/piecewise segmentation analysis and wavelet transform, showed the predominance of nearly linear downslope motion, suggesting the presence of a constantly acting force on the landslide. This force can be related to groundwater infiltration and subsequent pore water pressure increase in nearby slopes caused by the reservoir impoundment (see Fig. 5.19a). Moreover, the fact that the reservoir is located at an approximate elevation of 1319-1350 m.a.s.l. while the landslide extends between an elevation of 1230 m.a.s.l. at the toe and 1340 m.a.s.l. at the main scarp, also strengthen the conclusion of water reservoir-related groundwater infiltration. It is worth highlighting that the reservoir impoundment occurred during four stages in four years until reaching the nominal operational condition in 2016. From our analysis starting in 2014, we observed a deformation rate increase after the water level peaked, with potential time gaps of 8 months and 2 years for the lower part, 2 and 5 months for the middle part and 5 months for the upper part (see Fig. 5.12a and c). The time gap is correlated to the distance that the infiltrated water needs to travel through the slope from the reservoir to the landslide amounting to several hundred meters (Wang et al. 2022). No in-situ data are available to quantify changes in the groundwater table in the region after reservoir construction. However, during the July and September 2019 field surveys, i.e., during the dry season, we documented several erosional features and sag ponds (see Fig. 5.2a and d) on the main landslide body and along the landslide flanks, supporting water seepage on the backside of the reservoir where the 2019 catastrophic failure occurred (Fig. 5.1d and g).

We observe that the effect of the reservoir impoundment on the pre-failure landslide kinematics translates into gradual changes in trend rather than abrupt transients. Long-lasting slow motions can generate fractures on and within the landslide, which can facilitate water infiltration into larger depths and consequently foster erosional processes and acceleration of the pore pressure increase (Okeke and Wang 2016).

A minor seasonal signal of ± 1 cm was detected only in the vertical component and it was positively correlated with precipitation (see Fig. 5.12d). These results suggest that in the pre-failure stage, precipitation variations caused only swelling and shrinkage movements of the shallower soil layers due to soil moisture changes and did not govern the main deep-seated landslide mechanism. Therefore, we conclude that the reservoir impoundment triggered landslide reactivation by producing critical changes in the groundwater conditions within the slope. In this process the shear strength degraded over time until the critical stage was reached and the landslide failed.

5.6.2 From slow-moving retrogressive mechanism to deep-seated translational failure

The co-failure ground deformation time series showed that the main landslide failure developed from the upper part and then progressed downslope with a typical deep-seated translational mechanism, resulting in a clear rupture scarp on the top and deposited mass on the bottom. The landslide failure followed the extreme precipitation period, which lasted from January to March 2019. The extreme precipitation also brought the reservoir to its maximum water elevation ever registered of 1353 m.a.s.l. (water level of 34 m) observed in March 2019.

While extreme precipitation seems to be a predominant force in triggering landslide failure, there are three more factors related to the dam reservoir, which most likely have contributed as well (see Fig. 5.19a and b). The first is the landslide geotechnical degradation due to the four and a half years of pre-failure slow motion, which in turn might have lowered the potential critical stress necessary to initiate a failure (Donati et al. 2021). The second is the already partially saturated landslide at the time before extreme precipitation due to either seepage or groundwater infiltration from the reservoir. The third is the further groundwater increase within the landslide due to the reservoir water level rise following the exceptional precipitation period, which exceeded the reservoir's maximum operational condition by 3 m. The exceptional 1354 m.a.s.l. reservoir water elevation was approximately 100 m away from the upper landslide scarp, and therefore, water infiltration might have acted faster in increasing the pore water pressure of the upper part of the landslide compared to the middle and lower parts.

Under these already critical conditions for landslide stability, the exceptional and concentrated amount of precipitation that fell between January and March most likely produced a sudden and significant further increase in pore water pressure within the landslide. Therefore, we conclude that the combined effect of reservoir impoundment, long-term slow motion and exceptional precipitation most likely contributed to the final landslide failure. A detailed investigation of the relation between landslide hydrogeological conditions and reservoir impoundment and precipitation, as well as the consequent subsurface stress–strain evolution, requires geomechanical and hydrological in situ measurements (data not available) and developing numerical models (Tschuchnigg et al. 2015; Mebrahtu et al. 2022), which is beyond the scope of this study.

5.6.3 Post-failure stabilization following reservoir discharge

The post-failure analysis showed that the landslide was still active after the main failure, moving initially at rates comparable to the final pre-failure stage of a maximum of -8 cm/yr between March 2018 and March 2019, with higher rates in the middle and lower parts. PCA decomposition showed an overall negative quadratic trend, which indicates that the landslide body stabilized slowly over time.

The clustering partition and analysis of the horizontal deformations showed different kinematic behaviours between the upper and lower zones (see Fig. 5.18a). The upper zone kinematics seem to be more susceptible to precipitation infiltration. This is explicable with the remotion of material during the failure and exposure of the sliding surface on the landslide head with consequent fostering of rainfall infiltration. On the other hand, the kinematics of the middle and lower parts were still governed by water impoundment. Displacement trends clearly indicate that the reservoir discharge during the 2019 and 2020

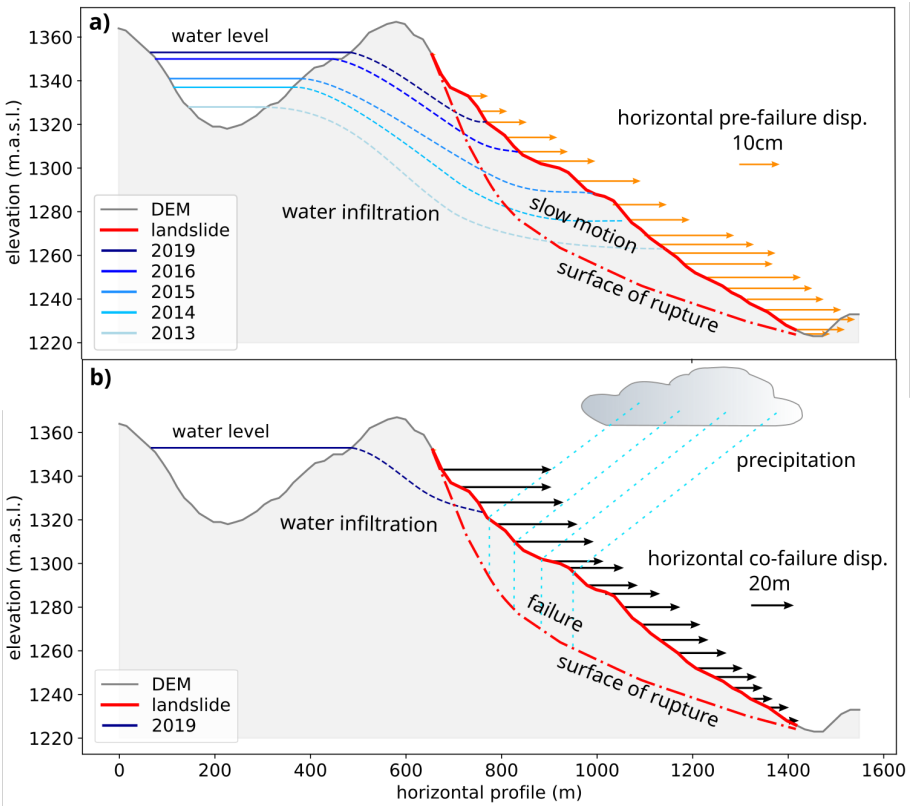


Figure 5.19: Schematic representation of the landslide reactivation and failure. Topographic profile (see profile position in Fig. 5.1a) shows the water level change for several years (blue lines), the landslide-affected area (red lines). (a) Pre-failure slow motion condition. Blue lines indicate the reservoir water level increase (dashed lines for alleged free water surface) for different years; orange arrows for pre-failure cumulative horizontal ground displacement for the period from October 2014 to March 2019. (b) Co-failure condition. Dark blue line for the maximum reservoir water elevation in March 2019; cyan lines for precipitation infiltration; black arrows for co-failure cumulative horizontal ground displacement for the period from 10 November 2018 to 28th May 2019.

dry seasons stabilized the middle and lower parts of the landslide, reducing the overall ground displacement trend each time (see Fig. 5.18b). Final stabilization was observed in October 2021. This shows that the reservoir clearly had a significant driving influence on the destabilization process of the landslide in both pre-failure and post-failure periods.

5.6.4 Landslide activities on surrounding slopes

Due to the main landslide failure, hundreds of buildings needed to be relocated in other areas around the village. In pre- and post-failure MT-InSAR analysis we also detected signs of instability in other adjacent slopes of the 2019 Hoseynabad-e Kalpush landslide, which highlights that the whole region is landslide-prone, and therefore a careful site selection for the relocation needs to be conducted (see Figs. 10d, 15d and 19). However, the governing forces on these other slopes need to be investigated more in detail by further geophysical and geotechnical investigations, which is beyond the scope of this study. The results also

show that the slope where the dam structure is sustained is relatively stable, and therefore, there is no risk of dam collapse under the present conditions. However, we cannot exclude future risk scenarios, such as in the case of the enlargement of the main and marginal scarps of the landslide, which might lead to overtopping failure of the same slope.

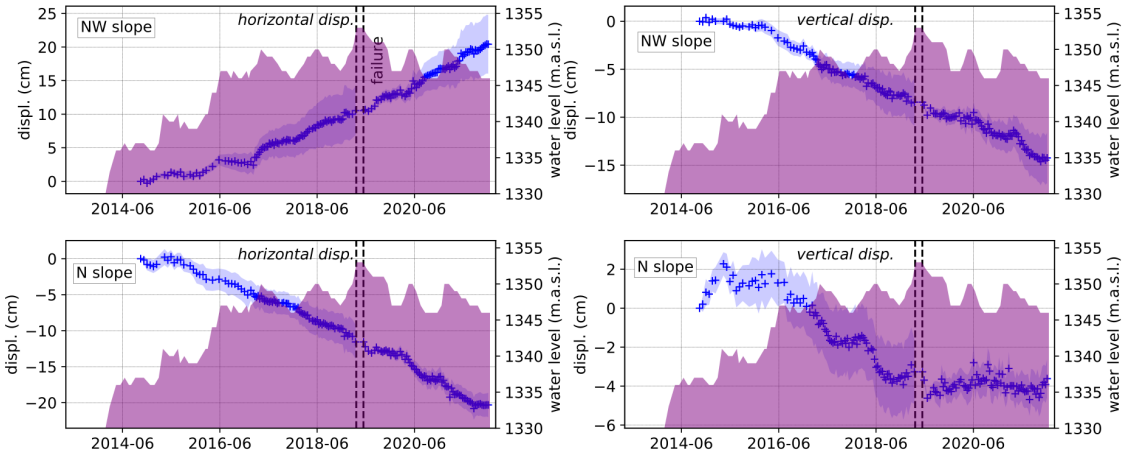


Figure 5.20: Horizontal and vertical component displacement for the north-western (NW) and northern (N) slopes (the extracted areas are shown in Figs. 10d and 15d as black dashed rectangles), combining pre and post-failure datasets. The post-failure dataset was offset by the pre-failure cumulative value.

5.7 Conclusions

In this paper, we analyzed the March–April 2019 Hoseynabad-e Kalpush landslide disaster in north–central Iran by exploiting multi-sensor SAR and optical satellite techniques combined with GIS and mathematical analysis. Our findings suggest that following a water reservoir impoundment of 34 m from 2013 to 2019 the previously inactive Hoseynabad-e Kalpush landslide was reactivated by a retrogressive destabilization mechanism with horizontal displacements of the order of 3 to 8 cm/yr. These long-term movements likely degraded the geomechanical properties of the landslide materials and led to a full failure following the exceptional precipitation that hit the region between January and March 2019. As a result, a typical translational landslide rupture developed, with a horizontal shift of $\leq$ 40 m next to the main scarp. The landslide was still active in the aftermath of its failure. However, the rate of ground displacement decreased as the water reservoir was discharged until the final stabilization of the whole landslide body in October 2021. This work is another example showing how a coupling effect between anthropogenic activities and climatic conditions increases the risk of landslide failure. It is worth noting that in Iran, only over the last four decades the number of major dams (locally called national dams) has increased by 10-fold, from only 19 dams until 1978, with a total reservoir capacity of approximately 13 bcm (billion cubic meters) to $\leq$ 200 dams, with a total reservoir capacity $>$ 50 bcm by 2021 (according to local news information). Moreover, thousands of smaller dams and embankments were built for irrigation and water supply, such as the dam in Hoseynabad-e Kalpush, and other purposes. In this regard, monitoring in situ instru-

ments are often not deployed for economic, security or accessibility reasons, and therefore, satellite remote sensing data are the only available observations.

The outcomes of our study highlight the great potential of designed satellite remote-sensing-based workflows for active landslide detection and monitoring and first-order analysis of the kinematic driving forces. Such methods are an essential contribution to landslide hazard assessment, especially in regions lacking in situ measurements. Indeed, high landslide hazard areas can be identified, and in situ surveys can be efficiently designed and deployed in those areas. Moreover, insight into the external triggering factors can also contribute to identifying which environmental parameters to monitor and choosing the proper in situ sensors to deploy. All these options open the potential for timely landslide hazard and risk reduction actions that will lower the social impact and costs.

5.8 Acknowledgment

The authors want to dedicate this work in memory to their late colleague Dr Hans-Ulrich Wetzel, a geologist and pioneer in the use of remote sensing in geology who worked for the German Research Centre for Geosciences since its foundation in 1992.

The authors acknowledge the Geological Survey of Iran for the geological map. The authors acknowledged the Copernicus programme for the free access to Sentinel-1 data available on https://scihub.copernicus.eu/dhus; the U.S. Geological Survey for Landsat 8 Collection 1 Tier 1 orthorectified scenes freely available on https://earthexplorer.usgs.gov/. The authors acknowledge The Planet Lab PBC, 2017, for providing the PlanetScope data via the Planet application program interface: In Space for Life on Earth. San Francisco, CA. https://api.planet.comand] the USGS Earth Resources Observation and Science (EROS) Center for creating and making freely available CHIRPS rainfall dataset. This work was partially supported by Helmholtz Imaging Platform (project: MultiSat4SLOWS).

6 Offshore earthquake in the eastern coast of Kamchatka peninsula

This chapter was published as:

Magdalena S. Vassileva, Mahdi Motagh, Thomas R. Walter, Hans-Ulrich Wetzel and Sergey L. Senyukov . **The 29 March 2017 Yuzhno-Ozernovskoe Kamchatka Earthquake: Fault Activity in An Extension of the East Kamchatka Fault Zone as Constrained by InSAR Observations.** *Bulletin of the Seismological Society of America* 110 (3): 1101–1114 (2020), doi.org/10.1785/0120190174

Some minor changes were applied with respect to the original publication: some minor typos were corrected.

Author contribution statement:

As first author, I contributed most to the work including conceptualization, methodology development, validation, SAR data collection, InSAR data processing, geophysical source inversion modelling, investigation, interpretation, writing- original draft, reviewing and editing and visualization. Hans-Ulrich Wetzel performed the geological mapping. All co-authors contributed to the discussion, reviewing and editing of the manuscript.

Method summary:

In this work, DInSAR analysis was performed to characterize the earthquake co-failure process. A multisensor dataset of Alos-2 (ascending and descending orbit paths) and Sentinel-1 (ascending orbit path) SAR acquisitions was used. All three InSAR datasets were jointly inverted to derive the best-fit fault elastic source models. Several global and local source focal mechanisms derived from seismic data were used to set up the initial parameters of the model. Main conclusions about the fault rupture and the regional geodynamic settings were finally derived based on the results.

Supplementary Material:

Supplementary material was not included in the chapter and can be found on the following link under the voice Supplements.

6.1 Abstract

Recent earthquakes off the northeastern Kamchatka coast reveal that this region is seismically active, although details of the locations and complexity of the fault system are lacking. The northern part of Kamchatka has poor coverage by permanent seismic stations and ground geodetic instruments. Here, we exploit the Differential Interferometric Synthetic Aperture Radar (DInSAR) technique to characterize the fault geometry and kinematics associated with the 29 March 2017 Mw 6.6 Yuzhno-Ozernovskoe earthquake. The aim is to contribute to identifying the active fault branches and to better understand the complex tectonic regime in this region using the DInSAR technique, which has never before been applied to the analysis of coseismic offsets in Kamchatka. We produced coseismic deformation maps using Advanced Land Observation Satellite-2 ascending and descending and Sentinel-1A descending Synthetic Aperture Radar (SAR) scenes and detected a predominant uplift up to 20 cm and a westward motion of approximately 7 cm near the shoreline. We jointly inverted the three geodetic datasets using elastic half-space fault modeling to retrieve source geometry and fault kinematics. The best-fit solution for the nonlinear inversion suggests a north–west-dipping oblique reverse fault with right-lateral rupture. The model fault geometry is not only generally consistent with the seismic data but also reveals that a hitherto unknown fault was ruptured. The identified fault structure is interpreted as the northern extension of the east Kamchatka fault zone, implying that the region is more complex than previously thought. Important implications arise for the presence of unknown faults at the edges of subduction zones that can generate earthquakes with magnitudes greater than Mw 6.

6.2 Introduction

The Kamchatka subduction zone is a consequence of the 77–83 mm=yr convergence between the Pacific plate and Okhotsk microplate, giving rise to mountain-building processes, active volcanoes, and high-tectonic seismicity (DeMets et al.,1990; Bürgmann et al., 2005). Some of the historical earthquakes have reached a moment magnitude Mw 9, such as in 1952, and more events have reached a moment magnitude Mw 8, such as in 1904 (M s 8), 1923 (Mw 8.5), and 1959 (Mw 8.2) (Bürgmann et al., 2005). Moreover, some strong earthquakes occurred inland following the volcanic belt, as in 2003 (Mw 6.9), 2004 (Mw 6.9), and 2016 (Mw 7.2) (data from the Seismological Data Information System [SDIS] of Kamchatka Branch of Geophysical Survey of Russian Academy of Sciences [KB GS RAS] Earthquakes Catalogue for Kamchatka and the Commander Islands [1962–present], see Data and Resources). Strong earthquakes also occurred off the western Kamchatka coast in 2013 (Mw 8.3) and 2008 (Mw 7.7 and 7.3) and along the Pacific–Aleutian transform boundary in 2003 (Mw 6.7), 2017 (Mw 7.7), and the recent 2018 (Mw 7.2) (data from the SDIS of KB GS RAS Earthquakes Catalogue for Kamchatka and the Commander Islands [1962–present], see Data and Resources) (see Fig. 6.1).

Associated with offshore earthquake activities are also potential tsunami hazards. The proper characterization of the factors that govern seismic energy accumulation and release and the identification of the locations and geometries of possibly seismogenic faults are essential for tsunami hazard assessment (Baer et al., 2008; Tong et al., 2010; Scott et al., 2018). The Differential Interferometric Synthetic Aperture Radar (DInSAR) technique has become a standard tool for the detection of co- and postseismic deformation (Çakir et al.,

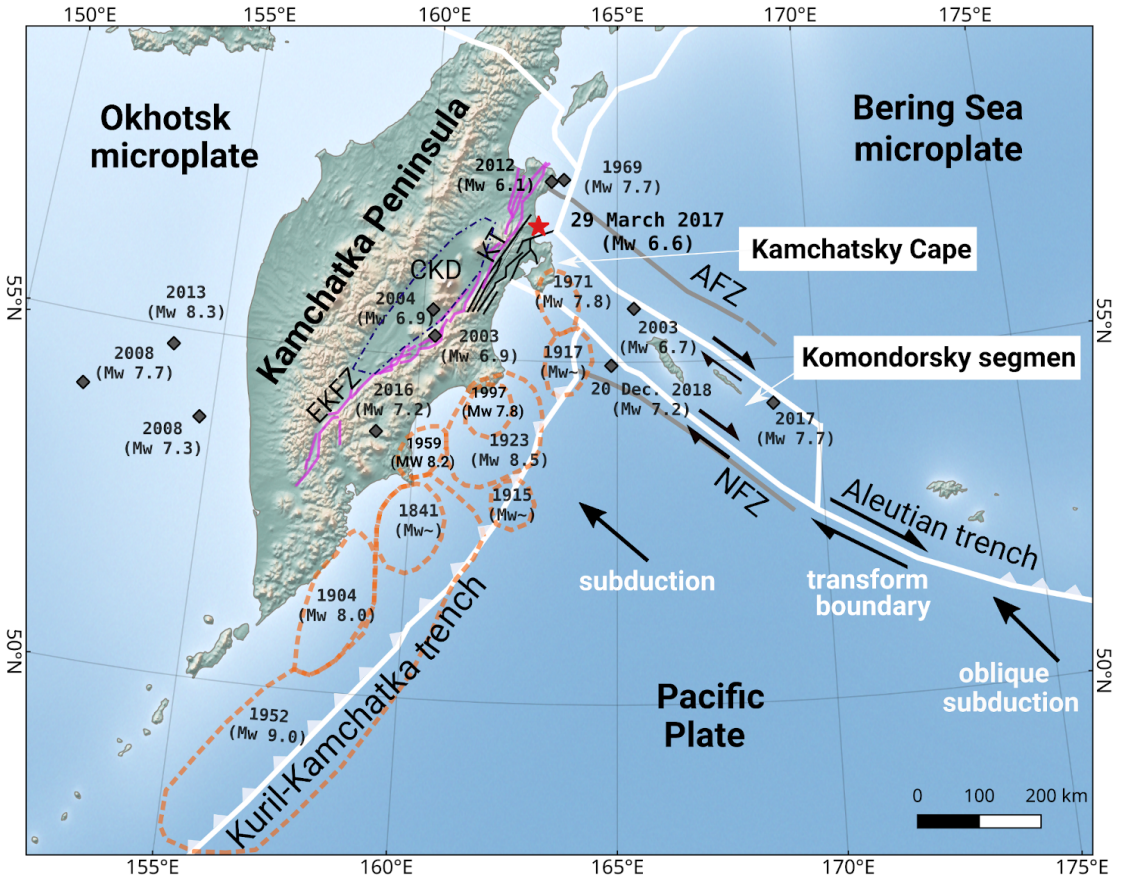


Figure 6.1: Overview depicting the main geographic and geological features and tectonic complexities of Kamchatka peninsula. Tectonic edges are represented by thick white lines; the main fault systems are represented by polyline segments: thin and lighter color for the east Kamchatka fault zone (EKFZ) and thin and black color for the thrust fault system of the Kumroch thrust belt (KT). Dashed and dotted polygons show the central Kamchatka depression (CKD) zone; lighter dashed polygons represent the rupture zones of the larger historical earthquakes (Johnson and Satake, 1999; Bürgmann et al., 2005). The location of the 29 March 2017 Yuzhno-Ozernovskoe earthquake is symbolized by a star; black diamond symbolizes the locations of the main historical earthquakes discussed in the Seismic Data section. Natural Earth image is used as background (see Data and Resources). AFZ, Alpha fault zone; NFZ, Naturalist fault zone. The color version of this figure is available only in the electronic edition.

2003; Atzori et al., 2008, 2009; Motagh et al., 2007, 2010). Despite the availability of proper Synthetic Aperture Radar (SAR) interferometric pairs across the region, a finite-fault model incorporating such data for the 29 March 2017 Yuzhno-Ozernovskoe earthquake has not been produced yet. In this study, we investigate the geometry and fault slip model of the Yuzhno-Ozernovskoe earthquake using both C- and L-band DInSAR measurements. In view of the complex tectonic processes that take place in this region, we contribute to identifying the active fault branches and provide a tectonic interpretation of the ongoing regional processes.

6.2.1 Tectonic background

The Kamchatka peninsula is located in a tectonically active region and has one of the highest seismic hazard potentials in the world (Gorbatov et al., 1997). The main geographic and geological features and tectonic complexities are illustrated in Figures 1 and 2 (see also supplemental material available to this article).

The northeastern part of the peninsula is located on a triple junction among the Pacific plate and the Bering Sea and Okhotsk microplates, in which a dramatic shift in subduction dynamics occurs (Cook et al., 1986; Pedoja et al., 2006; Gordeev et al., 2015). On one hand, the Pacific plate subducts northwest beneath Kamchatka, forming the Kuril–Kamchatka trench, with a gradually decreasing angle from 55° to 35° (Gorbatov et al., 1997). On the other hand, the Pacific slab subducts with an oblique angle northward along the Aleutian trench, in which it turns into a transform boundary along the westernmost part of the trench. The Kuril–Kamchatka and Aleutian trenches intersect in the area of the Kamchatsky Cape, situated at approximately 56° N, at almost a right angle, forming an active junction in which the subduction and transform boundary processes cause the collision of the westernmost segment of the Aleutian arc, referred to as the Komandorsky shear zone, with the Kamchatka peninsula (Levina et al., 2013; Gordeev et al., 2015). North of the junction, no subduction occurs (Gaedicke et al., 2000), and the present trench is considered extinct (Alexeiev et al., 2006).

Because of the arc-continental collision, this area is fragmented into several fracture zones, which splay onshore on Kamchatsky Cape and are enclosed between the Alpha fracture zone in the north and the Naturalist fracture zone in the south. General dextral strike-slip faulting emerges due to the relative velocities between the rapidly moving Pacific plate and the slow-moving Komandorsky segment (Gaedicke et al., 2000).

The Kumroch Range, also called the Kumroch thrust belt, located directly west of Kamchatsky Cape, is the onshore response to the collision, as suggested by the folded rocks to the east and the fault systems that are right lateral to the north and left lateral to the south (Geist and Scholl, 1994). Some recent studies show that the Kumroch Range is actually part of a larger active fault system named as the east Kamchatka fault zone (Kozhurin et al., 2006; Kozhurin and Zelenin, 2017). This fault zone stretches along the east coast over two-thirds of the peninsula and is composed of a hundred small predominantly normal northeast–southwest-oriented faults, which are connected to the late Quaternary volcanism of the region. The east Kamchatka fault zone is bounded on the west by the central Kamchatka depression, a wide valley that hosts some of the most active Kamchatka volcanoes: the Klyuchevskoy group of volcanoes, including Klyuchevskoy, Benzimiani, and Tolbachik, and the Shiveluch volcano (Kozhurin et al., 2006). The main geological structure of the peninsula is composed of folded Cretaceous–Tertiary rocks, overlain by Quaternary units and overprinted by volcanic activity.

6.2.2 Earthquake-related faulting north of the subduction zone

It was believed that strong earthquakes and tsunamis are improbable north of the Pacific subduction zone. However, the 22 November 1969 Mw 7.7 Ozernovskoe earthquake (Levina et al., 2013), the 24 June 2012 Mw 6.1 near the east coast of Kamchatka earthquake, and the latest 29 March 2017 Mw 6.6 Yuzhno-Ozernovskoe earthquake reveal the active faulting structure and resulting seismogenic and tsunamigenic potential hazards of this region (see Fig. 6.1).

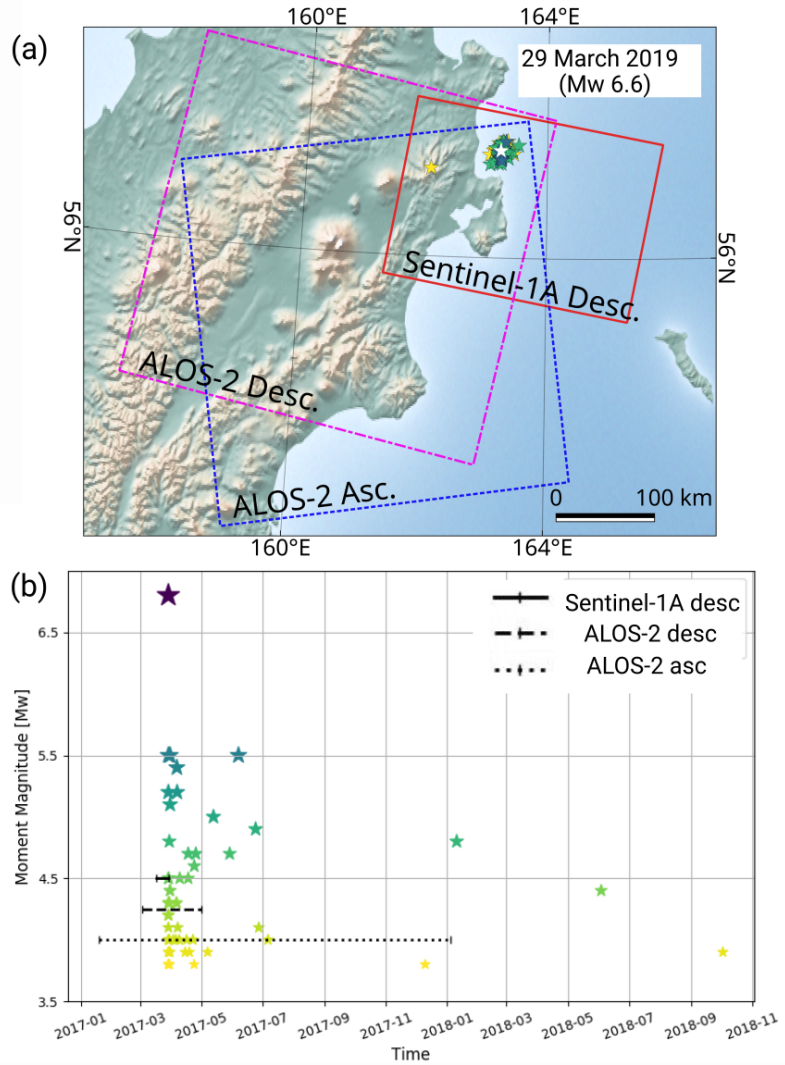


Figure 6.2: Spatial and temporal coverage of the Synthetic Aperture Radar (SAR) scenes used in the coseismic Differential Interferometric Synthetic Aperture Radar (DInSAR) analysis and the seismic sequence following the 29 March Mw 6.6 earthquake are shown (data from the Seismological Data Information System [SDIS] of Kamchatka Branch of Geophysical Survey of Russian Academy of Sciences [KB GS RAS] Earthquakes Catalog for Kamchatka and the Commander Islands (1962–present) (SDIS—KB GS RAS); (a) SAR image footprints: Advanced Land Observation Satellite (ALOS)-2 ascending (light dotted lines), ALOS-2 descending (dark dashed and dotted lines), and Sentinel-1A (light solid line); polyline segments show: in thin and lighter color the EKFZ (after Kozhurin et al., 2006; Kozhurin and Zelenin, 2017) and in thin and black color the KT; black triangles show the location of the seismic stations (see Data and Resources); white star shows the 29 March M w 6.6 earthquake; the scaled by magnitude, stars symbolize the aftershocks. Natural Earth image is used as background (see Data and Resources). (b) The seismic sequence in time domain is shown; sized and scaled stars emphasize the magnitude; lines show the SAR temporal baselines for ALOS-2 ascending (asc.; dotted lines), ALOS-2 descending (desc., dashed and dotted lines), and Sentinel-1A (solid line). The color version of this figure is available only in the electronic edition.

Most of the seismic activity is concentrated offshore in the fractured region frontal to the collision zone and along the Pacific–Aleutian transform boundary, and normally achieves magnitudes of approximately Mw 6. The last strong Mw 7.2 earthquake along the transform region occurred close to Komandorskiye Island on 20 December 2018. The onshore collision zone coincident with the Kumroch thrust belt is associated with low-level seismicity.

The 29 March 2017 Yuzhno-Ozernovskoe earthquake occurred immediately north of Kamchatsky Cape, in which three different geological and tectonic structures interact with each other: the Pacific slab subduction edge, the east Kamchatka fault zone, and the Komandorsky segment collision with the Kamchatka peninsula. According to the Kamchatka Regional Seismic Network (KRSN; see Data and Resources), the epicenter was located at 56.97° N and 162.22° E at a depth of approximately 43 km. Dozens of aftershocks have been recorded mainly in the first three months after the mainshock, some of them exceeding magnitude Mw 5 (see Fig. 6.2).

6.3 Data and methods

6.3.1 Seismic data

We exploit seismic records identified by the regional instrumental network. The KRSN was initially set up in 1961. It currently includes 83 permanent seismic stations in the region (see Data and Resources). The KRSN is composed of three networks with different extents and resolution capabilities: a network of stationary digital seismic stations, a network of telemetered seismic stations, and a strong-motion network (Chebrov et al., 2013; Gordeev et al., 2013). The KRSN is currently operated by the KB GS RAS, and the seismic data are available through the SDIS (see Data and Resources). The station distribution has a higher density in the northeastern part of the central Kamchatka depression and over the Kamchatka East Ridge, the two regions that host the most active volcanoes in Kamchatka, while only a few stations are located in the northern part of the peninsula where the Yuzhno-Ozernovskoe earthquake occurred (see Fig. 6.2). The hypocenter seismic source location is estimated using the arrival times of P and S waves. According to the local seismic catalog, the epicenter was located 25 km offshore at a depth of 43 km with accuracies of 16 km in horizontal location and 20 km in depth (see Data and Resources).

As is well known, the source focal mechanism derived from seismic data provides two possible fault-plane solutions (nodal planes) that are located at right angles with respect to each other. The fault-plane ambiguity can be solved only by taking into consideration geological and additional geophysical data. The source focal mechanism as in Chebrov et al. (2017) is retrieved by fixing the depth to 10 km and shows a northeast–southwest-oriented reverse fault with a small oblique component. The mainshock was also detected by several global seismological centers: the Global Centroid Moment Tensor (Global CMT) Project catalog, the U.S. Geological Survey (USGS), the GEOFOrschungsNetz (GEOFON), the National Institute of Geophysics and Volcanology (INGV), and the Global Network of Broadband Seismic Stations (GEOSCOPE; see Data and Resources). All seismic-derived results agree with the orientation of the fault and show dip angles ranging between 39° and 55°, although they disagree in the seismic source localization in the range of dozens of kilometers due to different seismic stations used for the inversion, different algorithms, and consequently the type of source location, which are either hypocenter (focus), corre-

	M (M_w)	Lat (°)	Long (°)	±Δ*L* (km)	*D* (km)	±Δ*D* (km)	Focal mechanism diagram	Dip (°)	Strike (°)
Geodetic Model*	6.6	57	162.9	1	10	1		72	213
SDIS KB GS RAS	6.5	57	163	16	43	20		55	224
								37	24
GCMT*	6.6	57	165	-	17	-		51	217
								41	19
USGS*	6.6	57	163	6.8	24	1.7		39	208
								51	25
GEOFON	6.6	57	163	-	21	-		40	201
								51	38
INGV	6.6	57	163	14.2	18	-	-	-	-
								-	-
GEOSCOPE*	6.5	57	163	-	22	-		51	217
								41	16

Figure 6.3: Comparison of the source parameters derived from the DInSAR geodetic modeling and the local and global seismological centers. The SDIS–KB GS RAS Earthquakes Catalog for Kamchatka and the Commander Islands (1962–present), focal mechanism solution as in (Chebrov et al., 2017); the Global Centroid Moment Tensor (Global CMT) catalog, the U.S. Geological Survey (USGS), the GEOFOrschungsNetz (GEOFON), the National Institute of Geophysics and Volcanology (INGV), and the Global Network of Broadband Seismic Stations (GEOSCOPE). Location uncertainty (ΔL) and depth uncertainty (ΔD) uncertainties are shown. The (*) symbol labels the seismological centers that provide centroid source location (geodetic model, Global CMT, USGS, and GEOSCOPE); the seismological centers that are not labeled provide the hypocenter or epicenter of the earthquake (SDIS—KB GS RAS, GEOFON, and INGV).

sponding to the starting point of the rupture, or centroid, corresponding to the center of energy released (see Fig. 6.3). The Global CMT, USGS, and GEOSCOPE provide the centroid solution of the earthquake, although they use different spectrums of the seismic waves; while the Global CMT uses both long-period (T > 45 s) body waves and very-long-period (T > 135 s) surface waves (Dziewonski et al., 1981; Ekström et al., 2012); the USGS applies the so-called W phase source inversion algorithm, which uses long-period (100–1000 s) phase arriving between the P- and S-wave phases (Hayes et al., 2009), and GEOSCOPE applies the Seismic source ChAracteristics Retrieved from DEConvolvolving teleseismic body waves (SCARDEC) method that uses teleseismic body waves (Vallée et al., 2011). GEOFON and INGV retrieve the seismic source hypocenter, the former using the body-wave amplitudes and polarities and the latter by applying the time-domain moment tensor technique using the broadband velocity waveforms. The Global CMT solution locates the seismic centroid offshore close to Pokaty Canyon, similar to the local seismic epicenter solution, whereas GEOFON locates the earthquake epicenter onshore in the eastern part of the Kumroch thrust belt, close to the locations estimated by the USGS and GEOSCOPE centroid solutions. Considering all these different source solutions and their uncertainties, we conclude that based on only seismic source solutions, it is difficult to find a unique interpretation, especially in such a complex tectonic setting. Therefore,

with the availability of coseismic information from DInSAR, we can better understand the seismic source and therefore provide a much more accurate tectonic interpretation (Çakir et al., 2003; Fialko et al., 2005; Lasserre et al., 2005; Grandin et al., 2016; Sangha et al., 2017; Vajedian and Motagh, 2018).

6.3.2 DInSAR analysis

Two different SAR satellites are available for the coseismic analysis: Advanced Land Observation Satellite (ALOS)-2 L-band and Sentinel-1A C-band SAR sensors (see Data and Resources). From the ALOS-2 sensor, both ascending and descending orbit passes with temporal baselines of 350 and 56 days, respectively, are suitable for interferometric analysis. For the Sentinel-1A mission, the ascending orbit pass does not cover the area of interest well; therefore, only data from a descending pass are processed. The precise orbits have been used for all datasets. The main characteristics of the three SAR interferometric couples are summarized in Table 1.

Interferometric Synthetic Aperture Radar (SAR) Pairs

Mission	Band	Acquisition Mode	Path and Frame	Orbit Path	Acquisition Date (yyyy/mm/dd)	Normal Baseline (m)	Temporal Baseline (Days)	Incidence Angle
ALOS-2	L (24 cm)	Stripmap Fine	109–1130	Asc.	2017/01/19 2018/01/04	47	350	41°
ALOS-2	L (24 cm)	Stripmap Fine	9–2460	Desc.	2017/03/06 2017/05/01	118	56	31°
Sentinel-1A	C (5.6 cm)	TOPSAR	89–404	Desc.	2017/03/17 2017/03/29	76	12	42°

Table 6.1: Main characteristics of the SAR scenes are used in the current coseismic displacement analysis. ALOS, Advanced Land Observation Satellite; Asc., ascending; Desc., descending; TOPSAR, Terrain Observation with Progressive Scans SAR.

The DInSAR processing was performed using the commercial interferometric SARscape version 5.4.1 module in the Environment for Visualizing Images platform. The 30 m Shuttle Radar Topography Mission digital elevation model (Farr et al., 2007) was used to remove the topographic phase contribution and perform the transformation from radar to geographic coordinates. To enhance the signal-to-noise ratio (SNR) of the interferograms, a modified Goldstein filter was applied to the interferograms with filter window sizes of 32, 128, and 256 pixels for ALOS-2 ascending and descending and Sentinel-1A descending dataset, respectively (Goldstein and Werner, 1998; Baran et al., 2003; Ghulam et al., 2010). The phase-wrapped maps are shown in Figure 4. The unwrapping step was performed by applying the minimum cost flow algorithm (Reigber and Moreira, 1997; Costantini, 1998) and selecting coherence thresholds of 0.15 for the ALOS-2 ascending and Sentinel-1A descending datasets and 0.1 for the ALOS-2 descending dataset. The low coherence values are mostly due to snow cover, and for the ALOS-2 datasets, they are also a result of temporal decorrelation related to the longer time span between the scenes. Finally, the unwrapped phase was transformed into a displacement value with respect to a selected reference point considered to be stable and geocoded to the projected coordinate system WGS84/UTM zone 58N (see Figs. 4 and 5).

From the interferometric analysis, three coseismic displacement maps were produced, each showing the 1D radar line of sight (LoS) displacement component, which corresponds to the direction between the ground target and the radar sensor. The deformation pat-

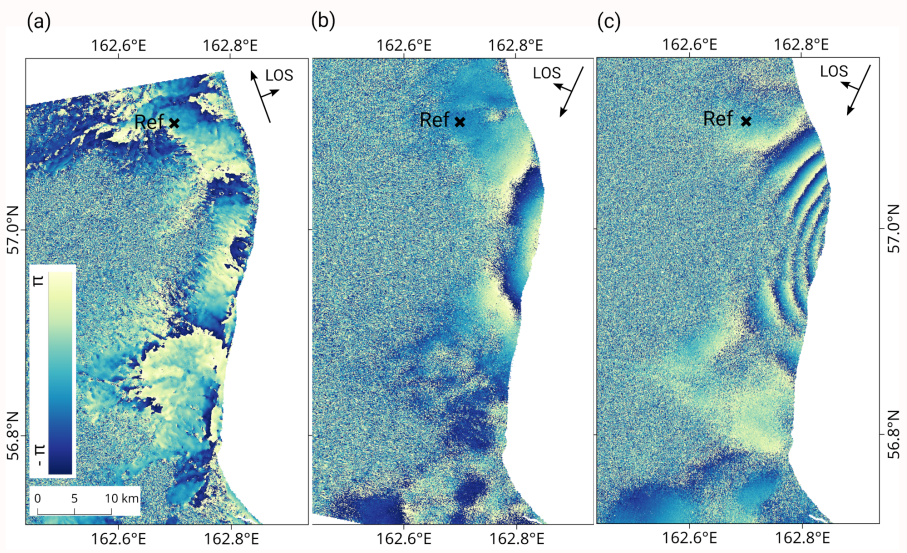


Figure 6.4: SAR interferometric images showing the coseismic displacement; each 2π cycle ("fringe") corresponds to the displacement (d) of half the wavelength of the radar signal in the line of sight (LoS) direction $\Delta\varphi = 4\pi \times d/\lambda$: (a) ALOS-2 asc. ($\lambda/2 = 12$ cm), (b) ALOS-2 desc. ($\lambda/2 = 12$ cm), and (c) Sentinel-1 desc. ($\lambda/2 = 2{:}8$ cm). Reference point used to transform the phase-wrapped displacement into absolute values is symbolized by black cross. The color version of this figure is available only in the electronic edition.

tern of the concentric to the coast displacement field clearly shows that the seismic source was located offshore. Motions of the ground toward the sensors were detected from both acquisition geometries, corresponding to uplift and westward movements. The maximum LoS displacement in the ascending orbit was 19 cm, whereas in the two descending orbit acquisitions, it is approximately 15 cm for Sentinel-1A and 19 cm for ALOS-2 (see Fig. 6.5). The observations from three different projections of the displacement vector allowed us to perform a 2D decomposition in the vertical and east–west directions, which show a maximum uplift of approximately 20 cm and a horizontal westward motion of approximately 7 cm (see supplemental material). The two ALOS-2 acquisitions, which include several months after the earthquake, are affected by postseismic deformation (see Fig. 6.2). An additional descending ALOS-2 interferogram was processed using radar scenes acquired on 27 June 2016 and 26 June 2017 to evaluate possible aftershock contributions. The residuals between the two ALOS-2 descending displacement maps show that the postseismic displacement is irrelevant, and thus the aftershock contribution may be neglected (see supplemental material).

6.3.3 Geodetic modeling and results

The three DInSAR datasets were jointly inverted using a two-step inversion procedure: first, a nonlinear inversion to define the source geometry and rupture mechanism and, second, a linear inversion to retrieve the slip distribution on the previously modeled fault plane. Both inversion steps were carried out using the least-squares approach. The overall modeling was conducted with the SARscape modeling module. As a preliminary stage, the datasets were subsampled in a regular grid using two different sampling densities of 150

and 500 m over the area affected by the maximum displacement and the surroundings, generating a set of approximately 3000 points. The first inversion step is a nonlinear inversion of the DInSAR displacement measurements assuming single rectangular uniform dislocation in a homogeneous and elastic half-space (Okada, 1985). The Levenberg–Marquardt least-squares algorithm (Marquardt, 1963) was applied to solve the optimization problem and implemented with multiple restarts to guarantee that the global minimum of the least-squares misfit between the model and observations is reached. The following cost function (CF) is minimized:

$$CF = \sum_{i=1}^{n} W_d \frac{1}{N} \sum_{i=1}^{n} \frac{(d_{iobs} - d_{imod})^2}{\sigma_i} \tag{6.1}$$

in which n is the number of datasets, W_d is the dataset weighting coefficient, N is the number of sampling points, d_{iobs} and d_{imod} are the observed and modeled displacement of the ith point, and σ_i is the standard deviation for all points (Atzori et al., 2009). We adopted the same weighting coefficient of 1 for all three datasets.

The focal mechanism derived from seismological data was used to define the initial parameter intervals, whereas length and width intervals were chosen in agreement with the empirical magnitude–area scale laws (Wells and Coppersmith, 1994).

Based on structural geology and geophysical data (Geist and Scholl, 1994; Gaedicke et al., 2000; Kozhurin et al., 2006), we assumed a west-dipping fault plane for the inversion. A global minimum of the square misfit and, therefore, the best fit between the model-predicted deformations and the three DInSAR datasets, is easily reached under the hypothesis of north–northwest reverse or oblique dipping. To facilitate the inversion process, we fixed the maximum slip to 2.5 m, in agreement with the empirical magnitude–slip scale laws (Wells and Coppersmith, 1994). Under the aforementioned conditions, the geodetic moment of the best-fit solution is consistent with the seismic moment 8:75 $\times$ 10 8 N $\cdot$ m, equivalent to a magnitude Mw 6.59. The overall root mean square (rms) misfits between the DInSAR data and the model-predicted deformation for a uniform slip patch are approximately 12, 6, and 3 mm for ALOS-2 ascending and descending and Sentinel-1A descending datasets, respectively.

In contrast to seismic solutions from the local and global seismological centers, which indicate the location of the earthquake being onshore or approximately 20 km offshore close to Pokaty Canyon, the location of the center of the fault retrieved from the first inversion step is approximately 5 km offshore. To check the location of the source, we constrained the coordinate intervals first closer to Pokaty Canyon, as suggested by the Global CMT centroid solution and the local seismic epicenter solution. Under the aforementioned conditions, the model cannot fit the observed displacement fields well, and the rms increases to approximately 24, 19, and 17 mm for ALOS-2 ascending and descending and Sentinel-1A descending datasets, respectively. Moreover, the geodetic moment is much higher than the seismic moment (1:66 $\times$ 10 9 N $\cdot$ m, equivalent to a magnitude Mw 6.78). We performed a second inversion by constraining the centroid location inland as suggested by the rest of the seismological centers. This also led to higher geodetic moment as compared to the seismic moment (1:41 $\times$ 10 9 N $\cdot$ m, equivalent to a magnitude Mw 6.73), although the model–observations misfit is lower (the rms values are approximately 12, 7, and 5 mm for ALOS-2 ascending and descending and Sentinel-1A descending datasets, respectively). Moreover, the estimated geometric parameters are not consistent with the empirical magnitude–area scale laws, as the estimated width of the fault plane is much

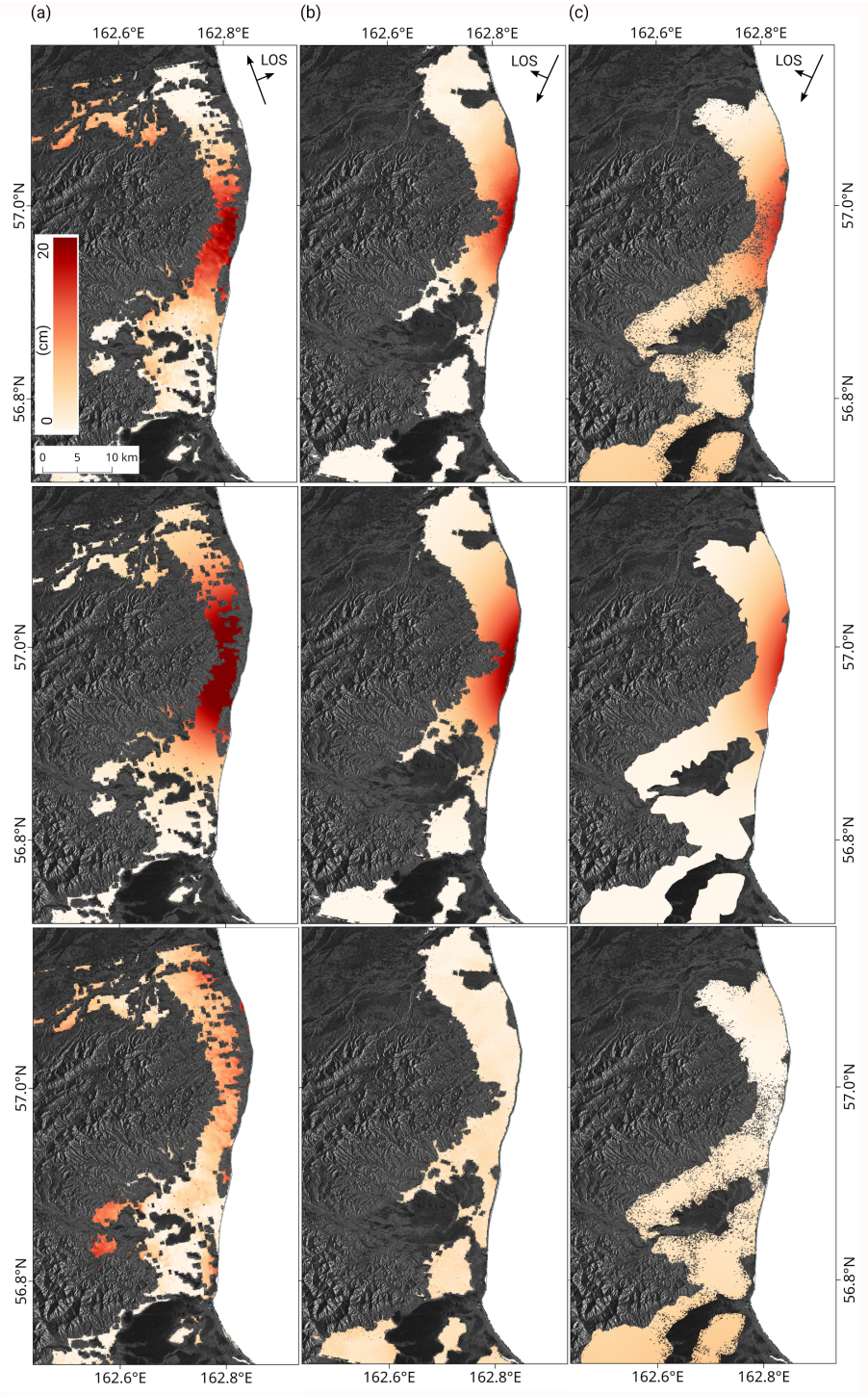


Figure 6.5: From top to bottom, ground displacement observed along the LoS, model-predicted displacement of best-fit slip-fault-plane solutions from the nonlinear inversion projected in LoS direction and respective residuals for (a) ALOS-2 asc., (b) ALOS-2 desc., and (c) Sentinel-1 desc. datasets. The color version of this figure is available only in the electronic edition.

larger than the respective estimated length. For the aforementioned reason, we excluded that the centroid's location is further offshore or inland. Finally, we also performed the modeling by assuming an east-dipping fault plane. Under this condition, we obtained a southeast-dipping thrust fault characterized by an approximately 22° dip angle and located approximately 5 km offshore, similar in location to the west-dipping assumption. The model fits the observations quite well (the rms values are approximately 12, 6, and 4 mm for ALOS-2 ascending and descending and Sentinel-1A descending datasets, respectively). However, the geodetic moment for the east-dipping fault is lower than the seismic moment ($7{:}57 \times 10\ 8$ N · m, equivalent to a magnitude Mw 6.55). Therefore, based on this final outcome and on the structural geology, we excluded the hypothesis of east-dipping fault.

The final fault model parameters are reported in Figure 4. The best-fit model suggests a shallow northwest-dipping reverse rupture with a right-lateral component. The three model-predicted deformations and respective residuals are shown in Figure 5. The residual signal is almost absent in the two descending geometries and indicates that no secondary fault structures were activated following the mainshock. The residual signal in the ascending geometry is higher and most likely related to temporal decorrelation errors due to the 1 yr temporal baseline.

To estimate the source parameter uncertainties and the parameter trade-off related to the propagation effect of noise in the DInSAR data, we solved the nonlinear inversion optimization for 120 independent samplings by adding to the initial datasets a certain correlated noise, which was estimated based on the interferometric data covariance in an area of the interferogram in which displacement is expected to be null (Cervelli et al., 2001; Sudhaus and Sigurjón, 2009). Source model parameters, covariances, and uncertainty intervals reporting the parameters' best fit, mean, and standard deviation values are shown in Figure 6a and Table 2. Compared to studies in which the deformation field of a fault is completely covered by DInSAR (Pedersen et al., 2003; Motagh et al., 2015), the standard deviation values that we derived for geometrical parameters, for example, length and width, are relatively large. This result is not surprising because the displacement field detected by geodetic measurements in offshore fault systems covers only the coastal area, and we have no information on what occurred under water (Motagh et al., 2008; Biggs et al., 2009; Hooper et al., 2013). However, the source location is quite well constrained, and the standard deviations of the east and north coordinates are approximately 1 km. The obvious trade-off between the dislocation area and slip is not visible as the maximum slip value was fixed in agreement with the empirical magnitude–slip scale laws to facilitate the nonlinear optimization. A significant trade-off is visible between the spatial coordinates and the dislocation geometry orientation (strike, dip, and rake) and between the plane dip angle and the source depth.

Once the fault geometry was modeled for a uniform slip, we divided the fault plane into 1 km 2 quadratic patches. We solved the linear inversion with respect to the slip using the non-negative least-squares algorithm (Lawson and Hanson, 1995) and considering a fixed rake direction of 109°. We extended the fault plane length to 30 km and width to 20 km to eliminate border effects. A smoothing Laplacian operator (∇^2) was applied, weighted by an empirical coefficient k of 0.001, to correlate the slip values of the neighbouring subareas. The slip distribution was obtained for each patch by linearly inverting the system:

$$\begin{bmatrix} Alos_{asc} \\ Alos_{desc} \\ S1_{desc} \end{bmatrix} = \begin{bmatrix} \mathbf{G} \\ k\nabla^2 \end{bmatrix} \mathbf{s} \tag{6.2}$$

in which $\mathbf{G}$ is Green's matrix and $\mathbf{s}$ is the slip model vector (Harris and Segall, 1987; Wright et al., 2003; Motagh et al., 2006). The centered dot represents the dot product.

The main dislocation region corresponds to an area of approximately 11 × 10 km, at a depth interval between 6 and 14 km (see Fig. 6.6b,d). The maximum slip is approximately 2.7 m at a depth of 10 km. The geodetic moment released from the distributed slip is 9 × 10 18 N · m, equivalent to Mw 6.6. The overall rms misfits between the DInSAR data and the model-predicted deformation in the linear inversion are, as in the nonlinear inversion, approximately 12, 6, and 3 mm for ALOS-2 ascending and descending and Sentinel-1A descending datasets, respectively.

In the case of linear inversion, it is much more difficult to compute and visually represent the slip distribution uncertainty because it must be computed for a large number of parameters equivalent to the number of patches and taking into account the propagation effect of the noise in the InSAR data and the uncertainty of the geometric fault parameters previously modeled. In this study, we obtained uncertainty related only to the data noise propagation by considering a fixed source geometry. The complete uncertainty covariance matrix is calculated as (Atzori et al., 2008)

$$[cov_m] = \mathbf{G}^{-g}[cov_d]\mathbf{G}^{-gT} \tag{6.3}$$

in which $\mathbf{G}^{-g}$ is the generalized inverse matrix, $[cov_d]$ is the interferometric data covariance, and $[cov_m]$ is the N × N symmetric parameter covariance matrix, in which N is the number of patches with diagonal equivalent to the slip variance for each patch, while off-diagonal values correspond to the covariance between two different patches. Figure 6c shows the slip distribution standard deviation for each patch, which is on the order of 1–3 cm. It is important to highlight that this is only the variance diagonal of the covariance matrix, and, therefore, it does not account for the slip correlations between different patches.

6.4 Discussion

A correct geodynamic interpretation in complex tectonic settings in which several structures interact with each other can be achieved only if the active fault location can be constrained as accurately as possible. The use of both seismic and geodetic data helps to improve the location accuracy (Elliott et al., 2010; Xu et al., 2010; Li et al., 2011; Fielding et al., 2013), although the presence of seismic stations and ground geodetic instruments is scattered in many remote and difficult-to-access regions. In this regard, the DInSAR satellite geodetic technique is a valuable tool for geodetic data measurement over large areas and for geodetic modeling of the seismic source (Wright et al., 2003; Biggs et al., 2006; Nissen et al., 2019).

In our case study, the regional seismic stations have an inhomogeneous distribution and poor coverage in the northern part of the peninsula exactly in which the Yuzhno-Ozernovskoe earthquake occurred. Moreover, the available ground geodetic instruments are sparse and far from the area of displacement; therefore, DInSAR measurements are

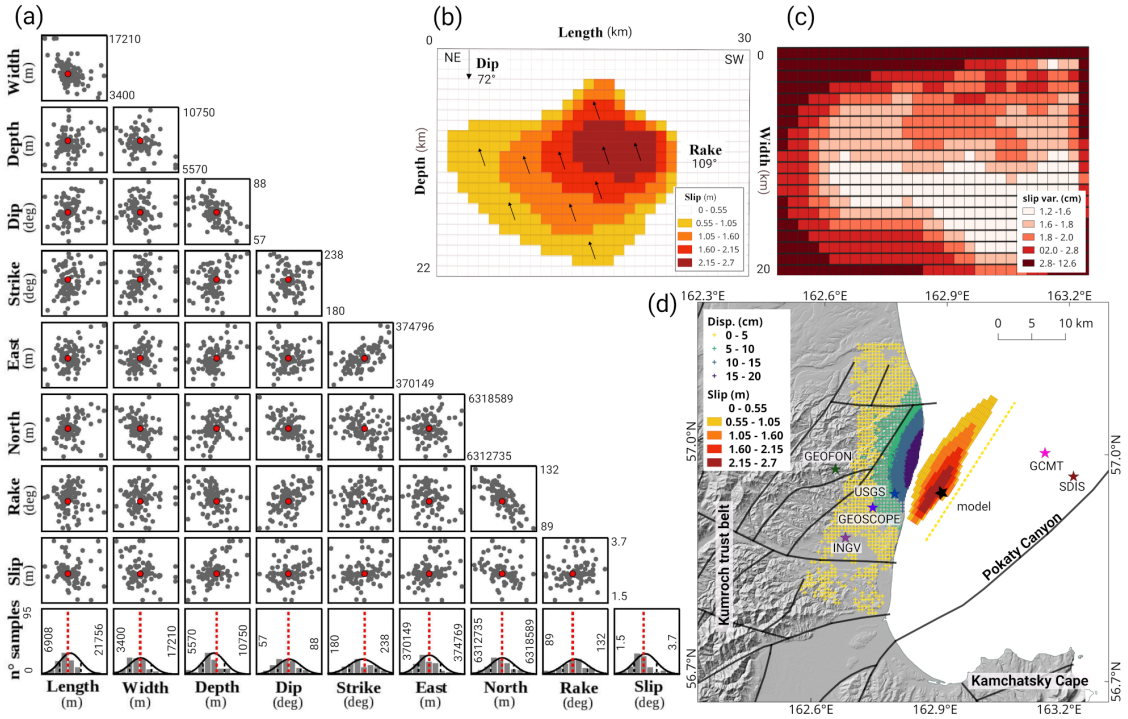


Figure 6.6: (a) Uncertainty analysis for the nonlinear inversion by performing 120 independent optimizations added to the data-correlated noise: standard deviations and parameter trade-off are shown; (b) slip distribution estimated from the linear inversion: the image shows the hanging wall relative to the footwall; slip magnitude is expressed by color scale; (c) slip distribution variance values; (d) fault model plane projected on the ground; star symbols show the epicenter or centroid locations from the different seismic and geodetic solutions (see Data and Resources); the main local fault system is shown by black lines; surface projection of the fault model is shown by light dotted line. The color version of this figure is available only in the electronic edition.

the only geodetic available data covering the region of interest. Because of the snow cover, temporal decorrelations, and low SNR, it was essential to apply interferometric phase filtering during the interferometric processing to enhance the signal and improve the readability of the deformation field.

With regard to the geodetic modeling, an essential aspect to take into account is the dependency of the source model on the initial source parameter intervals and constraints. The optimization algorithm may lead to completely different global minimum values and thus also to geophysically unrealistic source models. Moreover, the ambiguity of the seismic-based focal mechanism solution leads to the definition of two equally probable nodal planes. It is fundamental at this initial step to use all geological and geodynamic knowledge and the empirical param- eter scale laws to set up the most appropriate initial conditions. In our study, we used the seismic solutions to define the initial intervals for the nonlinear inversion. The fault model that best fits the three displacement observations and that is characterized by a geodetic moment compatible with the seismic one has the following initial conditions: (1) north-northwest dip, (2) reverse or oblique movement, and (3) maximum uniform slip of 2.5 m. The fault model parameter uncertainties and parameter trade-offs were estimated by considering the propagation effects of noise in the DInSAR

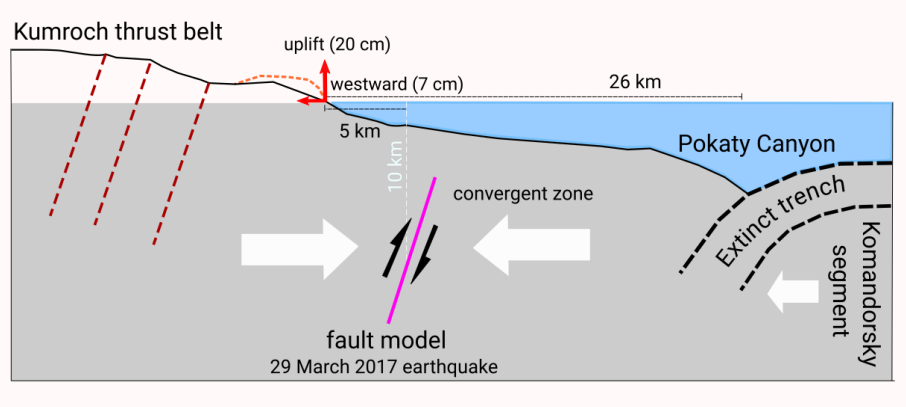


Figure 6.7: Conceptual diagram of the geodynamic interpretation of the 29 March 2017 earthquake fault model (not to scale). The color version of this figure is available only in the electronic edition.

data. The results show that the source location (east, north, and depth) is quite well constrained with an accuracy of approximately 1 km, although what seems less constrained is the fault size, as the derived accuracy of the length and width is approximately 2.4 km. However, considering that length and width are approximately 10 km, an accuracy of 2.4 km is well acceptable. The slip distribution variance was also estimated; however, the method used only takes into account the propagation effect of noise in the InSAR data, without considering the propagation effects of the fault model parameter uncertainties and the correlations between the different patches. The slip distribution variance obtained is of the order of 2-3 cm.

Our final fault model is consistent with the type and orientation of the source derived from seismic data, although there are two main discrepancies related to the fault location and dip angle. From local seismic data, the epicenter was located approximately 20 km offshore, close to the Global CMT centroid location. These two solutions could suggest that the rupture occurred on a fault coincident with Pokaty Canyon or part of the extinct trench. However, based on the DInSAR coseismic measurements, we obtained that to generate such onshore deformations a much higher magnitude earthquake is required. The other seismic solutions locate the epicenter onshore on Kumroch Ridge. However, under this constraint, we obtained an unrealistic fault plane geometry. The concentric fringe pattern of coseismic deformation on the coast, in fact, is an explicit indicator that the fault plane is most likely to be located offshore (Motagh et al., 2008). We also tested the hypothesis of an east-dipping fault plane. Under this condition, the geodetic moment obtained for the best-fit source model is lower than the seismic moment, indicating that for the east-dipping plane, a lower magnitude earthquake would have been responsible for the measured coseismic deformations.

Our detailed reconstruction of the regional fault system based on currently available studies (Ponomareva et al., 2007; Timofeev et al., 2012; Hindle et al., 2019) and Russian geological data (see Data and Resources) allowed us to interpret the retrieved new fault as part of an offshore prolongation of the Kumroch Ridge, which in recent studies (Kozhurin et al., 2006; Kozhurin and Zelenin, 2017) is considered part of a larger fault system named the east Kamchatka fault zone. The steep dip angle indicates that the rupture did not occur at the edge of the Pacific subduction slab, which dips at an angle of approximately

35°. The northwest-dipping fault and the reverse mechanism with consequent uplift and westward ho

6.5 Conclusions

In this study, we investigate the potential of DInSAR for understanding complex tectonic settings in which ground geodetic observations are absent and seismic stations are not well distributed. The coseismic displacement produced by the 29 March 2017 Mw 6.6 South-Ozernovskoe Kamchatka earthquake is successfully detected from multisensor and multi-orbit DInSAR measurements. Three independent SAR datasets, ALOS-2 ascending and descending and Sentinel-1A descending, are processed and jointly inverted using an elastic half-space fault model.

An uplift of approximately 20 cm and a westward displacement component of approximately 7 cm were induced by the earthquake on the coast north of Kamchatsky Cape. The final fault model suggests a crustal reverse fault with a right-lateral component, located approximately 5 km offshore, dipping northwest at an angle of 72°, and producing a maximum slip of 2.7 m at a depth of approximately 10 km. The seismic moment released from the distributed slip is estimated to have been 9×10 18 N · m, equivalent to Mw 6.6. The fault model suggests that the rupture occurred on a fault system that is the offshore extension of the Kumroch thrust belt. This earthquake provides evidence for neotectonic activity related to the arc-continental collision process. Moreover, the Kumroch thrust belt can be considered part of the east Kamchatka fault zone, a larger active fault system stretching over two-thirds of the Kamchatka peninsula. In addition, our fault model confirms that the fault system extends farther north, likely to the Okhotsk microplate boundary with the North American plate. The outcomes of this research demonstrate that the area north of the Pacific slab subduction zone, which had long been considered aseismic, is characterized by higher seismic and tsunamigenic hazards than previously thought. In general, we provide evidence for the great potential of using InSAR techniques for better insight into complex tectonic settings, especially in remote and difficult-to-access regions.

6.6 Acknowledgment

The authors thank the Japanese and European Space Agency for Advanced Land Observation Satellite (ALOS)-2 and Sentinel-1 satellite radar data, respectively, and all the seismological agencies (Global Centroid Moment Tensor Project, the U.S. Geological Survey, GEOFOrschungsNetz, National Institute of Geophysics and Volcanology, Global Network of Broadband Seismic Stations, and Seismological Data Information System of Kamchatka Branch of Geophysical Survey of Russian Academy of Sciences Earthquakes Catalogue for Kamchatka and the Commander Islands [1962–present]) for the earthquake mechanism parameter values used to set up the initial model parameter intervals. The authors thank the Geological Research Institute of the Ministry of Natural Resources and Ecology of the Russian Federation (Federal Agency of Mineral Resources, Russia) for the geological data. The authors thank Harris Geospatial Solutions, Inc., and sarmap for developing and providing SARscape version 5.4.1 (v.5.4.1) module in the Environment for Visualizing Images (ENVI) platform used to perform the main processing steps. The authors thank QGIS project for providing the geographic information system tool used in this work.

7 Cyclical geothermal unrest at Fagradalsfjall volcano

This chapter includes the co-author contributions published as:

Ólafur G. Flóvenz, Rongjiang Wang, Gylfi Páll Hersir, Torsten Dahm, Sebastian Hainzl, **Magdalena S. Vassileva**, Vincent Drouin, Sebastian Heimann, Marius Paul Isken, Egill Á. Gudnason, Kristján Ágústsson, Thorbjörg Ágústsdóttir, Josef Horálek, Mahdi Motagh, Thomas R. Walter, Eleonora Rivalta, Philippe Jousset, Charlotte M. Krawczyk and Claus Milkereit. **Cyclical geothermal unrest as a precursor to Iceland's 2021 Fagradalsfjall eruption.** *Nature Geoscience* 15, 397–404 (2022), doi.org/10.1038/s41561-022-00930-5

This work was part of a scientific task-force led by the German Research Centre for Geosciences (GFZ) and the Iceland GeoSurvey (ÍSOR) established to investigate the 2020 geothermal unrest in Iceland using a multi-disciplinary approach. InSAR, together with seismic and gravitational data, constituted the core dataset to build a model of the potential ground deformation source and provide insight into the interaction between volcanic processes and geothermal systems. The importance of this co-author's contribution to the PhD research is to demonstrate how InSAR observation can be used in a multi-disciplinary approach and when in-situ measurements such as seismic and gravitational stations are available.

Some changes were applied with respect to the original publication: Abstract and Introduction (original chapter Main) are unchanged; a chapter InSAR Data and Method was added (original Methods-InSAR data processing); a new chapter Results was created which includes the subchapters Transient deformation at the Svartsengi HT field (original chapter Transient deformation at the Svartsengi HT field), Free-air gravity change and Elastic (original chapter Free-air gravity change), Seismicity (original chapter Seismicity) and Elastic poroelastic models (adapted after original chapter Models of pre-eruptive processes - the proposed conceptual model discusses in the second half of this chapter was not included).

Author contribution statement:

As one of the main co-authors, my contribution to the work is related to MTI analysis and elastic source modeling. Regarding these parts, it includes methodology development, inversion source modeling (Mogi and Okada), SAR data collection, MTI data processing, validation, interpretation, writing the original draft, reviewing and editing successive manuscript versions and visualization. Rongjiang Wang performed the poroelastic modeling. Ólafur G. Flóvenz and Torsten Dahm were coordinating the work. All other contributions can be seen in the original paper (under Contributions).

Method summary:

In this work, MTI analysis was performed to detect the geothermal cyclic unrest. Sentinel-1 (ascending and descending orbit paths) SAR acquisition dataset was used. Ascending and descending InSAR datasets were jointly inverted to derive the best-fit point and rectangle dislocation elastic source models. Additional poroelastic model contributed to better explaining the material of the observed ground deformation. Main conclusions about the influence of magma and gas intrusion on geothermal unrest were finally derived based on the results.

Supplementary Material:

Supplementary material was not included in the chapter and can be found on the following link under the voices Extended Data and Supplementary information.

7.1 Abstract

Understanding and constraining the source of geodetic deformation in volcanic areas is an important component of hazard assessment. Here, we analyse deformation and seismicity for one year before the March 2021 Fagradalsfjall eruption in Iceland. We generate a high-resolution catalogue of 39,500 earthquakes using optical cable recordings and develop a poroelastic model to describe three pre-eruptional uplift and subsidence cycles at the Svartsengi geothermal field, 8 km west of the eruption site. We find the observed deformation is best explained by cyclic intrusions into a permeable aquifer by a fluid injected at 4 km depth below the geothermal field, with a total volume of 0.11 ± 0.05 km3 and a density of 850 ± 350 kg m^{-3}. We therefore suggest that ingression of magmatic CO2 can explain the geodetic, gravity and seismic data, although some contribution of magma cannot be excluded.

7.2 Intruduction

Our results demonstrate that inflation and deflation cycles with periods of several months over scales of tens of square kilometres commonly observed in volcanic systems around the world can be caused by the migration of deep magmatic fluids and gases into upper crustal hydrothermal systems. It highlights the interaction of volcanic processes and the behaviour of geothermal systems to address hazard assessments.

Recent volcanic and seismic unrest with surface deformation at the Reykjanes Peninsula (RP) plate boundary in southwest Iceland, in and around the Svartsengi high-temperature (HT) field (Fig. 1), reveals a previously unexplored cyclic interaction of tectonic spreading, magmatic reservoirs and supercritical magmatic fluids with hydrothermal reservoirs.

On 22 January 2020, an earthquake swarm started 3 km east of Svartsengi. Simultaneously, uplift was recorded at the geothermal field close to the re-injection site (Flóvenz et al. 2021) of the power plant, followed by subsidence. Three such cycles of inflation and deflation occurred until July 2020, where each inflation was followed by continuous deflation and diminishing seismicity (Fig. 2c). Similar inflation started in August 2020 at the centre of the Krýsuvík HT field, 20 km east of Svartsengi (Fig. 1). In February 2021, crustal extension and an intense earthquake swarm revealed the formation of a northeast-striking magmatic dyke between the two HT fields, followed by the Fagradalsfjall eruption 8 km east of Svartsengi on 19 March 2021.

The spreading axis of the Mid-Atlantic Ridge comes on land at the southwest corner of the RP. There, it bends into a 60-km-long N 70 °E striking oblique plate boundary, expressed by a 5- to 10-km-wide seismic and volcanic zone, where large episodic earthquake swarms occur every 20–40 years (Björnsson et al. 2020) with magnitudes up to M 6, mostly on north–south trending strike-slip faults. Volcanic eruptions have occurred at intervals of 800–1,000 years during the past 4,000 years, the last one ending in AD 1240 (Sæmundsson et al. 2013). Each volcanic episode might last for one to three centuries, with basaltic lava flows from N 45° E-trending fissures extending into the adjacent plates (Sæmundsson et al. 2010). HT geothermal fields with reservoir temperature of 240–330 °C at 1–3 km depth (ref. De Freitas 2018) have formed at the intersection of the seismic zone and the main volcanic fissure swarms (Fig. 1). One well, IDDP-2 at the Reykjanes HT field (Fig.1), was drilled to 4.6 km depth (ref. Friðleifsson et al. 2020) close to the brittle–ductile transition (BDT) where bottom hole temperature is estimated to be about 600°C (ref. Bali et al.

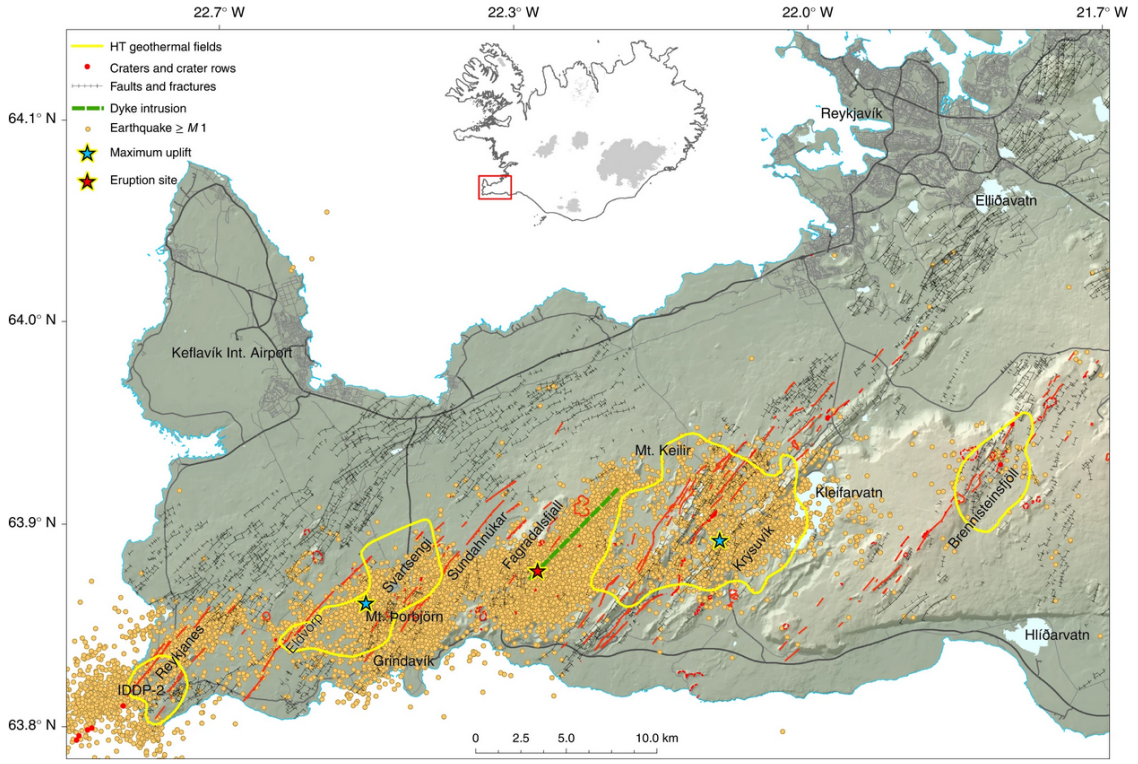


Figure 7.1: Overview of the tectonics and seismicity of the RP. The red and black fault lines denote postglacial volcanic eruption fissures and opening fissures, respectively. Yellow dots show the seismicity from September 2019 to May 2021. Yellow lines show the extent of the HT geothermal fields on the peninsula, according to resistivity measurements1. Only the Reykjanes and Svartsengi geothermal fields are currently operated. The blue stars indicate the centres of uplift in Svartsengi and Krýsuvík, and the red star indicates the 2021 eruption site at Fagradalsfjall. The dashed green line shows the northeast-striking magmatic dyke intrusion according to InSAR analysis and seismicity. Main roads are in black, and topography is indicated as coloured background. Main landmarks referenced in the text are shown on the map.

2020) just beneath a hydrostatic pressurized aquifer (~35 MPa). Corresponding results were obtained in the IDDP-1 well at the Krafla HT field in North Iceland. The crust above the aquifers is in both cases fully elastic, and the fluid pressure in the rock is hydrostatic down to the BDT.

The upper crust of the RP is approximately 4.5 km thick (Pálmason 1971, Flóvenz 1980, Weir et al. 2001) and composed of basaltic extrusives with a downward-increasing alteration and a higher proportion of intrusives. The lower crust down to Moho at ~15 km depth is thought to be made of intrusives with no evidence of melt (Weir et al. 2001, Hersir et al. 2020, Karlsdóttir et al. 2020). The BDT is generally at 6–7 km depth beneath the RP, rising up to 4–5 km depth below the HT fields(Blanck et al. 2020, Kristjánsdóttir 2013, Gudnason et al. 2021) with an estimated temperature of ~600 °C (Flóvenz et al. 2021, Bali et al. 2020, Ágústsson and Flóvenz 2005, Violay et al. 2012).

The 76 megawatt electricity (MWe) power plant at the Svartsengi HT field and the Blue Lagoon Spa (Extended Data Fig. 1) are the heart of the Geothermal Resource Park, providing electricity and hot and cold water to 25,000 residents and local industries

(Albertsson and Jónsson et al. 2010). The average annual production rate is about 0.45 m3 s^{-1}, of which about 0.3 m^3 s^{-1} is re-injected into the reservoir. These re-injection rates are an order of magnitude smaller than the rates needed to explain the observed uplift in 2020.

The cyclic deformation and earthquake activity at two distinct HT fields at the RP plate boundary and the time lag before a distant fissure eruption is unusual and was previously not observed. Using a comprehensive modelling approach, we show that the ascent of magma-derived volatiles into a sealed aquifer above the BDT beneath the Svartsengi HT field can explain the uplift and subsidence cycles and can be interpreted as a precursor to a coming eruption.

7.3 InSAR Data and Method

We exploited the Copernicus Sentinel-1A and 1B satellite SAR data, which are available over Iceland in ascending (8 January to 15 December 2020) and descending (6 January to 13 December 2020) orbits with a revisit time of six days for each track. The time-series analysis was carried out using the Small Baseline Subset algorithm38, implemented in SARscape, which is based on the combination of interferograms characterized by small, normal and temporal baselines, maximizing spatial and temporal coherence and therefore the quality of the interferograms (maximum temporal baseline 18 days), resampling with a multi-look of 7:2 for range and azimuth direction, respectively (Goldstein filter39 window size of 32 pixels, coherence threshold of 0.2, ground resolution of 30 m). The topographic phase contribution was subtracted using the ArcticDEM digital terrain model of 2 m spatial resolution. The InSAR time series was validated with data from a GNSS station provided by the IMO and available through the University of Iceland (IMO GPS data). Ascending and descending LOS displacement maps were combined to derive the vertical and the east–west components of the ground motion.

7.4 Results

7.4.1 Transient deformation at the Svartsengi HT field

Analysis of 12 months of satellite interferometric synthetic aperture radar (InSAR) time-series data supported by Global Navigation Satellite System (GNSS) data (Methods), processed in both ascending and descending configuration, reveals an elliptical area exceeding 80 km^2 affected by uplift and subsidence at Svartsengi, along with minor horizontal displacements (Fig. 2a and Extended Data Fig. 2). The major axis of the elliptical area is ~12 km long, striking N 60° E, and the perpendicular axis is 8.5 km long. The major axis follows the dominant strike of the geothermal reservoir (Extended Data Fig. 1) but deviates both from the N 45° E strike of volcanic fissures and the north to northeast trending strike-slip faults mapped at the surface on the RP.

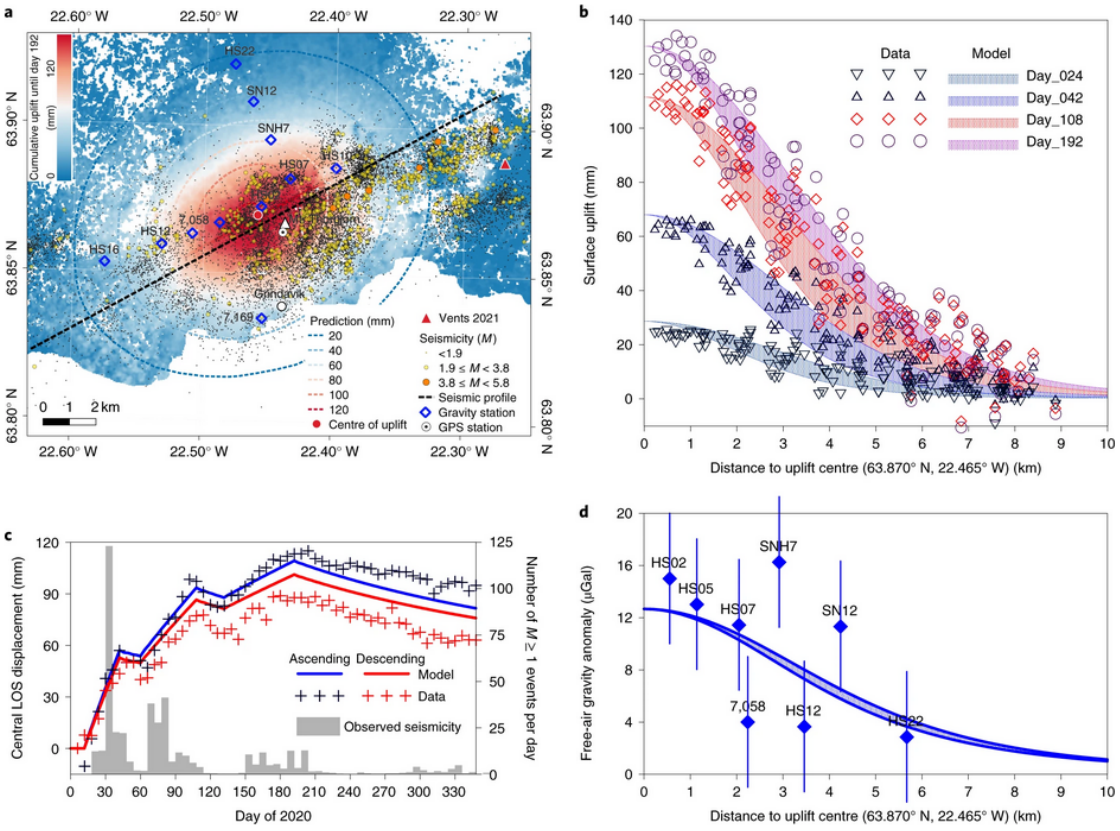


Figure 7.2: Results from the poroelastic model. **a**, Map of maximum cumulative uplift from 6 January to 17 July 2020 (day 192). The colour map shows the vertical component calculated by combining the ascending and descending line-of-sight (LOS) displacements, in comparison with the predicted uplift (dashed contour lines) based on the poroelastic model for the same time period. The GNSS time series from the station marked by the white with black dot circle was used for the InSAR validation. The centre of uplift is obtained from the Mogi source inversion. The dashed line shows the cross-section profile in Fig. 3a. The location of the Fagradalsfjall eruption is shown as a red triangle. **b**, Temporal snapshots of surface uplift derived from the InSAR data compared with the model predictions. The double model curves for each snapshot show the values along the major and minor axes of the elliptic uplift pattern. **c**, Comparison of the predicted and measured ascending and descending LOS displacements at the pixel nearest to the uplift centre. The grey bars show the observed seismicity rates within 5 km distance from the centre. **d**, Free-air gravity anomalies (blue diamonds) from campaign measurements between 27 January and 20 April 2020 compared with the model predictions (solid curves) along the major and minor axes of the elliptic uplift pattern. Estimated error (shown as vertical lines) is ±5 μGal.

The duration of successive uplift episodes increased while the uplift rate decreased correspondingly (Extended Data Fig. 3). The first episode had the highest uplift rate of 2.2 mm d^{-1} and a total uplift of 66 mm over 30 days (Fig. 2b). It was followed by 18 days of subsidence, totalling less than 10 mm. The second episode had an uplift rate of 1.1 mm d^{-1} and a total uplift of 55 mm over 48 days. It was followed by a faster subsidence episode lasting approximately 24 days, with a total subsidence of 16 mm. The final episode, with an uplift rate of 0.5 mm d^{-1}, produced a total uplift of 32 mm over 60 days. On 18 July, an earth-

quake of magnitude M 4.1 occurred near the inflation centre (https://skjalftalisa.vedur.is) (Extended Data Fig. 1). It was followed by a period of subsidence visible on InSAR until mid-December with an average subsidence rate of 0.2 mm d^{-1} and a total subsidence of 38 mm. The cumulative uplift observed at the centre of displacement was slightly less than 150 mm, and by December 2020 the actual uplift was reduced to 90 mm.

7.4.2 Free-air gravity change

Gravity provides additional insights as changes in gravity depend on the mass of the intruded fluids while deformation depends on volume change. We measured gravity in four consecutive campaigns (Supplementary Table 1) at 10–12 existing permanent stations along an L-shaped profile extending north and west from the centre of uplift (Extended Data Fig. 4).

The first campaign was conducted a week after the start of the first uplift episode and repeated shortly after the end of the second one. Measured gravity changes between the first and second campaign show a consistent free-air corrected gravity increase of 10–14 µGal around the centre of uplift (Extended Data Fig. 5 and Supplementary Table 1). A consistent free-air corrected gravity decrease of 4–8 µGal is observed at the uplift centre from April to October, during the third uplift episode and the following deflation. Between October 2020 and February 2021, the free-air corrected gravity decrease continues at most stations. The maximum decrease averaged over the three closest stations to the centre of uplift was 5 µGal.

To estimate the cumulative gravity increase, we need to account for the gravity changes during the first week and during the third uplift episode that were not directly covered by the gravity campaigns. This is done by assuming the same ratio of gravity increase to the uplift at the inflation centre (170 µGal m^{-1}) as measured during the first two uplift episodes. In addition, we corrected for the long-term background gravity decrease caused by the geothermal production. The resulting cumulative gravity increase of all three inflation episodes equals 27 µGal at the centre of uplift. However, 13 months after the start of the unrest period, the corrected net free-air gravity change was reduced to 14 µGal, implying that almost half of the intruded mass had disappeared or migrated away from the inflation centre.

7.4.3 Seismicity

To evaluate the background seismicity and the rate changes during the transient deformation, we used the national catalogue (Böðvarsson et al. 1999) of the Icelandic Meteorological Office (IMO). For a more detailed analysis of the spatio-temporal patterns during the unrest period, we created a new catalogue for the year 2020, using 26 seismic stations spaced up to 30 km around Svartsengi. For the first time, we integrated distributed acoustic sensing (DAS) data from a 21-km-long fibre-optic telecommunication cable buried 80–90 cm below the ground from the southern tip of Reykjanes to Grindavík, crossing the Svartsengi HT field20 (Extended Data Fig. 4). To detect and locate the smallest earthquakes, we modified a waveform stacking and migration method21 to combine seismic and continuous DAS data. The new and more complete catalogue covers the period from 1 February to 30 August. We detected 39,500 earthquakes with magnitudes of $M > -1$, that is, a factor of 1.9 more events, and localized the majority automatically. The locations have high quality, both laterally and vertically, since sensors and DAS cable were

located directly above the uplift zone, and the azimuthal distribution of all stations was unusually good.

Seismicity shallower than 4 km depth occurs mainly within the elliptical uplift region, with the shallowest events at the centre of uplift (Fig.3b and Extended Data Fig.6). This suggests that many of these earthquakes are triggered by elastic bending stresses in the roof above the aquifer. The absence of earthquakes deeper than 4 km depth at the uplift centre supports the hypothesis of an updoming BDT rising from 6–7 km depth (Fig. 3).

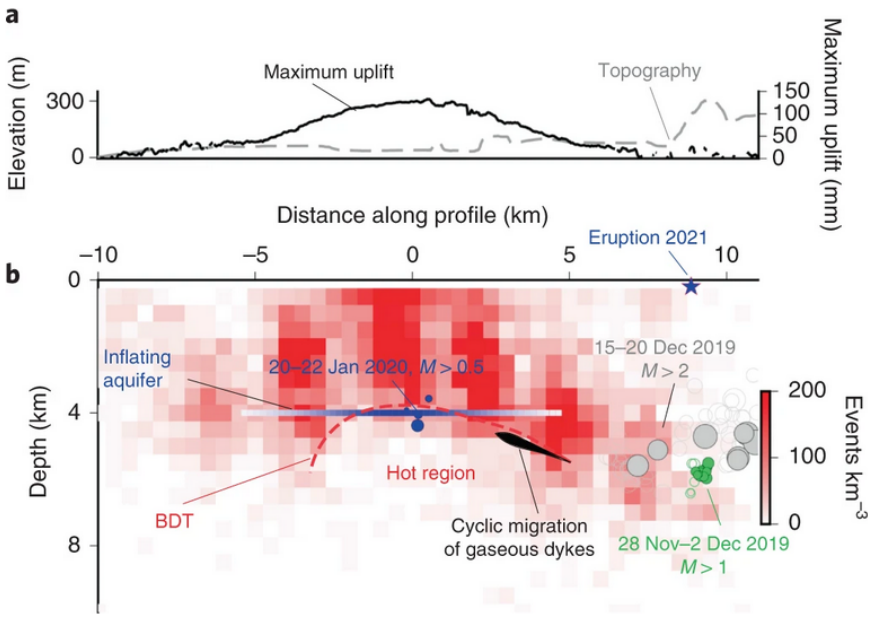


Figure 7.3: Sketch of fluid migration paths and aquifer location compared with observed seismicity and uplift. **a**, Maximum uplift (solid black line) and topography (dashed grey line) along the profile in Fig. 2a (x = 0 at Mt. Thorbjörn). **b**, Density of micro-earthquakes between February and August 2020 (gridded file and colour scale) estimated in a 1-km-wide band along the profile. The inferred BDT is indicated by the red dashed line. The manually relocated, largest events from the earthquake swarms from November (green circles) and December 2019 (grey circles) and at the beginning of unrest at Svartsengi (blue circles) are shown. The position and source intensity of the aquifer model are indicated.

7.4.4 Elastic and poroelastic models

The deformation pattern suggests an inflation source at depth. We first tested an isotropic point-source (Mogi) model (Mogi 1958 and Lisowski 2007) to retrieve information about the source location, depth and strength. For the three uplift episodes, the best-fitting parameters from inversion of the InSAR data result in source depths ranging from 4.0 to 4.9 km with horizontal location differences within 330 m. The inferred volume changes are estimated to be 4.70, 3.55 and 2.75×10^6m^3, respectively, and cumulatively explain over 90% of the observed deformation (see Tab. 1).

To better match the elliptical shape of the uplift pattern, we also tested rectangular dislocation models (Okada 1985). The uplift episodes can be modelled by three 10-m-thick, 7- to 9-km-long and 30- to 50-m-wide nearly horizontal intrusions at a depth between 3.7

and 4.4 km, with an average strike of N 60° E. However, the subsidence rate after each uplift episode seems too fast and large (Fig. 2c) to be explained by a cooling-related volume reduction of a magma intrusion. Similarly, it is difficult to explain the significant decrease of the free-air gravity observed in the central area following the uplift episodes. Furthermore, the induced change in Coulomb failure stress is concentrated directly around the presumed magma body and therefore cannot explain the triggered seismicity, which has been observed over a wider area (Fig. 4). Anomalously low Vp/Vs ratios are also observed in the lower crust beneath Svartsengi (Geoffroy and Dorbath 2008, Hobé et al. 2021), indicating gas-saturated porous rocks rather than partial melt. Analysis of ambient seismic noise before the unrest27 indicates a drop in S-wave velocities beneath Svartsengi, while a 1% temporary drop in seismic velocities is also reported during the unrest period at Svartsengi (Cubuk-Sabuncu 2021). In both cases, the observations can be explained by spatial or temporary changes in crack density without a need for magma involvement.

As an alternative, we employ a poroelastic model considering a strongly coupled diffusion and deformation process (Wang and Küumpel 2003). The domain consists of a thin, permeable, porous aquifer layer at a depth of approximately 4 km, embedded in a multi-layered poroelastic half-space. The elastic parameters are adopted from the seismic reference model used for earthquake locations. During the three uplift episodes, the aquifer is pressurized by a fluid intrusion (injection) along a N 60° E-trending line source with the strength of the fluid intrusion modelled by a Gaussian distribution with a standard deviation of 2 km. We inverted the InSAR data for the 12-month period of unrest, with fluid inflow during uplift and no inflow during subsidence. The resulting intrusion rates depend on the Skempton coefficient (B) used to describe how much of intruded fluid can be accommodated by the aquifer through a given pressurization. The smaller B, the more the intruded fluid volume (Extended Data Fig. 8). On the basis of previous interdisciplinary observations, including a realistic estimate of temperature, pressure and porosity within the aquifer, we estimate $0.08 \leq \mathrm{B} \leq 0.19$ as a realistic variation range for the assumed aquifer. Uncertainties in other parameters on the volume and density estimations are negligible compared with the effect of the uncertainty in the Skempton coefficient. (Supplementary Sheet 3). Accordingly, the total intrusion volume can be estimated realistically to be 0.07-0.16 km^3.

The fluid intrusion causes a poroelastic response resulting in surface deformation, fluid flow in the aquifer and the Coulomb stress changes on the fault planes. It explains the InSAR time series, particularly the rapid subsidence following each cyclic uplift.

The total mass of the intruded fluid, which best fits the campaign gravity data (Fig. 2d and Extended Data Fig. 5), is about 82 Mt. It yields a fluid density in the range of 500–1,200 kg m^{-3}. We estimate the range of pressure (P) and temperature (T) within the aquifer to be $110 < P < 50$ MPa and $350 < T < 600$ °C. These values imply that the intruded fluid could be water (≤ 670 kg m^{-3}), carbon dioxide (≤ 740 kg m^{-3}), supercritical sulfur dioxide or a mixture of gas and magma (2,700 kg m^{-3}) with maximum 33% volume ratio of the magma (Supplementary Sheet 3). Although re-injection of fluid from the power plant might comply with the density value, the re-injection rates are far too small to explain the observed volume and gravity change. Since both H2O and SO2 remain dissolved in magma until close to the surface (Sigmundsson et al. 2020), carbon dioxide is practically the only possible fluid candidate. Therefore, we conclude that the injected fluid is either pure CO2 or a CO2 mixture with up to 33% magma volume.

The poroelastic model also explains the seismic rate changes relative to the background activity. Specifically, we analysed the seismicity rate changes during the deformation relative to the average background rate between the years 2000 and 2020 in the region surrounding the deformation centre. The observed seismicity rate changes were compared with those predicted by a rate-and-state friction response (Dieterich 1994) based on the Coulomb failure stress changes calculated from the poroelastic aquifer model. The predicted seismicity changes (Fig. 4) are in good agreement with the observed spatio-temporal earthquake patterns, providing further evidence for the poroelastic aquifer model.

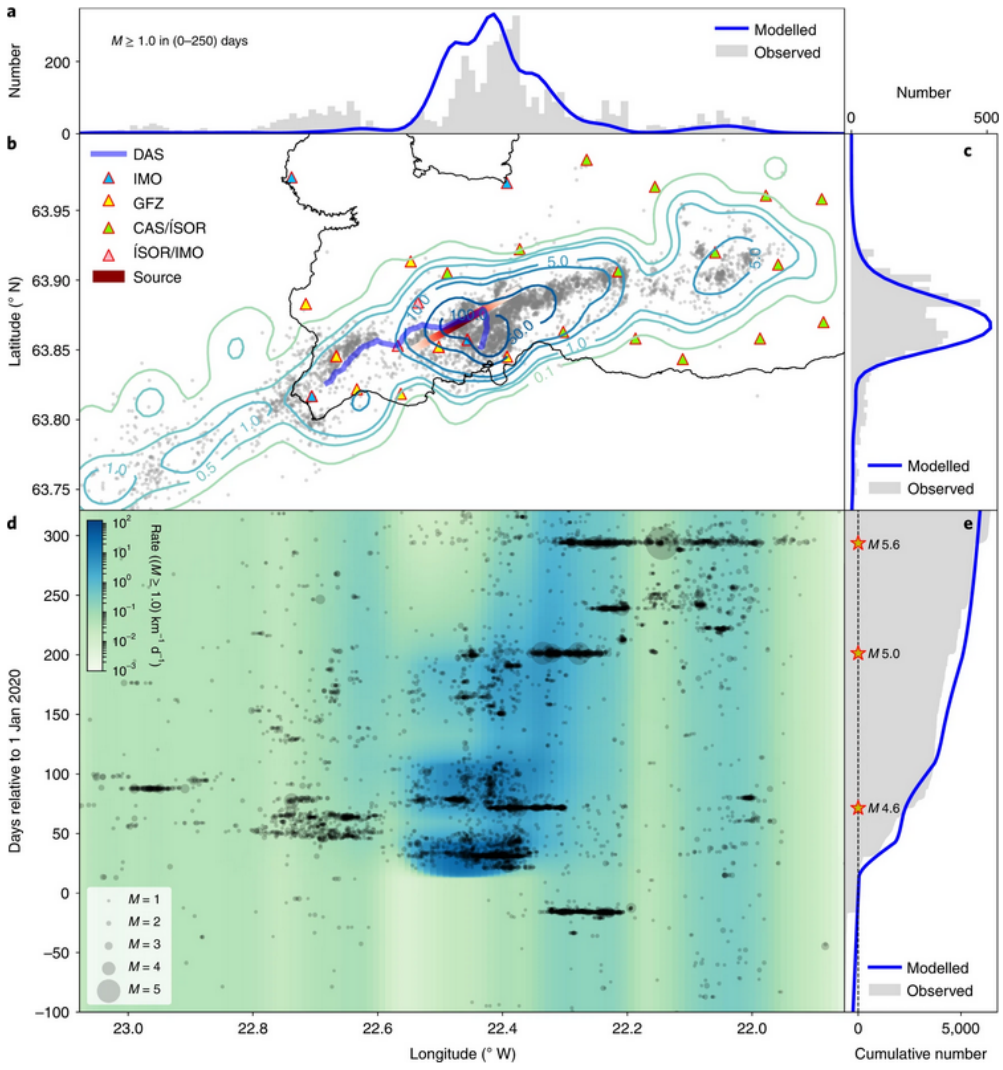


Figure 7.4: Sketch of fluid migration paths and aquifer location compared with observed seismicity and uplift. **a**, Maximum uplift (solid black line) and topography (dashed grey line) along the profile in Fig. 2a (x = 0 at Mt. Thorbjörn). **b**, Density of micro-earthquakes between February and August 2020 (gridded file and colour scale) estimated in a 1-km-wide band along the profile. The inferred BDT is indicated by the red dashed line. The manually relocated, largest events from the earthquake swarms from November (green circles) and December 2019 (grey circles) and at the beginning of unrest at Svartsengi (blue circles) are shown. The position and source intensity of the aquifer model are indicated.

7.5 Acknowledgment

The authors are grateful to all those who assisted to generate this article, including H. Geirsson, University of Iceland, for providing the time series of a permanent GNSS station, allowing us to control InSAR data; I. Þór Magnússon for collecting and processing the gravity data; Þ. Þórðarson, University of Iceland, and A. Hobé, Uppsala University, for useful discussions; E. Bali and G. H. Guðfinnsson, University of Iceland, for valuable assistance with the geochemical calculations; Mila Telecommunication Company for access to the fibre-optic cable; Iceland Met Office for the access to the earthquake catalogue, seismic waveforms and GNSS stations; and C. Wollin, K. Erbas and T. Reinsch for DAS assistance. The fieldwork of GFZ was part of a HART rapid response activity funded by GFZ. DEM(s) were created from DigitalGlobe, Inc., imagery and funded under National Science Foundation awards 1043681, 1559691 and 1542736. The work of M.P.I. was supported by the DEEPEN project (BMWI 03EE4018).

8 Flank collapse at Anak Krakatau volcano

This chapter includes the co-author contributions published as:

Edgar U. Zorn, **Magdalena S. Vassileva**, Thomas R. Walter, Herlan Darmawan, Leonie Röhler and Falk Amelung. **Interactions of magmatic intrusions with the multiyear flank instability at Anak Krakatau volcano, Indonesia: Insights from InSAR and analogue modeling.**. *Geology* (2023) 51 (4): 340–344., doi.org/10.1130/G50693.1

This work was part of a collaboration with the Physics of Earthquakes and Volcanoes Section at GFZ.

Some changes were applied with respect to the original publication: Abstract and Introduction are unchanged; a chapter InSAR data and method was added (original in Supplementary materialProcessing Methods); a new chapter Results was created which includes the subchapters Deformations on the southwest flank of Anak Krakatau (original chapter Deformations on the southwest flank of Anak Krakatau) and Interaction of flank motions and magma intrusions simulated in analogue experiments (original chapter Interaction of flank motions and magma intrusions simulated in analogue experiments). Discussion (original chapter Conjoint flank slip acceleration and volcanic activity increase) is unchanged.

Author contribution statement:

As one of the main co-authors, my contribution to the work is related to MTI analysis which includes methodology development, SAR data collection, MTI data processing, validation, interpretation, writing parts of the original draft, and reviewing and editing successive manuscript versions. Edgar U. Zorn is the main author and performed the analogue model. All co-authors contributed to the discussion, reviewing and editing of the manuscript.

Method summary:

In this work, MTI analysis was performed to detect the geothermal cyclic unrest. Sentinel-1 (ascending and descending orbit paths) SAR acquisition dataset was used. Ascending and descending InSAR datasets were jointly inverted to derive the best-fit point and rectangle dislocation elastic source models. Additional poroelastic model contributed to better explaining the material of the observed ground deformation. Main conclusions about the influence of magma and gas intrusion on geothermal unrest were finally derived based on the results.

Supplementary Material:

Supplementary material was not included in the chapter and can be found on the following link under the voices Extended Data and Supplementary information.

8.1 Abstract

Volcano flank collapses have been documented at ocean islands worldwide and are capable of triggering devastating tsunamis, but little is known about the precursory processes and deformation changes prior to flank failure. This makes the 22 December 2018 flank collapse at Anak Krakatau in Indonesia a key event in geosciences. Here, we provide direct insight into the precursory processes of the final collapse. We analyzed interferometric synthetic aperture radar (InSAR) data from 2014 to 2018 and studied the link between the deformation trend and intrusion occurrence through analogue modeling. We found that the flank was already moving at least 4 yr prior to collapse, consistent with slow décollement slip. Movement rates averaged ~27 cm/yr, but they underwent two accelerations coinciding with distinct intrusion events in January/February 2017 and in June 2018. Analogue models suggest that these accelerations occurred by (re)activation of a décollement fault linked to a short episode of magma intrusion. During intrusion, we observed a change in the internal faults, where the outward-directed décollement accelerated while inward faults became partially blocked. These observations suggest that unstable oceanic flanks do not disintegrate abruptly, but their collapse is preceded by observable deformations that can be accelerated by new intrusions.

8.2 Introduction

Tall volcanoes tend to become structurally unstable and experience catastrophic flank collapses, capable of producing major tsunamis if they enter the sea (Siebert, 1984; van Wyk De Vries and Francis, 1997). Persistent flank motion may precede complete failure, sometimes forming characteristic deformations, morphology, and faults at the surface (Poland et al., 2017), which may be followed by changing magma pathways (Maccaferri et al., 2017). Here, we investigated the preparation phase of a flank collapse at Anak Krakatau, Indonesia, which has a history of instability and produced at least eight tsunamis in the past (Paris et al., 2014; Hidayat et al., 2020). The most significant tsunami occurred in 1883 with the collapse of the Krakatau edifice, killing over 34,000 people on the shorelines of Southeast Asia. Renewed volcanic activity rapidly rebuilt the island afterwards, resurfacing as Anak Krakatau in 1927, which had reached a height of 320 m by 2018 (Ismail et al., 2020). Its southwest flank then collapsed on 22 December 2018 (Walter et al. 2019), producing another tsunami and killing 437 people around nearby shores (Syamsidik et al., 2020). A tsunami early warning system was installed and active in the area during the collapse (Lauterjung et al., 2010; Annunziato et al., 2019), but it was designed for earthquake-generated tsunamis and thus could not produce a warning. This highlights the need for alternative means to monitor flank instability prior to the occurrence of catastrophic failure.

Volcanic flank instability is often associated with gradual movement along a deep-seated basal décollement (van Wyk De Vries and Borgia, 1996; Byrne et al., 2013). Flank instability, intrusions, and volcanism may be closely related and even cause complex structural interactions (Delaney et al., 1998; Schaefer et al., 2019). Volcanoes with higher rates of magmatism generally show increased rates of flank motion (Poland et al., 2017), and earthquakes or magmatic intrusions may intermittently accelerate flank slip (Famin and Michon, 2010; Chaput et al., 2014; Schaefer et al., 2015), although this strongly depends on the depth of the intrusion (Cayol et al., 2000). On the other hand, ongoing décollement slip is

also known to favor further magmatic intrusions, which follow topographic stress (Varugu and Amelung, 2021). Understanding such short-term accelerations is vital, as they may culminate in catastrophic flank failure with potentially devastating consequences (Ward and Day, 2001; Abadie et al., 2012). Here, we compared new interferometric synthetic aperture radar (InSAR) data and experimental modeling on Anak Krakatau's destabilizing southwest flank preceding the December 2018 collapse. The results show how magmatic intrusions interact with a destabilizing flank, accelerating deformations that lead to catastrophic failure.

8.3 InSAR data and method

We measured the displacement flank evolution using multi-temporal InSAR technique and exploited the Sentinel-1 data in both ascending (orbit 171) and descending (orbit 47) acquisition orbit in the period between 08th Oct 2014 and 19th Dec 2018. We adopted the Small BAseline (SB) method as implemented in the ENVI SARscape® software, using standard processing methods (Berardino et al., 2002). SB allows for a maximisation of the spatial and temporal coherence, and therefore maximises the displacement measurements over the flank, owing to the combination of interferograms with small normal and temporal baselines. We generate interferograms connecting each image with two previous and two following acquisitions. The original data has been multi-looked resulting in a pixel size of 15 m. We used the 30m resolution Shuttle Radar Topography Mission (SRTM) digital elevation model (DEM) via the Earth Resources Observation And Science (EROS) Center 2017 to remove the topographic component from the interferograms and we filter the results using Goldstein filter (Goldstein and Werner, 1998) with tile sizes of 18px×18px. Finally, we unwrap the interferograms masking out coherence lower than 0.2 and applying the two-dimensional phase unwrapping algorithm Snaphu and we refer to the displacement measurement using a reference point located on the most northern part of the island considered stable (Fig. 2A). The results are displacement maps in ascending and descending line-of-sight (LOS). We further combined these two geometries using the incidence angle (e.g. Yun et al., 2006; Pepe and Calò, 2017) and derived vertical and horizontal components of displacement (Fig. 2A-F and S1D-F).

Due to a significant increase in eruptive activity of Anak Krakatau beginning towards the end of May 2018, coherence was significantly reduced on the SW-flank and many unwrapped points became unreliable and had to be filtered out. To capitalise on the previously better coverage, we split our analyses into two separate datasets, one for interpreting data before the 29th May 2018, containing more reliable points on the SW-flank, and one dataset with fewer points used to interpret activity after.

8.4 Result

8.4.1 Deformations on the southwest flank of Anak Krakatau

We measured the evolution of flank instability using multitemporal InSAR data with the small baseline (SB) method applied to Sentinel-1 data in both ascending (orbit 171) and descending (orbit 47) acquisition orbits over an ~4 yr period prior to the sector collapse (detailed processing methods are provided in Supplement A of the Supplemental Material 1). The data acquired between 8 October 2014 and 19 December 2018 showed that the

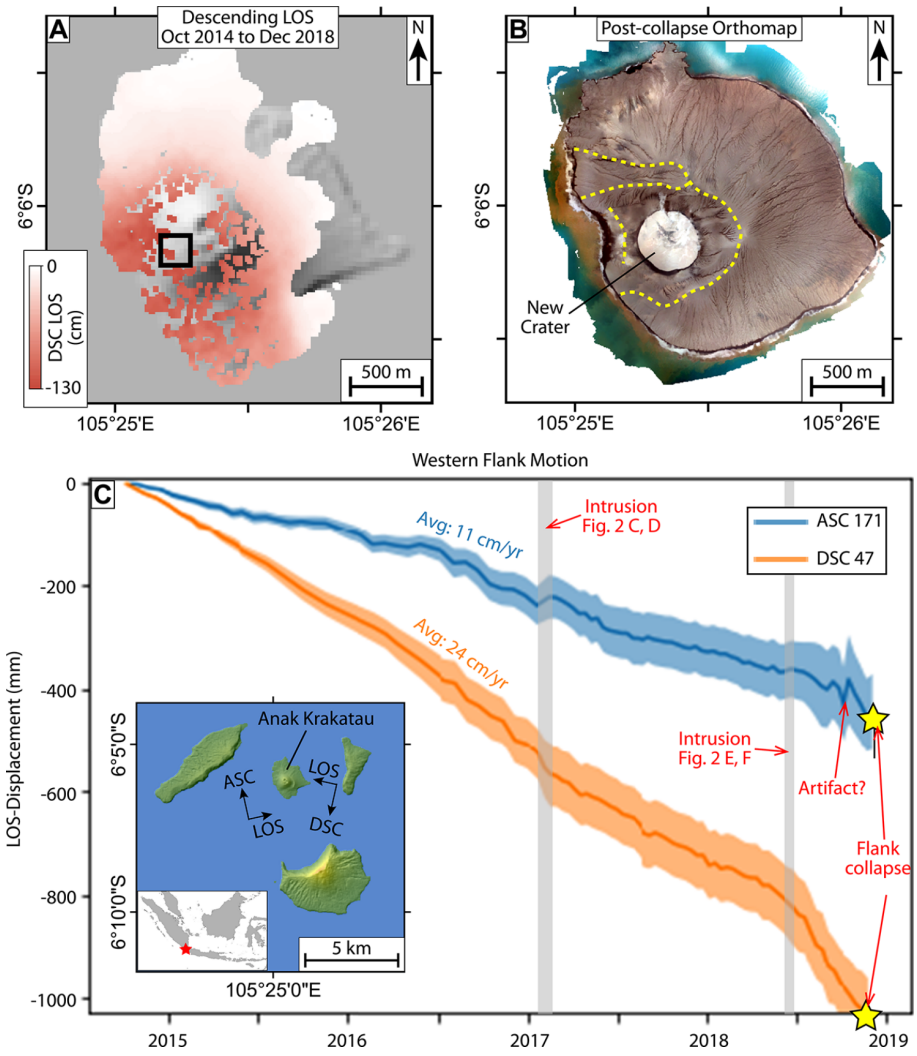


Figure 8.1: (A) 2014–2018 ground displacement of Anak Krakatau from the descending orbit in line-of-sight (LOS). (B) Orthomap of Anak Krakatau after its collapse, modified after Darmawan et al.(2020). Remnant structures are highlighted with yellow lines. (C) Displacement time series for the southwest flank from both ascending and descending orbits over a 4 yr observation period. Solid lines represent average values, while colored regions show standard deviation measured inside the black box marked in A. Gray-shaded areas mark magmatic intrusion events. Ascending (ASC) and descending (DSC) acquisition geometries are shown in the regional map inset.

southwest flank of Anak Krakatau had been gradually sliding seaward with an average line-of-sight (LOS) velocity of ~11 cm/yr (ascending) and ~24 cm/yr (descending), respectively (Fig. 1). Flank sliding accelerated between late January and February 2017 and again in June 2018. After both events, a lasting increase in flank instability was observed for ~2 mo in 2017 and ~6 mo in 2018 until the catastrophic flank collapse (Fig. 1C). The data from June 2018 were previously characterized by Walter et al. (2019), and our measured rates agree well.

Vertical and horizontal displacement maps from decomposed LOS deformations show that the flank was moving downward at a rate of ~25 cm/yr and westward at ~11 cm/yr

(Figs. 2A and 2B), which are consistent with a total seaward displacement occurring at ~27 cm/yr with an ~65° downward angle at the upper cone (inferred from the ratio of vertical and horizontal motions). In total, the flank moved a cumulative ~1.1 m over the entire 4 yr observation period. A sliding direction steeper than the slope in the upper region suggests a rotational landslide mechanism, which agrees with postcollapse assessments (Walter et al., 2019; Williams et al., 2019). The consistent long-term motion suggests gravitational flank failure, which is considered to be the most likely explanation (Hunt et al., 2021; Cutler et al., 2022). Over a 24 d period between 22 January and 18 February 2017, the velocities on the southwest flank reached values equivalent to ~92 cm/yr downward and ~118 cm/yr westward (or a total of ~150 cm/yr; Figs. 2C and 2D). During this same period, the eastern flank showed an additional eastward velocity of ~76 cm/yr, indicating a spreading pattern around the central cone (Fig. 2D). This coincided with increased thermal emission (Supplement C) and a short eruptive episode producing Strombolian explosions and a lava flow. This evidence points to a short-lived magmatic intrusion. In June 2018, the velocities increased again, likely caused by another intrusion. At this time, the flank slip rates in the 12 d between 10 June and 25 June 2018 were equivalent to ~26 cm/yr downward and ~70 cm/yr westward (equivalent to ~75 cm/yr total displacement; Figs. 2E and 2F). As with the previous intrusion, the eastern flank also moved eastward at ~89 cm/yr, spreading the central cone (Fig. 2F). However, due to lower coherence, the pattern was not as clear compared to that observed for January/February 2017. This time, the velocities stayed elevated until the flank catastrophically failed on 22 December 2018 (Fig. 1C).

8.4.2 Interaction of flank motions and magma intrusions simulated in analogue experiments

We studied the interaction of décollement flank failure and magmatic intrusions by conducting analogue sandbox experiments (details on the experimental setup, scaling, recording, processing, and limitations are provided in Supplement B). We reconstructed Anak Krakatau with sand by building a simplified circular cone on a flat surface. We then tested two types of deformation mechanisms consecutively: (1) gradual sliding of the flank through a basal décollement, and (2) magma ascent through a circular conduit. As a result of the artificial décollement in the first stage, the flank started to slide in two blocks separated by a set of steep antithetic faults (Figs. 3B and 3D). This is consistent with similar experiments incorporating décollement slip in cones (Acocella, 2005; Le Corvec and Walter, 2009). While the outer block moved laterally, we found that the inner block moved both down and outward. This included the cone summit, reducing the overall height of the sand-volcano. The inner block motion was also remarkably consistent with the type of motion observed by InSAR at the southwest flank of Anak Krakatau (cf. Figs. 2A, 2B, 2G, and 2H), including the angle of the forming fault, which dipped ~62° downward (Fig. 3E), similar to the inferred ~65° dip from InSAR. The outer block produced positive vertical change; however, this was not due to upward movement, but rather the horizontal outward-directed slide next to the inclined slope (Fig. 2G).

During the second stage, we intruded a circular column of sand into the center of the sand cone (with the preexisting décollement). This simulated an intrusion through an assumed circular conduit, similar to lava dome growth (Zorn et al., 2020), which was observed at Anak Krakatau in October 2018 (Hochfeld et al., 2022). During the initial intrusion, we observed a reactivation of the décollement fault, meaning the intrusion caused further slip, despite the décollement being stopped before (Figs. 3F and 3G). With continued intrusion,

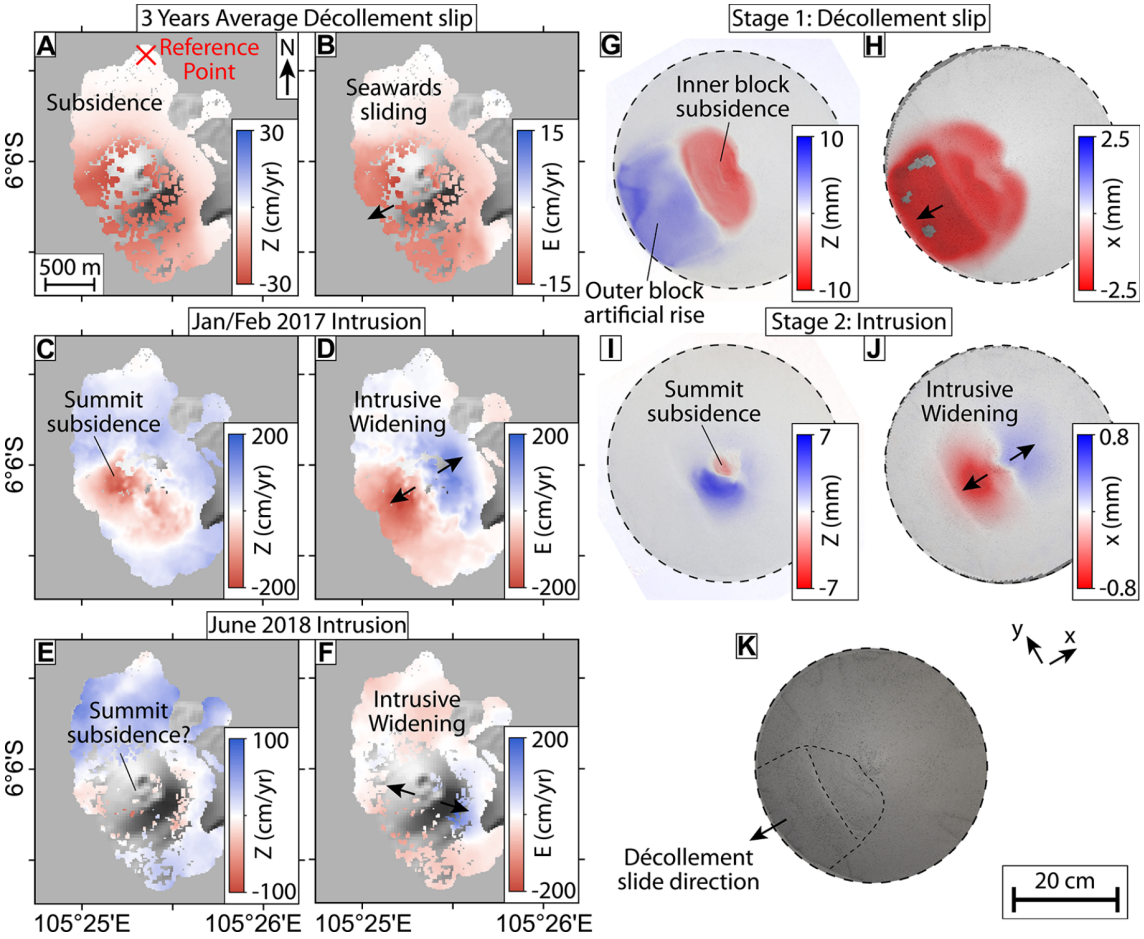


Figure 8.2: (A–F) Decomposed interferometric synthetic aperture radar (InSAR) maps and (G–K) analogue modeling data showing ground deformation in vertical (z) and horizontal eastward (E or x) components. (A,B) 3 yr average flank motion due to décollement slip, which is compared against artificial décollement deformation (stage 1) in G and H. Both show a matching pattern of subsidence on the upper cone and lateral movement toward the west. Height increase of the lower flank in G is due to the purely horizontal décollement plane, which moves the lower block outward and thus causes an artificial height increase. (C,D) January-February 2017 intrusion. (E,F) June 2018 intrusion. (G,H) Analogue décollement deformation (stage 1). (I,J) Analogue intrusion (stage 2). These changes caused summit subsidence and lateral spreading of the cone. (K) Photo of experiment cone for reference.

the magma then was deflected toward the unstable flank; however, in repeated experiments, we saw that it could also be deflected toward the opposite side. Evidently, the intrusion did not result in uplift of the summit cone, but rather its subsidence (Fig. 2I). We found this to be caused by a set of inward-dipping faults originating at the conduit, which are similar to the spine-bounding faults seen in Zorn et al. (2020). These laterally pushed the outer flanks, in turn causing subsidence at the summit. As a result, the vertical change showed a height reduction in the cone center and height gain (or bulging) in the outer flanks (Figs. 2I and 2J). This deformation pattern also agrees well with modeled cryptodome intrusions (e.g., Donnadieu et al., 2003).

8.5 Discussion

Based on geomorphologic studies, a possible flank collapse and tsunami were already anticipated at Anak Krakatau prior to 2018 (Giachetti et al., 2012). Our InSAR observations demonstrate that the southwest flank of Anak Krakatau had gradually been sliding seaward for at least 4 yr prior to the catastrophic collapse in December 2018 (Fig. 1C). It is likely that the instability persisted for longer, as earlier studies had already noted subsidence, but they interpreted it to be magma chamber deflation and not flank instability (Chaussard and Amelung, 2012). Thus, we speculate that the flank instability may have been ongoing for over a decade before the collapse. This sheds light on the potential precursors of sector collapses, as the instability can be clearly identified years in advance, which may become highly relevant for mitigating potential future disasters at volcanoes elsewhere. Our data also provide insights into the geologic processes occurring during the developing instability and the interaction of the unstable flank with magmatic intrusions. The flank accelerations of Anak Krakatau coincided with significant rises in the volcanic radiative power seen in Moderate Resolution Imaging Spectroradiometer (MODIS) data, indicating an increase in eruptive activity (Supplement C). This occurred in January-February 2017 and again, more intensely and prolonged, in June 2018 onward. Additionally, there were significant peaks in the thermal activity of Anak Krakatau between 2008 and 2012 (Supplement C), and it is likely that these changes also caused décollement slip accelerations similar to those we identified here (Fig. 1C). While no other tangible data linking flank accelerations as a precursor to catastrophic collapse exist for volcanoes so far, there is abundant evidence for this from nonvolcanic giant landslides (e.g., Kilburn and Petley, 2003; Kang et al., 2019; Chen et al., 2021). A key difference is the gradual deformation increase interpreted to occur as a result of slow cracking (Kilburn and Petley, 2003), as opposed to episodic accelerations corresponding to discrete intrusion events (Fig. 1C), highlighting the increased role of magmatism in the collapse of volcanic flanks.

Our findings are consistent with the suggestion that the flank of Anak Krakatau moved and failed via a décollement (Walter et al., 2019; Borrero et al., 2020). Despite the simplification to a conduit-like intrusion and a horizontal sliding plane in our analogue experiments, both the resulting deformation patterns and the geometry of the developing main fault matched the InSAR displacement observations well. The experiments predicted subsidence of the summit both during décollement slip and during magmatic intrusions, which can be seen in the upper portion of the cone at Anak Krakatau (Figs. 2A, 2C, and 2E) and in the analogue experiments (Figs. 2G and 2I). Similarly, the horizontal spreading associated with the intrusions can be seen in both the volcano and the model (Figs. 2D, 2F, and 2J). Our analogue experiments also produced a set of horseshoe-shaped detachment faults. While we could not observe any such discrete surface faults at Anak Krakatau via InSAR, similar faults did appear in the final Sentinel-1 image on the day of the collapse, separating the flank into distinct blocks with two failure planes from a rotational slide (cf. Williams et al., 2019, their figure 2). The postcollapse ortho-map also shows a north-south–striking structure that could be indicative of the antithetic fault in our models (Fig. 1B).

Finally, we observed a direct impact of the sand intrusion on the preexisting fault structures that formed through the décollement slip. Despite no active slip being induced, the faults were reactivated during the start of the intrusion, causing further décollement slip (Figs. 3F and 3G). This appears to have been induced by the added stress field from the conduit intrusion, as it had a similar shear direction as the décollement fault and resulted

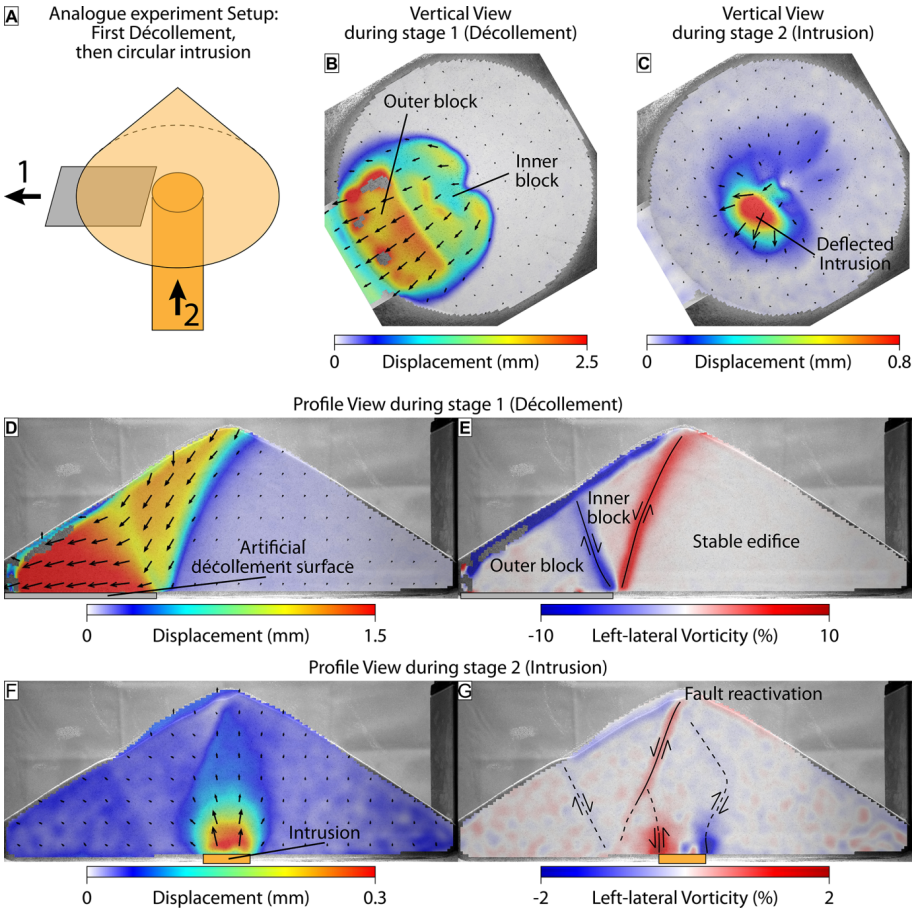


Figure 8.3: Particle displacement tracking from (A) two-stage analogue sandbox models, with (B,C) vertical views, and (D–G) profile views for both décollement slip (stage 1) and intrusion (stage 2). Décollement slip produced faults that are consistent with proposed long-term motion of Anak Krakatau. Subsequent intrusion reactivated these faults, potentially explaining increased flank slip during intrusion events.

in a favored fault activation. In turn, the developing shear faults along the conduit margins were redirected toward the unstable side (Fig. 3G), which may explain the shift of the vent toward the unstable southwest flank at Anak Krakatau in July 2018 (Hunt et al., 2021), and which may indicate a stress reorientation resulting from the onset of edifice collapse (Maccaferri et al., 2017). We observed the interaction of intrusion and increased décollement slip twice during our observation period as the accelerations matched well with the January-February 2017 and June 2018 intrusions (Figs. 1C and 2C–2F). While the January-February 2017 intrusion was short-lived, it did cause a brief increase in the décollement slip rates to more than 5 times the normal rate. The June 2018 intrusion caused an increase of ~3 times the normal rate, but, this time, the slip rates stayed elevated until the collapse 6 mo later.

Our results highlight the conclusion that intrusions may act as destabilizing forces on the flank, making their detection vital for hazard and risk assessments. The deformation patterns and structural insights provided here may further aid in identifying key areas for monitoring instruments to characterize flank instability. At Anak Krakatau, our findings point to distinct magmatic intrusions playing a major role in the instability progression

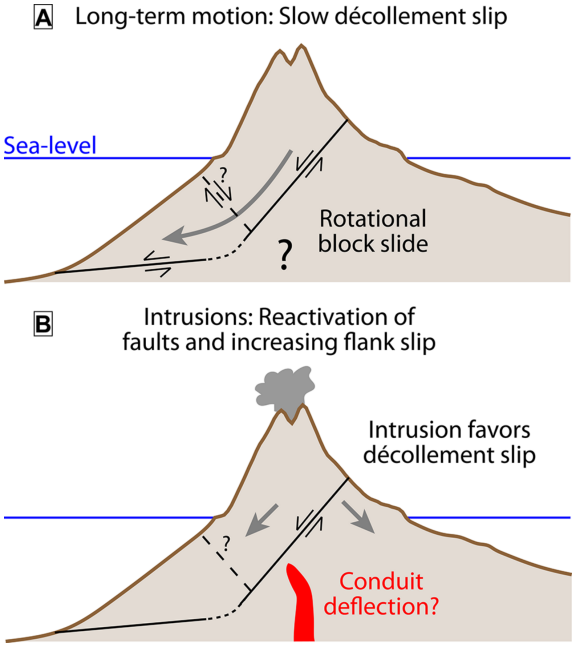


Figure 8.4: Schematic illustration of deformations associated with (A) décollement and (B) intrusions at Anak Krakatau increasing décollement slip.

because they can significantly accelerate ongoing destabilization by activating existing faults (Fig. 4). Previous studies found no evidence for a direct magmatic trigger for the 22 December 2018 collapse (Cutler et al., 2022), but it is clear that magmatic intrusions at least significantly affected the long-term movement and stability of the flank.

8.6 Acknowledgment

We acknowledge financial support by the Federal Ministry of Education and Research of Germany in the framework of TSUNAMI_RISK (project number 03G0906A), a part of the funding initiative CLIENT-II. We further acknowledge the past contributions made by the German-Indonesian Tsunami Early Warning System for the Indian Ocean (GITEWS), upon which this project builds.

9 Summary and Future Perspectives

9.1 Summary

This PhD research demonstrates the valuable contribution of InSAR observations to the understanding of several geological processes related to geohazard events, including kinematic characterization of process mechanisms, identification of the deformation source and influencing external forces. The initially formulated general research questions have been addressed in the case studies presented in chapters 4 to 8.

- **How does the specific geological process occur on the surface? What is the magnitude of ground deformation? Does it evolve in space and time and how? Are there any transients in displacement detectable as evidence for potential forthcoming more severe events?**

MTI is able to detect the onset of different time-dependent geological events caused by both anthropogenic (Chapters 4 and 5) and tectonic (Chapters 6, 7 and 8) activities. It successfully measured the spatiotemporal evolution of the ground deformations in the order of a few cm/year to a few dm/year, identifying transients in trend as well as seasonal oscillatory signals (Chapters 4, 5, 7 and 8). The cm-precision detection capability of DInSAR allowed the successful measurement of dm level deformations related to seismic events (Chapter 6). The evolution of large deformations in the order of several metres was measured with pixel offset using high-resolution optical images (Chapter 5).

For slowly developing geohazards, the choice of post-processing methods for detecting transients and separating different signal contributions (trends, seasonality, noise) in the ground displacement time series can affect the final interpretation (Chapter 5). One method can be more suitable than the other, and identify better one contribution than another based on the predominant pattern in the time series, the noise level and the number of datasets. Therefore, it is always a good practice to perform and compare more than one method.

Decorrelation issues due to vegetation or low temporal resolution, specifically valid for past SAR missions, can limit the density of InSAR measurements over the area of interest. In these cases, low coherence thresholds can still be applied to improve the data coverage, even if this is at the expense of measurement accuracy. In that case, it is important to base the ground deformation time-series analysis on average values over defined clusters or areas rather than pointwise extracted time-series values (Chapter 5).

The validation of MTI is not always possible. When GNSS measurements are available, a comparison with the MTI over the same GNSS station location can be used (Chapter 7). In other cases, the InSAR measurement over a hypothetically stable area can be used as the level of precision, although the error changes in space and time (Chapters 4 and 5). The case studies have also shown that for localized analyses such as single landslide cases or local land subsidence and for deformations of the order of a few cm/year, atmospheric

effects can be effectively reduced by exploiting the high spatial and low temporal correlation character of those anomalies (Chapters 4, 5, 7 and 8).

- **What is the type of underground process which is the source of the observed ground deformation? Where is the main source located? What is its overall and approximate geometry? How does it evolve in space and time?**

Simple elastic geophysical models and geometries such as point pressure and rectangle dislocation models can provide important insight into the location and geometry of the ground deformation source contributing to identifying the geological process involved (Chapters 4, 6 and 7). In the case of no or limited number of in-situ measurements, InSAR drastically improves the capacity to better constrain the location and geometry of the deformation source (Chapter 6). However, this is only achievable when multi-geometry and multi-platform measurements are available (Chapters 4 and 7). The use of more sophisticated models, including distinct element method, poroelastic numerical models and analogue models, contribute to providing more details about the material involved and the stress/strength underlying evolution (Chapters 4, 7 and 8).

- **What are the main environmental, climatic and anthropogenic factors controlling the evolution of the geological process? How do they correlate with the ground deformation observation and the deeper processes?**

Onset and transients of ground deformations can be correlated to specific external environmental, climatic and anthropogenic factors, both time-dependent or single events (Chapters 4, 5, 7 and 8) and increase the geohazard potential. Knowledge of the triggers and influence of certain geological processes and their kinematic behavior is of fundamental importance for the mitigation of geohazards. However, a lack of measurements on potential external factors can limit the final interpretation. Therefore, if in-situ measurements are unavailable, remote sensing data can be used to extract geospatial data, i.e. underground mining and water reservoir impoundment (Chapters 4 and 5). Magmatic intrusion episodes and intense precipitation periods have also been shown to accelerate the trend of ground displacement see Chapter 7) and even cause more catastrophic events (Chapter 5).

9.1.1 Land subsidence in the municipality of Maceió (Brazil)

The multi-sensor and multi-orbit MTI analysis detected a 4 cm/year displacement trend since 2003, which gradually increased to 17 cm/year during the following 13 years. A drastic acceleration then occurred during the second half of 2017, reaching a maximum of 27 cm/year which concurred with the extreme May-July 2017. From July 2004 until November 2020 a cumulative subsidence of more than 2 m was estimated close to the lagoon coast. The MTI observations also detected a second minor subsiding area in the densely populated areas south of the lagoon, characterized by an elliptic northwest-southeast aligned block-caving pattern of a cumulative value of 50 cm for the same period. The inverse elastic source best fitting model identifies the source depth between 700 to 1000 m which coincides with the layer containing the salt cavities. The source model results showed also an upward source migration, also identified in the finite element method simulation, which is explicable with episodes of cavity roof failure. The simulation also highlighted that

in both active/pressurized and inactive/depressurized salt mining conditions the cavities underwent mechanical instability causing partial to total cavity collapses and cracks propagation towards shallower layers. This last, indeed creates a preferential path for the rainfall infiltration with consequent enhanced local subsidence as seen in the MTI observations.

9.1.2 Landslide failure in Hoseynabad-e Kalpush village (north–central Iran)

Multi-sensor and multi-orbit MTI and multi-temporal optical image correlation combined with GIS and mathematical analysis showed that the previously stable landslide reservoir was reactivated due to the reservoir impoundment which started in 2013 and reached a maximum nominative value of 31m in spring 2017. In the pre-failure period, the landslide followed a retrogressive destabilization mechanism with a gradual increase in horizontal ground deformation trend to 8 cm/yr on the bottom and 3 cm/year on the upper parts. The four and a half years of slow creeping progressively degraded the geomechanical slope properties. The main landslide failure developed with a typical deep-seated translational with some rotational component mechanism, following the exceptional precipitation that hit the region between January and March 2019. However, during this rainfall period the water reservoir also drastically increased to a level 3-4 m above the maximum nominative values. Most likely the contribution of all these effects, although it is not possible to separate their contributions, provoke the. The landslide was still active in the aftermath of its failure with decreasing rates in time as the water reservoir was discharged until the final stabilization of the whole landslide body in October 2021.

9.1.3 Offshore earthquake in the eastern coast of Kamchatka peninsula (Russia)

Multi-sensor and multi-orbit InSAR and inverse elastic numerical model detected the co-seismic onshore displacement of the 29 March 2017 Mw 6.6 South-Ozernovskoe Kamchatka earthquake. The seismic event induced an uplift of 20 cm and a westward motion of 7 cm on the coast. The best-fitting fault model located the epicentre 5 km offshore and suggests a shallow northwest-dipping reverse rupture with a right-lateral component. The maximum produced slip is of 2.7 m at a depth of approximately 10 km. The geological analysis suggests that the rupture occurred on a fault system that is the offshore extension of the Kumroch thrust belt which can be considered part of a larger active fault system stretching over two-thirds of the Kamchatka peninsula. This earthquake demonstrates that the area north of the Pacific slab subduction zone has higher seismic and tsunamigenic hazards than previously thought.

9.1.4 Cyclical geothermal unrest at Fagradalsfjall volcano (Iceland)

Multi-orbit MTI analysis, elastic and poroelastic source modelling, combined with seismic and gravitational measurements described the 12 months of cyclical unrest at the Svartsengi geothermal field, 8 km west of the March 2021 Fagradalsfjall eruption site. An area of 80 km2 was affected, with the centre close to the re-injection site of the power plant. Three uplift episodes followed by subsidence produced a maximum cumulative uplift of 15 cm in July 2020 and then reduced to 9 cm by December 2020. The ground deformation, particularly the rapid subsidence following each uplift episode, the free-air gravity changes

and the seismicity variations in time and space, were best explained by cyclic intrusions into a permeable aquifer by a fluid injected at 4 km depth below the geothermal field. It was estimated a total injected volume of $0.11 \pm 0.05\ km^3$ and fluid density of 850 ± 350 kg m^{-3} most likely of magmatic CO2, although some magma contributions are not excluded. The result suggests the migration of deep magmatic fluids and gases into upper crustal hydrothermal systems, highlighting the interaction of volcanic processes and geothermal systems for geohazard analysis.

9.1.5 Flank collapse at Anak Krakatau volcano (Indonesia)

Multi-orbit MTI analysis and analogue sandbox experiments demonstrate that the southwest flank of Anak Krakatau had gradually been sliding seaward for at least 4 years prior to the catastrophic collapse in December 2018. An average downward rate of 25 cm/year and a westward rate of 11 cm/year were estimated. The flank ground displacement trend increased temporally between January and February 2017 and then permanently in June 2018 until the final catastrophic collapse on 22 December 2018. Both acceleration episodes coincided with significant rises in the volcanic radiative power seen in Moderate Resolution Imaging Spectroradiometer (MODIS) data. Both analogue experiments, i.e. horizontal sliding plane (décollement) and successive conduit-like magma intrusion (stable décollement) explained well the MTI observations. Indeed, in the first stage, the décollement slip produced faults that were consistent with the observed ground deformations. Subsequent intrusion reactivated those preexisting fault structures, potentially explaining increased flank slip during intrusion events. The results showed that distinct magmatic intrusions play a major role in the flank instability progression, making their detection vital for hazard and risk assessments.

9.2 Outlook and ongoing challenges

InSAR has become a widely used tool for the systematic measurement of slow ground deformations and the estimation of geophysical parameters. However, there are still many open scientific and technical challenges to be addressed in order to improve its capabilities for near-real-time monitoring and forecasting of geohazards.

Geohazard early warning systems can be based on the timely detection of precursor signals for ground deformations. The difficulty in identifying short and small trend changes before potential major events is related to the temporal frequency of the SAR acquisitions on the one hand and to the level of noise and reliability of the time series on the other. Regarding time frequency, the Sentinel-1 mission, constituted by only one functioning satellite at the moment, since the second launched satellite failed at the end of 2022, is anticipating the launch of the next satellite in 2024. The NISAR L-band mission is also scheduled to start at the beginning of 2024 and provide further data. Therefore, a scientific challenge will be to harmonize and fuse the InSAR observations from Sentiel-1 and NISAR acquisitions in order to improve the temporal density of ground deformation observations.

Regarding the reliability of the displacement measurements, important transients in ground deformations can be easily identified retrogressively if a longer time series of data is available. However, the challenge to detect the start of acceleration in semi-real time remains. This challenge can be addressed by improving the MTI algorithms, e.g. by integrating AI methods for separating errors from actual deformation signals, developing

automatic methods for selecting high-quality interferograms and improving the selection of coherent points. In addition to that, new auxiliary products developed by ESA (with DLR as a contractor) for Sentinel-1, i.e. Extended Timing Annotation Dataset (ETAD), are provided with each SAR acquisition. They contain information about the atmospheric delays, the solid Earth tidal deformation, and SAR processor-related effects, and can be used to correct the SLC images and improve the geometric accuracy of the final ground deformation observations. The timely detection of precursors is also related to the timely delivery of the acquired SAR image and auxiliary products. Sentinel-1 data are nowadays delivered within an hour of reception for Near Real-Time (NRT) emergency response, within three hours for NRT priority areas and within 24 hours for systematically archived data. In many cases, there is no prior information on when and where a geohazard might occur. Therefore, many potential areas are not considered for emergency response, and providing images after several hours can be problematic for near-real-time monitoring purposes.

Another current challenge is the processing automatization, from the SAR and auxiliary data download to the final ground deformation anomaly detection and geohazard mapping. This can be essential in many applications, especially for rapidly accelerating processes that predict events (i.e. the current volcanic unrest detected by InSAR and GPS near Grendevik in Iceland). Moreover, the automation will provide users and scientific experts with the final ground deformation map, which can then be interpreted and investigated. There are several services that provide already processed InSAR products over some specific region of interest. An example is Looking Into Continents from Space with Synthetic Aperture Radar (LiCSAR), implemented at the Centre for Observation and Modelling of Earthquakes, Volcanoes and Tectonics (COMET, UK, web portal) which provides continuously updated large-scale interferometric products of Sentinel-1 data over the main seismically and volcanic active areas. Another service is ARIA, the Advanced Rapid Imaging and Analysis project from a collaboration between Jet Propulsion Laboratory (JPL, California) and Caltech, the California Institute of Technology (web portal) which plans to provide global InSAR products in near real-time for disaster response. A final example is the EPOSAR service from IREA-CNR (web portal), acting within the umbrella of the European Plate Observing System (EPOS) platform (web portal) which generates automatically co-seismic interferograms when a strong earthquake has occurred. A current technological challenge is to deal with big data storage and processing. However, with the goal of sustainable development, the challenge includes also reducing and containing the energy consumption of such data centres.

An additional challenge in automatic InSAR production is the automatic extraction of further products from these observations. This includes the creation of source models, geohazard maps that delineate the active regions, the classification of geohazards based on spatiotemporal patterns and the correlation of these patterns with potential external trigger factors. An example of such a service is the implementation of a processing chain for fully automatic modeling of the seismic source parameters and its slip distribution, using the InSAR EPOSAR products, developed at the National Institute of Geophysics and Volcanology (INGV, web portal).

Finally, it is important to mention that all these scientific and technological challenges can be irrelevant if they are not used effectively to reduce the risk of geohazards. Therefore, close collaboration at a global level between scientists, policymakers and emergency management stakeholders is needed to achieve the benefits for society as a whole.

Bibliography

Aati S, Avouac J-P (2020) Optimization of Optical Image Geometric Modeling, Application to Topography Extraction and Topographic Change Measurements Using PlanetScope and SkySat Imagery. Remote Sensing 12:3418. https://doi.org/10.3390/rs12203418

Abadie, S.M., Harris, J.C., Grilli, S.T. and Fabre, R., 2012. Numerical modeling of tsunami waves generated by the flank collapse of the Cumbre Vieja Volcano (La Palma, Canary Islands): Tsunami source and near field effects. Journal of Geophysical Research: Oceans, 117(C5). DOI: 10.1029/2011JC007646

Ablay G, Hürlimann M (2000) Evolution of the north flank of Tenerife by recurrent giant landslides. Journal of Volcanology and Geothermal Research 103:135–159. https://doi.org/10.101/S0377-0273(00)00220-1

Acocella, V., 2005. Modes of sector collapse of volcanic cones: Insights from analogue experiments. Journal of Geophysical Research: Solid Earth, 110(B2). DOI: 10.1029/2004JB003166

Ágústsson, K. & Flóvenz, Ó. G. The thickness of the seismogenic crust in Iceland and its implications for geothermal systems. In Proc. World Geothermal Congress 2005 0743 (International Geothermal Association, 2005).

Al-Halbouni D, Watson RA, Holohan EP, et al (2021) Dynamics of hydrological and geomorphological processes in evaporite karst at the eastern Dead Sea – a multidisciplinary study. Hydrology and Earth System Sciences 25:3351–3395. https://doi.org/10.5194/hess-25-3351-2021

Al-Halbouni, D. et al. Distinct element geomechanical modelling of the formation of sinkhole clusters within large-scale karstic depressions. Solid Earth 10, 1219–1241 (2019) doi:http://dx.doi.org/10.5194/se-10-1219-2019.

Al-Halbouni, D. et al. Dynamics of hydrological and geomorphological processes in evaporite karst at the eastern Dead Sea - a multidisciplinary study. Hydrology and Earth System Sciences Discussions 1–57 (2021) doi:https://doi.org/10.5194/hess-2021-37.

Al-Halbouni, D. et al. Geomechanical modelling of sinkhole development using distinct elements: model verification for a single void space and application to the Dead Sea area. Solid Earth 9, 1341–1373 (2018) doi:http://dx.doi.org/10.5194/se-9-1341-2018.

Al-Halbouni, D. et al. Sinkholes, subsidence and subrosion on the eastern shore of the Dead Sea as revealed by a close-range photogrammetric survey. Geomorphology 285, 305–324 (2017) doi:http://dx.doi.org/10.1016/j.geomorph.2017.02.006.

Albertsson, A.&Jónsson J. The Svartsengi resource park. In Proc. World Geothermal Congress 2010 3313 (International Geothermal Association, 2010).

Alexeiev, D.V., Gaedicke, C., Tsukanov, N.V., Freitag, R., 2006. Collision of the Kronotskiy arc at the NE Eurasia margin and structural evolution of the Kamchatka–Aleutian junction. Int. J. Earth Sci. 95, 977–993. https://doi.org/10.1007/s00531-006-0080-z

Allen, R. V. Automatic earthquake recognition and timing from single traces. Bull. Seism. Soc. Am. 68, 1521–1532 (1978).

Amoruso, A.&Crescentini, L. Shape and volume change of pressurized ellipsoidal cavities from deformation and seismic data. J. Geophys. Res. Solid Earth https://doi.org/10.1029/2008JB005946 (2009).

Annunziato, A., Prasetya, G. and Husrin, S., 2019. Anak Krakatau volcano emergency tsunami early warning system. Science of Tsunami Hazards, 38(2).

Apperson, K.D., 1991. Stress Fields of the Overriding Plate at Convergent Margins and Beneath Active Volcanic Arcs. Science 254, 670–678. https://doi.org/10.1126/science.254.5032.670

Aslan G, Foumelis M, Raucoules D, et al (2020) Landslide Mapping and Monitoring Using Persistent Scatterer Interferometry (PSI) Technique in the French Alps. Remote Sensing 12:1305. https://doi.org/10.3390/rs12081305

Atzori S, Monterroso F, Antonioli A, et al (2023) Automatic seismic source modeling of InSAR displacements. International Journal of Applied Earth Observation and Geoinformation 123:103445. https://doi.org/10.1016/j.jag.2023.103445

Atzori S, Salvi S, Atzori S, Salvi S (2014) SAR Data Analysis in Solid Earth Geophysics: From Science to Risk Management. In: Land Applications of Radar Remote Sensing. IntechOpen

Atzori, S., Hunstad, I., Chini, M., Salvi, S., Tolomei, C., Bignami, C., Stramondo, S., Trasatti, E., Antonioli, A., Boschi, E., 2009. Finite fault inversion of DInSAR coseismic displacement of the 2009 L'Aquila earthquake (central Italy). Geophys. Res. Lett. 36. https://doi.org/10.1029/2009GL039293

Authority: The European Union Per, Regulation 305/2011, Directive 98/34/EC, Directive, 2004/18/EC&Authority: The European Union Per Regulation 305/2011, Directive 98/34/EC, Directive 2004/18/EC (2004). Eurocode 7: Geotechnical design - Part 1: General rules.

Baer, G., Funning, G.J., Shamir, G., Wright, T.J., 2008. The 1995 November 22, Mw 7.2 Gulf of Elat earthquake cycle revisited. Geophys. J. Int. 175, 1040–1054. https://doi.org/10.1111/j.1365-246X.2008.03901.x

Bagheri-Gavkosh M, Hosseini SM, Ataie-Ashtiani B, et al (2021) Land subsidence: A global challenge. Science of The Total Environment 778:146193. https://doi.org/10.1016/j.scitotenv.2021.146193

Bagnardi, M., Hooper, A., 2018. Inversion of Surface Deformation Data for Rapid Estimates of Source Parameters and Uncertainties: A Bayesian Approach. Geochem. Geophys. Geosystems 19, 2194–2211. https://doi.org/10.1029/2018GC007585

Bali, E. et al. Geothermal energy and ore-forming potential of 600°C mid-ocean-ridge hydrothermal fluids. Geology https://doi.org/10.1130/G47791.1 (2020).

Baran, I., Stewart, M.P., Kampes, B.M., Perski, Z., Lilly, P., 2003. A modification to the Goldstein radar interferogram filter. IEEE Trans. Geosci. Remote Sens. 41, 2114–2118. https://doi.org/10.1109/TGRS.2003.817212

Bell, J. W., Amelung, F., Ferretti, A., Bianchi, M.&Novali, F. Permanent scatterer InSAR reveals seasonal and long-term aquifer-system response to groundwater pumping and artificial recharge: PERMANENT SCATTERER INSAR. Water Resour. Res. 44, (2008).

Berardino P, Fornaro G, Lanari R, Sansosti E (2002) A new algorithm for surface deformation monitoring based on small baseline differential SAR interferograms. IEEE Transactions on Geoscience and Remote Sensing 40:2375–2383. https://doi.org/10.1109/TGRS.2002.803792

Bernardi MS, Africa PC, de Falco C, et al (2021) On the Use of Interferometric Synthetic Aperture Radar Data for Monitoring and Forecasting Natural Hazards. Math Geosci 53:1781–1812. https://doi.org/10.1007/s11004-021-09948-8

Berti M, Corsini A, Franceschini S, Iannacone JP (2013) Automated classification of Persistent Scatterers Interferometry time series. Natural Hazards and Earth System Sciences 13:1945–1958. https://doi.org/10.5194/nhess-13-1945-2013

Bianchini S, Ciampalini A, Raspini F, et al (2015) Multi-Temporal Evaluation of Landslide Movements and Impacts on Buildings in San Fratello (Italy) By Means of C-Band and X-Band PSI Data. Pure Appl Geophys 172:3043–3065. https://doi.org/10.1007/s00024-014-0839-2

Bickel VT, Manconi A, Amann F (2018) Quantitative Assessment of Digital Image Correlation Methods to Detect and Monitor Surface Displacements of Large Slope Instabilities. Remote Sensing 10:865. https://doi.org/10.3390/rs10060865

Biggs J, Pritchard ME (2017) Global Volcano Monitoring: What Does It Mean When Volcanoes Deform? Elements 13:17–22. https://doi.org/10.2113/gselements.13.1.17

Biggs, J., Bergman, E., Emmerson, B., Funning, G.J., Jackson, J., Parsons, B., Wright, T.J., 2006. Fault identification for buried strike-slip earthquakes using InSAR: The 1994 and 2004 Al Hoceima, Morocco earthquakes. Geophys. J. Int. 166, 1347–1362. https://doi.org/10.1111/j.1365-246X.2006.03071.x

Binte Mostafiz R, Noguchi R, Ahamed T (2021) Agricultural Land Suitability Assessment Using Satellite Remote Sensing-Derived Soil-Vegetation Indices. Land 10:223. https://doi.org/10.3390/land10020223

Björnsson, S., Einarsson, P., Hjartardóttir, Á. R.&Tulinius, H. Seismicity of the Reykjanes Peninsula 1971–1976. J. Volcanol. Geotherm. Res. 391, 106369 (2020).

Blanck, H., Jousset, P., Hersir, G. P., Ágústsson, K.&Flóvenz, Ó. G. Analysis of 2014–2015 on- and off-shore passive seismic data on the Reykjanes Peninsula, SW Iceland. J. Volcanol. Geotherm. Res. 391, 106548 (2020).

Böðvarsson, R., Rögnvaldsson, S. T., Slunga, R.&Kjartansson, E. The SIL data acquisition system at present and beyond year 2000. Phys. Earth Planet. Inter. 113, 89–101 (1999).

Bonali FL, Tibaldi A, Corazzato C (2015) Sensitivity analysis of earthquake-induced static stress changes on volcanoes: the 2010 Mw 8.8 Chile earthquake. Geophysical Journal International 201:1868–1890. https://doi.org/10.1093/gji/ggv122

Borrero, J.C., Solihuddin, T., Fritz, H.M., Lynett, P.J., Prasetya, G.S., Skanavis, V., Husrin, S., Kushendratno, Kongko, W., Istiyanto, D.C., Daulat, A., Purbani, D., Salim, H.L., Hidayat, R., Asvaliantina, V., Usman, M., Kodijat, A., Son, S. and Synolakis, C.E., 2020. Field Survey and Numerical Modelling of the December 22, 2018 Anak Krakatau Tsunami. Pure and Applied Geophysics, 177(6): 2457-2475. DOI: 10.1007/s00024-020-02515-y

Bovenga F, Pasquariello G, Refice A (2021) Statistically-Based Trend Analysis of MTInSAR Displacement Time Series. Remote Sensing 13:2302. https://doi.org/10.3390/rs13122302

Bovenga F, Wasowski J, Nitti DO, et al (2012) Using COSMO/SkyMed X-band and ENVISAT C-band SAR interferometry for landslides analysis. Remote Sensing of Environment 119:272–285. https://doi.org/10.1016/j.rse.2011.12.013

BRASIL, C.-S. G. D. Estudos sobre a instabilidade do terreno nos bairros Pinheiro, Mutange e Bebedouro, Maceió (AL): volume I, relatório síntese dos resultados n. 1. http://rigeo.cprm.gov.br/jspui/handle/doc/21133 (2019).

Braskem sees higher costs from Alagoas salt mine damage | S&P Global Platts. https://www.spglobal.com/platts/en/market-insights/latest-news/petrochemicals/091520-braskem-sees-higher-costs-from-alagoas-salt-mine-damage (2020).

Bürgmann, R., Kogan, M.G., Steblov, G.M., Hilley, G., Levin, V.E., Apel, E., 2005. Interseismic coupling and asperity distribution along the Kamchatka subduction zone. J. Geophys. Res. Solid Earth 110. https://doi.org/10.1029/2005JB003648

Burland, J. B.&Wroth, C. P. SETTLEMENT OF BUILDINGS AND ASSOCIATED DAMAGE. (1975). Byrne, P.K., Holohan, E.P., Kervyn, M., van Wyk de Vries, B., Troll, V.R. and Murray, J.B., 2013. A sagging-spreading continuum of large volcano structure. Geology, 41(3): 339-342. DOI: 10.1130/g33990.1

Cabral-Cano, E. et al. Space geodetic imaging of rapid ground subsidence in Mexico City. Geological Society of America Bulletin 120, 1556–1566 (2008).

Çakir, Z., Chabalier, J.-B. de, Armijo, R., Meyer, B., Barka, A., Peltzer, G., 2003. Coseismic and early post-seismic slip associated with the 1999 Izmit earthquake (Turkey), from SAR interferometry and tectonic field observations. Geophys. J. Int. 155, 93–110. https://doi.org/10.1046/j.1365-246X.2003.02001.x

Carnemolla F, De Guidi G, Bonforte A, et al (2023) The ground deformation of the south-eastern flank of Mount Etna monitored by GNSS and SAR interferometry from 2016 to 2019. Geophysical Journal International 234:664–682. https://doi.org/10.1093/gji/ggad088

Casagli N, Cigna F, Bianchini S, et al (2016) Landslide mapping and monitoring by using radar and optical remote sensing: Examples from the EC-FP7 project SAFER. Remote Sensing Applications: Society and Environment 4:92–108. https://doi.org/10.1016/j.rsase.2016.07.001

Casu F, Manzo M, Lanari R (2006) A quantitative assessment of the SBAS algorithm performance for surface deformation retrieval from DInSAR data. Remote Sensing of Environment 102:195–210. https://doi.org/10.1016/j.rse.2006.01.023

Cayol, V., Dieterich, J.H., Okamura, A.T. and Miklius, A., 2000. High Magma Storage Rates Before the 1983 Eruption of Kilauea, Hawaii. Science, 288(5475): 2343-2346. DOI: 10.1126/science.288.5475.2343

Cervelli, P., Murray, M.H., Segall, P., Aoki, Y., Kato, T., 2001. Estimating source parameters from deformation data, with an application to the March 1997 earthquake swarm off the Izu Peninsula, Japan. J. Geophys. Res. Solid Earth 106, 11217–11237. https://doi.org/10.1029/2000JB900399

Chaput, M., Pinel, V., Famin, V., Michon, L. and Froger, J.L., 2014. Cointrusive shear displacement by sill intrusion in a detachment: A numerical approach. Geophysical Research Letters, 41(6): 1937-1943. DOI: 10.1002/2013GL058813

Chaussard E, Bürgmann R, Shirzaei M, et al (2014) Predictability of hydraulic head changes and characterization of aquifer-system and fault properties from InSAR-derived ground deformation. Journal of Geophysical Research: Solid Earth 119:6572–6590. https://doi.org/10.1002/2014JB011266

Chaussard, E. and Amelung, F., 2012. Precursory inflation of shallow magma reservoirs at west Sunda volcanoes detected by InSAR. Geophysical Research Letters, 39(21). DOI: 10.1029/2012GL053817

Chebrov, D.V., Kugaenko, Yu.A., Lander, A.V., Abubakirov, I.R., Voropaev, P.V., Gusev, A.A., Droznin, D.V., Droznina, S.Ya., Ivanova, E.I., Kravchenko, N.M., Matveenko, E.A., Mitushkina, S.V., Ototuk, D.A., Pavlov, V.M., Rayevskaya, A.A., Saltikov, V.A., Senyukov, S.L., Skorkina, A.A., Serafimova, Yu.K., 2017. ЮЖНО-ОЗЕРНОВСКОЕ ЗЕМЛЕТРЯСЕНИЕ 29.03.2017 г. с MW = 6.6, KS = 15.0, I = 6 (КАМЧАТКА) .The Match 29th, 2017 earthquake with KS = 15.0, MW = 6.6, I = 6 in the Ozernoy Gulf (Kamchatka) Vestnik KRAUNC, 7–21.

Chebrov, V.N., Droznin, D.V., Kugaenko, Yu.A., Levina, V.I., Senyukov, S.L., Sergeev, V.A., Shevchenko, Yu.V., Yashchuk, V.V., 2013. The system of detailed seismological observations in Kamchatka in 2011. J. Volcanol. Seismol. 7, 16–36. https://doi.org/10.1134/S0742046313010028

Chen, M. et al. Imaging Land Subsidence Induced by Groundwater Extraction in Beijing (China) Using Satellite Radar Interferometry. Remote Sensing 8, 468 (2016).

Cho SE (2017) Prediction of shallow landslide by surficial stability analysis considering rainfall infiltration. Engineering Geology 231:126–138. https://doi.org/10.1016/j.enggeo.2017.10.018

Choe B-H, Blais-Stevens A, Samsonov S, Dudley J (2021) Sentinel-1 and RADARSAT Constellation Mission InSAR Assessment of Slope Movements in the Southern Interior of British Columbia, Canada. Remote Sensing 13:3999. https://doi.org/10.3390/rs13193999

Ciampalini A, Solari L, Giannecchini R, et al (2019) Evaluation of subsidence induced by long-lasting buildings load using InSAR technique and geotechnical data: The case study of a Freight Terminal (Tuscany, Italy). International Journal of Applied Earth Observation and Geoinformation 82:101925. https://doi.org/10.1016/j.jag.2019.101925

Cigna F, Esquivel Ramírez R, Tapete D (2021) Accuracy of Sentinel-1 PSI and SBAS InSAR Displacement Velocities against GNSS and Geodetic Leveling Monitoring Data. Remote Sensing 13:4800. https://doi.org/10.3390/rs13234800

Cigna, F.&Tapete, D. Present-day land subsidence rates, surface faulting hazard and risk in Mexico City with 2014–2020 Sentinel-1 IW InSAR. Remote Sensing of Environment 112161 (2020) doi:10.1016/j.rse.2020.112161.

Cohen-Waeber J, Bürgmann R, Chaussard E, et al (2018) Spatiotemporal Patterns of Precipitation-Modulated Landslide Deformation From Independent Component Analysis of InSAR Time Series. Geophysical Research Letters 45:1878–1887. https://doi.org/10.1002/2017GL075950

Colesanti C, Wasowski J (2006) Investigating landslides with space-borne Synthetic Aperture Radar (SAR) interferometry. Engineering Geology 88:173–199. https://doi.org/10.1016/j.enggeo.2006.09.013

Coltice N, Husson L, Faccenna C, Arnould M (2019) What drives tectonic plates? Science Advances 5:eaax4295. https://doi.org/10.1126/sciadv.aax4295

Contreras D, Chamorro A, Wilkinson S (2020) Review article: The spatial dimension in the assessment of urban socio-economic vulnerability related to geohazards. Natural Hazards and Earth System Sciences 20:1663–1687. https://doi.org/10.5194/nhess-20-1663-2020

Cook, D.B., Fujita, K., McMullen, C.A., 1986. Present-day plate interactions in Northeast Asia: North American, Eurasian, and Okhotsk plates. J. Geodyn., Proceedings of the Symposium Polar Geophysics 6, 33–51. https://doi.org/10.1016/0264-3707(86)90031-1

Cooper, A. H. Chapter 14 Geological hazards from salt mining, brine extraction and natural salt dissolution in the UK. Geological Society, London, Engineering Geology Special Publications 29, 369–387 (2020).

Cooper, A. Halite karst geohazards (natural and man-made) in the United Kingdom. Environmental Geology 42, 505–512 (2002).

Corsa B, Barba-Sevilla M, Tiampo K, Meertens C (2022) Integration of DInSAR Time Series and GNSS Data for Continuous Volcanic Deformation Monitoring and Eruption Early Warning Applications. Remote Sensing 14:784. https://doi.org/10.3390/rs14030784

Costantini, M., 1998. A novel phase unwrapping method based on network programming. IEEE Trans. Geosci. Remote Sens. 36, 813–821. https://doi.org/10.1109/36.673674

Cubuk-Sabuncu, Y. et al. Temporal seismic velocity changes during the 2020 rapid inflation at Mt. Þorbjörn-Svartsengi, Iceland, using seismic ambient noise. Geophys. Res. Lett. 48, e2020GL092265 (2021). Cundall, P. A.&Strack, O. D. L. A discrete numerical model for granular assemblies. Géotechnique 29, 47–65 (1979).

Cutler, K.S., Watt, S.F.L., Cassidy, M., Madden-Nadeau, A.L., Engwell, S.L., Abdurrachman, M., Nurshal, M.E.M., Tappin, D.R., Carey, S.N., Novellino, A., Hayer, C., Hunt, J.E., Day, S.J., Grilli, S.T., Kurniawan, I.A. and Kartadinata, N., 2022. Downward-propagating eruption following vent unloading implies no direct magmatic trigger for the 2018 lateral collapse of Anak Krakatau. Earth and Planetary Science Letters, 578: 117332. DOI: 10.1016/j.epsl.2021.117332

Dahm, T. et al. MAGIC - Seismic Network MAGma in Iceland (GFZ Data Services, 2020); https://doi.org/10.14470/4U7575229166

Dahm, T. On the shape and velocity of fluid-filled fractures in the Earth. Geophys. J. Int. 142, 181–192 (2000).

Dahm, T., Cesca, S., Hainzl, S., Braun, T.&Krüger, F. Discrimination between induced, triggered, and natural earthquakes close to hydro-carbon reservoirs: a probabilistic approach based on the modeling of depletion-induced stress changes and seismological source parameters. J. Geophys. Res. 120, 2491–2509 (2015).

Dai FC, Lee CF, Ngai YY (2002) Landslide risk assessment and management: an overview. Engineering Geology 64:65–87. https://doi.org/10.1016/S0013-7952(01)00093-X

Darmawan, H., Mutaqin, B.W., Harijoko, A., Wibowo, H.E., Haerani, N., Surmayadi, M., Jati, R. and Asriningrum, W., 2020. Topography and structural changes of Anak Krakatau due to the December 2018 catastrophic events. The Indonesian Journal of Geography, 52(3): 402-410. DOI: 10.22146/ijg.53740

Darvishi M, Schlögel R, Bruzzone L, Cuozzo G (2018) Integration of PSI, MAI, and Intensity-Based Sub-Pixel Offset Tracking Results for Landslide Monitoring with X-Band Corner Reflectors—Italian Alps (Corvara). Remote Sensing 10:409. https://doi.org/10.3390/rs10030409

Darvishi M, Schlögel R, Kofler C, et al (2018) Sentinel-1 and Ground-Based Sensors for Continuous Monitoring of the Corvara Landslide (South Tyrol, Italy). Remote Sensing 10:1781. https://doi.org/10.3390/rs10111781

De Freitas, M. A. Numerical Modelling of Subsidence in Geothermal Reservoirs: Case Study of the Svartsengi Geothermal System, SW-Iceland. MSc thesis, Univ. Iceland (2018). de la Barreda-Bautista B, Boyd DS, Ledger M, et al (2022) Towards a Monitoring

Approach for Understanding Permafrost Degradation and Linked Subsidence in Arctic Peatlands. Remote Sensing 14:444. https://doi.org/10.3390/rs14030444

De Vries, B.V.W. and Borgia, A., 1996. The role of basement in volcano deformation. Geological Society, London, Special Publications, 110(1): 95. DOI: 10.1144/GSL.SP.1996.110.01.07 Delac K, Grgic M, Grgic S (2005) Independent comparative study of PCA, ICA, and LDA on the FERET data set. International Journal of Imaging Systems and Technology 15:252–260. https://doi.org/10.1002/ima.20059

Delaney, P.T., Denlinger, R.P., Lisowski, M., Miklius, A., Okubo, P.G., Okamura, A.T. and Sako, M.K., 1998. Volcanic spreading at Kilauea, 1976–1996. Journal of Geophysical Research: Solid Earth, 103(B8): 18003-18023. DOI: 10.1029/98JB01665

DeMets, C., Gordon, R.G., Argus, D.F., Stein, S., 1990. Current plate motions. Geophys. J. Int. 101, 425–478. https://doi.org/10.1111/j.1365-246X.1990.tb06579.x

Desir G, Gutiérrez F, Merino J, et al (2018) Rapid subsidence in damaging sinkholes: Measurement by high-precision leveling and the role of salt dissolution. Geomorphology 303:393–409. https://doi.org/10.1016/j.geomorph.2017.12.004

Di Maio C, De Rosa J, Vassallo R, et al (2020) Hydraulic Conductivity and Pore Water Pressures in a Clayey Landslide: Experimental Data. Geosciences 10:102. https://doi.org/10.3390/geosciences10030102 Diao, F., Walter, T.R., Motagh, M., Prats-Iraola, P., Wang, R., Samsonov, S.V., 2015. The 2015 Gorkha earthquake investigated from radar satellites: slip and stress modeling along the MHT. Front. Earth Sci. 3. https://doi.org/10.3389/feart.2015.00065

Dieterich, J. H. A constitutive law for rate of earthquake production and its applications to earthquake clustering. J. Geophys. Res. 99, 2601–2618 (1994).

Dieterich, J., Cayol, V.&Okubo, P. The use of earthquake rate changes as a stress meter at Kilauea volcano. Nature 408, 457–460 (2000).

Donati D, Westin AM, Stead D, et al (2021) A reinterpretation of the Downie Slide (British Columbia, Canada) based on slope damage characterization and subsurface data interpretation. Landslides 18:1561–1583. https://doi.org/10.1007/s10346-020-01601-5https://doi.org/10.3390/rs10111781

Draper BA, Baek K, Bartlett MS, Beveridge JR (2003) Recognizing faces with PCA and ICA. Computer Vision and Image Understanding 91:115–137. https://doi.org/10.1016/S1077-3142(03)00077-8

Du Y, Fu H, Liu L, et al (2021) Orbit error removal in InSAR/MTInSAR with a patch-based polynomial model. International Journal of Applied Earth Observation and Geoinformation 102:102438. https://doi.org/10.1016/j.jag.2021.102438

Dualeh EW, Ebmeier SK, Wright TJ, et al (2023) Rapid pre-explosion increase in dome extrusion rate at La Soufrière, St. Vincent quantified from synthetic aperture radar backscatter. Earth and Planetary Science Letters 603:117980. https://doi.org/10.1016/j.epsl.2022.117980

Duc DM (2013) Rainfall-triggered large landslides on 15 December 2005 in Van Canh District, Binh Dinh Province, Vietnam. Landslides 10:219–230. https://doi.org/10.1007/s10346-012-0362-4

Ducrocq, C. et al. Inflation-deflation episodes in the Hengill and Hrómundartindur volcanic complexes, SW Iceland. Front. Earth Sci. 9, 725109 (2021).

E. D. Chaves M, C. A. Picoli M, D. Sanches I (2020) Recent Applications of Landsat 8/OLI and Sentinel-2/MSI for Land Use and Land Cover Mapping: A Systematic Review. Remote Sensing 12:3062. https://doi.org/10.3390/rs12183062

Earth Resources Observation And Science (EROS) Center (2017) Shuttle Radar Topography Mission (SRTM) 1 Arc-Second Global

Ebmeier SK, Biggs J, Mather TA, Amelung F (2013) Applicability of InSAR to tropical volcanoes: insights from Central America. Geological Society, London, Special Publications 380:15–37. https://doi.org/10.1144/SP380.2

El-Shirbeny MA, Abutaleb KA (2018) Monitoring of Water-Level Fluctuation of Lake Nasser Using Altimetry Satellite Data. Earth Syst Environ 2:367–375. https://doi.org/10.1007/s41748-018-0053-y

Elliott A, Elliott J, Hollingsworth J, et al (2020) Satellite imaging of the 2015 M7.2 earthquake in the Central Pamir, Tajikistan, elucidates a sequence of shallow strike-slip ruptures of the Sarez-Karakul fault. Geophysical Journal International 221:1696–1718. https://doi.org/10.1093/gji/ggaa090

Elliott, J.R., Walters, R.J., England, P.C., Jackson, J.A., Li, Z., Parsons, B., 2010. Extension on the Tibetan plateau: recent normal faulting measured by InSAR and body wave seismology: Extension on the Tibetan plateau. Geophys. J. Int. 183, 503–535. https://doi.org/10.1111/j.1365-246X.2010.04754.x

Emil MK, Sultan M, Alakhras K, et al (2021) Countrywide Monitoring of Ground Deformation Using InSAR Time Series: A Case Study from Qatar. Remote Sensing 13:702. https://doi.org/10.3390/rs13040702

Euillades P, Euillades L, Pepe A, et al (2021) Recent advancements in multi-temporal methods applied to new generation SAR systems and applications in South America. Journal of South American Earth Sciences 111:103410. https://doi.org/10.1016/j.jsames.2021.103410

Famin, V. and Michon, L., 2010. Volcano destabilization by magma injections in a detachment. Geology, 38(3): 219-222. DOI: 10.1130/g30717.1

Fan H, Wang L, Wen B, Du S (2021) A New Model for three-dimensional Deformation Extraction with Single-track InSAR Based on Mining Subsidence Characteristics. International Journal of Applied Earth Observation and Geoinformation 94:102223. https://doi.org/10.1016/j.jag.2020.102223

Fernández-Torres EA, Cabral-Cano E, Novelo-Casanova DA, et al (2022) Risk assessment of land subsidence and associated faulting in Mexico City using InSAR. Nat Hazards 112:37–55. https://doi.org/10.1007/s11069-021-05171-0

Festa D, Novellino A, Hussain E, et al (2023) Unsupervised detection of InSAR time series patterns based on PCA and K-means clustering. International Journal of Applied Earth Observation and Geoinformation 118:103276. https://doi.org/10.1016/j.jag.2023.103276

Fialko, Y., Sandwell, D., Simons, M., Rosen, P., 2005. Three-dimensional deformation caused by the Bam, Iran, earthquake and the origin of shallow slip deficit. Nature 435, 295. https://doi.org/10.1038/nature03425

Fielding, E.J., Sladen, A., Li, Z., Avouac, J.-P., Bürgmann, R., Ryder, I., 2013. Kinematic fault slip evolution source models of the 2008 M7.9 Wenchuan earthquake in China from SAR interferometry, GPS and teleseismic analysis and implications for Longmen Shan tectonics. Geophys. J. Int. 194, 1138–1166. https://doi.org/10.1093/gji/ggt155

Figueroa-Miranda S, Hernández-Madrigal VM, Tuxpan-Vargas J, Villaseñor-Reyes CI (2020) Evolution assessment of structurally-controlled differential subsidence using SBAS and PS interferometry in an emblematic case in Central Mexico. Engineering Geology 279:105860. https://doi.org/10.1016/j.enggeo.2020.105860

Flóvenz, Ó. G. et al. The interaction of the plate boundary movement in 2020 and exploitation of geothermal fields on the Reykjanes Peninsula, Iceland. In Proc. World Geothermal Congress 2020+1 13013 (International Geothermal Association, 2021).

Flóvenz, Ó. G. Seismic structure of the Icelandic crust above layer three and the relation between body wave velocity and the alteration of the basaltic crust. J. Geophys. 47, 211–220 (1980).

Fobert M-A, Singhroy V, Spray JG (2021) InSAR Monitoring of Landslide Activity in Dominica. Remote Sensing 13:815. https://doi.org/10.3390/rs13040815

Fournier, R. O. Hydrothermal processes related to movement of fluid from plastic into brittle rock in the magmatic-epithermal environment. Econ. Geol. 94, 1193–1211 (1999).

Freitag, R., Gaedicke, C., Baranov, B., Tsukanov, N., 2001. Collisional processes at the junction of the Aleutian–Kamchatka arcs: new evidence from fission track analysis and field observations. Terra Nova 13, 433–442. https://doi.org/10.1046/j.1365-3121.2001.00375.x

Friðleifsson, G. Ó. et al. The Iceland deep drilling project at Reykjanes: drilling into the root zone of a black smoker analog. J. Volcanol. Geotherm. Res. 391, 106435 (2020).

Fuhrmann T, Garthwaite MC (2019) Resolving Three-Dimensional Surface Motion with InSAR: Constraints from Multi-Geometry Data Fusion. Remote Sensing 11:241. https://doi.org/10.3390/rs11030241

Funk C, Peterson P, Landsfeld M, et al (2015) The climate hazards infrared precipitation with stations—a new environmental record for monitoring extremes. Sci Data 2:150066. https://doi.org/10.1038/sdata.2015.66

Furst SL, Doucet S, Vernant P, et al (2021) Monitoring surface deformation of deep salt mining in Vauvert (France), combining InSAR and leveling data for multi-source inversion. Solid Earth 12:15–34. https://doi.org/10.5194/se-12-15-2021

Gaedicke, C., Baranov, B., Seliverstov, N., Alexeiev, D., Tsukanov, N., Freitag, R., 2000. Structure of an active arc-continent collision area: the Aleutian–Kamchatka junction. Tectonophysics 325, 63–85. https://doi.org/10.1016/S0040-1951(00)00131-1

Gariano SL, Rianna G, Petrucci O, Guzzetti F (2017) Assessing future changes in the occurrence of rainfall-induced landslides at a regional scale. Science of The Total Environment 596–597:417–426. https://doi.org/10.1016/j.scitotenv.2017.03.103

Geist, E.L., Scholl, D.W., 1994. Large-scale deformation related to the collision of the Aleutian Arc with Kamchatka. Tectonics 13, 538–560. https://doi.org/10.1029/94TC00428

Geoffroy, L.&Dorbath, C. Deep downward fluid percolation driven by localized crust dilatation in Iceland. Geophys. Res. Lett. 35, 117302 (2008).

Geological map 1:100000, sheet Dozin, Created/Published by Geological Survey of Iran Ghulam, A., Amer, R., Ripperdan, R., 2010. A filtering approach to improve deformation accuracy using large baseline, low coherence DInSAR phase images, in: 2010 IEEE International Geoscience and Remote Sensing Symposium. Presented at the 2010 IEEE International Geoscience and Remote Sensing Symposium, pp. 3494–3497. https://doi.org/10.1109/IGARSS.2010.5652581

Giachetti, T., Paris, R., Kelfoun, K. and Ontowirjo, B., 2012. Tsunami hazard related to a flank collapse of Anak Krakatau Volcano, Sunda Strait, Indonesia. Geological Society, London, Special Publications, 361(1): 79-90. DOI: doi:10.1144/SP361.7

Gill JC, Malamud BD (2017) Anthropogenic processes, natural hazards, and interactions in a multi-hazard framework. Earth-Science Reviews 166:246–269. https://doi.org/10.1016/j.earscirev.2017.01.002

Goldstein RM, Werner CL (1998) Radar interferogram filtering for geophysical applications. Geophysical Research Letters 25:4035–4038. https://doi.org/10.1029/1998GL900033@10.1002/(ISSN)1944-8007.GRL40

Gomes VCF, Queiroz GR, Ferreira KR (2020) An Overview of Platforms for Big Earth Observation Data Management and Analysis. Remote Sensing 12:1253. https://doi.org/10.3390/rs12081253

Gorbatov, A., Kostoglodov, V., Suárez, G., Gordeev, E., 1997. Seismicity and structure of the Kamchatka Subduction Zone. J. Geophys. Res. Solid Earth 102, 17883–17898. https://doi.org/10.1029/96JB03491

Gordeev, E.I., Fedotov, S.A., Chebrov, V.N., 2013. Detailed seismological investigations in Kamchatka during the 1961–2011 period: Main results. J. Volcanol. Seismol. 7, 1–15. https://doi.org/10.1134/S0742046313010041

Gordeev, E.I., Pinegina, T.K., Lander, A.V., Kozhurin, A.I., 2015. Beringia: Seismic hazard and fundamental problems of geotectonics. Izv. Phys. Solid Earth 51, 512–521. https://doi.org/10.1134/S1069351315030039

Grandin, R., Klein, E., Métois, M., Vigny, C., 2016. Three-dimensional displacement field of the 2015 Mw8.3 Illapel earthquake (Chile) from across- and along-track Sentinel-1 TOPS interferometry. Geophys. Res. Lett. 43, 2552–2561. https://doi.org/10.1002/2016GL067954

Grinsted A, Moore JC, Jevrejeva S (2004) Application of the cross wavelet transform and wavelet coherence to geophysical time series. Nonlinear Processes in Geophysics 11:561–566. https://doi.org/10.5194/npg-11-561-2004

Gudmundsson, M. T. et al. Gradual caldera collapse at Bárdarbunga volcano, Iceland, regulated by lateral magma outflow. Science https://doi.org/10.1126/science.aaf8988 (2016).

Gudnason, E. Á. et al. Seismic monitoring during drilling and stimulation of well RN-15/IDDP-2 in Reykjanes, SW-Iceland. In Proc. World Geothermal Congress 2020+1 13015 (International Geothermal Association, 2021).

Guizar-Sicairos M, Thurman ST, Fienup JR (2008) Efficient subpixel image registration algorithms. Opt Lett, OL 33:156–158. https://doi.org/10.1364/OL.33.000156

Guo C, Zhang Y, Li X, et al (2020) Reactivation of giant Jiangdingya ancient landslide in Zhouqu County, Gansu Province, China. Landslides 17:179–190. https://doi.org/10.1007/s10346-019-01266-9 Guzy A, Malinowska AA (2020) Assessment of the Impact of the Spatial Extent of Land Subsidence and Aquifer System Drainage Induced by Underground Mining. Sustainability 12:7871. https://doi.org/10.3390/su12197871

Haghshenas Haghighi M, Motagh M (2016) Assessment of ground surface displacement in Taihape landslide, New Zealand, with C- and X-band SAR interferometry. New Zealand Journal of Geology and Geophysics 59:136–146. https://doi.org/10.1080/00288306.2015.1127824

Hainzl, S., Steacy, S.&Marsan, D. Seismicity Models Based on Coulomb Stress Calculations (Community Online Resource for Statistical Seismicity Analysis, 2010); https://doi.org/10.5078/corssa-32035809

Handwerger AL, Fielding EJ, Huang M-H, et al (2019) Widespread Initiation, Reactivation, and Acceleration of Landslides in the Northern California Coast Ranges due to Extreme Rainfall. Journal of Geophysical Research: Earth Surface 124:1782–1797. https://doi.org/10.1029/2019JF005035

Hanssen RF (2001) Radar Interferometry: Data Interpretation and Error Analysis. Springer Netherlands, Dordrecht

Haque U, da Silva PF, Devoli G, et al (2019) The human cost of global warming: Deadly landslides and their triggers (1995–2014). Science of The Total Environment 682:673–684. https://doi.org/10.1016/j.scitotenv.2019.03.415

Heimann, S. et al. Pyrocko—An Open-Source Seismology Toolbox and Library v.0.3 (GFZ Data Services, 2017); https://doi.org/10.5880/GFZ.2.1.2017.001

Heimisson, E. R.&Segall, P. Physically consistent modeling of dike-induced deformation and seismicity: application to the 2014 Bàrðarbunga dike, Iceland. J. Geophys. Res. 125, e2019JB018141 (2020).

Heimlich, C. et al. Uplift around the geothermal power plant of Landau (Germany) as observed by InSAR monitoring. Geothermal Energy 3, 2 (2015).

Herrera-García G, Ezquerro P, Tomás R, et al (2021) Mapping the global threat of land subsidence. Science 371:34–36. https://doi.org/10.1126/science.abb8549

Hersir, G. P., Árnason, K.&Vilhjálmsson, A. M. Krýsuvík high temperature geothermal area in SW Iceland: geological setting and 3D inversion of magnetotelluric (MT) resistivity data. J. Volcanol. Geotherm. Res. 391, 106500 (2020).

Hidayat, A., Marfai, M.A. and Hadmoko, D.S., 2020. Eruption on Indonesia's volcanic islands: a review of potential hazards, fatalities, and management. IOP Conference Series: Earth and Environmental Science, 485(1): 012061. DOI: 10.1088/1755-1315/485/1/012061

Hilley GE, Bürgmann R, Ferretti A, et al (2004) Dynamics of Slow-Moving Landslides from Permanent Scatterer Analysis. Science 304:1952–1955. https://doi.org/10.1126/science.1098821

Himanshu N, Burman A (2019) Seepage and Stability Analysis of Durgawati Earthen Dam: A Case Study. Indian Geotech J 49:70–89. https://doi.org/10.1007/s40098-017-0283-1

Hindle, D., Sedov, B., Lindauer, S., Mackey, K., 2019. The Ulakhan fault surface rupture and the seismicity of the Okhotsk–North America plate boundary. Solid Earth 10, 561–580. https://doi.org/10.5194/se-10-561-2019

Hobé, A., Gudmundsson, O., Tryggvason, A.&the SIL seismological group Imaging the 2010–2011 inflationary source at Krýsuvík, SW Iceland, using time-dependent Vp/Vs tomography. In Proc. World Geothermal Congress 2020+1 13178 (International Geothermal Association, 2021).

Hochfeld, I., Hort, M., Schwalbe, E. and Dürig, T., 2022. Eruption dynamics of Anak Krakatau volcano (Indonesia) estimated using photogrammetric methods. Bulletin of Volcanology, 84(8): 73. DOI: 10.1007/s00445-022-01579-z

Hou AY, Kakar RK, Neeck S, et al (2014) The Global Precipitation Measurement Mission. Bulletin of the American Meteorological Society 95:701–722. https://doi.org/10.1175/BAMS-D-13-00164.1

Hrubcová, P., Doubravová, J.& Vavryčuk, V. Non-double-couple earthquakes in 2017 swarm in Reykjanes Peninsula, SW Iceland: sensitive indicator of volcano–tectonic movements at slow-spreading rift. Earth Planet. Sci. Lett. 563, 116875 (2021).

Hu X, Xue L, Yu Y, et al (2021) Remote Sensing Characterization of Mountain Excavation and City Construction in Loess Plateau. Geophysical Research Letters 48:e2021GL095230. https://doi.org/10.1029/2021GL095230

Huang Z, Zhang G, Shan X, et al (2019) Co-Seismic Deformation and Fault Slip Model of the 2017 Mw 7.3 Darbandikhan, Iran–Iraq Earthquake Inferred from D-InSAR Measurements. Remote Sensing 11:2521. https://doi.org/10.3390/rs11212521

Hunt, J.E., Tappin, D.R., Watt, S.F.L., Susilohadi, S., Novellino, A., Ebmeier, S.K., Cassidy, M., Engwell, S.L., Grilli, S.T., Hanif, M., Priyanto, W.S., Clare, M.A., Abdurrachman, M. and Udrekh, U., 2021. Submarine landslide megablocks show half of Anak Krakatau island failed on December 22nd, 2018. Nature Communications, 12(1): 2827. DOI: 10.1038/s41467-021-22610-5

Hussain S, Pan B, Afzal Z, et al (2023) Landslide detection and inventory updating using the time-series InSAR approach along the Karakoram Highway, Northern Pakistan. Sci Rep 13:7485. https://doi.org/10.1038/s41598-023-34030-0

Isken, M. et al. DAS Convert—Convert Distributed Acoustic Sencing Data Version 1.0 (GFZ Data Services, 2021); https://doi.org/10.5880/GFZ.2.1.2021.005

Ismail, T., Abdurrachman, M., Rizal, Y. and Hardjawidjaksana, K., 2020. Volcanostratigraphy of Krakatoa Islands, South Lampung District, Lampung Province. IOP Conference Series: Earth and Environmental Science, 589(1): 012010. DOI: 10.1088/1755-1315/589/1/012010

Iverson RM (2000) Landslide triggering by rain infiltration. Water Resources Research 36:1897–1910. https://doi.org/10.1029/2000WR900090

Jiang Q, Wei W, Xie N, Zhou C (2015) Stability analysis and treatment of a reservoir landslide under impounding conditions: a case study. Environ Earth Sci 75:2. https://doi.org/10.1007/s12665-015-4790-z

Johnson, J.M., Satake, K., 1999. Asperity Distribution of the 1952 Great Kamchatka Earthquake and its Relation to Future Earthquake Potential in Kamchatka, in: Sauber, J., Dmowska, R. (Eds.), Seismogenic and Tsunamigenic Processes in Shallow Subduction Zones. Birkhäuser Basel, Basel, pp. 541–553. https://doi.org/10.1007/978-3-0348-8679-6_8

Johnson, K. S. Evaporite-karst problems and studies in the USA. Environ Geol 53, 937–943 (2008). Jones J, Jones CE, Bekaert DPS (2022) Value of InSAR for Monitoring Land Subsidence to Support Water Management in the San Joaquin Valley, California. JAWRA Journal of the American Water Resources Association 58:995–1001. https://doi.org/10.1111/1752-1688.12942

Jones S, Kasthurba AK, Bhagyanathan A, Binoy BV (2021) Impact of anthropogenic activities on landslide occurrences in southwest India: An investigation using spatial models. J Earth Syst Sci 130:70. https://doi.org/10.1007/s12040-021-01566-6

Jousset, P. et al. Dynamic strain determination using fibre-optic cables allows imaging of seismological and structural features. Nat. Commun. https://doi.org/10.1038/s41467-018-04860-y (2018).

Jousset, P. et al. MAGIC (Magma Iceland) (2020); https://doi.org/10.14470/0W7575244885

K, M. Relations between the eruptions of various volcanoes and the deformations of the ground surface around them. Bull. Earthquake Res. Inst. Univ. Tokyo 36, 99–134 (1958).

Kaczmarek H, Tyszkowski S, Banach M (2015) Landslide development at the shores of a dam reservoir (Włocławek, Poland), based on 40 years of research. Environ Earth Sci 74:4247–4259. https://doi.org/10.1007/s12665-015-4479-3

Kanamori H, Brodsky EE (2004) The physics of earthquakes. Rep Prog Phys 67:1429. https://doi.org/10.1088/0034-4885/67/8/R03

Kang X, Wang S, Wu W, et al (2022) Soil–water interaction affecting a deep-seated landslide: From field monitoring to experimental analysis. Bull Eng Geol Environ 81:82. https://doi.org/10.1007/s10064-021-02556-0

Kang Y, Zhao C, Zhang Q, et al (2017) Application of InSAR Techniques to an Analysis of the Guanling Landslide. Remote Sensing 9:1046. https://doi.org/10.3390/rs9101046

Karlsdóttir, R. TEM-viðnámsmælingar í Svartsengi 1997 (Orkustofnun, 1998).

Karlsdóttir, R., Vilhjálmsson, A. M.& Gudnason, E. Á. Three dimensional inversion of magnetotelluric (MT) resistivity data from Reykjanes high temperature field in SW Iceland. J. Volcanol. Geotherm. Res. 391, 106498 (2020).

Kennedy, B. et al. Pressure controlled permeability in a conduit filled with fractured hydrothermal breccia reconstructed from ballistics from Whakaari (White Island), New Zealand. Geosciences 10, 138 (2020).

Keys TA, Scott DT (2018) Monitoring volumetric fluctuations in tropical lakes and reservoirs using satellite remote sensing. Lake and Reservoir Management 34:154–166. https://doi.org/10.1080/10402381.2017.1402226

Khan J, Ren X, Hussain MA, Jan MQ (2022) Monitoring Land Subsidence Using PS-InSAR Technique in Rawalpindi and Islamabad, Pakistan. Remote Sensing 14:3722. https://doi.org/10.3390/rs14153722

Khan S, Kirschbaum DB, Stanley T (2021) Investigating the potential of a global precipitation forecast to inform landslide prediction. Weather and Climate Extremes 33:100364. https://doi.org/10.1016/j.wace.2021.100364

Kim, J.-W., Lu, Z., Jia, Y.& Shum, C. K. Ground subsidence in Tucson, Arizona, monitored by time-series analysis using multi-sensor InSAR datasets from 1993 to 2011. ISPRS Journal of Photogrammetry and Remote Sensing 107, 126–141 (2015).

Kostrov, B. Seismic moment and energy of earthquakes, and seismic flow of rock. Izv. Acad. Sci. USSR Phys. Solid Earth 1, 23–40 (1974).

Kozhurin, A., Acocella, V., Kyle, P.R., Lagmay, F.M., Melekestsev, I.V., Ponomareva, V., Rust, D., Tibaldi, A., Tunesi, A., Corazzato, C., Rovida, A., Sakharov, A., Tengonciang, A., Uy, H., 2006. Trenching studies of active faults in Kamchatka, eastern Russia: Palaeoseismic, tectonic and hazard implications. Tectonophysics 417, 285–304. https://doi.org/10.1016/j.tecto.2006.01.004

Kozhurin, A., Zelenin, E., 2017. An extending island arc: The case of Kamchatka. Tectonophysics 706–707, 91–102. https://doi.org/10.1016/j.tecto.2017.04.001

Kristjánsdóttir, S. Microseismicity in the Krýsuvík Geothermal Field, SW Iceland, from May to October 2009. MSc thesis, Univ. Iceland (2013).

Lacroix P, Gavillon T, Bouchant C, et al (2022) SAR and optical images correlation illuminates post-seismic landslide motion after the Mw 7.8 Gorkha earthquake (Nepal). Sci Rep 12:6266. https://doi.org/10.1038/s41598-022-10016-2

Lacroix P, Handwerger AL, Bièvre G (2020) Life and death of slow-moving landslides. Nat Rev Earth Environ 1:404–419. https://doi.org/10.1038/s43017-020-0072-8

Lanari R, Casu F, Manzo M, et al (2007) An Overview of the Small BAseline Subset Algorithm: A DInSAR Technique for Surface Deformation Analysis. In: Wolf D, Fernández J (eds) Deformation and Gravity Change: Indicators of Isostasy, Tectonics, Volcanism, and Climate Change. Birkhäuser, Basel, pp 637–661

Lasserre, C., Peltzer, G., Crampé, F., Klinger, Y., Van der Woerd, J., Tapponnier, P., 2005. Coseismic deformation of the 2001 M-w=7.8 Kokoxili earthquake in Tibet, measured by synthetic aperture radar interferometry. J. Geophys. Res.-Solid Earth 110.

Lauterjung, J., Münch, U. and Rudloff, A., 2010. The challenge of installing a tsunami early warning system in the vicinity of the Sunda Arc, Indonesia. Nat. Hazards Earth Syst. Sci., 10(4): 641-646. DOI: 10.5194/nhess-10-641-2010

Le Corvec, N. and Walter, T.R., 2009. Volcano spreading and fault interaction influenced by rift zone intrusions: Insights from analogue experiments analyzed with digital image correlation technique.

Journal of Volcanology and Geothermal Research, 183(3): 170-182. DOI: 10.1016/j.jvolgeores.2009.02.006 Lee Y-H, Ryu J-H, Lee T-H, et al (2022) Failure Behavior Attributed to Internal Erosion Caused by Conduit Cracks in Homogeneous Embankment. Applied Sciences 12:6305. https://doi.org/10.3390/app12136305

Levina, V.I., Lander, A.V., Mityushkina, S.V., Chebrova, A.Yu., 2013. The seismicity of the Kamchatka region: 1962–2011. J. Volcanol. Seismol. 7, 37–57. https://doi.org/10.1134/S0742046313010053

Li X, Handwerger AL, Buscarnera G (2023) Viscoplastic modelling of rainfall-driven slow-moving landslides: application to California Coast Ranges. Landslides 20:1101–1113. https://doi.org/10.1007/s10346-023-02039-1

Li Z-L, Leng P, Zhou C, et al (2021) Soil moisture retrieval from remote sensing measurements: Current knowledge and directions for the future. Earth-Science Reviews 218:103673. https://doi.org/10.1016/j.earscirev.2021.103673

Li, Z., Elliott, J.R., Feng, W., Jackson, J.A., Parsons, B.E., Walters, R.J., 2011. The 2010 M W 6.8 Yushu (Qinghai, China) earthquake: Constraints provided by InSAR and body wave seismology. J. Geophys. Res. 116. https://doi.org/10.1029/2011JB008358

Lisowski, M. in Volcano Deformation (ed. Dzurisin, D.) 279–304 (Springer, 2007).

Liu X, Zhao C, Zhang Q, et al (2021) Three-dimensional and long-term landslide displacement estimation by fusing C- and L-band SAR observations: A case study in Gongjue County, Tibet, China. Remote Sensing of Environment 267:112745. https://doi.org/10.1016/j.rse.2021.112745

López-Comino, J. A. et al. Characterization of hydraulic fractures growth during the Aspo Hard Rock Laboratory experiment (Sweden). Rock Mech. Rock Eng. 50, 298–3001 (2017).

Løvholt F, Glimsdal S, Harbitz CB (2020) On the landslide tsunami uncertainty and hazard. Landslides 17:2301–2315. https://doi.org/10.1007/s10346-020-01429-z

Lucha, P., Cardona, F., Gutiérrez, F.& Guerrero, J. Natural and human-induced dissolution and subsidence processes in the salt outcrop of the Cardona Diapir (NE Spain). Environ Geol 53, 1023–1035 (2008).

Maccaferri, F., Richter, N. and Walter, T.R., 2017. The effect of giant lateral collapses on magma pathways and the location of volcanism. Nature Communications, 8(1): 1097. DOI: 10.1038/s41467-017-01256-2

Mancini, F., Stecchi, F., Zanni, M.& Gabbianelli, G. Monitoring ground subsidence induced by salt mining in the city of Tuzla (Bosnia and Herzegovina). Environ Geol 58, 381–389 (2009).

Mansour MF, Morgenstern NR, Martin CD (2011) Expected damage from displacement of slow-moving slides. Landslides 8:117–131. https://doi.org/10.1007/s10346-010-0227-7

Marano KD, Wald DJ, Allen TI (2010) Global earthquake casualties due to secondary effects: a quantitative analysis for improving rapid loss analyses. Nat Hazards 52:319–328. https://doi.org/10.1007/s11069-009-9372-5

Marquardt, D., 1963. An Algorithm for Least-Squares Estimation of Nonlinear Parameters. J. Soc. Ind. Appl. Math. 11, 431–441. https://doi.org/10.1137/0111030

Martinez, J. D., Johnson, K. S.& Neal, J. T. Sinkholes in Evaporite Rocks: Surface subsidence can develop within a matter of days when highly soluble rocks dissolve because of either natural or human causes. American Scientist 86, 38–51 (1998).

Martins, J. E. et al. 3D S-wave velocity imaging of Reykjanes Peninsula high-enthalpy geothermal fields with ambient-noise tomography. J. Volcanol. Geotherm. Res. 391, 106685 (2020).

Mazzanti P, Caporossi P, Muzi R (2020) Sliding Time Master Digital Image Correlation Analyses of CubeSat Images for landslide Monitoring: The Rattlesnake Hills Landslide (USA). Remote Sensing 12:592. https://doi.org/10.3390/rs12040592

Mebrahtu TK, Heinze T, Wohnlich S, Alber M (2022) Slope stability analysis of deep-seated landslides using limit equilibrium and finite element methods in Debre Sina area, Ethiopia. Bull Eng Geol Environ 81:403. https://doi.org/10.1007/s10064-022-02906-6

Mendiratta P, Gedam S (2018) Assessment of urban growth dynamics in Mumbai Metropolitan Region, India using object-based image analysis for medium-resolution data. Applied Geography 98:110–120. https://doi.org/10.1016/j.apgeog.2018.05.017

Mirmazloumi SM, Wassie Y, Navarro JA, et al (2022) Classification of ground deformation using sentinel-1 persistent scatterer interferometry time series. GIScience& Remote Sensing 59:374–392. https://doi.org/10.1080/15481603.2022.2030535

Mogi K (1958) Relations between the Eruptions of Various Volcanoes and the Deformations of the Ground Surfaces around them

Moretto S, Bozzano F, Mazzanti P (2021) The Role of Satellite InSAR for Landslide Forecasting: Limitations and Openings. Remote Sensing 13:3735. https://doi.org/10.3390/rs13183735

Motagh M, Roessner S, Akbari B, Behling R, Stefanova Vassileva M, Haghshenas-Haghighi M, and Ulrich-Wetzel H (2020) Landslides triggered by 2019 extreme rainfall and flood events in Iran: Results from satellite remote sensing and field survey, EGU General Assembly 2020, Online, 4–8 May 2020, EGU2020-10715, https://doi.org/10.5194/egusphere-egu2020-10715, 2020.

Motagh M, Wetzel H-U, Roessner S, Kaufmann H (2013) A TerraSAR-X InSAR study of landslides in southern Kyrgyzstan, Central Asia. Remote Sensing Letters 4:657–666. https://doi.org/10.1080/2150704X.2013.782111

Motagh, M. et al. Land subsidence in Iran caused by widespread water reservoir overexploitation. Geophysical Research Letters 35, (2008).

Motagh, M. et al. Quantifying groundwater exploitation induced subsidence in the Rafsanjan plain, southeastern Iran, using InSAR time-series and in situ measurements. Engineering Geology 218, 134–151 (2017).

Motagh, M., Hoffmann, J., Kampes, B., Baes, M., Zschau, J., 2007. Strain accumulation across the Gazikoy–Saros segment of the North Anatolian Fault inferred from Persistent Scatterer Interferometry and GPS measurements. Earth Planet. Sci. Lett. 255, 432–444. https://doi.org/10.1016/j.epsl.2007.01.003

Motagh, M., Schurr, B., Anderssohn, J., Cailleau, B., Walter, T.R., Wang, R., Villotte, J.-P., 2010. Subduction earthquake deformation associated with 14 November 2007, Mw 7.8 Tocopilla earthquake in Chile: Results from InSAR and aftershocks. Tectonophysics 490, 60–68. https://doi.org/10.1016/j.tecto.2010.04.033

Müller, R.D., Dyksterhuis, S., Rey, P., 2012. Australian paleo-stress fields and tectonic reactivation over the past 100 Ma. Aust. J. Earth Sci. 59, 13–28. https://doi.org/10.1080/08120099.2011.605801

Nappo N, Peduto D, Mavrouli O, et al (2019) Slow-moving landslides interacting with the road network: Analysis of damage using ancillary data, in situ surveys and multi-source monitoring data. Engineering Geology 260:105244. https://doi.org/10.1016/j.enggeo.2019.105244

Nielsen F (2016) Hierarchical Clustering. In: Nielsen F (ed) Introduction to HPC with MPI for Data Science. Springer International Publishing, Cham, pp 195–211

Nissen, E., Ghods, A., Karasözen, E., Elliott, J.R., Barnhart, W.D., Bergman, E.A., Hayes, G.P., Jamal-Reyhani, M., Nemati, M., Tan, F., Abdulnaby, W., Benz, H.M., Shahvar, M.P., Talebian, M., Chen, L., 2019. The 12 November 2017 Mw 7.3 Ezgeleh-Sarpolzahab (Iran) Earthquake and Active Tectonics of the Lurestan Arc. J. Geophys. Res. Solid Earth 124, 2124–2152.

Ogie RI, Pradhan B (2019) Natural Hazards and Social Vulnerability of Place: The Strength-Based Approach Applied to Wollongong, Australia. Int J Disaster Risk Sci 10:404–420. https://doi.org/10.1007/s13753-019-0224-y

Okada, Y., 1985. Surface deformation due to shear and tensile faults in a half-space. Bull. Seismol. Soc. Am. 75, 1135–1154.

Okeke AC-U, Wang F (2016) Critical hydraulic gradients for seepage-induced failure of landslide dams. Geoenvironmental Disasters 3:9. https://doi.org/10.1186/s40677-016-0043-z

Owen LA, Kamp U, Khattak GA, et al (2008) Landslides triggered by the 8 October 2005 Kashmir earthquake. Geomorphology 94:1–9. https://doi.org/10.1016/j.geomorph.2007.04.007

Pálmason, G. Crustal Structure of Iceland (Societas Scientarium Islandica, 1971). Pan B, Li K (2011) A fast digital image correlation method for deformation measurement. Optics and Lasers in Engineering 49:841–847. https://doi.org/10.1016/j.optlaseng.2011.02.023

Panizzo A, De Girolamo P, Di Risio M, et al (2005) Great landslide events in Italian artificial reservoirs. Natural Hazards and Earth System Sciences 5:733–740. https://doi.org/10.5194/nhess-5-733-2005

Paris, R., Switzer, A.D., Belousova, M., Belousov, A., Ontowirjo, B., Whelley, P.L. and Ulvrova, M., 2014. Volcanic tsunami: a review of source mechanisms, past events and hazards in Southeast Asia (Indonesia, Philippines, Papua New Guinea). Natural Hazards, 70(1): 447-470. DOI: 10.1007/s11069-013-0822-8

Parmar, H., Yarahmadi Bafghi, A.& Najafi, M. Impact of ground surface subsidence due to underground mining on surface infrastructure: the case of the Anomaly No. 12 Sechahun, Iran. Environ Earth Sci 78, 409 (2019).

Patrick MR, Houghton BF, Anderson KR, et al (2020) The cascading origin of the 2018 Kīlauea eruption and implications for future forecasting. Nat Commun 11:5646. https://doi.org/10.1038/s41467-020-19190-1

Pedoja, K., Bourgeois, J., Pinegina, T., Higman, B., 2006. Does Kamchatka belong to North America? An extruding Okhotsk block suggested by coastal neotectonics of the Ozernoi Peninsula, Kamchatka, Russia. Geology 34, 353–356. https://doi.org/10.1130/G22062.1

Peng M, Lu Z, Zhao C, et al (2022) Mapping land subsidence and aquifer system properties of the Willcox Basin, Arizona, from InSAR observations and

independent component analysis. Remote Sensing of Environment 271:112894. https://doi.org/10.1016/j.rse.2022.112894

Perski, Z., Hanssen, R., Wojcik, A.& Wojciechowski, T. InSAR analyses of terrain deformation near the Wieliczka Salt Mine, Poland. Engineering Geology 106, 58–67 (2009).

Petley D (2012) Global patterns of loss of life from landslides. Geology 40:927–930. https://doi.org/10.1130/G33217.1

Picarelli L, Lacasse S, Ho KKS (2021) The Impact of Climate Change on Landslide Hazard and Risk. In: Sassa K, Mikoš M, Sassa S, et al. (eds) Understanding and Reducing Landslide Disaster Risk: Volume 1 Sendai Landslide Partnerships and Kyoto Landslide Commitment. Springer International Publishing, Cham, pp 131–141

Picchiani M, Del Frate F, Schiavon G, Stramondo S (2012) Features extraction from SAR interferograms for tectonic applications. EURASIP Journal on Advances in Signal Processing 2012:155. https://doi.org/10.1186/1687-6180-2012-155

Pipitone C, Maltese A, Dardanelli G, et al (2018) Monitoring Water Surface and Level of a Reservoir Using Different Remote Sensing Approaches and Comparison with Dam Displacements Evaluated via GNSS. Remote Sensing 10:71. https://doi.org/10.3390/rs10010071

Piter A, Vassileva M, Haghshenas Haghighi M, Motagh M (2021) EXPLORING CLOUD-BASED PLATFORMS FOR RAPID INSAR TIME SERIES ANALYSIS. The International Archives of the Photogrammetry, Remote Sensing and Spatial Information Sciences XLIII-B3-2021:171–176. https://doi.org/10.5194/isprs-archives-XLIII-B3-2021-171-2021

Poland MP, Zebker HA (2022) Volcano geodesy using InSAR in 2020: the past and next decades. Bull Volcanol 84:27. https://doi.org/10.1007/s00445-022-01531-1

Poland, M.P., Peltier, A., Bonforte, A. and Puglisi, G., 2017. The spectrum of persistent volcanic flank instability: A review and proposed framework based on Kīlauea, Piton de la Fournaise, and Etna. Journal of Volcanology and Geothermal Research, 339: 63-80. DOI: 10.1016/j.jvolgeores.2017.05.004

Ponomareva, V., Melekestsev, I., Braitseva, O., Churikova, T., Pevzner, M., Sulerzhitsky, L., 2007. Late Pleistocene-Holocene volcanism on the Kamchatka Peninsula, Northwest Pacific Region, in: Eichelberger, J., Gordeev, E., Izbekov, P., Kasahara, M., Lees, J. (Eds.), Geophysical Monograph Series. American Geophysical Union, Washington, D. C., pp. 165–198. https://doi.org/10.1029/172GM15

Potyondy, D. O.& Cundall, P. A. A bonded-particle model for rock. International Journal of Rock Mechanics and Mining Sciences 41, 1329–1364 (2004).

Qu C, Zuo R, Shan X, et al (2017) Coseismic deformation of the 2016 Taiwan Mw6.3 earthquake using InSAR data and source slip inversion. Journal of Asian Earth Sciences 148:96–104. https://doi.org/10.1016/j.jseaes.2017.08.027

Rabus B, Eineder M, Roth A, Bamler R (2003) The shuttle radar topography mission—a new class of digital elevation models acquired by spaceborne radar. ISPRS Journal of Photogrammetry and Remote Sensing 57:241–262. https://doi.org/10.1016/S0924-2716(02)00124-7

Reigber, A., Moreira, J., 1997. Phase unwrapping by fusion of local and global methods, in: IGARSS'97. 1997 IEEE International Geoscience and Remote Sensing Symposium Proceedings. Remote Sensing - A Scientific Vision for Sustainable Development. Presented at the IGARSS'97. 1997 IEEE International Geoscience and Remote Sensing Sympo-

sium Proceedings. Remote Sensing - A Scientific Vision for Sustainable Development, pp. 869–871 vol.2. https://doi.org/10.1109/IGARSS.1997.615282

Riesgo Fernández, P., Rodríguez Granda, G., Krzemień, A., García Cortés, S.& Fidalgo Valverde, G. Subsidence versus natural landslides when dealing with property damage liabilities in underground coal mines. International Journal of Rock Mechanics and Mining Sciences 126, 104175 (2020).

Rizzoli P, Martone M, Gonzalez C, et al (2017) Generation and performance assessment of the global TanDEM-X digital elevation model. ISPRS Journal of Photogrammetry and Remote Sensing 132:119–139. https://doi.org/10.1016/j.isprsjprs.2017.08.008

Roccati A, Paliaga G, Luino F, et al (2020) Rainfall Threshold for Shallow Landslides Initiation and Analysis of Long-Term Rainfall Trends in a Mediterranean Area. Atmosphere 11:1367. https://doi.org/10.3390/atmos11121367

Rosi A, Tofani V, Tanteri L, et al (2018) The new landslide inventory of Tuscany (Italy) updated with PS-InSAR: geomorphological features and landslide distribution. Landslides 15:5–19. https://doi.org/10.1007/s10346-017-0861-4

Ruiz-Villanueva V, Allen S, Arora M, et al (2017) Recent catastrophic landslide lake outburst floods in the Himalayan mountain range. Progress in Physical Geography: Earth and Environment 41:3–28. https://doi.org/10.1177/0309133316658614

Rygus M, Novellino A, Hussain E, et al (2023) A Clustering Approach for the Analysis of InSAR Time Series: Application to the Bandung Basin (Indonesia). Remote Sensing 15:3776. https://doi.org/10.3390/rs15153776

Sæmundsson, K.& Sigurgeirsson, M. Á. in Náttúruvá á Íslandi (eds Sólnes, J. et al.) 379–401 (Viðlagatrygging Íslands/Háskólaútgáfan, 2013).

Sæmundsson, K., Jóhannesson, H., Hjartarson, Á., Kristinsson, S. G. & Sigurgeirsson, M. Á. Geological Map of Southwest Iceland, 1:100.000 (Iceland GeoSurvey, 2010).

Samieie-Esfahany S, Hanssen RF, van Thienen-Visser K, Muntendam-Bos A (2010) On the Effect of Horizontal Deformation on InSAR Subsidence Estimates. 677:39

Sangha, S., Peltzer, G., Zhang, A., Meng, L., Liang, C., Lundgren, P., Fielding, E., 2017. Fault geometry of 2015, Mw7.2 Murghab, Tajikistan earthquake controls rupture propagation: Insights from InSAR and seismological data. Earth Planet. Sci. Lett. 462, 132–141. https://doi.org/10.1016/j.epsl.2017.01.018

Schaefer LN, Di Traglia F, Chaussard E, et al (2019) Monitoring volcano slope instability with Synthetic Aperture Radar: A review and new data from Pacaya (Guatemala) and Stromboli (Italy) volcanoes. Earth-Science Reviews 192:236–257. https://doi.org/10.1016/j.earscirev.2019.03.009

Schmincke H-U (2004) Volcanism. Springer Science & Business Media

Scholz CH (2019) The Mechanics of Earthquakes and Faulting. Cambridge University Press Scott, C.P., Arrowsmith, R., Nissen, E., Lajoie, L., Maruyama, T., Chiba, T., 2018. The M7 2016 Kumamoto, Japan, Earthquake: 3-D Deformation Along the Fault and Within the Damage Zone Constrained From Differential Lidar Topography. J. Geophys. Res. Solid Earth 123, 6138–6155. https://doi.org/10.1029/2018JB015581

Seropian G, Kennedy BM, Walter TR, et al (2021) A review framework of how earthquakes trigger volcanic eruptions. Nat Commun 12:1004. https://doi.org/10.1038/s41467-021-21166-8

Serrano-Juan, A., Pujades, E., Vázquez-Suñè, E., Crosetto, M. & Cuevas-González, M. Leveling vs. InSAR in urban underground construction monitoring: Pros and cons. Case of la sagrera railway station (Barcelona, Spain). Engineering Geology 218, 1–11 (2017).

Sevil, J. et al. Sinkhole investigation in an urban area by trenching in combination with GPR, ERT and high-precision leveling. Mantled evaporite karst of Zaragoza city, NE Spain. Engineering Geology 231, 9–20 (2017).

Sharma K, Saraf AK, Das J, et al (2018) Mapping and Change Detection Study of Nepal-2015 Earthquake Induced Landslides. J Indian Soc Remote Sens 46:605–615. https://doi.org/10.1007/s12524-017-0720-8

Shi X, Wang J, Jiang M, et al (2022) Extreme rainfall-related accelerations in landslides in Danba County, Sichuan Province, as detected by InSAR. International Journal of Applied Earth Observation and Geoinformation 115:103109. https://doi.org/10.1016/j.jag.2022.103109

Shirzaei M, Freymueller J, Törnqvist TE, et al (2021) Measuring, modelling and projecting coastal land subsidence. Nat Rev Earth Environ 2:40–58. https://doi.org/10.1038/s43017-020-00115-x

Sibson, R. H. Preparation zones for large crustal earthquakes consequent on fault-valve action. Earth Planets Space https://doi.org/10.1186/s40623-020-01153-x (2020).

Sigmundsson, F. et al. Unexpected large eruptions from buoyant magma bodies within viscoelastic crust. Nat. Commun. 11, 2403 (2020).

Simeoni U, Tessari U, Corbau C, et al (2017) Impact of land subsidence due to residual gas production on surficial infrastructures: The Dosso degli Angeli field study (Ravenna, Northern Italy). Engineering Geology 229:1–12. https://doi.org/10.1016/j.enggeo.2017.09.008

Simon RN, Tormos T, Danis P-A (2015) Very high spatial resolution optical and radar imagery in tracking water level fluctuations of a small inland reservoir. International Journal of Applied Earth Observation and Geoinformation 38:36–39. https://doi.org/10.1016/j.jag.2014.12.007

Singhroy V (2009) Satellite Remote Sensing Applications for Landslide Detection and Monitoring. In: Sassa K, Canuti P (eds) Landslides – Disaster Risk Reduction. Springer, Berlin, Heidelberg, pp 143–158 Skempton, A. W. & Macdonald, D. H. The allowable settlements of buildings. Proceedings of the Institution of Civil Engineers 5, 727–768 (1956).

Smith, B., Sandwell, D., 2003. Coulomb stress accumulation along the San Andreas Fault system: COULOMB STRESS ALONG THE SAN ANDREAS FAULT. J. Geophys. Res. Solid Earth 108. https://doi.org/10.1029/2002JB002136

Solano-Rojas, D., Wdowinski, S., Cabral-Cano, E. & Osmanoğlu, B. Detecting differential ground displacements of civil structures in fast-subsiding metropolises with interferometric SAR and band-pass filtering. Sci Rep 10, 15460 (2020).

Sreejith, K. M., Agrawal, R. & Rajawat, A. S. Constraints on the location, depth and yield of the 2017 September 3 North Korean nuclear test from InSAR measurements and modelling. Geophysical Journal International 220, 345–351 (2020).

Stefánsson, R. et al. Earthquake prediction research in the South Iceland seismic zone and the SIL project. Bull. Seism. Soc. Am. 83, 696–716 (1993).

Sudhaus, H., Sigurjón, J., 2009. Improved source modelling through combined use of InSAR and GPS under consideration of correlated data errors: application to the June 2000 Kleifarvatn earthquake, Iceland. Geophys. J. Int. 176, 389–404. https://doi.org/10.1111/j.1365-246X.2008.03989.x

Syamsidik, Benazir, Luthfi, M., Suppasri, A. and Comfort, L.K., 2020. The 22 December 2018 Mount Anak Krakatau volcanogenic tsunami on Sunda Strait coasts, Indonesia:

tsunami and damage characteristics. Nat. Hazards Earth Syst. Sci., 20(2): 549-565. DOI: 10.5194/nhess-20-549-2020

Talwani P (2017) On the nature of intraplate earthquakes. J Seismol 21:47–68. https://doi.org/10.1007/s10950-016-9582-8

Tan Q, Bai M, Zhou P, et al (2021) Geological hazard risk assessment of line landslide based on remotely sensed data and GIS. Measurement 169:108370. https://doi.org/10.1016/j.measurement.2020.108370

ten Brink, U., 2004. Stress interaction between subduction earthquakes and forearc strike-slip faults: Modeling and application to the northern Caribbean plate boundary. J. Geophys. Res. 109. https://doi.org/10.1029/2004JB003031

Teshebaeva K, Roessner S, Echtler H, et al (2015) ALOS/PALSAR InSAR Time-Series Analysis for Detecting Very Slow-Moving Landslides in Southern Kyrgyzstan. Remote Sensing 7:8973–8994. https://doi.org/10.3390/rs70708973

Timofeev, V.Yu., Ardyukov, D.G., Solov'ev, V.M., Shibaev, S.V., Petrov, A.F., Gornov, P.Yu., Shestakov, N.V., Boiko, E.V., Timofeev, A.V., 2012. Plate boundaries in the Far East region of Russia (from GPS measurement, seismic-prospecting, and seismological data). Russ. Geol. Geophys. 53, 376–391. https://doi.org/10.1016/j.rgg.2012.03.002

Toda, S., Stein, R. S. & Sagiya, T. Evidence from the ad 2000 Izu Islands earthquake swarm that stressing rate governs seismicity. Nature 419, 58–61 (2002).

Tomás R, Li Z (2017) Earth Observations for Geohazards: Present and Future Challenges. Remote Sensing 9:194. https://doi.org/10.3390/rs9030194

Tong, X., Sandwell, D., Luttrell, K., Brooks, B., Bevis, M., Shimada, M., Foster, J., Smalley, R., Parra, H., Báez Soto, J.C., Blanco, M., Kendrick, E., Genrich, J., Caccamise, D.J., 2010. The 2010 Maule, Chile earthquake: Downdip rupture limit revealed by space geodesy: DOWNDIP RUPTURE MAULE, CHILE EARTHQUAKE. Geophys. Res. Lett. 37, n/a-n/a. https://doi.org/10.1029/2010GL045805

Torrence C, Compo GP (1998) A Practical Guide to Wavelet Analysis. Bulletin of the American Meteorological Society 79:61–78. https://doi.org/10.1175/1520-0477(1998)079<0061:APGTWA>2.0.CO;2

Torres DL, Turnes JN, Soto Vega PJ, et al (2021) Deforestation Detection with Fully Convolutional Networks in the Amazon Forest from Landsat-8 and Sentinel-2 Images. Remote Sensing 13:5084. https://doi.org/10.3390/rs13245084

Tosi L, Teatini P, Carbognin L, Brancolini G (2009) Using high resolution data to reveal depth-dependent mechanisms that drive land subsidence: The Venice coast, Italy. Tectonophysics 474:271–284. https://doi.org/10.1016/j.tecto.2009.02.026

Tschuchnigg F, Schweiger HF, Sloan SW (2015) Slope stability analysis by means of finite element limit analysis and finite element strength reduction techniques. Part I: Numerical studies considering non-associated plasticity. Computers and Geotechnics 70:169–177. https://doi.org/10.1016/j.compgeo.2015.06.018

Tu G, Huang D, Deng H (2019) Reactivation of a huge ancient landslide by surface water infiltration. J Mt Sci 16:806–820. https://doi.org/10.1007/s11629-018-5315-5

Tzampoglou P, Ilia I, Karalis K, et al (2023) Selected Worldwide Cases of Land Subsidence Due to Groundwater Withdrawal. Water 15:1094. https://doi.org/10.3390/w15061094

UNCTAD 2022 https://hbs.unctad.org/total-and-urban-population/

UNDRR 2022 https://www.preventionweb.net/understanding-disaster-risk/disaster-losses-and-statistics

Uwihirwe J, Riveros A, Wanjala H, et al (2022) Potential of satellite-derived hydrometeorological information for landslide initiation thresholds in Rwanda. Natural Hazards and Earth System Sciences 22:3641–3661. https://doi.org/10.5194/nhess-22-3641-2022

van Natijne AL, Bogaard TA, van Leijen FJ, et al (2022) World-wide InSAR sensitivity index for landslide deformation tracking. International Journal of Applied Earth Observation and Geoinformation 111:102829. https://doi.org/10.1016/j.jag.2022.102829

Varga P, Krumm F, Riguzzi F, et al (2012) Global pattern of earthquakes and seismic energy distributions: Insights for the mechanisms of plate tectonics. Tectonophysics 530–531:80–86. https://doi.org/10.1016/j.tecto.2011.10.014

Varugu, B. and Amelung, F., 2021. Southward growth of Mauna Loa's dike-like magma body driven by topographic stress. Scientific Reports, 11(1): 9816. DOI: 10.1038/s41598-021-89203-6

Vassileva M, Al-Halbouni D, Motagh M, et al (2021) A decade-long silent ground subsidence hazard culminating in a metropolitan disaster in Maceió, Brazil. Sci Rep 11:7704. https://doi.org/10.1038/s41598-021-87033-0

Vassileva M, Giulio Tonolo F, Riccardi P, et al (2017) Satellite SAR interferometric techniques in support to emergency mapping. European Journal of Remote Sensing 50:464–477. https://doi.org/10.1080/22797254.2017.1360155

Verberne M, Koster K, Lourens A, et al (2023) Disentangling Shallow Subsidence Sources by Data Assimilation in a Reclaimed Urbanized Coastal Plain, South Flevoland Polder, the Netherlands. Journal of Geophysical Research: Earth Surface 128:e2022JF007031. https://doi.org/10.1029/2022JF007031

Verdecchia A, Pace B, Visini F, et al (2018) The Role of Viscoelastic Stress Transfer in Long-Term Earthquake Cascades: Insights After the Central Italy 2016–2017 Seismic Sequence. Tectonics 37:3411–3428. https://doi.org/10.1029/2018TC005110

Violay, M. et al. An experimental study of the brittle–ductile transition of basalt at oceanic crust pressure and temperature conditions. J. Geophys. Res. Solid Earth https://doi.org/10.1029/2011JB008884 (2012) .

Walsh, J. B. & Rice, J. R. Local changes in gravity resulting from deformation. J. Geophys. Res. 84, 165–170 (1979).

Walter, T.R., Haghshenas Haghighi, M., Schneider, F.M., Coppola, D., Motagh, M., Saul, J., Babeyko, A., Dahm, T., Troll, V.R., Tilmann, F., Heimann, S., Valade, S., Triyono, R., Khomarudin, R., Kartadinata, N., Laiolo, M., Massimetti, F. and Gaebler, P., 2019. Complex hazard cascade culminating in the Anak Krakatau sector collapse. Nature Communications, 10(1): 4339. DOI: 10.1038/s41467-019-12284-5

Wang H, Elliott JR, Craig TJ, et al (2014) Normal faulting sequence in the Pumqu-Xainza Rift constrained by InSAR and teleseismic body-wave seismology. Geochemistry, Geophysics, Geosystems 15:2947–2963. https://doi.org/10.1002/2014GC005369

Wang L, Qiu H, Zhou W, et al (2022) The Post-Failure Spatiotemporal Deformation of Certain Translational Landslides May Follow the Pre-Failure Pattern. Remote Sensing 14:2333. https://doi.org/10.3390/rs14102333

Wang Y, Tang H, Huang J, et al (2022) A comparative study of different machine learning methods for reservoir landslide displacement prediction. Engineering Geology 298:106544. https://doi.org/10.1016/j.enggeo.2022.106544

Wang, R. & Küumpel, H.-J. Efficient modeling of strongly coupled, slow deformation processes in a multilayered half-space. Geophysics 68, 705–717 (2003).

Ward, S.N. and Day, S., 2001. Cumbre Vieja Volcano—Potential collapse and tsunami at La Palma, Canary Islands. Geophysical Research Letters, 28(17): 3397-3400. DOI: 10.1029/2001GL013110

Weir, N. R. W. et al. Crustal structure of the northern Reykjanes Ridge and the Reykjanes Peninsula, southwest Iceland. J. Geophys. Res. 106, 6347–6368 (2001).

Weis, P., Driesner, T.&Heinrich, C. A. Porphyry–copper ore shells form at stable pressure–temperature fronts within dynamic fluid plumes. Science https://doi.org/10.1126/science.1225009 (2012).

Wells, D.L., Coppersmith, K.J., 1994. New empirical relationships among magnitude, rupture length, rupture width, rupture area, and surface displacement. Bull. Seismol. Soc. Am. 84, 974–1002.

Williams, R., Rowley, P. and Garthwaite, M.C., 2019. Reconstructing the Anak Krakatau flank collapse that caused the December 2018 Indonesian tsunami. Geology, 47(10): 973-976. DOI: 10.1130/G46517.1

World Bank 2022 https://pip.worldbank.org/home

Wright, T.J., Lu, Z., Wicks, C., 2003. Source model for the Mw 6.7, 23 October 2002, Nenana Mountain Earthquake (Alaska) from InSAR. Geophys. Res. Lett. 30. https://doi.org/10.1029/2003GL018014

Wu S, Hu X, Zheng W, et al (2022) Displacement behaviour and potential impulse waves of the Gapa landslide subjected to the Jinping Reservoir fluctuations in Southwest China. Geomorphology 397:108013. https://doi.org/10.1016/j.geomorph.2021.108013

Wyss, M., Wiemer, S., 2000. Change in the Probability for Earthquakes in Southern California Due to the Landers Magnitude 7.3 Earthquake. Science 290, 1334–1338. https://doi.org/10.1126/science.290.5495.1334

Xia Z, Motagh M, Li T, et al (2023) A methodology to characterize 4D post-failure slope instability dynamics using remote sensing measurements: A case study of the Aniangzhai landslide in Sichuan, Southwest China. ISPRS Journal of Photogrammetry and Remote Sensing 196:402–414. https://doi.org/10.1016/j.isprsjprs.2023.01.006

Xiong Z, Feng G, Feng Z, et al (2020) Pre- and post-failure spatial-temporal deformation pattern of the Baige landslide retrieved from multiple radar and optical satellite images. Engineering Geology 279:105880. https://doi.org/10.1016/j.enggeo.2020.105880

Xu W, Xie L, Bürgmann R, et al (2023) The 2022 Eruption of Wolf Volcano, Galápagos: The Role of Caldera Ring-Faults During Magma Transfer From InSAR Deformation Data. Geophysical Research Letters 50:e2023GL103704. https://doi.org/10.1029/2023GL103704

Xu Y, Kim J, George DL, Lu Z (2019) Characterizing Seasonally Rainfall-Driven Movement of a Translational Landslide using SAR Imagery and SMAP Soil Moisture. Remote Sensing 11:2347. https://doi.org/10.3390/rs11202347

Xu, C., Liu, Y., Wen, Y., Wang, R., 2010. Coseismic Slip Distribution of the 2008 Mw 7.9 Wenchuan Earthquake from Joint Inversion of GPS and InSAR Data Coseismic Slip Distribution of the Wenchuan Earthquake from Joint Inversion of GPS and InSAR Data. Bull. Seismol. Soc. Am. 100, 2736–2749. https://doi.org/10.1785/0120090253

Yang K-H, Nguyen TS, Rahardjo H, Lin D-G (2021) Deformation characteristics of unstable shallow slopes triggered by rainfall infiltration. Bull Eng Geol Environ 80:317–344. https://doi.org/10.1007/s10064-020-01942-4

Yao J, Yao X, Liu X (2022) Landslide Detection and Mapping Based on SBAS-InSAR and PS-InSAR: A Case Study in Gongjue County, Tibet, China. Remote Sensing 14:4728.

https://doi.org/10.3390/rs14194728 Yechieli, Y., Abelson, M. & Baer, G. Sinkhole formation and subsidence along the Dead Sea coast, Israel. Hydrogeol J 24, 601–612 (2016).

Yi Z, Xingmin M, Allesandro N, et al (2022) Characterization of pre-failure deformation and evolution of a large earthflow using InSAR monitoring and optical image interpretation. Landslides 19:35–50. https://doi.org/10.1007/s10346-021-01744-z

Yin Y, Huang B, Wang W, et al (2016) Reservoir-induced landslides and risk control in Three Gorges Project on Yangtze River, China. Journal of Rock Mechanics and Geotechnical Engineering 8:577–595. https://doi.org/10.1016/j.jrmge.2016.08.001

Zhang B, Zhu W, Ding X, et al (2022a) A review of methods for mitigating ionospheric artifacts in differential SAR interferometry. Geodesy and Geodynamics 13:160–169. https://doi.org/10.1016/j.geog.2021.12.001

Zhang K, Gong F, Li L, et al (2022b) Mapping the Long-Term Evolution of the Post-Event Deformation of the Guang'an Village Landslide, Chongqing, China Using Multi-baseline InSAR Techniques. Forests 13:887. https://doi.org/10.3390/f13060887

Zhang Y, Zhang Z, Xue S, et al (2020a) Stability analysis of a typical landslide mass in the Three Gorges Reservoir under varying reservoir water levels. Environ Earth Sci 79:42. https://doi.org/10.1007/s12665-019-8779-x

Zhang Y, Zhu S, Tan J, et al (2020b) The influence of water level fluctuation on the stability of landslide in the Three Gorges Reservoir. Arab J Geosci 13:845. https://doi.org/10.1007/s12517-020-05828-3

Zheng Y, Chen C, Liu T, et al (2019) Analysis of a retrogressive landslide with double sliding surfaces: a case study. Environ Earth Sci 79:21. https://doi.org/10.1007/s12665-019-8741-y

Zhu L, Gong H, Li X, et al (2015) Land subsidence due to groundwater withdrawal in the northern Beijing plain, China. Engineering Geology 193:243–255. https://doi.org/10.1016/j.enggeo.2015.04.020

Zhu, C. et al. Assessments of land subsidence along the Rizhao–Lankao high-speed railway at Heze, China, between 2015 and 2019 with Sentinel-1 data. Natural Hazards and Earth System Sciences 20, 3399–3411 (2020).

Zhuo L, Dai Q, Han D, et al (2019) Evaluation of Remotely Sensed Soil Moisture for Landslide Hazard Assessment. IEEE Journal of Selected Topics in Applied Earth Observations and Remote Sensing 12:162–173. https://doi.org/10.1109/JSTARS.2018.2883361

Zorn EU, Le Corvec N, Varley NR, et al (2019) Load Stress Controls on Directional Lava Dome Growth at Volcán de Colima, Mexico. Frontiers in Earth Science 7:

Zorn, E.U., Walter, T.R., Heap, M.J. and Kueppers, U., 2020. Insights into lava dome and spine extrusion using analogue sandbox experiments. Earth and Planetary Science Letters, 551: 116571. DOI: 10.1016/j.epsl.2020.116571

List of Figures

2.1 Scheme of the methodology pillars 7

2.2 InSAR deformation sensitivity from ascending and descending orbital path: (a) with respect to the azimuth direction; (b) concerning the LOS direction; positive movement in red and negative movement in blue, vertical component (in green uplift movement and in violet downward movement) and east-west component (in orange from west to east movement) (from Vassileva et al. 2017) 9

2.3 Scheme of DIC basic principle 11

2.4 Mogi source scheme and simulated velocities in (a) vertical and (b) horizontal components and (c) ascending and (d) descending LOS directions (adapted from Fuhrmann and Garthwaite 2019) 12

2.5 Rectangle source model scheme and simulated interferograms using the Okada forward mode for a normal fault (upper row), strike-slip fault (middle row) and thrust fault (lower row) (adapted Picchiani et al. 2012 and Atzori et al. 2014) 13

3.1 Fieldwork photos depicting building and infrastructure damages due to land subsidence: **a** and **b** from Maceio' (Brazil) taken in December 2022; **c**, **d** and **e** from Hambach area (Germany) taken by M. Vassileva in June 2023 . 15

3.2 Scheme of land subsidence causes 16

3.3 Land subsidence over Manila region (Philippines) derived from Sentinel-1 ARIA products for the period between October 2014 and March 2020. **a**, average displacement ascending LOS velocity maps; red triangles represent the displacement time series plotted in **c**; **b**, InSAR connection graphs. Background imagery Google Earth Image Landsat/Copernicus, Map data ©2021. (adapted after Piter et al. 2021) 18

3.4 Fieldwork photos depicting landslide affected areas: **a**, Dorud (Lorestan, Iran) taken in September 2019;**b**, and **c**, Golestan Province (Iran) taken in September 2019;**d**, Maceio' (Brazil) taken by M. Vassileva in December 2022 19

3.5 Scheme of landslide main external driving factors 20

3.6 Scheme of landslide main features (after Idaho Geological Survey) 20

3.7 Regional scale average ascending LOS velocity for 2020-2021 using Sentinel-1 data over north-west Iran; zoomed rectangles show some landslide-affected slopes. Data processed by M. Vassileva. 21

3.8 InSAR LOS sensitivity to slope motion for different slope angles. **a**, ascending and **b**, descending acquisition geometries; jet-coloured arrows define the amount of ground deformation of the unit vector detectable from ascending **c** and descending **d** viewing geometries for different downslope motions; negative values (hot colours) indicate slope moving away from the sensor, and positive values (cold colours) indicate slope moving toward the sensor; grey arrows define the deformation of the unit vector; the grey area defines the slope angles with no sensitivity in LOS (adapted after Aslan et al. 2020). 22

3.9 InSAR LOS sensitivity to slope motion for different aspect angles. **a**, ascending and **b**, descending acquisition geometries; jet-coloured arrows define the amount of ground deformation of the unit vector detectable from ascending **c** and descending **d** viewing geometries for different aspect motion directions; negative values (hot colours) indicate slope moving away from the sensor, and positive values (cold colours) indicate slope moving toward the sensor; grey arrows define the deformation of the unit vector (adapted after Aslan et al. 2020). 23

3.10 **a**, Scheme of the plate tectonic main activities (after ©2023 Encyclopædia Britannica, Inc.). **b**; global distribution of major earthquakes and active volcanoes (after thegeographeronline.net under the licence CC BY-NC-SA 4.0 Deed). 25

3.11 Private visit photos depicting earthquake-affected areas: **a**, surface rupture of the fault along Monte Vettor (central Italy) caused by the 24th of August 2016 earthquake; **b** and **c** building damages caused by the same earthquake in a nearby village. Photos taken by M. Vassileva in August 2023. 26

3.12 Types of faults (after ©2006 Brooks/Cole - Thomson). 27

3.13 InSAR and pixel offset descending LOS ground displacement maps of the February 6 2023 Turkey/Syrian earthquake; same Sentinel-1 image pairs, orbit 21, acquired on January 29 and February 10 2023. InSAR processed by M. Vassileva. Pixel offset processed by Mahmud Haghshenas Haghighi. Active fault from Emre et Al. 2013. Epicentres of main shocks and moment tensors from Geofon. Background Google Satellite Map (Imagery @2023 TerraMetrics). 28

3.14 **a**, volcanic scheme with main features; **a**, types of volcanic edifice related to magma viscosity and type of eruption (source National Park Service / Astrid Garcia) 30

3.15 Fieldwork photos. **a**, active dome growth on Shiveluch (Russia); **b**, Fagradalsfjall 2023 effusive eruption (Iceland); **c**, sinkhole formations over lava and tephra deposits in Askja (Iceland); **d**, landslide on Askja crater (Iceland); **e**, rock glacier instabilities at Hekla summit (Iceland); **f**, hydrothermal alterations at the eastern slope of Askja crater. Photos taken by M. Vassileva in July/August 2023 31

3.16 InSAR ground displacement observations for the 3 weeks before the 19th March Fagradalsfjall 2021 eruption; Sentinel-1 data in ascending and descending geometry were used; vertical and horizontal ground displacement components were derived by combining the two LOS geometries; positive values in Ascending and Descending maps for motion away from the sensor, positive values for uplift motion and positive values for eastward motion. Data processed by M. Vassileva. 32

4.1 (a) Overview of the study area. Yellow, orange, and red polygons represent respectively areas with low, medium and high concentrations of fractures in buildings and infrastructures (assessment conducted by CPRM in 201825). Blue and magenta diamonds show the locations of all installed salt wells since 1970. Specifically, magenta diamonds highlight the two cavities used in the DEM. The White dashed polygon is the area in Fig. 4.3a. Inset shows the geographical location of Maceió. (b) Simplified geological stratigraphic model and table of the rock material properties used in this study. Background for (a) Google Earth CNES/Airbus imagery. (a) was plotted in QGIS (v 3.16, https://www.qgis.org/en/site/). 35

4.2 InSAR time series results. (a-c) Cumulative vertical subsidence maps obtained by projecting the LOS component into vertical only and combining in time and space all available displacement datasets. Red, green, and black dots show the locations of the time series plotted in Fig. 4.6 respectively point 1 (in the main subsiding area), point 2 (in the minor subsiding area) and point 3 (in the hypothetically stable area). White lines show profiles 1 and 2 plotted in (d) where the blue line refers to the period 07.2004-01.2011, green for 07.2004-03.2015, and red for 07.2004-11.2020. Ascending and descending displacements have been combined for the periods where both geometries were available to retrieve (e-i) vertical and (l-p) horizontal average displacement velocities. The horizontal negative values refer to westward motion. Background Google Earth CNES/Airbusimagery. The figures (except d) were plotted in QGIS (v. 3.16, https://www.qgis.org/en/site/). 40

4.3 Inverse numerical model results. (a) Horizontal location of the best-fitting source models between 2016 and 2019: triangle symbology for point source model and dashed rectangle symbology for rectangular crack source model with different colours expressing the different dates as in legend. Dashed white isolines represent the cumulative displacement for the period 07.2004-11.2020. Magenta diamonds show the detailed location of the two cavities (M31D and M30D) modelled in DEM. The blue-white line shows the profile P1 used for the DEM subsidence simulation (see Figs. 4b and 5b). (b) Vertical profile reveals the depth of the best-fitting source models: triangles for point pressure source and rectangles for rectangle crack source (same colour convention indicating the date). X-axes is an indicative NW-SE along with the coast profile, not in scale. (c) InSAR ascending (Alos-2 data) and descending (Sentinel-1 data) observations for the period 2018-2019, best-fit model and relative residuals calculated by subtracting the model to the observations. PS indicates point source model; RS indicates rectangle crack source model. Background Google Earth CNES/Airbus imagery. The figures (except b) were plotted in QGIS (v. 3.16, https://www.qgis.org/en/site/). 43

4.4 Simulated DEM subsidence models for pressurized cavity scenario (S1, P = 2.758 MPa). (a) Crack and fracture evolution representation of the four stages of cavity collapse is shown in a black-purple-yellow colour scale; the stratified background represents the geological layering model (see data and methods). (b) Induced surface deformations for the four stages (black-purple-yellow colour scale) compared to InSAR surface subsidence results along profile P1 (Fig. 4.3a). The figures were plotted using Matplotlib python library using data from simulations and InSAR time series data along profile P1. 44

4.5 Simulated DEM subsidence models for depressurized cavity scenario (S2, P = 1.5 MPa). (a) Maximum compressive stress representation of the four stages of cavity collapse; blue colour shows higher values of compressive stress. (b) Induced surface deformations for the four stages (black-purple-yellow colour scale) compared to InSAR surface subsidence results along profile P1 (Fig. 4.3a). The figures were plotted using Matplotlib python library using data from simulations and InSAR time series data along profile P1. 45

4.6 Long and short term vertical displacement time-series and local rainfall data. The location of the plotted points is shown in Fig. 4.2a. (a) 16-year long time-series: red (point 1) in the area of maximum displacement and green (point 2) in the minor subsiding region. Displacement values are on the right axis. Rainfall values are on the left axis: black dots and lines for local station mean values; purple dots and lines for CHIRPS mean values; blue histogram for local station monthly cumulative precipitations; pink histogram for CHIRPS monthly cumulative precipitations. (b) 4-year short time series for points 1 and 2 and histogram of local station monthly cumulative precipitations. Black-lines are the linear displacement interpolation representing the velocity trends; white dots show changes in a linear trend. (c) Seasonal trends: red and green dots of the residual estimated by subtracting a 3-grad polynomial trend from the displacement time-series for point 1 (point 1 res.) and point 2 (point 2 res.) respectively and black dots showing the displacement time-series of point 3 in a potentially stable area. The figures were plotted using Matplotlib python library using InSAR time series and precipitation data. 47

4.7 Subsidence hazard based on angular distortion values (horizontal strain). (a-d) Cumulative hazard maps are classified into five levels based on an appropriate threshold (see data and method). (e) Hazard simulation of accumulated subsidence predicted by adding one further year (11.2020 - 11.2021) assuming constant displacement rate same as 2019-2020 (f) Angular distortion velocity, estimated over the period 2016-2020, highlights in red the areas with faster hazard evolution. Background Google Earth CNES/Airbus imagery. The figures were plotted in QGIS (v. 3.16, https://www.qgis.org/en/site/). 49

5.1 Overview of the regional setting and landslide area. (a) Satellite optical image (Google ©Imagery CNES/ Airbus Maxar Technologies) and country scale inset map (Natural Earth I with Shaded Relief and Water © 2012. Natural Earth). (b) Geological map modified after ©Geological Survey of Iran for the Dozin geological map 1:100000 using remote sensing data interpretation; Qcf indicates clay flat, Ngm indicates red to brownish marl, siltstone and sandstone with intercalations of conglomerate (Upper red Formation equivalent), Jmz indicates Pale-gray, thick-bedded to massive cherty limestone (Mozduran Formation); Jcb indicates Pale-gray to cream, thin to medium bedded argillaceous limestone with marl intercalations (Chamanbid Formation). 55

5.2 Field photos of the landslide area from July 2019: (a) damaged buildings and sag ponds; (b) damaged road on the upper part of the landslide; (c) post-failure satellite optical images over Hoseynabad-e Kalpush village from June 2019 (Google ©Imagery CNES/ Airbus Maxar Technologies) same extent as red rectangle in Fig. 5.1a; topographic contours (white lines) derived from the 30 m resolution Shuttle Radar Topography Mission (SRTM) digital elevation model; yellow rectangle locate the dam; magenta outline shows the landslide extent; (d) sag ponds in proximity to the northeastern flank; (e) tension cracks and fissures on the landslide northeastern scarp (f) and (g) Southwestern adjacent old landslide showing gully erosion features. 56

5.3 Time distribution of the SAR and optical satellite remote sensing acquisitions. The abbreviations indicate Land-8 (Landsat-8), PLS (PlanetScope), Env (Envisat), S-1 (Sentinel-1), asc (ascending) and desc (descending) orbit paths. The data used for the reservoir water elevation extraction are indicated with "wl". 58

5.4 Flowchart of the main data and processing workflow. Abbreviation: DIC-FFT (Digital Image Correlation with Fast Fourier Transform), MT-InSAR (Multi-temporal Synthetic Aperture Radar Interferometry), NIR (near-infrared), SLC (single-look-complex), CHIRPS (Climate Hazards Group InfraRed Precipitation with Station data), CWT (Continuous Wavelet Transform), XWT (Cross Wavelet Transform), PCA (Principal Component Analysis), FastICA (Fast Independent Component Analysis). Bold rectangles show the input data. The red star indicates the processing steps where the Digital Elevation Model was used as input. 59

5.5 Precipitation dataset from CHIRPS and reservoir water elevation derived from optical remote sensing data. (a) Monthly precipitation since 2000 (blue histograms) and reservoir water elevation (purple area); black lines mark the start of the landslide main failure. (b) Annual precipitation; the horizontal blue dotted line shows the estimated 22-year average annual precipitation. (c) 22-year monthly average precipitation. 63

5.6 Landsat-8 and PlanetScope (Near Infrared band) show the reservoir impoundment. The white line shows the profile used to estimate the water height on the northern shoreline (same profile as in Fig. 5.1a); the yellow triangle depicts the dam structure location; white arrow indicates North. . . 64

5.7 Cross Wavelet Transform between monthly precipitation and reservoir water elevation for the period April 2013 to December 2021. Color scale indicates the magnitude squared coherence; arrows indicate the phase difference between the two time series: arrows directed toward right for in-phase relationship; arrows directed toward left for anti-phase relationship. White dashed line shows the cone of influence where the edge effects might disturb the wavelet analysis results. 65

5.8 Pre-dam cumulative ground displacement from ENVISAT data. a) LOS ascending and b) LOS descending radar geometries; positive values in (a) and (b) refer to displacement toward the sensor. White dashed outlines depict the landslide-affected area. The landslide cluster partition is shown in a). The map extent is the same as in Fig. 5.2c. Background Google ©Imagery CNES/ Airbus Maxar Technologies. 66

5.9 Pre-dam construction time series. a) Line of sight (LOS) ground displacements for the upper (only in ascending geometry) and lower (in both ascending and descending geometries) landslide clusters (clusters shown in Fig. 5.8a). Crosses for average values and shaded areas for standard deviation. b) Cumulative precipitation (blue histograms) from June to May successive years (data from CHIRPS). 66

5.10 Pre-failure cumulative ground displacement from Sentinel-1 data. a) LOS ascending, b) LOS descending radar geometries; positive values in (a) and (b) refer to displacement toward the sensor. (c) Vertical motion; negative values correspond to subsidence. (d) Horizontal motion; negative values refer to westward motion. White dashed outline depicts the landslide-affected area. Black dashed rectangles in d) show additional active landslides. The landslide cluster partition is shown in d). The map extent is the same as in Fig. 5.2c. Background Google ©Imagery CNES/ Airbus Maxar Technologies. 67

5.11 Pre-failure PCA and ICA over the landslide area for the horizontal and vertical ground displacement components. The plots show the three largest principal components (left) and independent components (right) together with the reservoir water elevation (purple) and respective score maps for the spatial distribution. 68

5.12 Pre-failure time series. Horizontal (a) and vertical (d) ground displacements from the cluster extraction (clusters are shown in Fig. 5.10d): cross symbol for average values; shaded areas for standard deviation; black dashed lines for piecewise segmentation models; black dots for trend changes. Horizontal (b) and vertical (e) residuals after removing the piecewise segmentation model. (c) Cumulative precipitation (blue histograms) from June to May of the successive year (data from CHIRPS). (f) Monthly precipitation (blue histogram) same data source as in c). Dam reservoir water elevation (purple area) plotted both in c and f; vertical black dotted line marks the start of the landslide main failure. 69

5.13 Cross Wavelet Transform between monthly precipitation and pre-failure horizontal (upper row) and vertical (lower row) displacement residuals from October 2014 to March 2019. Color scale indicates the magnitude squared coherence; arrows indicate the phase difference between the two time series: arrows directed toward right for in-phase relationship; arrows directed toward left for anti-phase relationship. White dashed line shows the cone of influence where the edge effects might disturb the wavelet analysis results. . 71

5.14 Co-failure cumulative horizontal displacement from PlanetScope data. Color scale represents the magnitude value in meters; arrows show the horizontal direction (arrow size proportional with magnitude to emphasize the strongest motion). The landslide-affected area is delimited by a white dashed outline. The map extent is the same as in Fig. 5.2c. Background Google ©Imagery CNES/ Airbus Maxar Technologies. 72

5.15 Post-failure cumulative ground displacement from Sentinel-1 data. a) LOS ascending, b) LOS descending radar geometries; positive values in (a) and (b) refer to displacement toward the sensor. (c) Vertical motion; negative values correspond to subsidence. (d) Horizontal motion; negative values refer to westward motion. White dashed line outlines depict the landslide-affected area. Black dashed rectangles in d) show additional active landslides. The landslide cluster partition is shown in d). The map extent is the same as in Fig. 5.2c. Background Google ©Imagery CNES/ Airbus Maxar Technologies. 74
5.16 Post-failure PCA and ICA over the landslide area for the horizontal and vertical ground displacement components. The plots show the three largest principle components (left) and independent components (right) together with the reservoir water elevation (purple) and respective score maps for the spatial distribution. 75
5.17 Post-failure time series. Horizontal (a) and (b) and vertical (d) ground displacements from the cluster extraction (clusters are shown in Fig. 5.15d): cross symbol for average values; shaded areas for standard deviation; black dashed lines for piecewise segmentation models; black dots for trend changes. (c) Dam reservoir water elevation (purple area) and cumulative precipitation (blue histograms) from June to May of the successive year (data from CHIRPS); arrows show water level decrease. (e) Vertical ground displacement residual vertical; (f) Dam reservoir water elevation (purple area) and monthly precipitation (blue histogram) same data source as in c). Vertical black dotted line in c) and f) marks the start and the end of the landslide main failure. 76
5.18 Cross Wavelet Transform between monthly precipitation and post-failure horizontal (upper row) and vertical (lower row) displacement residuals from May 2019 to December 2021. Color scale indicates the magnitude squared coherence; arrows indicate the phase difference between the two time series: arrows directed toward right for in-phase relationship; arrows directed toward left for anti-phase relationship. White dashed line shows the cone of influence where the edge effects might disturb the wavelet analysis results. . 77
5.19 Schematic representation of the landslide reactivation and failure. Topographic profile (see profile position in Fig. 5.1a) shows the water level change for several years (blue lines), the landslide-affected area (red lines). (a) Pre-failure slow motion condition. Blue lines indicate the reservoir water level increase (dashed lines for alleged free water surface) for different years; orange arrows for pre-failure cumulative horizontal ground displacement for the period from October 2014 to March 2019. (b) Co-failure condition. Dark blue line for the maximum reservoir water elevation in March 2019; cyan lines for precipitation infiltration; black arrows for co-failure cumulative horizontal ground displacement for the period from 10 November 2018 to 28th May 2019. 80
5.20 Horizontal and vertical component displacement for the north-western (NW) and northern (N) slopes (the extracted areas are shown in Figs. 10d and 15d as black dashed rectangles), combining pre and post-failure datasets. The post-failure dataset was offset by the pre-failure cumulative value. . . . 81

6.1 Overview depicting the main geographic and geological features and tectonic complexities of Kamchatka peninsula. Tectonic edges are represented by thick white lines; the main fault systems are represented by polyline segments: thin and lighter color for the east Kamchatka fault zone (EKFZ) and thin and black color for the thrust fault system of the Kumroch thrust belt (KT). Dashed and dotted polygons show the central Kamchatka depression (CKD) zone; lighter dashed polygons represent the rupture zones of the larger historical earthquakes (Johnson and Satake, 1999; Bürgmann et al., 2005). The location of the 29 March 2017 Yuzhno-Ozernovskoe earthquake is symbolized by a star; black diamond symbolizes the locations of the main historical earthquakes discussed in the Seismic Data section. Natural Earth image is used as background (see Data and Resources). AFZ, Alpha fault zone; NFZ, Naturalist fault zone. The color version of this figure is available only in the electronic edition. 85

6.2 Spatial and temporal coverage of the Synthetic Aperture Radar (SAR) scenes used in the coseismic Differential Interferometric Synthetic Aperture Radar (DInSAR) analysis and the seismic sequence following the 29 March Mw 6.6 earthquake are shown (data from the Seismological Data Information System [SDIS] of Kamchatka Branch of Geophysical Survey of Russian Academy of Sciences [KB GS RAS] Earthquakes Catalog for Kamchatka and the Commander Islands (1962–present) (SDIS—KB GS RAS); (a) SAR image footprints: Advanced Land Observation Satellite (ALOS)-2 ascending (light dotted lines), ALOS-2 descending (dark dashed and dotted lines), and Sentinel-1A (light solid line); polyline segments show: in thin and lighter color the EKFZ (after Kozhurin et al., 2006; Kozhurin and Zelenin, 2017) and in thin and black color the KT; black triangles show the location of the seismic stations (see Data and Resources); white star shows the 29 March M w 6.6 earthquake; the scaled by magnitude, stars symbolize the aftershocks. Natural Earth image is used as background (see Data and Resources). (b) The seismic sequence in time domain is shown; sized and scaled stars emphasize the magnitude; lines show the SAR temporal baselines for ALOS-2 ascending (asc.; dotted lines), ALOS-2 descending (desc., dashed and dotted lines), and Sentinel-1A (solid line). The color version of this figure is available only in the electronic edition. 87

6.3 Comparison of the source parameters derived from the DInSAR geodetic modeling and the local and global seismological centers. The SDIS–KB GS RAS Earthquakes Catalog for Kamchatka and the Commander Islands (1962–present), focal mechanism solution as in (Chebrov et al., 2017); the Global Centroid Moment Tensor (Global CMT) catalog, the U.S. Geological Survey (USGS), the GEOFOrschungsNetz (GEOFON), the National Institute of Geophysics and Volcanology (INGV), and the Global Network of Broadband Seismic Stations (GEOSCOPE). Location uncertainty (ΔL) and depth uncertainty (ΔD) uncertainties are shown. The (*) symbol labels the seismological centers that provide centroid source location (geodetic model, Global CMT, USGS, and GEOSCOPE); the seismological centers that are not labeled provide the hypocenter or epicenter of the earthquake (SDIS—KB GS RAS, GEOFON, and INGV). 89

6.4 SAR interferometric images showing the coseismic displacement; each 2π cycle ("fringe") corresponds to the displacement (d) of half the wavelength of the radar signal in the line of sight (LoS) direction $\Delta\varphi = 4\pi \times d/\lambda$: (a) ALOS-2 asc. ($\lambda/2$ = 12 cm), (b) ALOS-2 desc. ($\lambda/2$ = 12 cm), and (c) Sentinel-1 desc. ($\lambda/2$ = 2:8 cm). Reference point used to transform the phase-wrapped displacement into absolute values is symbolized by black cross. The color version of this figure is available only in the electronic edition. 91

6.5 From top to bottom, ground displacement observed along the LoS, model-predicted displacement of best-fit slip-fault-plane solutions from the non-linear inversion projected in LoS direction and respective residuals for (a) ALOS-2 asc., (b) ALOS-2 desc., and (c) Sentinel-1 desc. datasets. The color version of this figure is available only in the electronic edition. 93

6.6 (a) Uncertainty analysis for the nonlinear inversion by performing 120 independent optimizations added to the data-correlated noise: standard deviations and parameter trade-off are shown; (b) slip distribution estimated from the linear inversion: the image shows the hanging wall relative to the footwall; slip magnitude is expressed by color scale; (c) slip distribution variance values; (d) fault model plane projected on the ground; star symbols show the epicenter or centroid locations from the different seismic and geodetic solutions (see Data and Resources); the main local fault system is shown by black lines; surface projection of the fault model is shown by light dotted line. The color version of this figure is available only in the electronic edition. 96

6.7 Conceptual diagram of the geodynamic interpretation of the 29 March 2017 earthquake fault model (not to scale). The color version of this figure is available only in the electronic edition. 97

7.1 Overview of the tectonics and seismicity of the RP. The red and black fault lines denote postglacial volcanic eruption fissures and opening fissures, respectively. Yellow dots show the seismicity from September 2019 to May 2021. Yellow lines show the extent of the HT geothermal fields on the peninsula, according to resistivity measurements1. Only the Reykjanes and Svartsengi geothermal fields are currently operated. The blue stars indicate the centres of uplift in Svartsengi and Krýsuvík, and the red star indicates the 2021 eruption site at Fagradalsfjall. The dashed green line shows the northeast-striking magmatic dyke intrusion according to InSAR analysis and seismicity. Main roads are in black, and topography is indicated as coloured background. Main landmarks referenced in the text are shown on the map. 102

7.2 Results from the poroelastic model. **a**, Map of maximum cumulative uplift from 6 January to 17 July 2020 (day 192). The colour map shows the vertical component calculated by combining the ascending and descending line-of-sight (LOS) displacements, in comparison with the predicted uplift (dashed contour lines) based on the poroelastic model for the same time period. The GNSS time series from the station marked by the white with black dot circle was used for the InSAR validation. The centre of uplift is obtained from the Mogi source inversion. The dashed line shows the cross-section profile in Fig. 3a. The location of the Fagradalsfjall eruption is shown as a red triangle. **b**, Temporal snapshots of surface uplift derived from the InSAR data compared with the model predictions. The double model curves for each snapshot show the values along the major and minor axes of the elliptic uplift pattern. **c**, Comparison of the predicted and measured ascending and descending LOS displacements at the pixel nearest to the uplift centre. The grey bars show the observed seismicity rates within 5 km distance from the centre. **d**, Free-air gravity anomalies (blue diamonds) from campaign measurements between 27 January and 20 April 2020 compared with the model predictions (solid curves) along the major and minor axes of the elliptic uplift pattern. Estimated error (shown as vertical lines) is ±5 µGal. 104

7.3 Sketch of fluid migration paths and aquifer location compared with observed seismicity and uplift. **a**, Maximum uplift (solid black line) and topography (dashed grey line) along the profile in Fig. 2a (x = 0 at Mt. Thorbjörn). **b**, Density of micro-earthquakes between February and August 2020 (gridded file and colour scale) estimated in a 1-km-wide band along the profile. The inferred BDT is indicated by the red dashed line. The manually relocated, largest events from the earthquake swarms from November (green circles) and December 2019 (grey circles) and at the beginning of unrest at Svartsengi (blue circles) are shown. The position and source intensity of the aquifer model are indicated. 106

7.4 Sketch of fluid migration paths and aquifer location compared with observed seismicity and uplift. **a**, Maximum uplift (solid black line) and topography (dashed grey line) along the profile in Fig. 2a (x = 0 at Mt. Thorbjörn). **b**, Density of micro-earthquakes between February and August 2020 (gridded file and colour scale) estimated in a 1-km-wide band along the profile. The inferred BDT is indicated by the red dashed line. The manually relocated, largest events from the earthquake swarms from November (green circles) and December 2019 (grey circles) and at the beginning of unrest at Svartsengi (blue circles) are shown. The position and source intensity of the aquifer model are indicated. 108

8.1 (A) 2014–2018 ground displacement of Anak Krakatau from the descending orbit in line-of-sight (LOS). (B) Orthomap of Anak Krakatau after its collapse, modified after Darmawan et al.(2020). Remnant structures are highlighted with yellow lines. (C) Displacement time series for the southwest flank from both ascending and descending orbits over a 4 yr observation period. Solid lines represent average values, while colored regions show standard deviation measured inside the black box marked in A. Gray-shaded areas mark magmatic intrusion events. Ascending (ASC) and descending (DSC) acquisition geometries are shown in the regional map inset. 114
8.2 (A–F) Decomposed interferometric synthetic aperture radar (InSAR) maps and (G–K) analogue modeling data showing ground deformation in vertical (z) and horizontal eastward (E or x) components. (A,B) 3 yr average flank motion due to décollement slip, which is compared against artificial décollement deformation (stage 1) in G and H. Both show a matching pattern of subsidence on the upper cone and lateral movement toward the west. Height increase of the lower flank in G is due to the purely horizontal décollement plane, which moves the lower block outward and thus causes an artificial height increase. (C,D) January-February 2017 intrusion. (E,F) June 2018 intrusion. (G,H) Analogue décollement deformation (stage 1). (I,J) Analogue intrusion (stage 2). These changes caused summit subsidence and lateral spreading of the cone. (K) Photo of experiment cone for reference. . 116
8.3 Particle displacement tracking from (A) two-stage analogue sandbox models, with (B,C) vertical views, and (D–G) profile views for both décollement slip (stage 1) and intrusion (stage 2). Décollement slip produced faults that are consistent with proposed long-term motion of Anak Krakatau. Subsequent intrusion reactivated these faults, potentially explaining increased flank slip during intrusion events. 118
8.4 Schematic illustration of deformations associated with (A) décollement and (B) intrusions at Anak Krakatau increasing décollement slip. 119

List of Tables

4.1 Elastic modelling parameters for point source model and 600 × 150 m rectangular crack source model for five-time intervals. 42

5.1 Summary information of the SAR and optical satellite remote sensing datasets. 57

6.1 Main characteristics of the SAR scenes are used in the current coseismic displacement analysis. ALOS, Advanced Land Observation Satellite; Asc., ascending; Desc., descending; TOPSAR, Terrain Observation with Progressive Scans SAR. 90

Eidesstattliche Erklärung

Hiermit versichere ich an Eides statt, dass ich

1. die Regeln der geltenden Promotionsordnung kenne und eingehalten habe und mit einer Prüfung nach den Bestimmungen der Promotionsordnung einverstanden bin;
2. die Dissertation selbst verfasst habe (Selbstständigkeitserklärung), keine Textabschnitte von Dritten oder eigener Prüfungsarbeit ohne Kennzeichnung übernommen habe und alle von mir benutzten Hilfsmittel und Quellen in meiner Arbeit angegeben habe;
3. Dritten weder unmittelbar noch mittelbar geldwerte Leistungen für Vermittlungstätigkeiten oder für die inhaltliche Ausarbeitung der Dissertation erbracht habe (d.h. die wissenschaftliche Arbeit wurde weder in Teilen noch in Gänze von Dritten gegen Entgelt oder sonstige Gegenleistung erworben oder vermittelt);
4. die Dissertation noch nicht als Prüfungsarbeit für eine staatliche oder andere wissenschaftliche Prüfung eingereicht habe;
5. die gleiche oder in wesentlichen Teilen ähnliche Arbeit nicht bei einer anderen Hochschule als Dissertation eingereicht habe; desgleichen habe ich keine andere Abhandlung als Dissertation eingereicht;
6. damit einverstanden bin, dass die Dissertation auch zum Zwecke der Überprüfung der Einhaltung allgemein geltender wissenschaftlicher Standards genutzt wird, insbesondere auch unter Verwendung elektronischer Datenverarbeitungsprogramme.

Hannover, March 28, 2024



Magdalena Vassileva

Curriculum Vitae

INFO AND CONTACTS

citizenship	Bulgarian
date of birth	26th Jan. 1988
languages	English, italian, bulgarian, german (basic)
e-mail	magdalena.stefanova.vassileva@gfz-potsdam.de
orcid	https://orcid.org/0000-0003-4650-0003

CURRENT POSITIONS

Feb. 2018 - present **Research Assistant**

based **German Research Centre for Geosciences (GFZ)**
Sec. 1.4 Remote Sensing and Geoinformatics
address Telegrafenberg, Building A 17, Room 01.12
14473 Potsdam, Germany

April 2021 - present **PhD student**

enrolled **Leibniz Universität Hannover (LUH)**
Institute of Photogrammetry and Geoinformation
PhD topic Satellite radar interferometry for tectonic and anthropogenic processes
Advisors Prof.Dr. Mahdi Motagh and Prof. Dr.-Ing. habil. Christian Heipke
email motagh@gfz-potsdam.de, heipkeipi.uni-hannover.de

MAIN RESEARCH TOPICS

Synthetic Aperture Radar Interferometry (InSAR)
Multi-scale and multi-sensor satellite data integration
Tectonic processes
Natural and anthropogenic geohazard

HIGHER EDUCATION

2011-2014 **Master degree in Environmental Engineering**

Faculty of Civil Engineering - University of Rome 'La Sapienza'

Specialization: Geotechnical and Hydraulic Defense of the Territory

Thesis title: An New Open Source Tool For Flood Extent Detection From Satellite SAR Imagery

Subject: Remote Sensing

Supervisor: prof. Mattia Giovanni Crespi

email: mattia.crespi@uniroma1.it

2007-2010 **1st level degree in Environmental Engineering**

Faculty of Civil Engineering - University of Rome 'La Sapienza'

Thesis title: Risk Mitigation on Urban Scale

Subject: Urban Planning

Supervisor: prof. Cutini Alessandro

email: alessandro.cutini@uniroma1.it

EMPLOYMENT HISTORY

Sep 2014 - Jan 2018 **GIS and Remote Sensing Specialist**

Employer: ITHACA (Information Technology for Humanitarian Assistance, Cooperation and Action)

Activities: Cartographic production for the Copernicus Emergency Management Service: optical and SAR satellite image processing, interpretation and geospatial data extraction; geospatial data management

Contact: Via P.C. Boggio 61, 10138 Turin, Italy

email: info@ithacaweb.org

Feb 2016 - Jan 2017 **Interferometric SAR analyst**

Employer: Collaboration with Geoworks

Activities: Research and application of SAR Interferometric techniques for landslide detection and monitoring

Contact: Via Molaretto 14,10050 Gravere, Italy

email: info@geoworks.it

PUBLICATION LIST

Peer-Reviewed

Engineering Geology, 2023 Vassileva, M., Motagh M., Roessner S. and Xia Z: Reactivation of an old landslide in north–central Iran following reservoir impoundment: results from multisensor satellite time-series analysis. **doi.org/10.1016/j.enggeo.2023.107337**

Geology, 2023 Zorn, E.U., Vassileva, M., Walter, T.R.,, Darmawan, H., Röhler, L., Amelung, F: Interactions of magmatic intrusions with the multiyear flank instability at Anak Krakatau volcano, Indonesia: Insights from InSAR and analogue modeling. Geology (2023) 51 (4): 340–344. **https://doi.org/10.1038/s43247-022-00491-w**

Commun Earth Environ, 2022 Walter, T.R., Zorn, E.U., Harnett, C.E. et al.: Influence of conduit and topography complexity on spine extrusion at Shiveluch volcano, Kamchatka. Commun Earth Environ 3, 169 (2022). https://doi.org/10.1038/s43247-022-00491-w

Nat. Geosci., 2022 Flóvenz, Ó.G., Wang, R., Hersir, G.P. et al.: Cyclical geothermal unrest as a precursor to Iceland's 2021 Fagradalsfjall eruption. - Nat. Geosci. 15, 397–404. https://doi.org/10.1038/s41561-022-00930-5

Sci.Rep., 2021 **Vassileva, M.**, Al-Halbouni, D., Motagh, M., Walter, T., Dahm, T., Wetzel, H.-U.: A decade-long silent ground subsidence hazard culminating in a metropolitan disaster in Maceió, Brazil. - Scientific Reports, 11, 7704. https://doi.org/10.1038/s41598-021-87033-0

IEEE, 2021 Ghosh, B., Motagh, M., Haghshenas Haghighi, **M., Stefanova Vassileva**, M., Walter, T., Maghsudi, S.: Automatic detection of volcanic unrest using blind source separation with a minimum spanning tree based stability analysis. - IEEE Journal of Selected Topics in Applied Earth Observations and Remote Sensing, 14, 7771-7787. https://doi.org/10.1109/JSTARS.2021.3097895

Frontiers., 2021 Shevchenko, A., Dvigalo, V. N., Zorn, E., **Stefanova Vassileva, M.**, Massimetti, F., Walter, T., Svirid, I. Y., Chirkov, S. A., Ozerov, A. Y., Tsvetkov, V. A., Borisov, I. A.: Constructive and Destructive Processes During the 2018–2019 Eruption Episode at Shiveluch Volcano, Kamchatka, Studied From Satellite and Aerial Data. - Frontiers in Earth Science, 9, 680051. https://doi.org/10.3389/feart.2021.680051

BSSA, 2020 **M Vassileva**, M Motagh, T R Walter, H-U Wetzel, S L Senyukov: The 29 March 2017 Yuzhno-Ozernovskoe Kamchatka Earthquake: Fault Activity in An Extension of the East Kamchatka Fault Zone as Constrained by InSAR Observations.- Bulletin of the Seismological Society of America (2020) 110 (3): 1101–1114. doi.org/10.1785/0120190174

TEJR, 2017 **M Vassileva**, F Giulio Tonolo, P Riccardi, D Lecci, P Boccardo, G Chiesa: Satellite SAR Interferometric Techniques In Support To Emergency Mapping. - EUROPEAN JOURNAL OF REMOTE SENSING, 2017VOL. 50, NO. 1, 464–477 doi.org/10.1080/22797254.2017.1360155

Conference papers

ISPRS, 2021 Piter, A., **Stefanova Vassileva, M.**, Haghshenas Haghighi, M., Motagh, M.: Exploring Cloud-Based Platforms for Rapid Insar Time Series Analysis. - International Archives of the Photogrammetry, Remote Sensing and Spatial Information Sciences - ISPRS Archives, XLIII-B3-2021, 171-176. https://doi.org/10.5194/isprs-archives-XLIII-B3-2021-171-2021

IEEE, 2015 **M Vassileva**, A Nascetti, F GiulioTonolo, P Boccardo: Unsupervised Flood Extent Detection From SAR Imagery Applying Shadow Filtering From SAR Simulated Image. doi.org/10.1109/IGARSS.2015.7326372

Wissenschaftliche Arbeiten der Fachrichtung Geodäsie und Geoinformatik der Leibniz Universität Hannover

(Eine vollständige Liste der Wiss. Arb. ist beim Geodätischen Institut, Nienburger Str. 1, 30167 Hannover erhältlich.)

Nr. 371	CHENG, Hao:	Deep Learning of User Behavior in Shared Spaces (Diss. 2021)
Nr. 372	MUNDT Reinhard Walter:	Schätzung von Boden- und Gebäudewertanteilen aus Kaufpreisen bebauter Grundstücke (Diss. 2021)
Nr. 373	WANG, Xin:	Robust and Fast Global Image Orientation (Diss. 2021)
Nr. 374	REN, Le:	GPS-based Precise Absolute and Relative Kinematic Orbit Determination of Swarm Satellites under Challenging Ionospheric Conditions (Diss. 2021)
Nr. 375	XU, Wei:	Automatic Calibration of Finite Element Analysis Based on Geometric Boundary Models from Terrestrial Laser Scanning (Diss. 2021)
Nr. 376	FENG, Yu:	Extraction of Flood and Precipitation Observations from opportunistic Volunteered Geographic Information (Diss. 2021)
Nr. 377	YANG, Chun:	A hierarchical deep learning framework for the verification of geospatial databases (Diss. 2021)
Nr. 378	MEHLTRETTER, Max:	Uncertainty Estimation for Dense Stereo Matching using Bayesian Deep Learning (Diss. 2021)
Nr. 379	KAZIMI, Bashir:	Self Supervised Learning for Detection of Archaeological Monuments in LiDAR Data (Diss. 2021)
Nr. 380	PETERS, Torben:	Learning Multi-View 2D to 3D Label Transfer for Semi-Supervised Semantic Segmentation of Point Clouds (Diss. 2022)
Nr. 381	WASSINK, Martin:	Kommunal- und Regionalentwicklung durch Kooperation und Teilung von Verantwortung in ländlichen Räumen - eine multiperspektivische Untersuchung an Beispielen aus dem Raum Steinwald/Fichtelgebirge (Diss. 2022)
Nr. 382	GOLDSCHMIDT, Jürgen:	Die Berücksichtigung künftiger Entwicklungen bei der Verkehrswertermittlung (Diss 2022)
Nr. 383	KRUSE, Christian:	Impact maps from bomb craters detected in aerial wartime images using marked point processes (Diss. 2023)
Nr. 384	ZOURLIDOU, Stefania:	Traffic Regulation Recognition from GPS Data (Diss. 2023)
Nr. 385	SLEDZ, Artuom:	Thermal anomaly detection based on information fusion from optical and infrared images (Diss. 2023)
Nr. 386	WITTICH, Dennis:	Deep Domain Adaptation for the Pixel-wise Classification of Aerial and Satellite Images (Diss. 2023)
Nr. 387	SINGH, Vishwa Vijay:	Lunar Laser Ranging - Improved Modelling and Parameter Estimation (Diss. 2023)
Nr. 388	HARTMANN, Jens:	Hochgenaue 3D-Erfassung von Großstrukturen durch kinematisches terrestrisches Laserscanning (Diss. 2023)
Nr. 389	ZHUGE, Xia:	Characterizing slope instability kinematics by integrating multi-sensor satellite remote sensing observations (Diss. 2023)
Nr. 390	DOROZYNSKI, Mareike Marianne:	Image Classification and Retrieval in the Context of Silk Heritage using Deep Learning (Diss. 2023)
Nr. 391	KNABE, Annike:	New Concepts for Gravity Field Recovery using Satellites (Diss. 2023)
Nr. 392	KALIA, Andre:	Landslide activity detection based on nationwide Sentinel-1 PSI datasets (Diss. 2023)
Nr. 393	BROCKMEYER, Marco:	Modellierung von Bodenbewegungen anhand heterogener Messverfahren am Beispiel der niedersächsischen Landesfläche (Diss. 2023)
Nr. 394	ZHANG, Mingyue:	Characteristics and Benefits of Differential Lunar Laser Ranging (Diss. 2023)
Nr. 395	DENNIG, Dirk:	Entwicklung eines kinematischen Profilvermessungssystems am Beispiel Kranbahnvermessung (Diss. 2024)
Nr. 396	FUEST, Stefan:	Nudging travelers to societally favorable routes by means of cartographic symbolization (Diss. 2024)
Nr. 397	MOFTIZADEH, Rozhin:	Advanced Particle Filtering for Vehicle Navigation based on Collaborative Information (Diss. 2024)
Nr. 398	VASSILEVA, Magdalena Stefanova:	Satellite Radar Interferometry for Geohazards: from ground deformation to processes understanding (Diss. 2024)